A Numerical and Experimental Investigation of the Mitigation of the Unbalanced Magnetic Pull in a Bridge Configured Induction Machine

Sivaramakrishnan N.

भारतीय प्रौद्योगिकी संस्थान गुवाहाटी
Indian Institute of Technology Guwahati

A Numerical and Experimental Investigation of the Mitigation of the Unbalanced Magnetic Pull in a Bridge Configured Induction Machine

A

Thesis submitted

for the award of the degree of

Doctor of Philosophy

By

Sivaramakrishnan N.

DEPARTMENT OF MECHANICAL ENGINEERING

INDIAN INSTITUTE OF TECHNOLOGY GUWAHATI

GUWAHATI - 781 039, ASSAM, INDIA

AUGUST 2019

To

My Parents

Smt Amsavalli Natesan and Shri Natesan Manickam

Certificate

This is to certify that the thesis entitled “**A Numerical and Experimental Investigation of the Mitigation of the Unbalanced Magnetic Pull in a Bridge Configured Induction Machine**”, submitted by **N Sivaramakrishnan** (10610323), a research scholar in the *Department of Mechanical Engineering, Indian Institute of Technology Guwahati*, for the award of the degree of **Doctor of Philosophy**, is a record of an original research work carried out by him under our supervision and guidance. The thesis has fulfilled all requirements as per the regulations of the institute and in our opinion has reached the standard needed for submission. The results embodied in this thesis have not been submitted to any other University or Institute for the award of any degree or diploma.

Dated:
Guwahati.

Dr. Karuna Kalita
Associate Professor
Department of Mechanical Engineering
Indian Institute of Technology Guwahati
Guwahati - 781 039, Assam, India.

Abstract

There is an increasing trend for integration of an electrical motor/generator into the overall rotating machine with a greater demand of higher power densities for economics and for efficiency. These features mean that there is an ever-increasing opportunity to exploit the capability of electrical motors/generators to exert controllable transverse forces on the rotor for the multiple purposes of minimising vibration, offsetting deflections due to external loads, alleviating bearing loads and enabling intelligent condition monitoring. Bridge configured winding (BCW) is a special stator winding scheme which can be used for both torque production as well as controllable transverse force production. One of the characteristics of the bridge configured winding is the capability to induce electromotive force for an eccentric rotor for passive control of rotor vibration. Eccentricity of the rotor has a profound effect on the bridge currents in a BCW induction machine. However, the effect of the eccentricity of the rotor on the bridge currents are not fully understood. An asymmetry in the magnetic fields in the airgap of an induction machine may arise due to the rotor eccentricity and due to the electromagnetic asymmetry. Due to the asymmetric distribution of the magnetic field a net radial magnetic force called Unbalanced Magnetic Pull (UMP) is generated towards the shortest airgap. The bridge configured winding has the capability to create this asymmetry of the magnetic fields in controlled manner to produce controllable transverse force by connecting voltage or current sources across the bridges. However, the nature of the bridge currents and the corresponding transverse forces produced are not fully understood.

The thesis establishes a relationship between the eccentricity present in the machine with the frequency components of the bridge currents. A finite element code for a 37 kW, 4-pole induction machine with BCW stator winding having 60 stator slots and 48 rotor bars

has been developed. The coupled magnetic field and circuit equation has been solved to calculate the bridge currents and the corresponding transverse forces. This machine has also been analysed using a commercial finite element package called OPERA. Torque speed characteristics of the machine has been developed.

An experimental setup has been developed to verify the numerical results with the experimental results. The induction machine used in the setup is a 37kW, 4-pole which has 60 stator slots and 48 rotor bars. The experimental setup has two discs where known unbalance masses can be incorporated. The original winding of the machine is replaced with an equivalent BCW stator winding. The bridge currents and the rotor responses have been used to compare the numerical results.

Further investigations of the bridge currents have been carried to develop a relationship between the dynamic eccentricity and the frequency components induced. An attempt has been made to develop a relationship between known unbalance masses or known eccentricity with the frequency component of the bridge currents. Several similar numerical experiments are also conducted to develop relationship between the known static eccentricity and the frequency component of the bridge currents. For this purpose a numerical model of a 4-pole induction machine with BCW stator winding having 36 stator slots and 26 rotor bars has been developed using COMSOL MULTIPHYSICS®. Active vibration capability of BCW has been demonstrated by supplying currents in a single bridge or in combination of bridges. The rotor orbits have been plotted to demonstrate vibration control.

Contents

List of Figures

List of Tables

List of Acronyms

AC	Alternating Current
AMB	Active magnetic bearing
BCW	Bridge configured winding
EMF	Electromotive Force
FEM	Finite element method
FFT	Fast fourier transform
UMP	Unbalanced magnetic pull

List of Symbols

$\overrightarrow{A}$	Magnetic vector potential
B	Magnetic flux density
$\underline{\hat{B}}_1$	Space vector representation of two pole magnetic field
$\underline{\hat{B}}_3$	Space vector representation of six pole magnetic field
d_r	Outer diameter of rotor
E	Electric field intensity
f_s	Stator supply frequency
f_{rot}	Rotor rotational frequency
$i_{phase\_A}, i_{phase\_B}, i_{phase\_C}$	Three phase currents of the stator
$\{\mathbf{i}_s\}_{u\times 1}$	Stator circuit current vector
$\overrightarrow{J}$	Current density
$\{\mathbf{J}_s^e\}_{n\times 1}$	Stator nodal current vector
$\lvert\,\mathbf{J}\,\rvert$	Jacobian
$[\mathbf{S}]_{n\times n}$	Global magnetic stiffness matrix
$\overrightarrow{k}$	Unit vector parallel to z axis
$[\mathbf{L}_{end}]$	End winding inductance of the stator coil
l_r	Axial length of the rotor
l	Length of the rotor bar
μ	Permeability
$\{\mathbf{N}\}$	Shape function
n	Number of nodes
ν	Magnetic reluctivity

n_0	No. of turns in the stator winding
p	No. of pole pair
$[\mathbf{P}_s]_{n\times z}$	Global matrix for the stator coil excitations
R	Stator coil resistance
$[\mathbf{R}_s]_{u\times u}$	Stator coil resistance matrix
S_s	Cross sectional area of the stator coil
σ_r	Electrical conductivity of the rotor bar
$[\mathbf{T}]_{z\times u}$	Transformation matrix for the transformation of phase currents to the coil side currents
t	Time
u	Number of stator circuit current
$\{\mathbf{u}_s\}_{u\times 1}$	Stator coil voltage vector
V	Electric Scalar potential
x, y	Cartesian coordinates
ξ, η	Natural coordinate system
z	Number of coil sides

1

Introduction

Contents

1.1 Introduction

Induction machines are widely used in industrial application because of its simple and rugged in construction, cheaper in cost and it can run in any kind of environment. Nowadays, most of the machines used are three phase induction machine which is good in speed regulation, high self-start and high power factor. Induction machines consist of two main parts: stator and rotor. Stator is a stationary member and it is made up of numbers of stamping of thin laminated steel sheets in which different slots are made to incorporate the three phase winding circuit which is connected to a three phase AC supply. A rotor is a cylindrical rotating member which is constructed by stacking of steel sheet laminations. Figure 1.1 shows the induction machine.

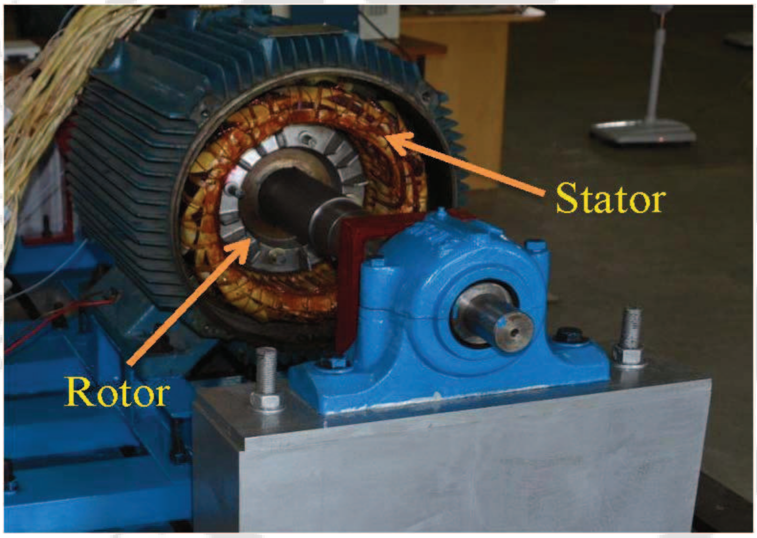

Figure 1.1: An induction machine.

1.2 Eccentricity in Rotors

The manufacturing tolerances in induction machines and misalignment of bearings can produce rotor eccentricity. Basically, rotor eccentricities appear in one of the two forms: static and dynamic. It can also be a combination of both the forms. Figure 1.2 shows the concentric rotor. Concentric rotor exists only when the machine is said to be perfectly balanced.

1.2.1 Static eccentricity

Static eccentricity is caused when the centre of axis of rotation of the rotor is not being aligned with the bearing axis while the rotor is still rotating about its own axis. Excessive static eccentricity

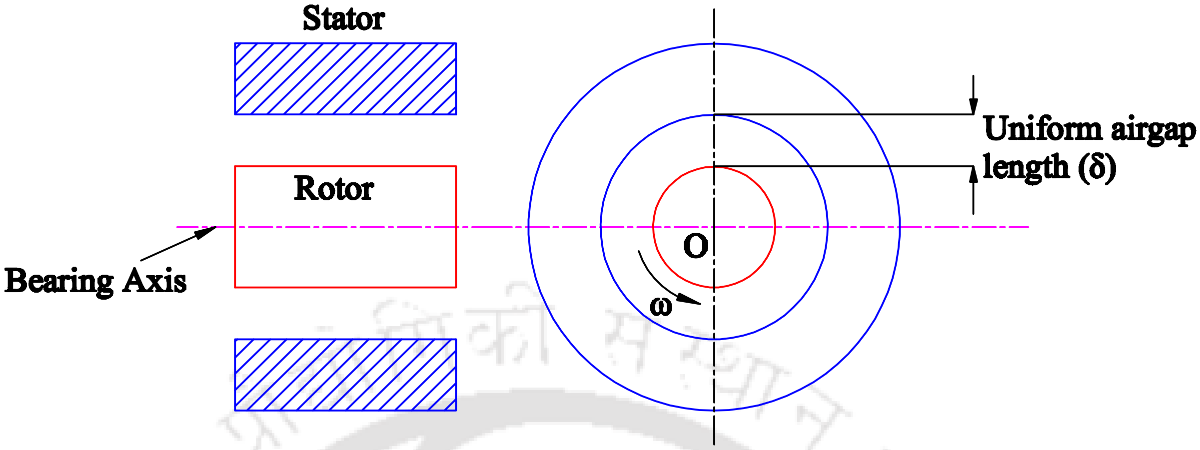

Figure 1.2: Concentric rotor.

can also occur when the bearings are incorrectly positioned or become worn. Figure 1.3 shows the static eccentricity in the rotors with the stator.

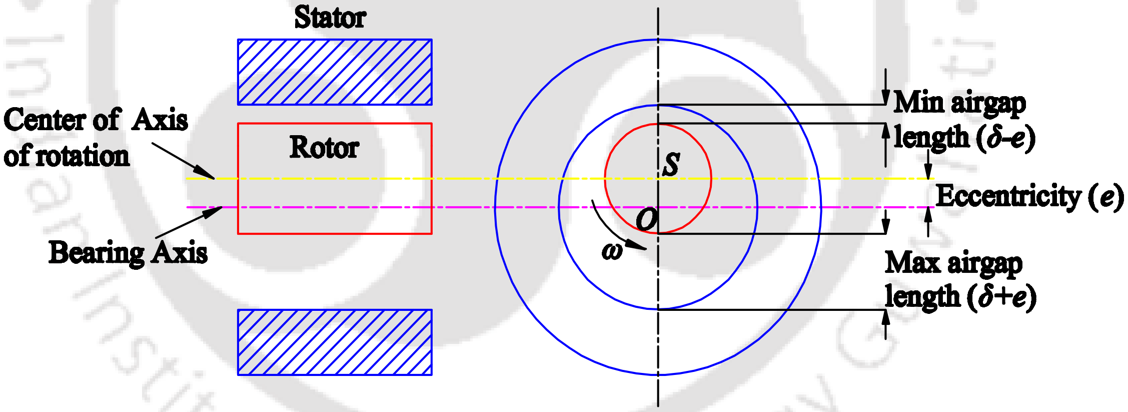

Figure 1.3: Static eccentricity in the rotor.

1.2.2 Dynamic eccentricity

Dynamic eccentricity is caused by the centre of rotations of the rotor not being aligned with the rotor axis. The centre of rotation can be a circular, elliptical or in any kind of shape. The usual causes of dynamic eccentricity are also manufacturing tolerances, wear and incorrect manufacture. Rotor 'whirl' near a critical speed is another source of dynamic eccentricity and is an important consideration in larger, flexible-shaft machines. Figure 1.4 shows the static and dynamic eccentricity in the rotor with the stator. Obviously, static and dynamic eccentricity can exist simultaneously.

In both the cases significant forces can be produced that try to pull the rotor even further from the concentric position.

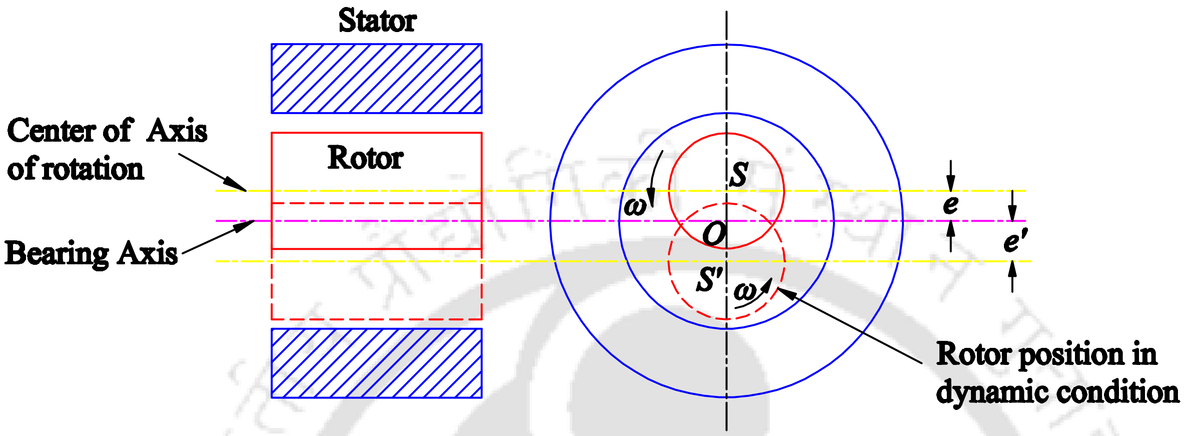

Figure 1.4: Static and dynamic eccentricity in the rotor.

1.3 Unbalanced Magnetic Pull(UMP)

Any form of eccentricity of the rotor of an electrical machine with respect to the stator will give rise to a transverse force on the rotor directed towards the smaller air-gap. This force is known as unbalanced magnetic pull (UMP). If the rotor becomes eccentric then unbalanced magnetic pull (UMP) occurs. The phenomenon can be described as an imbalance of the radial and tangential forces acting upon the rotor (or stator) surface such that a net radial force is developed. The UMP tends to further increase the rotor eccentricity and may severely degrade the performance of the machine, causing acoustic noise, vibration, excessive wear of bearing, rotor and stator rubbing. It can also lead to a reduction in the critical speed, which is an important criterion in high-speed machine design. Static UMP is caused by the rotor axis being positioned parallel to, rather than being on, the stator axis and is due to manufacturing tolerances. Dynamic UMP is caused by the rotor not rotating about its axis; this could be produced by either manufacturing tolerances or rotor “whirl” near a critical speed.

The usual approach for predicting UMP is to approximate the air-gap length by a constant plus a cosine term due to the rotor eccentricity.

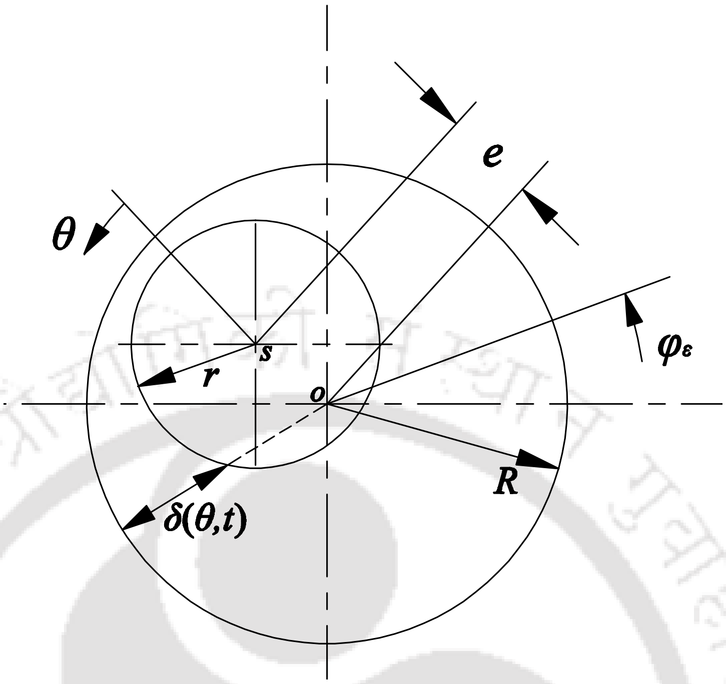

Figure 1.5: Air-gap of a motor with an eccentric rotor.

$$\delta\left(\theta,t\right) = \delta_m\left[1-\epsilon\cos\left(\theta-\omega_\varepsilon t-\varphi_\varepsilon\right)\right] \tag{1.1}$$

where ϵ is relative eccentricity, $\varepsilon = \left\{\frac{e}{\delta_m}\right\} = \left\{\frac{e}{R-r}\right\}$, e is eccentricity of the rotor, R is the radius of the stator, θ is the arc angle, r is the radius of the rotor, δ_m is the average air-gap length, φ_ε is phase angle, ω_ε is whirling frequency, $\omega_\epsilon = 0$.

This air-gap length is inverted to produce a permeance expression, in terms of a Fourier series, called air-gap permeance.

$$\wedge\left(\theta,t\right) = \left\{\frac{1}{\delta\left(\theta,t\right)}\right\} = \sum_{\lambda=0}^{\infty}\wedge_\lambda\cos\left(\lambda\left(\theta-\omega_\varepsilon t-\varphi_\varepsilon\right)\right) \tag{1.2}$$

The fourier co-efficient are,

$$\wedge_\lambda = \begin{cases} \frac{1}{\delta_m}, & \text{when } (\lambda = 0) \\ \frac{2}{\delta_m}\frac{1}{\sqrt{1-\varepsilon^2}}\left\{1-\frac{\sqrt{1-\varepsilon^2}}{\varepsilon}\right\}^{\lambda}, & \text{when } (\lambda > 0) \end{cases} \tag{1.3}$$

The expression for the air-gap MMF is usually assumed to be a sinusoid of known amplitude. The permeance series will modulate the MMF to give the fundamental flux density field together with a series of harmonic components of order both greater and lower than the fundamental.

1.4 Bridge configured winding

The bridge configured winding (BCW) can produce both torque as well as a controllable transverse force. The bridge configured winding was proposed by Khoo [1]. Figure 1.6 shows the double layered distributed three phase, four pole winding. The stator winding connection has been done according to the circuit connection as shown in Figure 1.7. An additional 2-pole magnetic field has been introduced purposefully with the 4-pole fundamental magnetic field by short circuiting the bridges. By the superimposition of this 2-pole magnetic field and 4-pole magnetic field can produce a force called levitation force or transverse force which can be used to counteract the UMP which may be present in the system due to the eccentric position of the rotor. Three isolated levitation power supply (i_{Alev}, i_{Blev}, and i_{Clev}) BCW can be applied along with the three phase main supply (i_{Aph}, i_{Bph}, and i_{Cph}). It is also possible to generate the radial forces in a passive manner simply by shot-circuiting the bridges S1, S2 and S3.

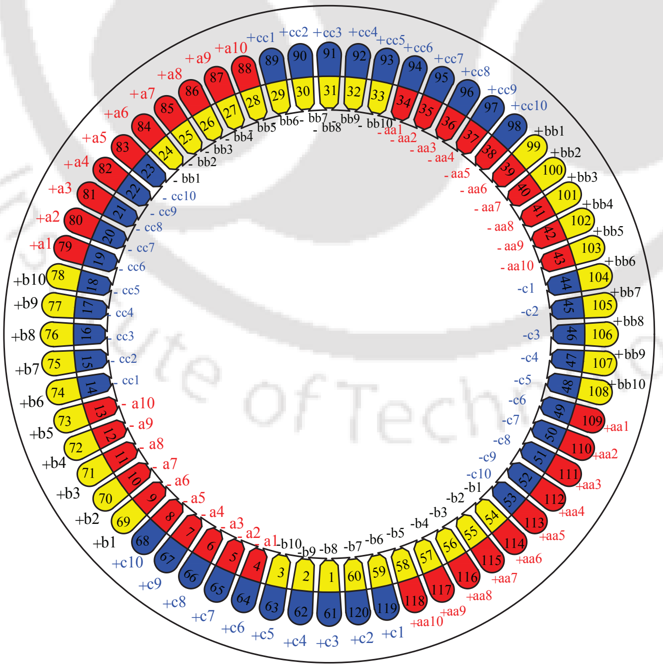

Figure 1.6: A winding scheme of a distributed double layered winding.

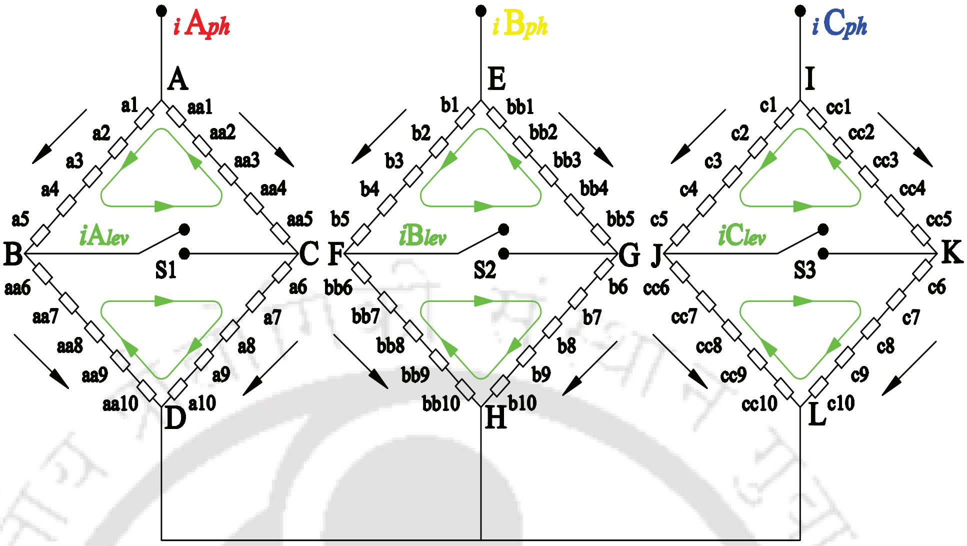

Figure 1.7: A bridge configured winding circuit.

The current responsible for the torque production are divided into two parallel paths in each phase. Consider Phase-A winding connection of the induction motor, with two parallel branches comprising ten series-connected coils each as shown in Figure 1.7. The currents flowing in arms AB and CD are same in direction and magnitude but both the arms were connected in diametrically opposite to each other at a span of 180^0. Similarly, AC and BD arms were connected in the same fashion. The branches AB and CD have the same polarity while both branches AC and BD have the opposite polarity with respect to AB and CD. The branches AB and CD have similar feature and they can be grouped together. Likewise, branches AC and BD are set to be an another group. These two coil groups are placed diametrically opposite to each other in the stator slots. The current flowing across BC is called levitation current or bridge current and it is very small when compared to the main supply current flowing across AD.

1.4.1 Working principle of bridge configured winding

An uneven flux density distribution due to rotor eccentricity or unbalance present in the system can produce an additional flux of pole pair ($p\pm1$), (where, p is the number of fundamental pole pairs). Any one of this additional flux pole pair can interact with the fundamental pole pair flux, a significant net transverse force (UMP) can be produced. BCW scheme works on this principle. An additional 2-pole field has been introduced purposefully with the 4-pole fundamental field by short circuiting the bridges. By superimposing this 2-pole field and 4-pole field, a levitation force can be produced to counteract the UMP which is already present in the system. The induced bridge currents has the capability of producing an additional 2-pole and 6-pole magnetic flux density components. These 2-pole and 6-pole fields can interact with the 4-pole main field and thus a radial magnetic flux density can be produced in the air gap. The radial magnetic flux density by the 2-pole, 4-pole and 6-pole fields has been given by Equation 1.4,

$$B(t,\varphi) = \mathrm{Re}\left\{\underline{\hat{B}}_1(t)\,e^{-j\varphi} + \underline{\hat{B}}_2(t)\,e^{-j2\varphi} + \underline{\hat{B}}_3(t)\,e^{-j3\varphi}\right\} \tag{1.4}$$

where t is the time, φ denotes the angular co-ordinate along the rotor periphery, $\underline{\hat{B}}_1$, $\underline{\hat{B}}_2$ and $\underline{\hat{B}}_3$ are the space vectors of the 2-pole, 4-pole and 6-pole magnetic flux density distribution in the airgap respectively.

Consider the Phase A winding connection of the Induction machine shown in Figure 1.7. When the induction machine is supplied with the main supply, the current will flow through the arm AB and BD in one path as well as AC and CD in an another path. A four pole magnetic field has been formed according to the winding pattern as shown in Figure 1.8. It has been realized that the presence of unbalance in the system, the current will flow through the arm BC, as soon as it is being short circuited and it is called as levitation current i_{Alev}. The levitation current i_{Alev} will flow in the arm AB through the arm CA in order to make a closed loop path. Similarly, the levitation current i_{Alev} will flow in the arm DB through CD. It has been observed in the arms AC and BD that the levitation current i_{Alev} flows in the opposite direction to the direction of main supply current i_{Aph} shown in Figure1.7. The polarity of the current flowing in the arms AC and BD have been reversed due the opposite direction of flow of levitation current which is shown in Figure 1.9 and thus the 2-pole field has been formed. The super imposed levitation field is a pole pair different with the main pole pair field. As a result, a net transverse force called levitation force is exerted on the rotor as shown in Figure 1.10. Therefore, a levitation force can be produced in any arbitrary direction with the combination of the bridge connections. The levitation force production by the interactions of a difference of one pole pair between the fields has been proved mathematically in [1].

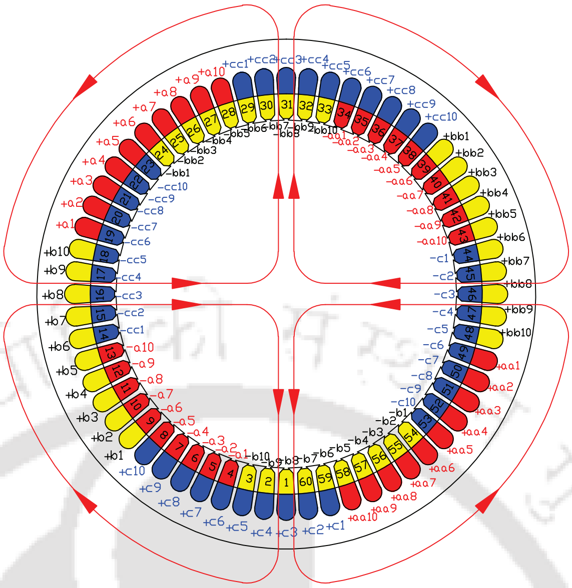

Figure 1.8: Main 4-Pole field formation.

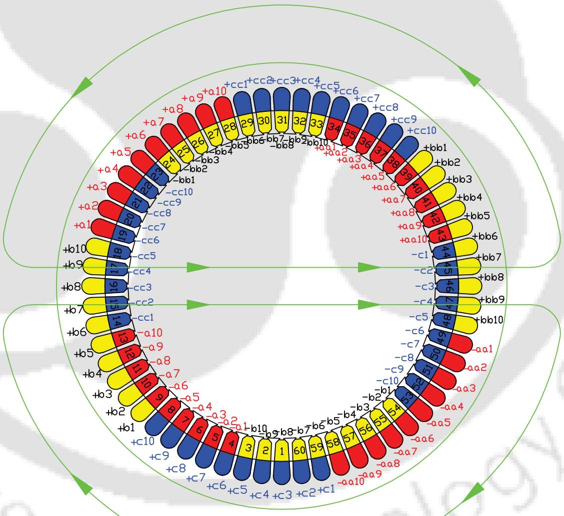

Figure 1.9: 2-Pole field formation.

1.5 Motivation

In general the flexible rotors are used for the most of the industrial applications where the length of the rotor is considerably quite long. In addition to the rotor, other components such as turbine, impeller may be added to the shaft system. Due to this addition of such components the stiffness of the system may decrease which may affect in the critical speed of the system.

- Attention has been focused on the various analytical models and experimental works on reduc-

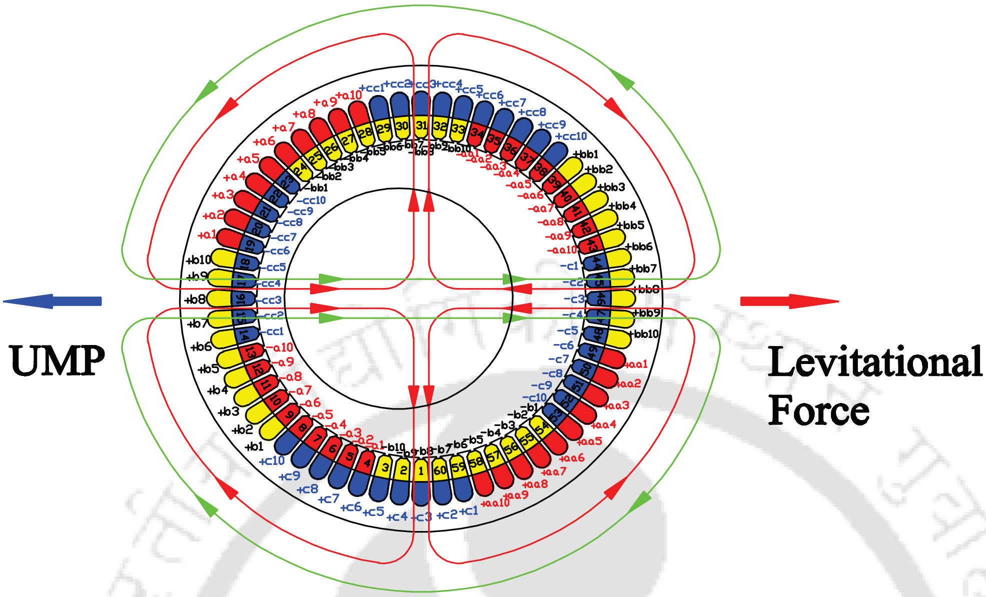

Figure 1.10: Superimposition of 4-Pole and 2-Pole fields.

ing the UMP in an induction machines.

- Attention has been given to the existing work on controlling UMP by means of different kind of winding scheme. These are series and parallel windings, equalizing winding connection, dual set of winding connection and single set of winding connection. It has been noticed that very limited experimental works exists.
- In dual set of winding connection, the primary winding carries the motor currents which drive the rotor, while the secondary winding carries the levitation currents which produce controllable transverse force. The controlling winding has been wounded in the same slot along with main stator winding. The dual set of winding produces less effectiveness in the total torque production and for this reason single set of winding has been proposed.
- Single set of winding can eliminate the drawbacks of the dual set of winding. It requires a relatively low current and low voltage for the radial force production.

1.6 Aim of the work

The main objective of this present work is to develop a relationship between the eccentricity of the rotor with the induced bridge currents in an induction machine with bridge configured winding in the stator. To achieve this aim the following tasks have been undertaken.

- A coupled numerical model of magnetic field equation and electric circuit equation has been developed to study the effect of eccentricity on bridge currents in an induction machine with bridge configured winding as the stator winding.
- An experimental rig has been developed to study the characteristics of the bridge currents with respect to the eccentricity of the rotor of an induction machine with bridge configured winding in the stator.
- A correlation between the dynamic eccentricity and the bridge currents has been developed using the bridge currents obtained from experiments.
- A series of numerical simulations has been carried out to develop a relationship between the static eccentricity and the bridge currents in an induction machine with bridge configured winding as the stator winding.
- A controller has been developed to demonstrate the vibration control.

1.7 Structure of the work

This work consists of three major topics: (1) Two dimensional FEM analysis of a BCW induction machine, (2) Development of an experimental rig set up for the demonstration of passive vibration control, (3) Establishment of a correlation between known mass unbalances and three phase bridge currents (4) Development of a controller for an active vibration control.

This thesis is organized in the following chapters:

Chapter 1 introduces the effect of eccentricity into the unbalanced magnetic pull (UMP) in the induction machine.

Chapter 2 illustrates briefly about the literature on the attenuation of vibration by using different kind of stator windings. Methods of calculating the UMP and factors affecting the UMP such as eccentricity, rotor skew and critical speed are also discussed in this chapter.

Chapter 3 discusses the development of the coupled magnetic field and electric circuit equation of a bridge configured based induction machine. A 2D finite element code has been developed in MATLAB to investigate the effect of different eccentricities on the bridge currents.

Chapter 4 explains about the development of a 2D finite element model of bridge configured based induction machine by using a commercial FE electromagnetic solver OPERA 2D. The FE model has been simulated for steady state and transient analysis.

The design and development of the experimental rig set up has been demonstrated in **Chapter 5**. A modified 37 kW three phase, four pole induction machine has been used. In this chapter, the characteristics of the experimental set up have been studied. Bridge currents and rotor displacements have been measured for the demonstration of passive vibration control.

Chapter 6 illustrates the experimental demonstration of developing the correlation between measured three phase bridge currents and the known mass unbalance. The experiments have been conducted at 10, 12 and 14 Hz main supply frequencies of input voltages and the three phase bridge currents have been measured. The peak amplitude of the measured three phase bridge currents at which $0.5f_s$, f_s, $1.5f_s$, $2f_s$ have been plotted against the known unbalance masses. It also discusses about a series of numerical experiments that has been carried out for developing a relationship between the static eccentricity of the rotor and the bridge currents.

Chapter 7 discusses the development of the controller set up for the active vibration control in the bridge configured induction machine.

Chapter 8 summaries the thesis work and discusses the results obtained.

2

Literature Review

Contents

2.1 Introduction

This chapter presents a comprehensive review of the various literature on vibration control in induction motors using different sets of stator windings. Non-uniformity in the airgap, caused due to the misalignment of the rotor, imbalances the magnetic flux density distribution. This asymmetric flux density can produce a transverse force in the direction of shortest airgap called unbalanced magnetic pull (UMP). The UMP further tends to increase the rotor eccentricity and also causes stator rotor rubbing action, vibration, acoustic noises, wear and tear of the internal parts of the induction machine and severely degrade the machine's performances. Over 50 years ago, researchers have been started to analyse the source, nature and the dynamics of UMP ([2] and [3]).

Later, the mitigation of UMP by using different sets of winding connections along with the main stator primary winding was analysed ([4]). There are some significant differences in the existing works on controlling of UMP with the help of built-in force actuator such as series winding connection, parallel winding connection, combination of series and parallel connection, dual set of winding connection, single set of winding connection. A transverse force exists in an electric machine when two or more magnetic fields are present and the difference between the pole pairs of any two magnetic fields is one. The transverse force that exists between the interactions of these magnetic fields can act in the opposite directions of the UMP. The bridge configured winding connection which has the capability of producing both torque as well as controllable transverse force was proposed by Khoo ([1]).

Literature review has been classified mainly based on the different methods of calculation, various methodologies of winding connections, numerical methods, experimental analysis and they are discussed individually:

- Calculation of UMP.
- Factors affecting the UMP.
- Stator windings.
- Electromagnetic and mechanical Interactions.

- Controlling of Motor vibrations.
- Condition monitoring of Induction machines.
- Search coil winding design.

2.1.1 Calculation of UMP

Frohne [2] studied the practical importance of UMP and developed a simple analytical model for the UMP calculation and established a method for damping the UMP. The static deflection of rotor is one of the main reasons for generation of UMP. The magnitude of the UMP is proportional to the eccentric deflection of the rotor δ_ϵ and, therefore, has the characteristic of the spring force. Whereas the mechanical spring acts in such a way that it tends to reduce the imposed deflection, UMP acts in the same direction as the deflection i.e., it tends to increase it. The result of this is that UMP must be regarded as a negative spring force. The static deflection of the shaft h_{mech} calculated for the rotor weight alone, is increased to $h = (1 + 1.1)h_{mech}$. The second important criterion is the critical speed of the shaft, which is

$$\omega_{eff} = \sqrt{\frac{K_{mech} - K_{mag}}{m_L}} \tag{2.1}$$

where, K_{mech} is the spring constant of the shaft and $K_{mech} = \left\{\frac{G_L}{h_{mech}}\right\}$, m_L is the mass of the rotor $m_L = \left\{\frac{G_L}{g}\right\}$ and K_{mag} is the negative spring constant

If the quotients are taken $\frac{G_L}{h_{mech}}$ as the imaginary magnetic fundamental angular frequency of the UMP, then the effective fundamental angular frequency on the critical speed of the rotor can be written as,

$$\omega_{eff} = \sqrt{\omega_{mech}^2 - \omega_{mag}^2} \tag{2.2}$$

$$n_{eff} = n_{mech}\sqrt{1 - \left\{\frac{n_{mag}}{n_{mech}}\right\}^2} \tag{2.3}$$

The UMP is derived from Maxwell's stress by means of air-gap permeance model. The damping of the eccentricity fields through any short-circuited winding. Damper windings, which reduces the fields caused by eccentricity of pole pairs numbers $(p+1)$ and $(p-1)$ and thus also the UMP, can in practice only be arranged in the stator or the rotor. Frohne in [2] concluded the following points:

- The voltages induced in the rotor winding with slip frequency by dynamic eccentricities cause such small damping currents that the damping effect of such windings in the rotor became practically zero.
- By using the damper winding in the rotor perhaps the influence of UMP on the static deflection can be prevented but not that on the reduction of the critical speed.
- Only a damper winding in the stator reduces the dynamic eccentricity fields and by about the same extent the static eccentricities.

Belman et al. [5] developed an analytical airgap permeance model for calculation of the magnetic flux density. The total magnetic energy has been used to derive the UMP of a 2-pole induction machine. The authors have used Ampere's law to derive the magnetic field distribution function in the airgap of an eccentric rotor. Using Ampere's law

$$\frac{d\,[b_A\delta(\theta,t)]}{d\theta} = \mu_o R a_m(\theta,t) \tag{2.4}$$

where a_m is the distribution function and $a_m(\theta,t) = -A_m sin(\theta-\omega t-\varphi_m)$, A_m is the amplitude of the distribution function, θ is the arc angle, ω is the frequency, φ_m is the phase angle.

Figure 1.5 shows the airgap of a motor with an eccentric rotor. Equation 1.1 gives the airgap length for any eccentric motor. Equation 1.2 gives the air-gap permeance expression in terms of the Fourier series. Equation 1.3 gives the Fourier co-efficients. Airgap permeance is used for the derivation of the magnetic flux density distribution. Equation 2.5 gives the flux density distribution,

$$b_A = \mu_o\varphi_m(\theta,t)A_m R\left\{\cos(\theta-\omega t-\varphi_m) - \frac{\Lambda_1}{2\Lambda_0}\frac{V}{V+1}\cos[(\omega-\omega_\epsilon)t+(\varphi_m-\varphi_\epsilon)]\right\} \tag{2.5}$$

where, $\wedge_0$ and $\wedge_1$ are the zeroth and first Fourier co-efficients respectively, V is the magnetic resistance, ω is the frequency of the rotor, ω_ϵ is the relative frequency of the rotor, (for static eccentricity, $\omega_\epsilon = 0$ and for dynamic eccentricity $\omega_\epsilon = (1-s)\,\omega$), φ_m and φ_ϵ are the initial phase angles.

The UMP is derived from the total magnetic energy i.e. magnetic energy in the machine front end W_{mS} and magnetic energy in airgap W_{mA}. Equation 2.6 gives the UMP F as,

$$F = \frac{1}{\delta_m}\frac{\delta W_m}{\delta_\epsilon} = \frac{1}{\delta_m}\left\{\frac{\delta W_{mA}}{\delta_\epsilon} + \frac{\delta W_{mS}}{\delta_\epsilon}\right\} \tag{2.6}$$

$$F = F_C + \hat{F}\cos[2(\omega - \omega_\epsilon)t + 2(\varphi_m - \varphi_\epsilon)] \tag{2.7}$$

where, F_C is the constant UMP, $\hat{F}$ is the amplitude of the sinusoidal component of the UMP.

The UMP contains a vibrational component and a small pulsating torque, both having either the double slip frequency if the rotor is dynamically eccentric and the double supply frequency for a statically eccentric machine rotor.

Belman et al. [6] developed an analytical model for the calculation of UMP from Maxwell's stress tensor by using his airgap permeance model in a 2-pole induction machine. They neglected all damping effects due to the eddy currents in the conducting parts (shaft, end shilds, bearings and etc.).

The UMP is derived by integrating the horizontal and vertical projection of the Maxwell's stress over the rotor surface;

$$F_y = \int_0^{2\pi} \frac{b_A^2(\theta,t)}{2\mu_o}\sin(\theta)\,Rld\theta \tag{2.8}$$

$$F_z = \int_0^{2\pi} \frac{b_A^2(\theta,t)}{2\mu_o}\cos(\theta)\,Rld\theta \tag{2.9}$$

where b_A is the magnetic flux density, θ is the arc angle, R is the radius of the stator, μ_o is the permeability of the free space, l is the length of the core. A homopolar flux is generated due to an eccentricity of the rotor in a two-pole squirrel cage induction motor which can cause a vibrational component of the UMP. This UMP could yield excessive vibrations if the double supply frequency equals the rotor natural frequency for the lateral vibrations.

Dorrell and Smith [4] developed an analytical model for the calculation of UMP with series and parallel winding connections. The model uses the conformal transformation technique coupled to a

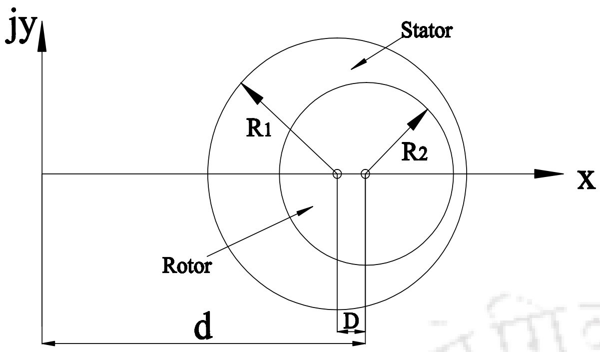

Figure 2.1: Conformal Mapping in Z-Plane.

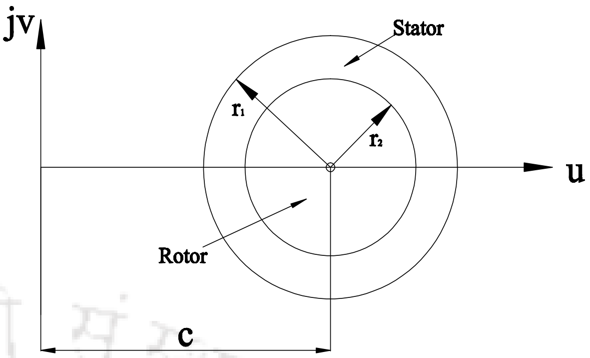

Figure 2.2: Conformal Mapping T-Plane.

winding impedance approach that is capable of accommodating any general stator winding connections.

The conformal transformation of two eccentric circles to two concentric circles is attained by utilizing a simple inversion as

$$\bar{Z} = \frac{1}{\bar{t}} \tag{2.10}$$

By finding appropriate values for d in Figure 2.1 and c in Figure 2.2, the eccentric rotor machine as represented by circles 1 and 2 in the Z-Plane, can be mapped on the T-Plane as two concentric circles (1 and 2). The transform results in an irregular slot pattern in the T-Plane and hence any method based upon this technique must be capable of accommodating general asymmetrical windings. The flux density distribution round the stator surface is different in the Z and T planes but due to the rearrangement of the windings by the transform, the flux linkage between windings is the same whether it is in the T-Plane or Z-Plane. The machine denoted in the T-plane can be used to find an impedance matrix linking the stator currents and terminal voltages.

Smith and Dorrell [7] developed an analytical model for the calculation and measurement of UMP and later verified it experimentally. The model was developed for motors having series and parallel winding connections along with rotor eccentricities. They have also shown that the motor is defined analytically in terms of the coupling impedances between individual circuits. Each series-connected winding on the stator is regarded as a separate circuit. This allows any series/parallel winding connections to be included. The rotor cage impedance varies with harmonic order, so coupling impedances are determined for each harmonic field. The coupling impedances are assembled into a matrix equation that relates the supply voltages to the unknown circuit currents. It has been concluded in [7] that

In series winding connections,

- A series-connected winding forces the individual coil currents to be constant and hence provides a sinusoidal current density distribution in the machine.
- It produces a non-sinusoidal flux density distribution with the flux concentrating around the narrowest airgap in the presence of eccentricity of the airgap.
- Significant UMP can exist in this situation and it will try to reinforce the eccentricity.

In parallel winding connections,

- A fully parallel-connected winding on the other hand allows the coil currents to redistribute themselves and forces a constant voltage across each coil.
- This ensures a much more sinusoidal flux density in the airgap and hence the level of UMP is greatly reduced.

Smith and Dorrell [8] also investigated the effects of parallel connections of stator winding and the damping nature of the cage rotor experimentally. The experimental investigation was carried out to verify the analytical model. Some important parameters of motor used in the experiment are given in Table 2.1

Table 2.1: Machine parameters.

Sl No	Description	Value
1	Number of slots	90
2	Coil Pitch (Slots)	9
3	Type of winding	Double layer winding
4	Resistance per coil	0.0427 Ω
5	Leakage Reactance per coil	0.13 Ω
6	Supply Frequency	50 Hz
7	Type of connection	star

The stator was mounted on a piezoelectric force table which could measure forces in three dimensions with the use of charge amplifiers. Low pass filters fitted to the charge amplifiers allowed high-frequency vibrations to be filtered out. The rotor was separately mounted using rigid pillar supports. Oversized holes for securing bolts and the use of shims allowed movement of the rotor in both vertical and horizontal directions.

Initially it was thought that this method of measurement would not be very accurate with smaller airgap, so the blank rotor has been constructed with a large airgap (1.5mm). Correlation between the measured and predicted results appears to be poor at high values of slip (as in the series-connected case). The parallel connection does provide some damping of the UMP but not to the same extent as with the blank rotor. The predicted and measured results gave good agreement when the blank rotor was used at low slip for the cage rotor. It has been noticed that the effects of high-order winding harmonics and rotor skew can be the influential factor on the magnitude of the UMP with a cage rotor.

Arkkio et al. [9] developed an analytical model for measuring the forces acting between the rotor and the stator of a cage induction motor when the rotor is performing cylindrical circular whirling motion. It reflects that the rotor remains aligned with the stator but the geometrical centreline of the rotor travels around the geometrical centreline of the stator in a circular orbit with a certain frequency, known as the whirling frequency and with a certain radius known as the whirling radius. The forces have been studied as a function of whirling frequency, whirling radius and supply voltage. The calculation of the magnetic field and the operating characteristics is based on time-stepping, finite-element analysis. The time dependence of the variables is modeled by the Crank-Nicolson method. The motion of the rotor is obtained by changing the finite-element mesh in the airgap. The center point of the rotor was forced to move along a circular path at constant speed to model the whirling motion. Second order, iso-parametric, triangular elements were used.

The rotor position is expressed by two complex numbers (indices 1 and 2 refer to the two ends of the machine):

$$pc_1(t) = px_1(t) + ipx_1(t) \tag{2.11}$$

$$pc_2(t) = px_2(t) + ipx_2(t) \tag{2.12}$$

The whirling frequency current (control currents) components in the X and Y directions are computed as

$$I_{Xn\omega} = \frac{2}{T}\int_T I_{Xn}(t)\exp(-i\omega t)dt \tag{2.13}$$

$$I_{Yn\omega} = \frac{2}{T}\int_T I_{Yn}(t)\exp(-i\omega t)dt \tag{2.14}$$

From the computed and measured results it was observed that the radial force has a sharp maximum at the synchronous whirling frequency. The additional harmonic fields usually rotate at a speed different from the speed of the rotor. With ths results, the author concluded that the fields are time-dependent and induce eddy currents in the rotor cage. The currents oppose the change of the flux, equalize the flux distribution and reduce the radial force.

Tenhunen [10] developed a numerical method for the calcuation of UMP in an eccentric rotor of an induction motor by time-stepping finite element method. The effects of the rotor eccentricity and equalizing currents on the unbalanced magnetic pull were studied by multi-slice, time-stepping, finite element model. The modeling has been done for the cases when the rotor is parallel or diagonal with respect to the stator. Analytical and few numerical results have been presented. The use of 3D FEM is one of the possibilities to study skewed rotor but the size of the problem and computation times limits the use of 3D modeling. Alternative way is a multi-slice model, in which 3D effects are included into the 2D FEM by taking a set of cross sections of the motor perpendicular to the stator shaft. These slices have to be connected together. The slices are connected together by forcing the currents in the stator windings and rotor cage to be continuous from slice to slice. The field equation and the circuit equations are solved together as a system of equations. From the results, the authors have concluded that the parallel connection of the stator winding reduces the unbalanced magnetic pull clearly when the eccentric rotor axis is parallel with respect to the stator axis.

Gerlando et al. [11] developed an analytical model of UMP in isotropic electrical machines and verified with FEM simulations. The development of an analytical model based on a critical re-formulation of the airgap magneto motive forces including the homopolar term has been addressed.

The nature of the eccentricity function and the force function have been analyzed for the lowest pole pair fields. The analytical results are compared with the finite element results.

Dorrell et al. [4] derived the unbalanced magnetic pull (UMP) with an eccentric rotor for a cage induction generator of a wind turbine and also investigated the reduction of bearing wear. Simulation works have been presented for both static and dynamic rotor eccentricity cases. An additional damper winding has also been used for the reduction of UMP. It has been found that the UMP reduces substantially when the machine is lightly loaded with dynamic eccentricity. The analytical model consists of UMP calculation for both static and dynamic eccentricity which is present at the one end of the shaft. Simulations have been done for 10-pole machine with low eccentricity and 10-pole machine with 50% eccentricity. A SPEED PC-IMD model (University of Glasgow software package) was developed and a set of performance curves were obtained. The UMP is reduced due to the dynamic eccentricity only when the machine is slightly loaded. The expression for UMP has been derived from the Maxwell's stress equation for the rotor surface,

$$F_u(t) = \int\limits_{x=o}^{x=L_{st}} \int\limits_{y=o}^{y=2\pi r} (\sigma(x,y,t)\cos(ky))dy \tag{2.15}$$

$$F_v(t) = \int\limits_{x=o}^{x=L_{st}} \int\limits_{y=o}^{y=2\pi r} (\sigma(x,y,t)\sin(ky))dy \tag{2.16}$$

where x and y are the orthogonal directions on the rotor, L_{st} is the axial core length of the stator, r is the mean air-gap length, and k is the inverse rotor radius.

2.1.2 Factors affecting the UMP

This section reports the literature on factors affecting the UMP such as rotor stability, eccentricity, slotting, tooth saturation and critical speed. Bradford [12] studied the steady state and transient measurements of the magnitude of UMP resulting from an eccentric air-gap on a specially constructed 6-pole 10kW induction motor. The measurement shows that the UMP depends critically on the saturation of the magnetic circuit. The determination of dependance of the UMP over supply voltage, eccentricity and loads for motors with series-connected and parallel-connected windings have been addressed. The experiments were conducted on three different types of rotors with varying eccentricity, voltage and load. They have found that

- A 25% of the supply voltage has been increased from 332 to 415 V and from 415 to 518 V has an impact of increase of 56% in UMP. The actual increases in UMP were 28% and 7%, respectively, for the wound-rotor motor, and 55% and 62% for the cage-rotor motor, both motors being on no load.
- The UMP in the cage-rotor motor increased approximately with the square of the line voltage whereas in the wound-rotor motor the increase in UMP was limited by the saturation.
- The increase of UMP with load current is equivalent to a reduction in the effect of rotor-winding equalizing currents, the increase being most pronounced at 332V and much less so at 518 V. It has been concluded that at 332V, saturation is negligible and the equalizing currents are governed mostly by the load current.

Binns and Dye [3] analyzed the relation between the unbalanced pull and the eccentricity of a cage rotor. The effect of eccentricity over UMP has been determined through measurements of the electromagnetic field at the rotor surface and he assessed the significance of the tangential-flux component in the machine airgap. The total force has been calculated by integrating the Maxwell's surface-field stress over a cylindrical surface enclosing the rotor as

$$F_n = \frac{1}{2}\mu_o\left(B_n^2 - B_t^2\right) \tag{2.17}$$

where B_n is normal flux density distribution, B_t is tangential flux density distribution and μ_o is permeability of the free space.

The Maxwell's stresses due to the normal and tangential field components may be summed separately. By considering the normal flux density B_{nA},

$$B_{nA} = B_o \sin(\sigma\omega t) + \{B'_u + B_u \sin(\sigma\omega t + \sigma_u)\} \sin(\omega_u t + \lambda_u) \tag{2.18}$$

Resulting UMP obtained from B_{nA},

$$P = 2\pi \frac{L_r}{2\mu_o} B_\sigma B_u \sin(\omega_u t + \lambda_u') \tag{2.19}$$

where, ω_u is the angular velocity, B_σ and B_u are slip frequency flux components.

A 7.5 kW 6-pole motor with a die cast cage rotor has been chosen for the experimental investigation. The main winding arrangement has been given enough space to wound the search coil winding. The stator bore and rotor surface have been machined slightly for improving the regularity for not more than 0.025 mm. The airgap is 0.525 mm. Experimental observations show that the tangential component has been increased with the increase of eccentricity and its value relative to the radial component varies from 28% at low values of eccentricity to 36% at higher values of eccentricity.

Belmans et al. [13] analyzed the stability of the flexible-shaft system. The main focused of the study was on the critical speed of the system and the UMP developed. The eccentricity also generates a normal rotating field when there are two-pole pairs. The UMP is damped by currents induced in the squirrel cage. If we do not account for the damping due to current induced by the 4-pole field in the rotor bars, the air-gap flux density distribution is

$$b_A(\alpha, t) = \frac{\mu_o F}{\delta_m} \left\{ \cos(\alpha - \omega_o t - \phi_m) + \frac{\epsilon}{2} \cos[2\alpha - (\omega_o + \omega_\epsilon) - (\phi_m + \phi_\epsilon)] + \frac{\epsilon}{2} [\alpha_o \cos\beta + \delta_o \sin\beta] \right\} \tag{2.20}$$

where, $\beta = (\omega_o - \omega_\epsilon)t - (\phi_m - \phi_\epsilon)$

From the above equation, the flux density distribution of a 2-pole induction machine with an eccentric rotor consists of three components:

- The normal, 2-pole fundamental field.
- An eccentricity field with rotational character (2-pole pairs).
- An eccentricity field with homopolar character with its pulsation equalling the slip pulsation.

The UMP can be calculated from the Maxwell's stress. The author combined the electromagnetic model with De-Laval rotor model in order to analyze the stability of the flexible shaft of the machine.

The motion of the rotor is described using the De-Laval model. The stability of the system was studied using the following set of linear, homogeneous differential equations,

$$\ddot{y}_s + 2\omega_\epsilon \zeta_t \dot{y}_s + \omega_{ne}^2 y_s = \omega_{ne}^2 u \sin(\omega_\epsilon t) \tag{2.21}$$

$$\ddot{z}_s + 2\omega_\epsilon \zeta_t \dot{z}_s + \omega_{ne}^2 z_s = \omega_{ne}^2 u \cos(\omega_\epsilon t) \tag{2.22}$$

They have concluded that if the electromagnetically induced damping coefficient is larger than the mechanical damping coefficient an instability will occur.

Dorrell and Hsieh [14] developed an algorithm for the calculation UMP with an influence of rotor skewness and eccentricity in a cage induction motor. The theoretical results were validated with the experimental results. The algorithm was developed for the motors having series and parallel winding connections along with rotor eccentricities. It has been concluded that the rotor skew does increase the UMP at higher slip when the rotor exhibits dynamic eccentricity although the accuracy is not good. The UMP is dominated by the fields produced by the higher MMF waves when there is no skew present in the machine. The no-load results are dominated by the magnetizing current (since there is little rotor current), this is why rotor skew has little effect on the UMP characteristic at no-load and it is more susceptible to variation due to core MMF drop and losses.

Arkkio [15] calculated the forces based on time-stepping, finite-element analysis of the magnetic field. He assumed the field to be two-dimensional and the forces are calculated from the airgap field using a method based on the principle of virtual work. The simulations carried out on a 30 kW two-pole motor and a 15 kW four-pole motor showed that each of the three types of asymmetry can produce forces larger than the weights of the rotors. The magnetic field in the core region of the motor is assumed to be two-dimensional and the field equation is discriticized by finite-element method. End-region fields are taken into account approximately by end winding impedances in the circuit equations of the windings. The field and circuit equations are solved together as a system of equations. The time-dependence of the field is modeled by the Crank-Nicolson method. The rotor is rotated during the simulation by changing the finite-element mesh in the airgap. The simulation results are compared for rotor broken bar, broken-end ring, eccentricity, number of rotor slots. The largest forces were produced by broken end-rings. The saturation of the core and equalizing currents in the parallel circuits of the stator winding reduces the unbalanced magnetic pull.

Dorrell [16] studied the influences affecting the magnitude of the unbalanced magnetic pull generated in an induction motor where the rotor is not centered. The surface force waves were calculated by using Maxwell's Stress tensor,

$$\sigma = \frac{B_n^2 - B_t^2}{2\mu_o}\left\{1 - \frac{1}{\mu_r}\right\} \tag{2.23}$$

where n and t subscripts indicates the normal and tangential components of the flux density and μ_r is the relative permeability of the tooth tip.

The permeability of the tooth-tip and also the net pull is reduced in the narrow airgap region because the localised flux levels are high. Therefore the UMP can be reduced by increasing the flux level in the motor (i.e., increasing the voltage) if it causes tooth-tip saturation. Tooth saturation may also cause a redistribution of the flux to a more regular form because the reluctance path is greatly increased round the narrow airgap by the concentration of flux. The author assumed the stator and rotor MMF distribution is unchanged by the tooth saturation (which is not strictly true but is used to give an approximate MMF distribution) then the airgap flux density can be calculated assuming infinite iron permeability to obtain the MMF at a point y round the airgap circumference and a distance x down the core length,

$$F(x,y,t) = \frac{b(x,y,t)g(x,y,t)}{\mu_o} + \frac{2b(x,y,t)l}{\mu_o\mu_r} \tag{2.24}$$

where l is the tooth length and the relative permeability can be obtained using linear interpolation of the BH curve for the magnetic core. The vibration was measured using a vertically-orientated accelerometer on the top of the stator casing at the axial centre-point for 45% uniform dynamic eccentricity. Tooth saturation is clearly seen to attenuate the UMP in both the experimental and predicted results. It can be observed that the inclusion of tooth saturation not only reduces the airgap flux density but also reduces irregular flux distribution due to the eccentricity hence reducing the UMP.

Berman [17] studied the behavior of an induction machine with off-center motor. The authors have used equalising winding connection in order to reduce the UMP present in the machine. The improvement in the reduction of UMP has been proved theoretically and it has been validated with the experimental results. By considering a four-pole, three-phase, induction motor with two parallel branches comprising of three series-connected coils. The additional connections equalize the voltage drop in coil pairs shifted in space by 180^0. The experimental setup consists of two induction motors with a common shaft where an external panel permitting a variety of connection patterns for the stator coils and a measuring device for the forces. Theoretical and laboratory results show that connections of coils of the stator winding in parallel, with equalizing branches, leads to drastic reduction in UMP.

Guo et al. [18] used the airgap permeance method to calculate the UMP in the study of noise and vibration calculation of electrical machines. UMP is analyzed for different pole-pair number. The non-linear vibratory responses of a Jeffcott rotor excited by the UMP and eccentric force are studied by use of Newmark integral method. The UMP includes the constant component and oscillatory components. The frequency of the oscillatory component is the double-supply frequency. If the pole-pair number is larger than three, only the constant unbalanced magnetic pull remains. The magnitude of the UMP is non-linear when the eccentricity is large.

Yang et al. [19] developed an analytical method for analyzing the instability and mechanical imbalance response of induction motors considering unbalanced electromagnetic forces produced in the induction machines with eccentric rotor and phase unbalance. The equations to be solved are a set of second-order differential equations that give matrices with periodic coefficients that are a function of time due to the unbalanced electromagnetic force. The evaluation method of rotor instability zones is presented in this paper by a time transfer matrix method. The Newmark-beta method is adapted to solve for an imbalance response.

Tenhunen et al. [20] investigated the effects of magnetic saturation on the radial magnetic forces in induction machines when the rotor is performing a cylindrical circular whirling motion. Impulse method in the finite element analysis is used to calculate the forces and eccentricity harmonics from both the airgap flux density and rotor currents. The forces are studied as a function of supply voltage in order to find the effects of saturation on them. The maximum radial force is found to be limited by saturation, which also couples the eccentricity harmonics together.

Pennacchi and Frosini ([21], [22]) developed a model to calculate the airgap distribution depending on the position in a general time instant of the rotor inside the stator. The UMP, which is calculated by means of the airgap permeance approach, is therefore function of both time and position. The Newmark method is used to integrate the non-linear dynamic equations of the fully assembled machine and the dynamical behavior is calculated. The numerical simulations has been carried out for 900 MVA, 1500 rpm 3-phase steam turbo-generator, which is modeled by means of standard beam elements normally used in rotor dynamics and has 1148 degrees of freedom. The effect of the UMP is rather evident if the shaft average dynamical deformation and the orbit of the nodes is compared after and before the magnetic field is generated in the airgap.

Calleecharan and Aidanpaa [23] studied the Jeffcott rotor model of an industrial hydropower generator together with a new UMP model that incorporates both the radial and tangential UMP components. Eigenvalue-based stability analysis is performed and showed that the damping and stiffness of the rotor and of the bearings are important when non-synchronous whirling of the rotor comes into play. The effect of damping ratio and the stiffness on the system shows that system becomes more stable with increasing stiffness and damping is required in order to increase the system stability.

Swann [24] developed a method for calculating the magnetic field in the airgap of an idealized machine without salient poles and with an eccentric rotor. The magnetic potential at any point is governed by the currents flowing in the windings and also by the magnetization induced on the cylindrical surfaces of the rotor and the stator. The potential functions appropriate to the stator, rotor and airgap are determined for several elementary conductor arrangements, and hence the complex potential function is derived at any point in the airgap. Finally, the application of the principal results of the analysis is exemplified by the calculation of the radial magnetic field at the surface of an eccentric rotor with an arbitrary stator winding.

Ellison and Yang [25] studied the variations of acoustic-noise power radiated from electric machines, having varying degrees of eccentricity of the rotor in the stator bore using a specially constructed rig in an anechoic chamber. The effects on the noise power of different numbers of stator parallel paths and of different ways of connecting together were investigated using specially wound machines. Information is given concerning the choice of parallel paths and connections for noise reduction.

Stoll [26] developed a model for two-pole turbo-generator airgap region to predict the unbalanced magnetic pull on the rotor, under no-load conditions, caused by static eccentricity. The effects of rotor magnetic saturation and eddy currents are taken into account using a set of rotor surface impedances. The valuable contribution of Swann's method 1963 [24] is that the eccentric airgap is transformed by conformal mapping into a concentric airgap. The addition of aluminium slot wedges to the winding portions of the rotor further reduced the UMP.

Dorrell et al, [27] developed a new theoretical analysis of the interaction between harmonic field components due to static and dynamic rotor eccentricity which previous research had not considered. The resultant non-supply-frequency current components produced in the supply current which were highlighted by the analysis are found to exist experimentally and indeed shown to be a function of the combined effect of both dynamic and static eccentricity.

Joksimovic [28] developed a method based on the winding function theory and extended of this theory to the non-uniform airgap case for calculating all inductances in a machine with both static and dynamic airgap eccentricity. In the static eccentricity condition, the main change in the frequency spectra is the appearance of the higher rotor slot harmonic at 1034 Hz. This is in agreement with the results obtained numerically, where it is shown that due to the static eccentricity conditions, only changes in magnitude of rotor slot harmonics can be expected. Higher frequency components due to the dynamic eccentricity conditions could not be observed and frequency components at 243Hz as predicted by numerical model could not be observed in the real spectra.

Hyun et al. [29] analyzed the feasibility of using the single-phase rotation test (SPRT) for detecting eccentricity, which has not been reported before. The single-phase rotation test (SPRT) is a simple and reliable offline test frequently used for detecting problems in the rotor cage of induction motors without motor disassembly. Experiments have been done for different cases of (i) concentricity,(ii) 50% eccentricity(theoretically), (iii) 20%,40%,80% Dynamic Eccentricity (Experimentally), (iv) 20%,40% Static Eccentricity, (v) Mixed Eccentricity with 20% Static Eccentricity + 20%,40%,60% Dynamic Eccentricity, (vi) Mixed Eccentricity with 40% Static Eccentricity + 20%,40%,60% Dynamic Eccentricity, (vii) 2 (0f 44) broken bars, (viii) 2 broken bars and Mixed Eccentricity (20% SE and 40% Dynamic Eccentricity).

2.1.3 Stator Windings

Debortoli et al. [30] investigated the rotor eccentricity and the effect of parallel windings in an induction motor by using the transient finite element model. Parallel connection of the stator poles has been employed to reduce UMP in motors with non-uniform airgaps. The authors have analyzed the effects of rotor eccentricity for the following cases:

- In each phase of the stator windings, all pole groups were connected in series for both static and dynamic rotor eccentricity.
- Two parallel stator winding branches with adjacent pole groups connected in parallel and opposite pole groups connected in series for static eccentricity only.
- Two parallel stator winding branches with opposite pole groups connected in parallel and adjacent pole groups connected in series for static eccentricity only.
- Four pole groups connected in parallel for both static and dynamic eccentricity.

A 2D-FFT analysis of airgap flux density distribution with eccentricity has been carried out. An important point has been noticed in this study is that the beneficial effects of parallel circuits are present even though the rotor remains eccentric; it is not necessary that the rotor be returned to its centered position for the reduction of the eccentricity induced force waves.

Arkkio and Burakov [31] evaluated the effects of parallel connections in the stator and rotor windings on the eccentricity force numerically. The performance of the induction machine with three different stator winding arrangements was investigated: 1) series connection (no parallel paths); 2) two parallel paths; 3) four parallel paths. In the whirling frequency range of the study four parallel stator windings ensure the smallest average value of the radial component of the UMP. The rotor cage was shown to effectively attenuate the UMP without causing its asymmetry. In both test machines, four parallel stator windings proved to be more effective in mitigating the UMP than the rotor cage. The electrical machines incorporating parallel circuits both in the rotor and in the stator operated with the smallest amount of UMP.

Oliveira et al. [32] performed the numerical analysis to measure the UMP and currents in the parallel circuits on a 12-pole generator which is having static eccentricity and the stator winding connected as one circuit or two parallel circuits. Experiments were conducted at no-load conditions. Two numerical studies of the force reduction were presented, i.e. i) by using a finite element code ii) by using an airgap permeance model. The generator has been constructed from a synchronous motor with a rated power of 185 kW. The results shows that the induced eddy currents were found to reduce the radial force component.

Dorell et al. [33] developed a wound-rotor model and includes the damper windings. It has been assumed that the eccentricity and damper cage have little effect on the torque, by considering the degree of eccentricity is low. The model has been used to calculate the additional cage rotor currents and damper winding currents. The analytical calculation of the airgap flux density, stator fluxes, rotor fluxes (for cage and wound rotor), flux wave interaction and UMP have been presented. The numerical simulation have been carried out for a 10-pole cage-rotor machine with static or dynamic rotor eccentricity and a 4-pole wound-rotor machine. The numerical and analytical results have then been compared.

Brown et al. [34] focused on two typical topologies of significant industrial relevance: machines with distributed windings with two slots per pole and phase and motors with concentrated coils and three slots per pole pair. The effect of stator-winding parallel paths is examined for both cases. When parallel connections are used, then “damping” of the UMP (meaning reduction of UMP compared to the series connection) can occur due to the ‘equal flux effect in the ideal case. Two-dimensional transient nonlinear-circuit-coupled first order- triangular-element finite-element models were used for the simulations of the two machines. For all simulation cases, the entire machine was modeled with a Dirichlet boundary condition applied to the stator outer diameter.

2.1.4 Electromagnetic and Mechanical Interactions

Holopainen [35] developed a parametric model developed for the calculation of UMP by numerical impulse method. An electromechanical rotor model was derived by combining the Jeffcott rotor model with the simple electromagnetic force model, including two additional variables for the harmonics currents of the rotor cage. Three induction motors were used in the numerical examples. The results obtained showed that the electromechanical interactions may decrease the flexural frequencies of the rotor, induce rotor damping or cause rotordynamic instability. The effect of these interactions are most significant in motors operating at, or near, the first flexural critical speed.

Laiho et al. [36] developed an efficient computational electromechanical model for vibration analysis of cage rotor machines. In this model, the interaction between the mechanical and electromagnetic system is distributed over the airgap of the machine. This enables the inclusion of rotor and stator deflections into the analysis and thus yields more realistic results in prediction of the effects of the electromechanical interactions. This model has been implemented in a 7 MW induction machine and a 21 MVA synchronous generator and tested. The rotational speed of the machines have been chosen very close to one of the rotor bending critical speeds. The effects of the electromechanical interactions on the vibrational characteristics of the machines have been studied in terms of frequency reduction, electromechanical damping and frequency response analysis. The obtained obtained confirmed the conclusion of the previous research that the electromechanical interactions decrease the natural frequencies of the rotor bending modes, induce additional damping or cause rotordynamic instability.

Laiho et al. [37] developed a new tool for model-based control of flexural rotor vibration in cage induction machines. An analytical model for an electromechanical rotor with built-in force actuator has been proposed. The force actuation based on unbalanced field distribution around the rotor is industrialized in active magnetic bearing (AMB) technology. The AMBs offer some advantages compared to the traditional sliding- or rolling-element bearings. Control force exerted on rotor is given by $F = (F_\alpha, F_\beta)^T$

$$\begin{pmatrix} F_\alpha \\ F_\beta \end{pmatrix} = MI \begin{bmatrix} -\cos(2\omega t) & \sin(2\omega t) \\ \sin(2\omega t) & \cos(2\omega t) \end{bmatrix} \begin{pmatrix} i_\alpha \\ i_\beta \end{pmatrix} \tag{2.25}$$

where, M is the spatial derivative of mutual inductance between the two and four-pole windings

$M = \left(\frac{\mu_o \pi N_2 N_4}{8 g_o^2}\right)$, l is the axial length of the rotor, r is the radius of the rotor, g_o is the radial airgap length, N_2 and N_4 are no of turns in the two-pole and four-pole winding.

The resultant force exerted on the rotor due to currents in the supplementary winding and the eccentric rotor is given by,

$$F_x = \left(\frac{\pi r l}{2\mu_o}\right)[B_2 B_4 \cos(\phi_4 - \phi_2) + e\cos(B_4^2)\cos(\alpha)] \tag{2.26}$$

$$F_y = \left(\frac{\pi r l}{2\mu_o}\right)[B_2 B_4 \sin(\phi_4 - \phi_2) + e\sin(B_4^2)\cos(\alpha)] \tag{2.27}$$

where, μ_o is the airgap permeability, e is the rotor eccentricity, B_2 and B_4 are the peak values of the two- and four-pole airgap flux-densities, ϕ_2 and ϕ_4 are the initial phase angles of the two- and four-pole MMF's, α is the direction of the minimum airgap. A control algorithm has been used in this built-in force actuator which was previously used in the active magnetic bearings for compensation of harmonic disturbance forces. In the simulations, the control algorithm has been embedded in the numerical analysis. The modeling and model-based controls were verified by experiments. A 30 kW two-pole cage induction motor with an extended rotor shaft is used for the measurements. The results both from simulations and experiments show that by using the built-in force actuator the model-based controller is suitable for flexural rotor vibration suppression in a cage induction machine. The stable operation at the critical speed of the machine can be achieved by using the methodology presented in this research.

Pennacchi [38] developed an analytical model for the non-linear behavior of generators with smooth poles of high-speed turbo-generators during and after the excitation of the magnetic field in the airgap in order to fully exploit the effect of the UMP. The analytical results are compared with simulation results. Initially, the simulation of the dynamic behavior of a flexible rotor caused by the UMP was carried out. The transient simulation of the magnetic field excitation in a turbo generator also had been done. The examination of forces during the transient is made by considering the calculated values of UMP and analyzing them by means of short time Fourier transforms.

Arkkio et al. [39] analyzed electromagnetic forces on a whirling rotor of a synchronous reluctance machine using time discretized 2D finite-element analysis. The whirling motion generates eccentricity harmonics in the airgap field. These harmonics may further induce circulating currents in the windings of the machine. The dynamics of the induced currents is coupled with the dynamics of the rotor, especially, when the machine is operated close to its first bending critical speed. In a synchronous reluctance machine, there is no rotor winding but the circulating currents may flow in the parallel branches of the stator.

2.1.5 Controlling of motor vibrations

Haase et al. [40] calculated the vibratory forces in a 2-pole induction machine. The 2-pole induction machine has low frequency unipolar fluxes which are likely to occur in their operational range. One sided electromagnetic pulls, designated as vibratory forces, in three-phase machines are caused by the interactions between the rotating field and permeance irregularities. The airgap permeance approach is used to calculate the vibratory forces. The magnetic flux density is derived from airgap permeance and it is used to derive the unipolar flux. Radial vibratory forces are derived from magnetic flux density by integrating it over rotor surface.

Kovacs [41] analysed the resulting eccentric airgap that creates the homopolar fluxes and these excite mechanical forces of double slip frequency, superposed on the double- frequency vibrations and on the force waves of the unbalanced magnetic pull. The authors analysed the origin of the alternating homopolar fluxes and the alternating homopolar fluxes created by them. The Airgap permeance approach is used to calculate the vibratory forces. The magnetic flux density is derived from the airgap permeance and it is used to derive the unipolar flux. The radial vibratory forces are derived from the magnetic flux density by integrating it over rotor surface.

Khoo [1] proposed a new winding called bridge configured winding which is a cost-saving winding scheme for electrical machines to exploit transverse magnetic forces on the rotors, in which passive as well as active vibration suppression are possible. The bridge configured winding in a polyphase self-bearing rotating electrical machines have some advantages such as: 1) requiring only one power supply for the torque production; 2) lateral forces are produced using auxiliary power supplies of relatively low current and voltage ratings; 3) relatively low power loss; and 4) preserving the flexibility for extensions to other polyphase machines. A three-phase, four-pole permanent-magnet (PM) synchronous self-bearing motor has been considered. The components of flux density that exist in the airgap are caused by the PM, motor current, and levitation current, ie, B_{PM}, B_{MC} and B_{LEV}.

Laiho et al. [42] developed an algorithm based on convergent control to control the rotor vibrations by means of attenuating harmonic rotor vibration components. This algorithm has been applied in a 30 kW two-pole cage induction machine. The machine is equipped with a four-pole supplementary winding for generation of lateral force on the rotor. A 30 kW cage induction motor with an extended rotor shaft is used to demonstrate the low-frequency rotor vibration. A standard squirrel-cage rotor stack was installed on an extended rotor shaft. In a machine with p pole pairs, the criterion for the force production is that an additional magnetic field with either $p - 1$ or $p + 1$ pole pairs is generated. Modal testing has been conducted for measuring the flexibility of the rotor and rotor support (bearings and bearing blocks). It has been observed from the experimental results that the rms values of the amplitude and velocity of the flexural rotor vibration were decreased by 97.50% and 57.60%, respectively, when control was switched on.

Sinervo et al. [43] performed the experiments on a modified two-pole 30kW induction machine (rated for 400 V, 50 Hz). The machine has been fitted with coils wound around the machine shaft inside the end shields of the machine. The amplitude of the measured vibration oscillates at twice the slip frequency due to the unipolar flux and the stator slot harmonics. Finite-element model simulations are presented to provide further analysis and to assess the contribution of the extra stator winding. Jeffcott Rotor model is used for the rotor vibration analysis.

The experimental findings of their work are summarized as follows: The test machine was a modified two-pole 30 kW induction motor rated for 400 V, 50 Hz. The stator was re-wound to have an extra four-pole winding and measurement coils for two- and four-pole fluxes. The test machine was also equipped with a unipolar flux measurement coil around the shaft inside one of the end shields. The path of the unipolar flux was assumed to go along the shaft, through the safety bearing into the shield; then from the shield through machine frame and into the stator; and finally, through the airgap back to the rotor. The test machine was connected to another 30 kW induction machine that acted as a load machine. A two-stage flexible coupling was used to prevent the load machine from causing extra radial forces to the test machine. The measurements were done at 25 Hz supply frequency with the two-pole flux in the airgap being 0.5 T. It was shown that the amplitude of the rotor vibration due to the dynamic eccentricity in two-pole machines depends on the location of the shortest airgap with respect to the two-pole flux. This dependence was shown to be caused by the unipolar flux and stator slot harmonics. The angle between the rotor displacement and the two-pole flux increases due to slip as the initial mechanical force is fixed to the rotation angle of the rotor. The extra winding does not damp the unipolar flux or the slot harmonics so the amplitude oscillation in the force becomes more visible. One of the novel contribution of this paper was to separate the force from the original mass unbalance and the magnetic forces.

Sinervo et al. [44] developed an experimental set up for three-phase two-pole induction machine which has been wounded with coils wound around the machine shaft inside the end shields of the machine. The coils induce unipolar flux in to the machine when supplied with a controllable voltage supply which acts as a unipolar actuator. The reason why unipolar flux is often neglected when studying induction machines is that it is very small and in an ideal machine it should not exist. The author implies that the unipolar flux and the slot harmonics of the magnetic flux have a definitive impact on the lateral force on the rotor if the four-pole flux is damped with an extra stator winding. The unipolar flux is induced into the machine with additional coils wound into the end shields of the machine. It is shown that the unipolar actuators can be used for active control of the rotor vibrations with some limitation. A 30 kW, 3-phase, two-pole induction machine has been chosen for the experimental analysis and the rotor of the motor had a 1200 mm long flexible shaft. The airgap length was 1 mm. The rotor displacement was measured from the shaft just outside the end-shields at both ends of the machine using eddy-current sensors. The four-pole winding was in short circuit and occupied 10% of every stator slot. The motor had also separate 2-phase two-pole and 2-phase four-pole search coils, a unipolar search coil and the unipolar actuator. The experimental findings of their work are summarized as follows: The experiments have been conducted at 25 Hz supply frequency in the two-pole main winding, with a 0.5 T two-pole flux density in the airgap, and with 0.5% slip. The machine had a small, about $10\mu m$ (1% of the airgap length) static eccentricity in horizontal direction due to misplaced bearings. The amplitude of dynamic eccentricity varied between $45\mu m$ and $130\mu m$ at twice the slip frequency. When the amplitude of the unipolar current has been raised to 1 A, the measured unipolar flux was close to zero and the maximum rotor displacement dropped to about $105\mu m$. When the current was increased to 3.4 A, the maximum dropped to below $50\mu m$ and the amplitude variation practically disappeared. The total rotor vibration amplitude was reduced over 50% by supplying a slip frequency current to the unipolar coils. The actuator can only produce force to the direction of the two-pole flux and therefore only control a part of the rotor vibration. One third of the vibration reduction was achieved when the unipolar flux was controlled to be zero.

2.1.6 Condition monitoring of induction machines

Cameron et al. [45] developed a theoretical model to detect airgap eccentricity in large 3-phase induction motors and the theoretical results were compared with experimental results. The philosophy of using a unified online monitoring strategy is presented and the reasons for selecting line current and frame vibration as the monitored parameters are discussed. The results indicate that the signature patterns obtained from the on-site tests are of the same form as the ones obtained in the laboratory. The vibration was sensed at numerous positions on the outer frame enclosure and on the bearing housing. It was found that an optimum sensing position for detecting the frequency components due to airgap eccentricity was in line with a core support plate opposite one of the core bars.

Williams et al. [46] have done experimental and theoretical investigation of the effect that rotor cage defects such as porosity and soldering effects of rotor have on the unbalanced magnetic pull (UMP) present in a single-phase motor. The experimental investigation was carried out on a two speed (doubly wound) single-phase motor having 36 stator slots and 57 rotor slots. Twenty of these machines, which were individually identified as having unacceptably high values of UMP, were tested in a specially designed test rig. Porosity defects in the rotor bars of the distribution and severity measured in the laboratory will produce a substantial UMP. Soldering defects are unlikely to produce a significant component of UMP provided end-ring resistances are not made high and the bar-to-iron resistance is not reduced below the levels measured by the laboratory. The UMP produced by rotor cage defects can be reduced to zero if the faults are symmetrically located around the rotor. While this cannot be ensured in practice, it is a strong argument for using symmetrically distributed gating positions during casting.

Benbouzid [47] introduced a fundamental theory with the results and practical applications of motor signature analysis for the detection and the localization of abnormal electrical and mechanical conditions that indicate, or may lead to, a failure of induction motors. The effects of current spectrum on airgap, broken rotor bar, bearing damage, load effects are detected. Modern measurement techniques in combination with advanced computerized data processing and acquisition show new ways in the field of induction machines monitoring by the use of spectral analysis of operational process parameters Time-domain analysis using characteristic values to determine changes by trend setting, spectrum analysis to determine trends of frequencies, amplitude and phase relations, as well as cepstrum analysis to detect periodical components of spectra are used as evaluation tools. Stator current monitoring was done by FFT analysis.

Joksimovie [48] derived an analytical expression for stator current harmonics frequencies in the spectrum of saturated cage and wound rotor induction motor. The analysis is based on the MMF-permeance wave approach. Analytical results obtained were confirmed by experimentally obtained stator current spectrum. Experimentally obtained stator current spectrum fully confirms the existence of current components at the frequencies predicted by derived analytical expressions.

Fireteanu and Taras [49] developed a finite element model for the electromagnetic field associated with the induction motors operation and with the diagnosis of rotor faults based on the time and space dependent magnetic field outside the motor. FE Analysis of the effects of one squirrel cage broken bar and of rotor eccentricity on the electromagnetic torque and force and on the external magnetic field is presented and compared with healthy machine. Results shows that the amplitude of the electromagnetic torque oscillations increase and low frequency oscillations appears for the BRB (Broken bar rotor) with dynamic eccentricity that will diminish the motor's life time.

Gieras and Saari [50] developed an analytical and finite element method for the design and prediction of performance characteristics for induction motors with solid steel rotor coated with copper layer. A computer program have been developed for the design and calculation of performance characteristics. Experiments also have been carried out on 300kW, 60000rpm three-phase induction motor. Results of analytical, numerical and experiments results were compared and it was observed that the solid rotor induction machine shows good performance as a high-speed induction motor.

2.1.7 Search coil winding design

Loiu and Wang [51] performed the experiments on switched reluctance motor to check the feasibility of using search coil to generate the rotor position instead of encoder. The effect of sensing current on output torque is negligible due to the small current search coil.

Ertan and Keysan [52] investigated that the airgap harmonics can be identified by using an external search coil placed on the frame of an induction motor. In the first stage of the study the type of search coil which maximizes the induced emf is sought, also the position of the coil on the induced emf is investigated. FFT analysis of the recorded data is performed in MATLAB environment. An algorithm is developed for identifying the rotor speed from analysis of the results. Search coil wounded around the iron frame of the motor, some of the flux is revolving at the synchronous speed induces the tiny voltage in the search coil. This tiny voltage has been used to find the position of the fields. A control algorithm was developed for identifying the rotor slot harmonics. Experiments for rotor speed with external search coil were carried out for motor driven with a sinusoidal supply and test motors driven with a PWM output inverter. PWM output inverter shows results of rotor speeds for the test motor driven which gives the excellent agreement than the results of rotor speeds for the motor driven by sinusoidal supply.

2.2 Summary of the review

This chapter provides a comprehensive review of the various analytical as well numerical methods used for the calculation of the unbalanced magnetic pull (UMP) in induction motors. It also summarizes the effect of rotor eccentricity, skewness of the rotor, tooth saturation, and critical speed on UMP. It has been observed that the air gap permeance method and the Maxwell's stress tensor method are the two methods that are being extensively used by researchers for predicting the UMP present in electrical machines.

The literature survey also revealed that an extensive amount of analytical, numerical, and experimental work is carried out in proposing various stator winding design methodologies for the reduction of UMP. Among them the dual set stator winding, the damper winding and, the unipolar winding with parallel and series connections are some of the prominent designs.

Basically, the UMP is reduced by means of controlling the imbalanced fields present in the air gap. A separate model or a control algorithm is required to control these fields or the electromechanical interactions in the air gap actively. There are so many model or control algorithm have been presented in the literature survey for different stator windings. However, there is no common model for all the types of stator winding. In recent work, Khoo [1] has introduced the single set of stator winding called Bridge Configured Winding which can mitigate the UMP. It has been identified that a special control algorithm will be required for the Bridge Configured Winding to achieve the active control of rotor vibrations. However, there is no study about the effect of eccentricity of the rotor on the bridge currents of an induction machine with bridge configured winding in the stator. This is paramount for developing a control algorithm for active vibration control in an induction machine with bridge configured winding in the stator.

3

Finite Element Modeling of BCW Based Induction Machine

Contents

3.1 Introduction

The real time engineering problems have been successfully applied in numerical methods with the help of modern high speed digital computers. Finite Element Method (FEM) is one of the important numerical methods which provide computational techniques for the analysis and the solution of the mathematical problems. A detailed literature review of the use of the finite element method for electromagnetic field analysis has been presented in the previous chapter. A brief introduction along with its working principle of a special stator winding scheme called Bridge Configured Winding (BCW) is also presented in Section 1.4 of Chapter 1. In BCW the coils are connected in two parallel paths in Wheatstone bridge format. When the mid-points of the Wheatstone bridge are short-circuited then it is called Bridge ON condition. For an eccentric rotor in Bridge ON condition an EMF will induce to drive currents in the links connecting the mid-points of the bridge. These currents are called levitation currents or bridge currents. The electromagnetic field analysis of an induction machine equipped with BCW has been carried out using FEM has been presented in this Chapter. The finite element modeling of a coupled magnetic field and electric circuit equation for a cage-induction machine has been presented in detail. A 2D finite element code has been developed by using MATLAB$^{\text{TM}}$ platform. The bridge currents and the transverse forces acting on the rotor are calculated for the static, dynamic and mixed eccentricity conditions of the rotor. The analysis of the bridge currents and the transverse forces acting on the rotor are presented.

3.2 2D finite element modeling of BCW induction machine using MATLAB^{TM}

In this section, a brief description about the coupled modeling of magnetic field and electric circuit equations for a cage-induction machine are presented. Detail derivation of the coupling of field-circuit equations have been presented by Bastos and Sadowski [53] and Salon et al. [54] and Savov et. al. [55]. The time-dependent magnetic diffusion equation forms the basis of coupling of the magnetic field and electric circuit equations. The coupled field-circuit equation for a conventional cage induction machine is extended to a cage induction machine equipped with bridge configured winding.

3.2.1 Overview of the electromagnetic field

Laws governing electromagnetic fields can be expressed very concisely by a single set of equations, namely those associated with the name of Maxwell. The Maxwell relations may be presented in differential form

$$\nabla \times \vec{H} = \vec{J} + \frac{d\vec{D}}{dt} \tag{3.1}$$

$$\nabla \cdot \vec{B} = 0 \tag{3.2}$$

$$\nabla \times \vec{E} = -\frac{\partial \vec{B}}{\partial t} \tag{3.3}$$

$$\nabla \cdot \vec{D} = \rho \tag{3.4}$$

Along with these differential relations the following constitutive relations are added

$$\vec{J} = \sigma \vec{E} \tag{3.5}$$

$$\vec{H} = \nu \vec{B} \tag{3.6}$$

$$\vec{D} = \epsilon \vec{E} \tag{3.7}$$

where $\vec{E}$ is electrical field strength, $\vec{D}$ is displacement field strength, $\vec{H}$ is magnetic field strength, $\vec{B}$ is magnetic flux, $\vec{J}$ is electric current density, ρ is electric charge density, ϵ is electric permittivity, σ is electric conductivity.

For most common and practical low frequency situations displacement current density is much smaller than and generally can be neglected, then

$$\nabla \times \vec{H} = \vec{J} \, as \, \frac{d\vec{D}}{dt} \ll \vec{J} \tag{3.8}$$

In the finite element formulation of electromagnetic field problems, magnetic vector potential, $\vec{A}$ can play an important role. It is commonly used in the solution of two-dimensional magnetic field, because in that case it reduces to a single component variable. To satisfy the non-divergence of the magnetic field, the vector potential is defined so that its *curl* is equal to the magnetic field density

$$\vec{B} = \nabla \times \vec{A} \tag{3.9}$$

Accordingly $\nabla \cdot (\nabla \times \vec{A})$ is satisfied for any $\vec{A}$. However, to define the vector potential uniquely, Equation 3.9 alone is not enough. In magneto static field problems the Coulomb gauge is usually used to specify the magnetic vector potential for the uniqueness of the solution.

$$\nabla \cdot \vec{A} = 0 \tag{3.10}$$

3.2.2 Fundamental time dependent magnetic diffusion equation

The time-dependent magnetic diffusion equation forms the basis of the electromagnetic field analysis. In this section, a derivation of the diffusion equation is summarized. Ampere's law (one of the Maxwell's equation Equation 3.8) can be presented neglecting the higher frequency effects as,

$$\nabla \times \vec{H} = \vec{J} \tag{3.11}$$

Using the constitutive relation from Equation 3.6 and substituted in Equation 3.11 to get

$$\vec{H} = \nu\vec{B} \tag{3.12}$$

Isotropic magnetic material is assumed in the present work and υ is constant.

$$\nabla \times \nu\vec{B} = \vec{J} \tag{3.13}$$

Now, introducing magnetic vector potential $\vec{A}$, defined as

$$\vec{B} = \nabla \times \vec{A} \tag{3.14}$$

$$\nabla \cdot \vec{A} = 0 \tag{3.15}$$

and substituting Equations 3.13 and 3.14 in Equation 3.11, the time-dependent magnetic diffusion equation is obtained as follows

$$\nabla \times \nu \left(\nabla \times \vec{A} \right) = \vec{J} \tag{3.16}$$

The present work is restricted to 2D field analysis, where the material quantities are independent of the z-coordinate and $\vec{J}$, $\vec{A}$ are assumed to be z-directed and independent of z, given as

$$\left.\begin{aligned} \vec{J} &= J\left(x, y, t\right)\hat{k} \\ \vec{A} &= A\left(x, y, t\right)\hat{k} \end{aligned}\right\} \tag{3.17}$$

Here, x and y are the cartesian coordinates and $\hat{k}$ is the unit vector parallel to the $z-$ axis (parallel to the axial length of the machine). Since vectors $\vec{J}$ and $\vec{A}$ have only one component, they can be treated as scalars and Equation 3.16 can be represented in component form as

$$\frac{\partial}{\partial x}\left(\nu \frac{\partial A}{\partial x}\right) + \frac{\partial}{\partial y}\left(\nu \frac{\partial A}{\partial y}\right) = -J \tag{3.18}$$

The expansion of the term J on the right hand side of Equation 3.18 in terms of quantities relevant to the external circuit depends on the type of conductors and source applied. Considering the term J consists of two components: one due to the applied source and another due to the induced electric field produced by time-varying magnetic field. Thus Equation 3.18 becomes

$$\frac{\partial}{\partial x}\left(\nu \frac{\partial A}{\partial x}\right) + \frac{\partial}{\partial y}\left(\nu \frac{\partial A}{\partial y}\right) = -\left(J^s - \sigma \frac{\partial A}{\partial t}\right) \tag{3.19}$$

where J^s is the applied source and σ is the electrical conductivity.

3.2.3 Discretization of the FE domain by Galerkin Method

Let A^e be the approximation for magnetic vector potential for differential equation Equation 3.18 in the e^{th} element. Then the residual for the element is given by

$$R^e = \frac{\partial}{\partial x}\left(\nu\frac{\partial A^e}{\partial x}\right) + \frac{\partial}{\partial y}\left(\nu\frac{\partial A^e}{\partial y}\right) - \sigma\frac{\partial A^e}{\partial t} + J_s^e \tag{3.20}$$

Let w^e be a suitable weight function. The weighted integral statement of the governing equation can be written as (where, Ω^e is the domain in which the condition is enforced)

$$\iint_{\Omega^e} w^e R^e d\Omega^e = 0 \tag{3.21}$$

$$\iint_{\sigma^e} w^e\left(\frac{\partial}{\partial x}\left(\nu\frac{\partial A^e}{\partial x}\right)\right)dxdy + \iint_{\sigma^e} w^e\left(\frac{\partial}{\partial y}\left(\nu\frac{\partial A^e}{\partial y}\right)\right)dxdy - \iint_{\sigma^e} w^e\left(\sigma\frac{\partial A^e}{\partial t}\right)dxdy + \iint_{\sigma^e} w^e J_s^e dxdy = 0 \tag{3.22}$$

Considering 1st term of Equation 3.22

$$T_1 = \iint_{\sigma^e} w^e\left(\frac{\partial}{\partial x}\left(\nu\frac{\partial A^e}{\partial x}\right)\right)dxdy \tag{3.23}$$

$$T_1 = \iint_{\sigma^e}\left(w^e\left(\frac{\partial G}{\partial x}\right)\right)dxdy, \text{ where } \left(\nu\frac{\partial A^e}{\partial x}\right) = G \tag{3.24}$$

$$T_1 = \iint_{\sigma^e}\left(\frac{\partial\left(w^e G\right)}{\partial x} - \frac{\partial w^e}{\partial x}G\right)dxdy \tag{3.25}$$

$\left(\text{since, } w^e\frac{\partial G}{\partial x} + \frac{\partial w^e}{\partial x}G = \frac{\partial(w^e G)}{\partial x}\right)$

$$T_1 = \iint_{\sigma^e}\frac{\partial\left(w^e G\right)}{\partial x}dxdy - \iint_{\sigma^e}\frac{\partial w^e}{\partial x}Gdxdy \tag{3.26}$$

$$T_1 = \oint_{\Gamma^e}\left(w^e G\right)n_x d\Gamma - \iint_{\sigma^e}\frac{\partial w^e}{\partial x}Gdxdy \tag{3.27}$$

since, $\left(\iint_{\sigma^e}\frac{\partial(w^e G)}{\partial x}d\Omega = \oint_{\Gamma^e}\left(w^e G\right)n_x d\Gamma\right)$

$$T_1 = \oint_{\Gamma^e}\left(w^e\left(\nu\frac{\partial A^e}{\partial x}\right)\right)n_x d\Gamma - \iint_{\sigma^e}\frac{\partial w^e}{\partial x}\left(\nu\frac{\partial A^e}{\partial x}\right)dxdy \tag{3.28}$$

Similar expressions have been derived for the second term T_2 and then combining the first two terms of Equation 3.22, we get

$$T_1 + T_2 = \iint_{\sigma^e} w^e \left(\frac{\partial}{\partial x}\left(\nu \frac{\partial A^e}{\partial x}\right)\right) dxdy + \iint_{\sigma^e} w^e \left(\frac{\partial}{\partial y}\left(\nu \frac{\partial A^e}{\partial y}\right)\right) dxdy \tag{3.29}$$

$$T_1 + T_2 = \oint_{\Gamma^e} w^e \left(\left(\nu \frac{\partial A^e}{\partial x}\right) n_x + \left(\nu \frac{\partial A^e}{\partial y}\right) n_y\right) d\Gamma - \iint_{\sigma^e} \nu \left(\frac{\partial w^e}{\partial x}\frac{\partial A^e}{\partial x} + \frac{\partial w^e}{\partial y}\frac{\partial A^e}{\partial y}\right) dxdy \tag{3.30}$$

$$T_1 + T_2 = \oint_{\Gamma^e} w^e \nu \left(\frac{\partial A^e}{\partial x}\hat{i} + \frac{\partial A^e}{\partial y}\hat{j}\right) . \left(n_x\hat{i} + n_y\hat{j}\right) d\Gamma - \iint_{\sigma^e} \nu \left(\frac{\partial w^e}{\partial x}\frac{\partial A^e}{\partial x} + \frac{\partial w^e}{\partial y}\frac{\partial A^e}{\partial y}\right) dxdy \tag{3.31}$$

$\left(\text{since}, \vec{B^e} = \nabla \times \vec{A^e} = +\frac{\partial A^e}{\partial y}\hat{i} - \frac{\partial A^e}{\partial x}\hat{j}\right)$

$$T_1 + T_2 = \oint_{\Gamma^e} w^e \nu \left(-B^e_y\hat{i} + B^e_x\hat{j}\right) . \left(n_x\hat{i} + n_y\hat{j}\right) d\Gamma - \iint_{\sigma^e} \nu \left(\frac{\partial w^e}{\partial x}\frac{\partial A^e}{\partial x} + \frac{\partial w^e}{\partial y}\frac{\partial A^e}{\partial y}\right) dxdy \tag{3.32}$$

$\left(\text{since}, \hat{k} \times \vec{B^e} = -B_y\hat{i} + B_x\hat{j}\right)$

$$T_1 + T_2 = \oint_{\Gamma^e} w^e \nu \left(\hat{k} \times \vec{B^e}\right) . \left(\vec{n}\right) d\Gamma - \iint_{\sigma^e} \nu \left(\frac{\partial w^e}{\partial x}\frac{\partial A^e}{\partial x} + \frac{\partial w^e}{\partial y}\frac{\partial A^e}{\partial y}\right) dxdy \tag{3.33}$$

$\left(\text{since}, \ \vec{B^e} \parallel \vec{n} \Rightarrow \left(\hat{k} \times \vec{B^e}\right) \perp \vec{n} \ => \left(\hat{k} \times \vec{B^e}\right) . \vec{n} = 0\right)$

$$T_1 + T_2 = -\iint_{\sigma^e} \nu \left(\frac{\partial w^e}{\partial x}\frac{\partial A^e}{\partial x} + \frac{\partial w^e}{\partial y}\frac{\partial A^e}{\partial y}\right) dxdy \tag{3.34}$$

$$\therefore \iint_{\sigma^e} w^e \left(\frac{\partial}{\partial x}\left(\nu \frac{\partial A^e}{\partial x}\right)\right) dxdy + \iint_{\sigma^e} w^e \left(\frac{\partial}{\partial y}\left(\nu \frac{\partial A^e}{\partial y}\right)\right) dxdy = -\iint_{\sigma^e} \nu \left(\frac{\partial w^e}{\partial x}\frac{\partial A^e}{\partial x} + \frac{\partial w^e}{\partial y}\frac{\partial A^e}{\partial y}\right) dxdy \tag{3.35}$$

Now substituting Equation 3.35 in Equation 3.22 we have

$$-\iint\limits_{\sigma^e} \nu\left(\frac{\partial w^e}{\partial x}\frac{\partial A^e}{\partial x}+\frac{\partial w^e}{\partial y}\frac{\partial A^e}{\partial y}\right)dxdy-\iint\limits_{\sigma^e} w^e\left(\sigma\frac{\partial A^e}{\partial t}\right)dxdy+\iint\limits_{\sigma^e} w^e J_s^e dxdy=0 \qquad (3.36)$$

In the above equation, the highest order of the derivative in the entire expression is one. Therefore, a single degree polynomial satisfies the completeness requirement. Also, we observe that the highest order of the derivative in the integrand is one. Thus, C^0 continuity is good enough for the approximating function.

Finite element equation for a $k-$noded element has been derived with the approximation given by Equation 3.37.

$$\left.\begin{array}{c} A^e=\lfloor \mathbf{N}\rfloor\left\{\mathbf{A}^{ke}\right\}=\lfloor N_1N_2\ldots N_k\rfloor\begin{Bmatrix} A_1\\ A_2\\ \vdots\\ A_k\end{Bmatrix} => \frac{\partial A^e}{\partial x}=\lfloor \mathbf{N}_{,x}\rfloor\left\{\mathbf{A}^{ke}\right\} \\ w^e=\left\lfloor \mathbf{w}^{ke}\right\rfloor\{\mathbf{N}\} => \frac{\partial w^e}{\partial x}=\left\lfloor \mathbf{w}^{ke}\right\rfloor\{\mathbf{N}_{,x}\} \end{array}\right\} \qquad (3.37)$$

Substituting Equation 3.37 in Equation 3.36 we have

$$\left.\begin{array}{l} -\iint\limits_{\sigma^e} \nu\left\lfloor \mathbf{w}^{ke}\right\rfloor\left(\{\mathbf{N}_{,x}\}\lfloor \mathbf{N}_{,x}\rfloor+\left\{\mathbf{N}_{,y}\right\}\left\lfloor \mathbf{N}_{,y}\right\rfloor\right)\left\{\mathbf{A}^{ke}\right\}dxdy- \\ \iint\limits_{\sigma^e} \sigma\left\lfloor \mathbf{w}^{ke}\right\rfloor\{\mathbf{N}\}\lfloor \mathbf{N}\rfloor\frac{d\{\mathbf{A}^{ke}\}}{dt}dxdy+\iint\limits_{\sigma^e}\left\lfloor \mathbf{w}^{ke}\right\rfloor\{\mathbf{N}\}J_s^e dxdy \end{array}\right\}=\{\mathbf{0}\} \qquad (3.38)$$

$$-\iint\limits_{\sigma^e} \nu\left(\{\mathbf{N}_{,x}\}\lfloor \mathbf{N}_{,x}\rfloor+\left\{\mathbf{N}_{,y}\right\}\left\lfloor \mathbf{N}_{,y}\right\rfloor\right)\left\{\mathbf{A}^{ke}\right\}dxdy-\iint\limits_{\sigma^e} \sigma\{\mathbf{N}\}\lfloor \mathbf{N}\rfloor\frac{d\left\{\mathbf{A}^{ke}\right\}}{dt}dxdy+\iint\limits_{\sigma^e}\{\mathbf{N}\}J_s^e dxdy=\{\mathbf{0}\} \qquad (3.39)$$

The nodal values of the weights are arbitrary and may be non-zero. Thus, the finite element discretization of Equation 3.18 using Galerkin method yields a system of ordinary differential Equation 3.39, which can be presented in matrix form as

$$[\mathbf{K}^e]\{\mathbf{A}^e\}+[\mathbf{C}^e]\frac{d\{\mathbf{A}^e\}}{dt}=\{\mathbf{J}_s{}^e\} \qquad (3.40)$$

Assuming a $k-$noded element and ($k = 8$), then

$$\{\mathbf{A}^e\} = \left\{\mathbf{A}^{ke}\right\} = \begin{Bmatrix} A_1 \\ A_2 \\ \vdots \\ A_8 \end{Bmatrix} \tag{3.41}$$

$$[\mathbf{K}^e] = \iint\limits_{\sigma^e} \nu\left(\{\mathbf{N}_{,x}\}\lfloor\mathbf{N}_{,x}\rfloor + \left\{\mathbf{N}_{,y}\right\}\left\lfloor\mathbf{N}_{,y}\right\rfloor\right) dxdy = \int_{1}^{-1}\int_{1}^{-1} \nu\{grad\mathbf{N}\}\lfloor grad\mathbf{N}\rfloor |\mathbf{J}|\, d\xi d\eta \tag{3.42}$$

$$[\mathbf{C}^e] = \iint\limits_{\sigma^e} \sigma\{\mathbf{N}\}\lfloor\mathbf{N}\rfloor\, dxdy = \int_{1}^{-1}\int_{1}^{-1} \sigma\{\mathbf{N}\}\lfloor\mathbf{N}\rfloor |\mathbf{J}|\, d\xi d\eta \tag{3.43}$$

$$\{\mathbf{J}_s{}^e\} = d_s \iint\limits_{\sigma^e} J_s\{\mathbf{N}\}\, dxdy = d_s \int_{1}^{-1}\int_{1}^{-1} J_s^e\{\mathbf{N}\}|\mathbf{J}|\, d\xi d\eta \tag{3.44}$$

where d_s dictates whether the current will be $+ve$ or $-ve$ and

$$d_s = \begin{cases} +1, \text{when the coil is } +ve\text{ly orinted} \\ -1, \text{when the coil is } -ve\text{ly orinted} \end{cases}$$

$$\lfloor\mathbf{N}\rfloor = \lfloor N_1\, N_2\, N_3\, N_4\, N_5\, N_6\, N_7\, N_8\rfloor = \{\mathbf{N}\}^T \tag{3.45}$$

$$\lfloor grad\mathbf{N}\rfloor_{2\times 8} = \mathbf{J}^{-1}\begin{bmatrix} \frac{\partial N_1}{\partial \xi} & \dots & \frac{\partial N_8}{\partial \xi} \\ \frac{\partial N_1}{\partial \eta} & \dots & \frac{\partial N_8}{\partial \eta} \end{bmatrix}_{(2\times 8)} = \mathbf{J}^{-1}\mathbf{B}_{2\times 8} \tag{3.46}$$

However, in global form Equation 3.40 is given as

$$[\mathbf{K}]\{\mathbf{A}\} + [\mathbf{C}]\frac{d\{\mathbf{A}\}}{dt} = \{\mathbf{J}_s\} \tag{3.47}$$

where, $\{\mathbf{A}\} = \{\mathbf{A}^{ne}\} = \begin{Bmatrix} A_1 \\ A_2 \\ \vdots \\ A_n \end{Bmatrix}$, n is the total no of nodes in the finite element domain

3.2.4 Solution of the elemental equation by Crank-Nicolson time discretization method

To solve the system of ordinary differential equation (Equation3.47), time-discretization schemes Crank-Nicolson method is used. It is a second-order finite difference method, implicit in time and is unconditionally stable. Let $\{\mathbf{A}\}^{k-1} = \{\mathbf{A}(t)\}^{k-1}$ has been solved at time t^{k-1} and $\{\mathbf{A}\}^{k} = \{\mathbf{A}(t)\}^{k}$ to be solved at time $t^{k} = t^{k-1} + \Delta t$. The nodal values of the next time step can be obtained using Crank-Nicolson method from

$$\{\mathbf{A}\}^{k} = \{\mathbf{A}\}^{k-1} + \frac{1}{2}\left(\left.\frac{d\{\mathbf{A}\}}{dt}\right|^{k} + \left.\frac{d\{\mathbf{A}\}}{dt}\right|^{k-1} \right)\Delta t \tag{3.48}$$

The differential equation is written at time steps t^{k} and t^{k-1} as

$$[\mathbf{K}]^{k}\{\mathbf{A}\}^{k} + [\mathbf{C}]\left.\frac{d\{\mathbf{A}\}}{dt}\right|^{k} = \{\mathbf{J}_s\}^{k} \tag{3.49}$$

$$[\mathbf{K}]^{k-1}\{\mathbf{A}\}^{k-1} + [\mathbf{C}]\left.\frac{d\{\mathbf{A}\}}{dt}\right|^{k-1} = \{\mathbf{J}_s\}^{k-1} \tag{3.50}$$

When the above two expressions are added together, we get the following equation

$$[\mathbf{K}]^{k}\{\mathbf{A}\}^{k} + [\mathbf{K}]^{k-1}\{\mathbf{A}\}^{k-1} + [\mathbf{C}]\left(\left.\frac{d\{\mathbf{A}\}}{dt}\right|^{k} + \left.\frac{d\{\mathbf{A}\}}{dt}\right|^{k-1} \right) = \{\mathbf{J}_s\}^{k} + \{\mathbf{J}_s\}^{k-1} \tag{3.51}$$

Using Equation 3.48

$$\left([\mathbf{K}]^{k} + \frac{2}{\Delta t}[\mathbf{C}]\right)\{\mathbf{A}\}^{k} = -\left([\mathbf{K}]^{k-1} + \frac{2}{\Delta t}[\mathbf{C}]\right)\{\mathbf{A}\}^{k-1} + \{\mathbf{J}_s\}^{k} + \{\mathbf{J}_s\}^{k-1} \tag{3.52}$$

In this equation, there are no more time derivatives. Furthermore, all the terms on the right hand side are known either as source terms or from the field solution at the previous time step. The magnetic vector potential is zero on the outer boundary, which means that the magnetic flux density has no normal components on the outer boundary. The insertion of boundary condition is performed when the global matrices are fully assembled.

3.2.5 Coupled field-circuit equation for cage induction machine

Conceptually the current density consists of three components: one due to the applied source, another due to the induced electric field produced by time-varying magnetic field and the third one due to the motion-induced. Thus Equation 3.53 becomes the time-dependent magnetic diffusion equation for cage induction motor considering three components of the current density i.e., due to the applied source, due to the induced electric field produced by time-varying magnetic field and due to the motion can be written as,

$$\frac{\partial}{\partial x}\left(\nu\frac{\partial A}{\partial x}\right)+\frac{\partial}{\partial y}\left(\nu\frac{\partial A}{\partial y}\right)=-\left(J^s-\sigma\frac{\partial A}{\partial t}+\sigma\overrightarrow{v}\times B\right) \tag{3.53}$$

where $A\left(x,y\right)$ is the z component of magnetic vector potential $\overrightarrow{A}$, J^s is the current density due to the applied source in the stator, $\overrightarrow{v}$ is the velocity of the rotor with respect to the magnetic field and σ is the electrical conductivity.

For a thin conductor J^s can be written as,

$$J^s=d_P^s\frac{N_{PC}}{\delta_{PC}S_{PC}}i_P^s \tag{3.54}$$

and if the rotor finite element mesh can be moved in such a way that the relative velocity $\overrightarrow{v}$ becomes zero, then the diffusion equation can be written as,

$$\frac{\partial}{\partial x}\left(\nu\frac{\partial A}{\partial x}\right)+\frac{\partial}{\partial y}\left(\nu\frac{\partial A}{\partial y}\right)-\sigma\frac{\partial A}{\partial t}+\beta_P^s i_P^s=0 \tag{3.55}$$

where $\beta_P^s=d_P^s\frac{N_{PC}}{\delta_{PC}S_{PC}}$, N_{PC} is the number of turns associated with one of the coil sides connected in series, δ_{PC} is the filling factor, S_{PC} is the cross-sectional area of a coil side, i_{PC}^s is the stator phase current and d_{PC}^s is 1 or -1 depending on whether the coil side is positively oriented or negatively oriented respectively. The field equation is also required to be coupled with the circuit equation of the stator because the device is voltage fed.

$$u_P^s=R_P^s i_P^s+L_{endP}^s\frac{di_P^s}{dt}+l\iint_S d_P^s\frac{N_{PC}}{\delta_{PC}S_{PC}}\frac{\partial A}{\partial t}ds \tag{3.56}$$

where u_P^s is the stator phase voltage, R_P^s is the total dc resistance of the phase winding $P\left(P=1,2,3\right)$

or ($P = A, B, C$), L^s_{endP} is the end inductance of the phase winding P and l is the axial length of the machine.

The above formulation is suited for the condition when there is no parallel path in the winding. Equation 3.55 and Equation 3.56 together form the coupled magnetic field and electric circuit equations for a cage-induction machine. In the above formulation, equation for rotor circuit is not explicitly coupled because the rotor bars are not externally fed and they are connected and short-circuited. However, the eddy currents induced in the non-laminated conducting parts of the rotor (i.e. the rotor bar regions) is included in the above formulation and this is represented by the term in Equation 3.22. Furthermore, in the formulation of Equation 3.21, it is assumed that the stator phase windings have no parallel path and each phase winding consists of successive coils as shown in Figure 3.1.

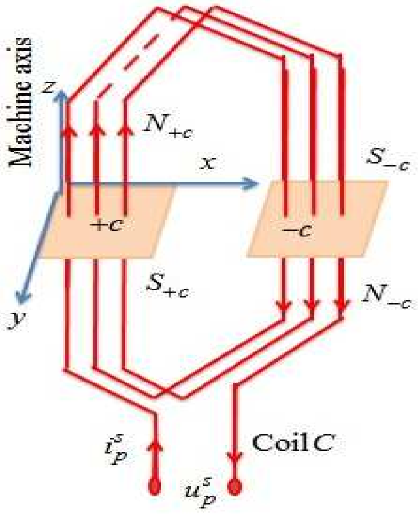

Figure 3.1: Stator coil representation.

However, in the bridge configured winding scheme, the currents responsible for torque production are divided into two parallel paths in each phase with an isolated supply between the midpoints of each path to generate lateral force (as shown in Figure 3.2 and Figure 3.3. Thus, there is a need to transform the conventional magnetic field and electric circuit equation so as to incorporate the bridge configured winding scheme that consists of parallel paths as well as additional terminals to mitigate the Unbalanced Magnetic Pull (UMP) which is caused due to the asymmetry in the magnetic field distribution.

After applying finite element discretization by Galerkin method (as presented in Section 3.2.3),

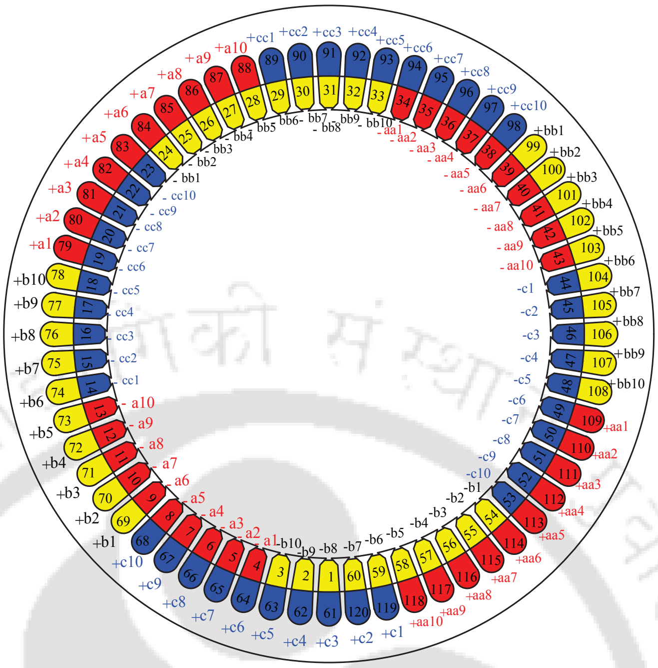

Figure 3.2: A winding scheme of a distributed double layered winding.

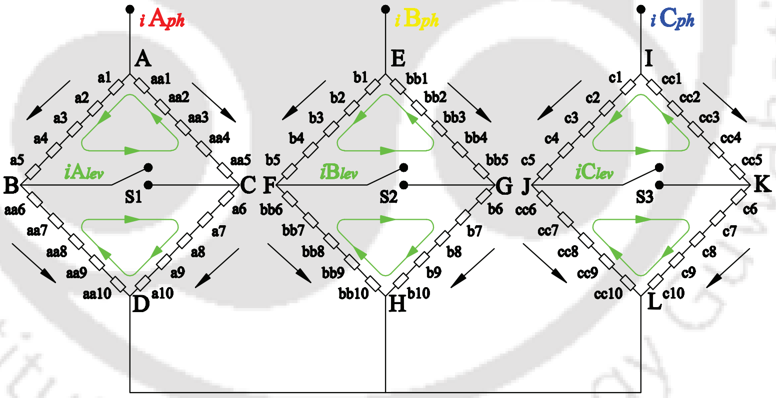

Figure 3.3: A bridge configured winding circuit.

Equations 3.55 and 3.56 can be written in matrix form

$$[\mathbf{S}]_{n\times n}\{\mathbf{A}\}_{n\times 1} + [\mathbf{C}^r]_{n\times n}\frac{d\{\mathbf{A}\}_{n\times 1}}{dt} - [\mathbf{P}^s]_{n\times 3}\{\mathbf{i}^s\}_{3\times 1} = \{\mathbf{0}\} \tag{3.57}$$

$$l.\,[\mathbf{P}^s]^T_{3\times n}\frac{d\{\mathbf{A}\}_{n\times 1}}{dt} + [\mathbf{R}^s]_{3\times 3}\{\mathbf{i}^s\}_{3\times 1} + [\mathbf{L}^s{}_{end}]_{3\times 3}\frac{d\{\mathbf{i}^s\}_{3\times 1}}{dt} = \{\mathbf{u}^s\}_{3\times 1} \tag{3.58}$$

Here, vector $\{\mathbf{A}\}$ is associated with nodal values of magnetic vector potential and hence of the order $(n \times 1)$, where n is the number of nodes in the whole domain.

$$\{\mathbf{u}^{s}\}_{3\times 1} = \begin{bmatrix} u_{phase\_A} & u_{phase\_B} & u_{phase\_C} \end{bmatrix}^{T} \tag{3.59}$$

$$\{\mathbf{i}^{s}\}_{3\times 1} = \begin{bmatrix} i_{phase\_A} & i_{phase\_B} & i_{phase\_C} \end{bmatrix}^{T} \tag{3.60}$$

$[\mathbf{R}^{s}]_{3\times 3}$ and $[\mathbf{L}^{s}{}_{end}]_{3\times 3}$ are diagonal matrices that represent total d.c. resistance and end winding inductance associated with the stator phase currents $\{\mathbf{i}^{s}\}_{3\times 1}$. The elemental form of matrices $[\mathbf{S}]$, $[\mathbf{C}^{r}]$ and $[\mathbf{P}^{s}]$ are are presented in Table 3.1.

Table 3.1: Elemental form of matrices

Sl No	Elemental Form	Value
1	$[\mathbf{S}^{e}]_{k\times k} = \int_{-1}^{1}\int_{-1}^{1} \nu[\mathbf{B}]^{T}\left([\mathbf{J}]^{-1}\right)^{T}[\mathbf{J}]^{-1}\,[\mathbf{B}]\,\lvert\mathbf{J}\rvert\,d\xi d\eta$	This applies to all the elements in the finite element domain.
2	$[\mathbf{C}^{re}]_{k\times k} = \int_{-1}^{1}\int_{-1}^{1} \sigma\,\{\mathbf{N}\}\,\lfloor\mathbf{N}\rfloor\,\lvert\mathbf{J}\rvert\,d\xi d\eta$	This applies to the elements only with conductivity (i.e. rotor bar region) else $[\mathbf{C}^{re}] = 0$
3	$\left[\mathbf{P}_{p}^{se}\right]_{k\times 1} = \int_{-1}^{1}\int_{-1}^{1} \beta_{p}^{s}\,\{\mathbf{N}\}\,\lfloor\mathbf{N}\rfloor\,\lvert\mathbf{J}\rvert\,d\xi d\eta$	This applies to the elements belonging to the thin conductor region (i.e. stator slot region) else $[\mathbf{P}^{se}] = 0$

Taking a $k-$ noded element for instance, and then

$$\left\{\mathbf{A}^{ke}\right\} = \begin{Bmatrix} A_1 \\ A_2 \\ \vdots \\ A_k \end{Bmatrix}, \text{ nodal values of } A \tag{3.61}$$

$$\lfloor\mathbf{N}\rfloor = \lfloor N_1\, N_2\, N_3 \ \ldots\ldots\ N_k \rfloor = \{\mathbf{N}\}^{T}, \text{ shape functions} \tag{3.62}$$

$$\mathbf{J}_{2\times 2} = \begin{bmatrix} \frac{\partial N_1}{\partial \xi} & \cdots & \frac{\partial N_k}{\partial \xi} \\ \frac{\partial N_1}{\partial \eta} & \cdots & \frac{\partial N_k}{\partial \eta} \end{bmatrix} \begin{bmatrix} x_1 & y_1 \\ \vdots & \vdots \\ \vdots & \vdots \\ \vdots & \vdots \\ x_k & y_k \end{bmatrix} \tag{3.63}$$

$$\mathbf{J}^{-1}[\mathbf{B}]_{2\times k} = \lfloor grad\mathbf{N}\rfloor_{2\times k} = \mathbf{J}^{-1}\begin{bmatrix} \frac{\partial N_1}{\partial \xi} & \cdots & \frac{\partial N_k}{\partial \xi} \\ \frac{\partial N_1}{\partial \eta} & \cdots & \frac{\partial N_k}{\partial \eta} \end{bmatrix}_{(2\times k)} \tag{3.64}$$

3.3 Transformations used in the FE analysis to implement BCW scheme

For each parallel path of the windings magnetic field and electric circuit equations are worked out and then the magnetic field and electric circuit equations for the entire stator winding is formed using an appropriate transformation. The term $\left[[\mathbf{P}^s]_{n\times 3}.\{\mathbf{i}^s\}_{3\times 1}\right]$ in Equation 3.57 stands for current density which is uniform for a given stator coil side. For a given coil side (say +a$_5$ as shown in Figure 3.2), the current through each filamentary wire is same (say i_{a_5}). Therefore, the current density for this coil side (which is constant throughout +a$_5$) can be represented as (referring to Figure 3.1).

$$J^s{}_{+a_5} = \frac{N_{+a_5} \times i_{a_5}}{\delta_{+a_5} \times S_{+a_5}} \tag{3.65}$$

where,

N_{+a_5} = number of filamentary coils that passes through coil side +a$_5$

δ_{+a_5} = filling factor

S_{+a_5} = cross – sectional area of +a$_5$

Now, with respect to Figure 3.2, there are such 120 coil sides and hence 120 coil side currents which can be expressed in terms of 6 terminal currents (3 phase currents and 3 levitation or bridge currents). The configured scheme is implemented using the following relation:

$$[\mathbf{P}^s]_{n\times 6}\{\mathbf{i}^s\}_{6\times 1} \equiv [\mathbf{P}^s]_{n\times 120}.\{\mathbf{i}^s{}_{coil\_side}\}_{120\times 1} = [\mathbf{P}^s]_{n\times 120}.[\mathbf{T}_s]_{120\times 6}.\left\{\mathbf{i}^s{}_{ph+lev}\right\}_{6\times 1} \tag{3.66}$$

where, $\left\{\mathbf{i}^s{}_{ph+lev}\right\}_{6\times 1} = \begin{bmatrix} i_{phase\_A} & i_{lev\_A} & i_{phase\_B} & i_{lev\_B} & i_{phase\_C} & i_{lev\_C} \end{bmatrix}^T$

The elemental form of $[\mathbf{P}^s]_{n\times 72}$ is similar to that of $[\mathbf{P}^s]_{n\times 3}$ as given in Table 3.1. However, in this case, the size of the global system of equations increases a little. The transformation matrix $[\mathbf{T_s}]$ relates the 120 coils side currents to the six terminal currents as discussed in the following sub-sections. Basically the transformation matrix $[\mathbf{T_s}]$ is obtained in the following three steps:

3.3.1 Transformation of the coil side currents to the stator slot currents in the stator

Every full coil current corresponds to two half-coil (i.e. coil side) currents. In Figure 3.3, $a5$ represents one full coil. This transformation imposes a constraint that current going down in slot $-a5$ is equal in magnitude to the current coming up in slot $+a5$ but opposite in sign. This transformation can be written by inspection and can be expressed as:

$$\{\mathbf{i}^{s}{}_{coil\_side}\}_{120\times1} = [\mathbf{T}_{s1}]_{120\times60}\cdot\left\{\mathbf{i}^{s}{}_{full\_coil}\right\}_{60\times1} \tag{3.67}$$

For the machine considered $\left\{\mathbf{i}^{s}{}_{full\_coil}\right\}$ will have 60 entries. The transformation can be written as,

$$\begin{Bmatrix} i_{+a_1} \\ i_{-a_1} \\ i_{+a_2} \\ i_{-a_2} \\ \vdots \end{Bmatrix} = \begin{bmatrix} 1 & 0 & \cdots & \cdots \\ -1 & 0 & \cdots & \cdots \\ 0 & 1 & \cdots & \cdots \\ 0 & -1 & \cdots & \cdots \\ \vdots & \vdots & \cdots & \cdots \end{bmatrix} \begin{Bmatrix} i_{a_1} \\ i_{a_2} \\ \vdots \end{Bmatrix} \tag{3.68}$$

where i_{+a_1} , i_{-a_1}, i_{+a_2} and i_{-a_2} are the coil side currents of coil sides $+a_1$, $-a_1$, $+a_2$ and $-a_2$ respectively and i_{a_1}, i_{a_2} are the full coil currents of full coils a_1 and a_2 respectively.

3.3.2 Transformation of the full coil currents to the coil group currents in the stator according to the bridge configured winding

Let us consider phase A (as shown in Figure 3.3). The five full coils a_1, a_3, a_3, a_4, and a_5 together form one ”coil group” and since they are connected in series, the ”coil group” have the same current. Therefore, the currents are

$$\begin{Bmatrix} i_{a_1} \\ i_{a_2} \\ i_{a_3} \\ i_{a_4} \\ i_{a_5} \\ i_{a_6} \end{Bmatrix} = \begin{bmatrix} 1 & 0 \\ 1 & 0 \\ 1 & 0 \\ 0 & 1 \\ 0 & 1 \\ 0 & 1 \end{bmatrix} \begin{Bmatrix} i_A \\ i_D \end{Bmatrix}_{phaseA} \tag{3.69}$$

Similarly, we can have transformations for other coil groups. Finally the transformation that transforms the full coil currents $\left\{\mathbf{i}^{s}{}_{full\_coil}\right\}_{(120\times1)}$ to the coil group currents $\left\{\mathbf{i}^{s}{}_{coil\_group}\right\}_{(12\times1)}$ is:

$$\left\{\mathbf{i}^{s}{}_{full\_coil}\right\}_{(120\times1)} = [\mathbf{T}_{s2}]_{(120\times12)}\left\{\mathbf{i}^{s}{}_{coil\_group}\right\}_{(12\times1)} \tag{3.70}$$

3.3.3 Transformation of the coil group currents to the terminal currents

A transformation matrix which transforms all the group currents (or branch currents) to the phase currents and levitation currents is obtained by assuming the same resistance in each branch of the bridge. The transformation matrix for the phase A is calculated as follows:

$$\begin{Bmatrix} i_A \\ i_B \\ i_C \\ i_D \end{Bmatrix}_{phase\_A} = \begin{bmatrix} \frac{1}{2} & \frac{1}{2} \\ \frac{1}{2} & -\frac{1}{2} \\ \frac{1}{2} & -\frac{1}{2} \\ \frac{1}{2} & \frac{1}{2} \end{bmatrix} \begin{Bmatrix} i_{phase\_A} \\ i_{lev\_A} \end{Bmatrix} \tag{3.71}$$

i_A, i_B, i_C, and i_D are the currents in four branches of the bridge for phase A. Similar transformations shown in Equation 3.71 are also obtained for phases B and C. Finally the transformation that transforms the coil group currents $\left\{\mathbf{i}^{s}{}_{coil\_group}\right\}_{(12\times1)}$ to six terminal currents (two for each phase) $\left\{\mathbf{i}^{s}{}_{ph+lev}\right\}_{6\times1}$ is:

$$\left\{\mathbf{i}^{s}{}_{coil\_group}\right\}_{(12\times1)} = [\mathbf{T}_{s3}]_{(12\times6)}\left\{\mathbf{i}^{s}{}_{ph+lev}\right\}_{6\times1} \tag{3.72}$$

The equation shows the transformation matrix for the six terminal currents. $[\mathbf{T}_s]_{(120\times6)}$ is the transformation matrix that transforms the terminal current vector (associated with the stator windings) to the 120 coil side currents.

3.3.4 Transformed field-circuit equations for bridge-configured cage induction machine

After applying Equation 3.66 for bridge configured winding scheme, Equations 3.57 and 3.58 become

$$[\mathbf{S}]_{n\times n}\{\mathbf{A}\}_{n\times1} + [\mathbf{C}^{r}]_{n\times n}\frac{d\{\mathbf{A}\}_{n\times1}}{dt} - [\mathbf{P}^{s}]_{n\times120}.[\mathbf{T}_{s}]_{120\times6}.\left\{\mathbf{i}^{s}{}_{ph+lev}\right\}_{6\times1} = \mathbf{0} \tag{3.73}$$

$$[\mathbf{S}]_{n\times n}\{\mathbf{A}\}_{n\times 1}+[\mathbf{C}^r]_{n\times n}\frac{d\{\mathbf{A}\}_{n\times 1}}{dt}-[\mathbf{P}_t{}^s]_{n\times 6}\cdot\left\{\mathbf{i}^s{}_{ph+lev}\right\}_{6\times 1}=\mathbf{0} \tag{3.74}$$

where, $[\mathbf{P}_t{}^s]_{n\times 6} = [\mathbf{P}^s]_{n\times 120}.[\mathbf{T}_s]_{120\times 6}$

$$l.\,[\mathbf{P}_t{}^s]^T_{6\times n}\frac{d\{\mathbf{A}\}_{n\times 1}}{dt}+[\mathbf{R}_t^s]_{6\times 6}\left\{\mathbf{i}^s{}_{ph+lev}\right\}_{6\times 1}+\left[\mathbf{L}^s_{endt}\right]_{6\times 6}\frac{d}{dt}\left\{\mathbf{i}^s{}_{ph+lev}\right\}_{6\times 1}=\left\{\mathbf{u}^s{}_{ph+lev}\right\}_{6\times 1} \tag{3.75}$$

$$[\mathbf{Q}_t]_{6\times n}\frac{d\{\mathbf{A}\}_{n\times 1}}{dt}+[\mathbf{R}_t^s]_{6\times 6}\left\{\mathbf{i}^s{}_{ph+lev}\right\}_{6\times 1}+\left[\mathbf{L}^s_{endt}\right]_{6\times 6}\frac{d}{dt}\left\{\mathbf{i}^s{}_{ph+lev}\right\}_{6\times 1}=\left\{\mathbf{u}^s{}_{ph+lev}\right\}_{6\times 1} \tag{3.76}$$

where,

$[\mathbf{Q}_t]_{6\times n} = l.[\mathbf{P}_t{}^s]^T{}_{6\times n}$

$\left\{\mathbf{u}^s{}_{ph+lev}\right\}_{6\times 1} = \begin{bmatrix} u_{phase\_A} & u_{lev\_A} & u_{phase\_B} & u_{lev\_B} & u_{phase\_C} & u_{lev\_C} \end{bmatrix}^T$

$\left\{\mathbf{i}^s{}_{ph+lev}\right\}_{6\times 1} = \begin{bmatrix} i_{phase\_A} & i_{lev\_A} & i_{phase\_B} & i_{lev\_B} & i_{phase\_C} & i_{lev\_C} \end{bmatrix}^T$

$[\mathbf{R}_t{}^s]_{6\times 6}$ and $\left[\mathbf{L}^s_{end\,t}\right]_{6\times 6}$ are diagonal matrices that represent total d.c. resistance and end winding inductance associated with the six stator terminal currents $\left\{\mathbf{i}^s{}_{ph+lev}\right\}_{6\times 1}$.

The combined magnetic field and electric circuit equations for thick and thin conductors are shown in Equations 3.74 and 3.76. After applying Crank-Nicolson time discretization, these two equations can be written as

$$\begin{aligned}&\begin{bmatrix}\left([\mathbf{S}]^k+\frac{2}{\Delta t}[\mathbf{C}^r]\right) & \left[\mathbf{P}_t^S\right]\\ \frac{2}{\Delta t}[\mathbf{Q}_t] & \left[\mathbf{R}_t^S\right]+\frac{2}{\Delta t}\left[\mathbf{L}^S_{endt}\right]\end{bmatrix}\{\mathbf{X}\}^k\\ &=-\begin{bmatrix}\left([\mathbf{S}]^{k-1}+\frac{2}{\Delta t}[\mathbf{C}^r]\right) & \left[\mathbf{P}_t^S\right]\\ \frac{2}{\Delta t}[\mathbf{Q}_t] & \left[\mathbf{R}_t^S\right]+\frac{2}{\Delta t}\left[\mathbf{L}^S_{endt}\right]\end{bmatrix}\{\mathbf{X}\}^{k-1}+\{\mathbf{F}\}^k+\{\mathbf{F}\}^{k-1}\end{aligned} \tag{3.77}$$

where

$$\{S\}=\begin{Bmatrix}\{\mathbf{0}\}_{n\times 1}\\ \left\{U^S_{ph+lev}\right\}_{6\times 1}\end{Bmatrix} \text{ and } \{\mathbf{X}\}=\begin{Bmatrix}\{\mathbf{A}\}_{n\times 1}\\ \{\mathbf{i}_s\}_{6\times 1}\end{Bmatrix}$$

3.3.5 Accommodating movement modeling in induction machine using airgap stitching method

In the present analysis, airgap stitching method is used for modeling the rotor movement. In this method, the rotor and stator are modeled using completely separate FE models in two frames of reference:

- In a fixed frame of reference - the stator including some fraction of the airgap.
- In a moving frame of reference - the rotor.

The two subsystem models are combined by stitching the outer diameter of the rotor and the inner diameter of the stator in the airgap. Quadrilateral quadratic finite elements are used to model the stator and rotor while second-order triangular elements have been incorporated for airgap stitching (shown in Figure 3.6). During the simulation, the airgap has to be re-meshed to account for the rotor movement. This means that the non-zero element matrices associated with the airgap must be derived at every time step during the simulation even if the magnetic saturation is not considered. A strong advantage of this method is that it can cope with the case of eccentric rotor provided that the eccentricity is smaller than the thickness of the stitched band.

In the present analysis, airgap stitching method is used for modeling the rotor movement. The air gap is divided into three equal annular regions. The model and the FE mesh has been developed by using both ANSYS and MATLAB. One stator sector $\left(\frac{360^\circ}{\text{No. of stator slots}}\right)$ has been developed in ANSYS. Two annular regions of the air gap have been attached to the stator sector and treated them as a part of the stator as shown in Figure. 3.4. Similarly one rotor sector $\left(\frac{360^\circ}{\text{No. of rotor bars}}\right)$ has been developed in ANSYS as shown in Figure 3.5 and the full model has been developed in MATLAB. The full model of the rotor and stator are combined by stitching the outer diameter of the full rotor model and the inner diameter of the full stator model. The complete mesh of the rotor and the stator has been generated as shown in Figure 3.6. The complete model comprises of 9936 elements and 30864 nodes. 8-noded quadrilateral elements are used to model the stator and the rotor while second-order triangular elements have been incorporated for airgap stitching. During the simulation, the airgap has been re-meshed to account for the rotor movement.

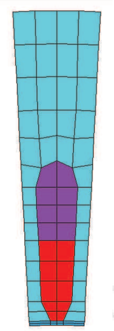

Figure 3.4: Finite element mesh for one sector of the stator slot

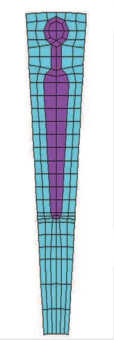

Figure 3.5: Finite element mesh for one sector of the rotor slot

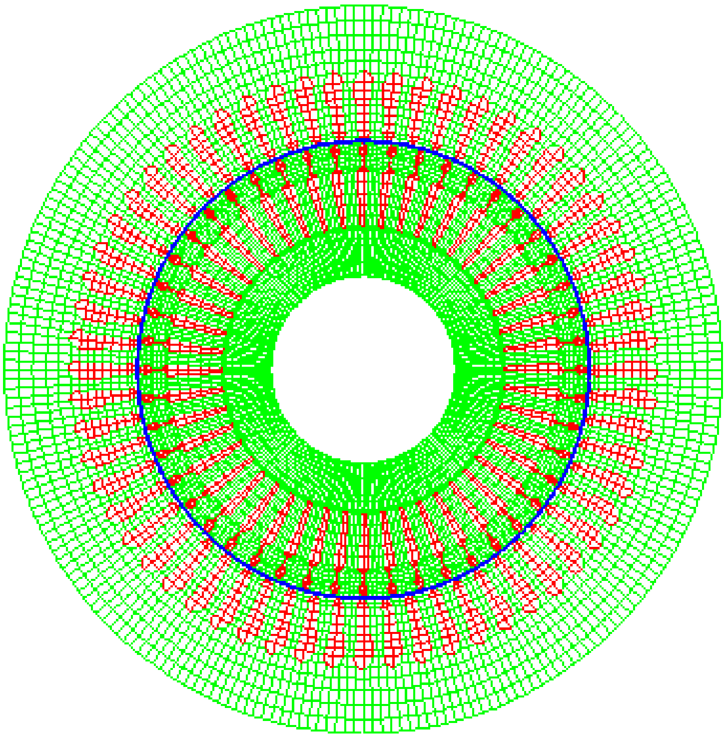

Figure 3.6: Finite element mesh for the entire machine

3.4 Numerical investigation

A 4-pole squirrel cage induction machine with 60 stator slots has been considered for conducting the numerical investigation. The parameters of the machine considered for the numerical investigation are shown in Table 3.2. The stator EMF is generated using bridge configured winding. It has been already mentioned that in bridge configured winding each one “coil” in a conventional machine winding would be divided into a pair of “half-coils”. Then a series-connected pair of coils on opposite sides of a machine would be connected instead in Wheatstone bridge format. When the mid-points of the Wheatstone bridge are left open then the bridge is called Bridge OFF condition and when the mid-points of the Wheatstone bridge are short-circuited then the bridge is called Bridge ON condition. As stated by Khoo, [1], the bridge configured winding scheme is bestowed with the capability to produce passive control to reduce UMP along with its provision for active control. Passive control of UMP can be accomplished by short circuiting the additional pairs of terminals or “closing the bridge” or ”Bridge ON”.

A 2D finite element code has been developed in MATLAB$^{\text{TM}}$ environment that can simulate and solve the differential equations of a bridge configured squirrel-cage induction machine. The code comprises of a pre-processor where the model is built and finite element mesh is generated; a solver where excitations mainly the supply voltages are applied and magnetic vector potentials at each node are computed; and a postprocessor for calculating the magnetic field at the airgap and the forces at the airgap. The simulation has been performed by the time stepping scheme with the rotor motion at constant speed allowing the FE model to take into account the harmonics due to the eccentric rotor motion. Simulations are performed applying 3-phase sinusoidal voltages at the stator terminals for static, dynamic and mixed eccentricity conditions for a particular slip condition. When the rotor is eccentric, it induces an EMF tending to drive currents in the closed circuit and thus produces a levitation field with a pole-pair difference. This causes a net transverse force or UMP which acts on the rotor. Active control can be deployed by connecting the terminals devoted to lateral forces to isolated controllable current or voltage sources. The bridge currents and the forces acting on the rotor are calculated to study the effect of these three eccentricity conditions. A summary of the bridge currents and the airgap forces are compiled in a table and presented in the conclusion.

Table 3.2: Parameters of the induction machine

Parameters	Value
No. of poles	4
No. of stator slots	60
No. of rotor bars	48
Outer dia. of stator	350 mm
Outer dia. of rotor	218.5 mm
Airgap length	1.25 mm
Axial length of the motor	212 mm
Resistance per phase	6.8 Ω
End winding inductance	3.94 e-4 A/m
Supply voltage	20 V, 20 Hz
Slip	0.02

For a concentric rotor with a electromagnetically symmetric stator, there will be no bridge currents even if the midpoints of the Wheatstone bridge or simply ”the bridge points” are short circuited. The bridge currents and the forces in the airgap have been calculated for Bridge ON condition, i.e. the midpoint of the Wheastone bridge is short-circuited. In case of an eccentric rotor, obviously there will be no net equalizing currents flowing when the equalizing links are not short circuited. The dominant frequency components of the bridge currents (also called induced equalizing or levitation currents) for static eccentricity is f_s, where f_s is the frequency of the supply voltage. The dominant frequency components of the bridge currents for dynamic eccentricity condition are given by Equation 3.78 as presented by Nandi et al. [28].

$$f_{bridge} = f_s \pm f_{rot} \tag{3.78}$$

where f_{rot} is the rotational frequency of the machine and $f_{rot} = \left\{(1-s) \times \frac{f_s}{p}\right\}$, f_s = supply frequency, p = fundamental pole-pair. The induction machine considered for the analysis is a $4-$ pole and is operated at 2% slip. The rotational frequency of the machine f_{rot} is 9.8 Hz when the supply frequency, f_s is 20 Hz.

The dominant component of the transverse forces acting on the rotor, also called UMP, are at $\left(\pm f_s \pm f_{bridge}\right)$ which are generated by the interactions between p and $(p \pm 1)$ pole pair magnetic fields as presented by Laiho and Kalita [56].

For the static eccentricity the rotor centre has been shifted along x-axis by 1.25e-04 mm which is 10% of the airgap and the rotor rotates about this point. Figures 3.7 and 3.9 show the variation of phase currents and bridge currents in time for a rotor with static eccentricity for 2% slip and a supply voltage of 20V at 20Hz in Bridge ON condition. Figure 3.8 shows the FFT of Phase A of the phase currents and Figure 3.10 shows the FFT of Phase A of the bridge currents for the rotor with static eccentricity. It has been observed in Figure 3.10 that the frequency component of the bridge current is 20 Hz. Figures 3.11 and 3.12 show the transverse forces acting on the rotor along x- and y- axes respectively due to static eccentricity condition. The dominant frequency components are 0 Hz and 40 Hz as expected from the relationship $\left(\pm f_s \pm f_{bridge}\right)$. However, there is also a force component with small magnitude at 20 Hz.

In case of dynamic eccentricity the rotor centre whirls about the centre point of the stator with a whirling radius of 1.25e-04 mm which is 10% of the airgap and the rotor also rotates about its own axis. Figures 3.13 and 3.15 show the variation of phase currents and bridge currents in time for a rotor with dynamic eccentricity for 2% slip and a supply voltage of 20V at 20Hz in Bridge ON condition. Figure 3.14 shows the FFT of Phase A of the phase currents and Figure 3.16 shows the FFT of Phase A of the bridge currents for the rotor with dynamic eccentricity. It has been observed in Figure 3.16 that the frequency of the bridge current are 10.2 Hz and 29.8 Hz. Similar frequency components are proposed by Equation 3.78. Figures 3.17 and 3.18 show the transverse forces acting on the rotor along x- and y- axes respectively due to dynamic eccentricity. The dominant frequency components are 9.8 Hz, 30.2 Hz and 49.8 Hz as expected from the relationship $\left(\pm f_s \pm f_{bridge}\right)$.

In case of mixed eccentricity condition the rotor centre has been shifted along x-axis by 6.25e-05 mm which is 5% of the airgap and the rotor centre whirls about this point with a whirling radius of 6.25e-05 mm which is 5% of the airgap and the rotor rotates about its own axis. Figures 3.19 and 3.21 show the variation of phase currents and bridge currents in time for a rotor with mixed eccentricity for 2% slip and a supply voltage of 20V at 20Hz in Bridge ON condition. Figures 3.20 shows the FFT of Phase A of the phase currents and Figure 3.22 shows the FFT of Phase A of the bridge currents for the rotor with mixed eccentricity. It has been observed in Figure 3.22 that the frequency of the bridge current are 10.2 Hz, 20 Hz and 29.8 Hz. The bridge currents induced in static and dynamic eccentricity conditions are present in mixed eccentricity conditions. Figures 3.23 and 3.24 show the

Table 3.3: Comparison of the frequency components of bridge current and UMP

	Bridge currents (Hz)	Transverse force on the rotor or UMP (Hz)
Static Eccentricity	20 (f_s)	0, 40 ($2f_s$)
Dynamic Eccentricity	10.2, 29.8 ($f_s \pm f_r$)	9.8, 30.2 and 49.8 ($\pm f_s \pm f_{bridge}$)
Mixed Eccentricity	20 (f_s), 10.2, 29.8 ($f_s \pm f_r$)	0, 9.8, 30.2, 40 and 49.8 ($\pm f_s \pm f_{bridge}$)

transverse forces acting on the rotor along x- and y- axes respectively due to mixed eccentricity. The dominant frequency components are 0 Hz, 9.8 Hz, 20 Hz, 30.2 Hz, 40 Hz and 49.8 Hz as expected from the relationship $\left(\pm f_s \pm f_{bridge}\right)$. However, similar to static eccentricity condition there is also a force component with small magnitude at 20 Hz. Another frequency component at 29.8 Hz is also found which needs further investigation.

Table 3.3 summarise the bridge currents and UMP due to static, dynamic and mixed eccentricity conditions.

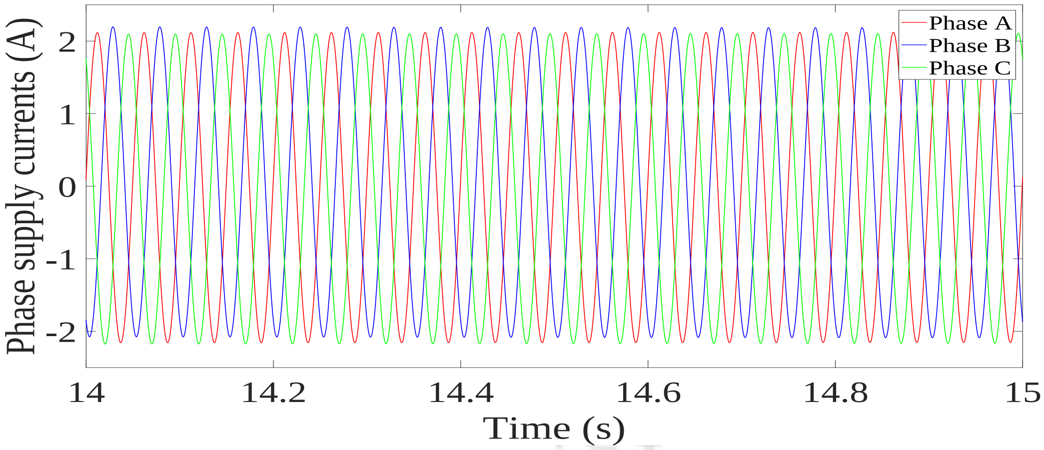

Figure 3.7: Three main currents for a supply voltage of 20 V with frequency 20 Hz in time domain when the rotor is in static eccentricity condition

3.5 Conclusions

Numerical simulation of bridge configured based induction machine using finite element method has been presented in this chapter. The FE simulation of a BCW based induction machine has been done for transient analysis. Transformation matrices have been derived to transform the phase currents to nodal currents. The coupled circuit and field equations are solved to calculate the main currents,

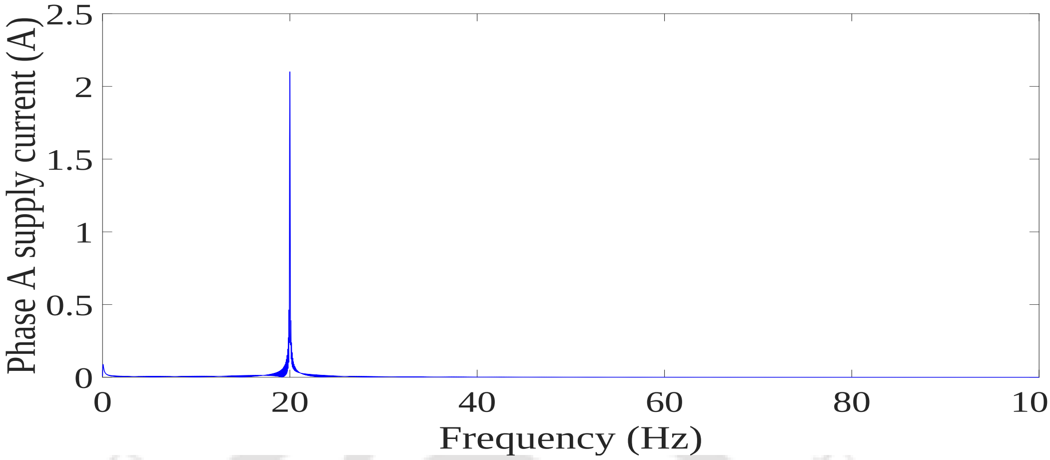

Figure 3.8: FFT of Phase A of the main current for a supply voltage of 20 V with frequency 20 Hz when the rotor is in static eccentricity condition

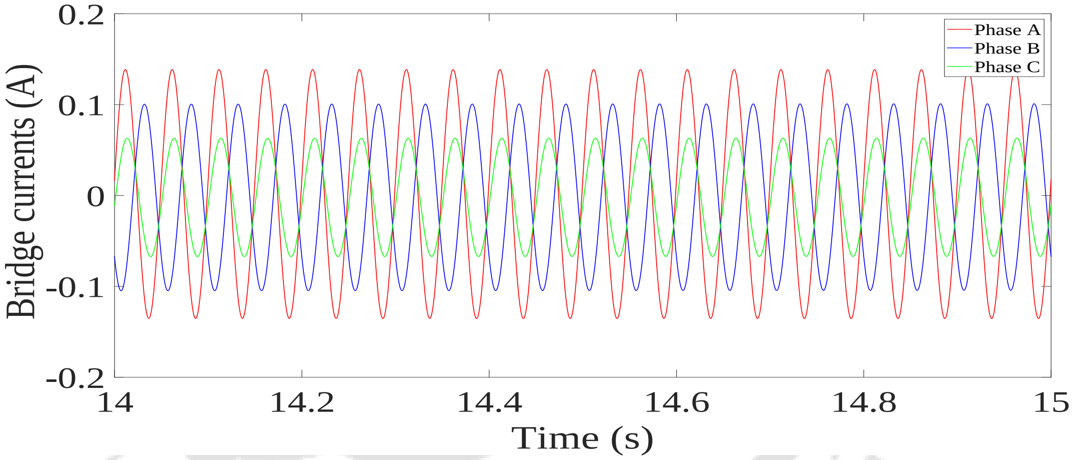

Figure 3.9: Three bridge currents for a supply voltage of 20 V with frequency 20 Hz in time domain when the rotor is in static eccentricity condition

bridge currents and also the magnetic vector potential at each node. Magnetic fields are calculated at the airgap from the magnetic vector potentials. The transverse forces acting in the rotor also called UMP are calculated from the magnetic fields. The bridge currents and The transverse forces acting in the rotor are calculated for three eccentricity conditions, i.e. static, dynamic and mixed eccentricity conditions. The numerical results presented in this chapter are verified using experimental results in Chapter 5.

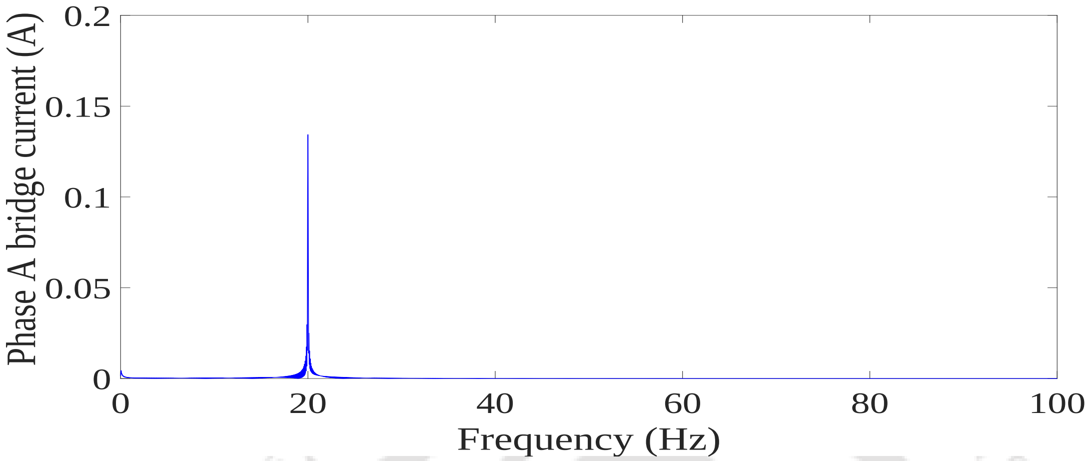

Figure 3.10: FFT of Phase A of the bridge Current for a supply voltage of 20 V with frequency 20 Hz when the rotor is in static eccentricity condition

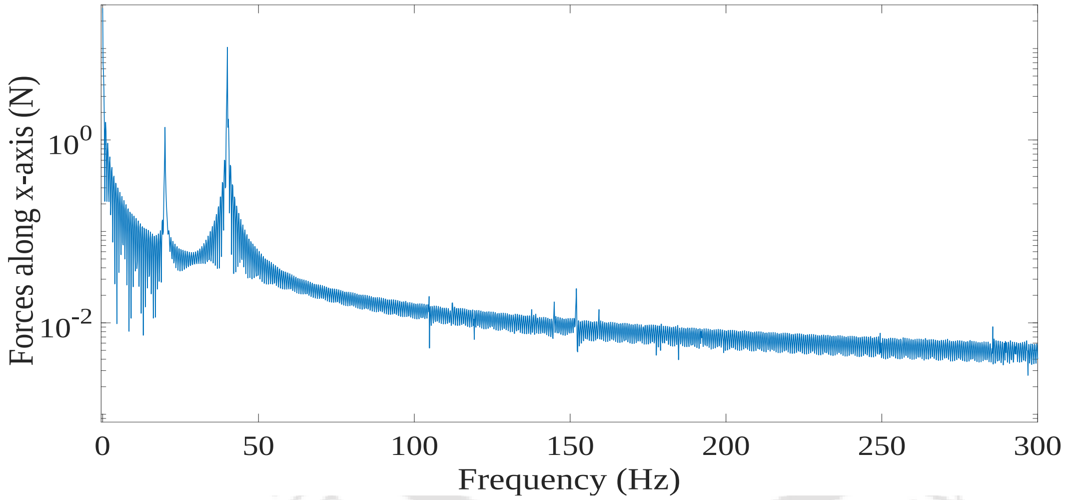

Figure 3.11: FFT of the force component along x-axis when the rotor is in static eccentricity condition

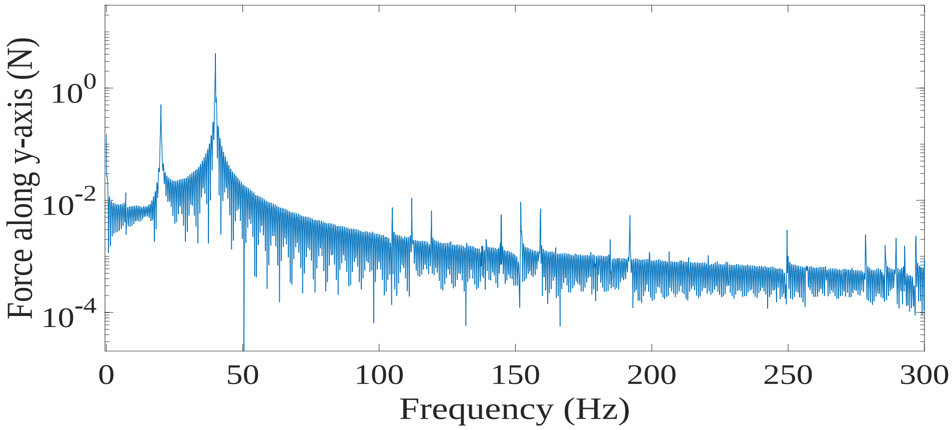

Figure 3.12: FFT of the force component along y-axis when the rotor is in static eccentricity condition

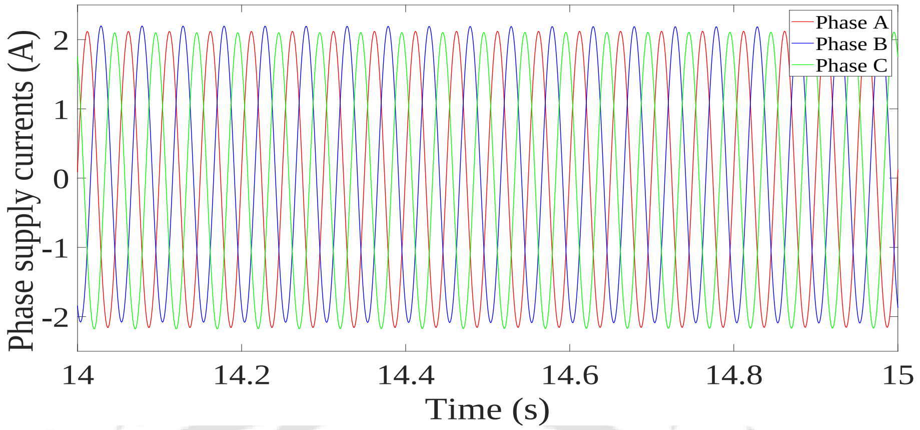

Figure 3.13: Three main currents for a supply voltage of 20 V with frequency 20 Hz in time domain when the rotor is in dynamic eccentricity condition

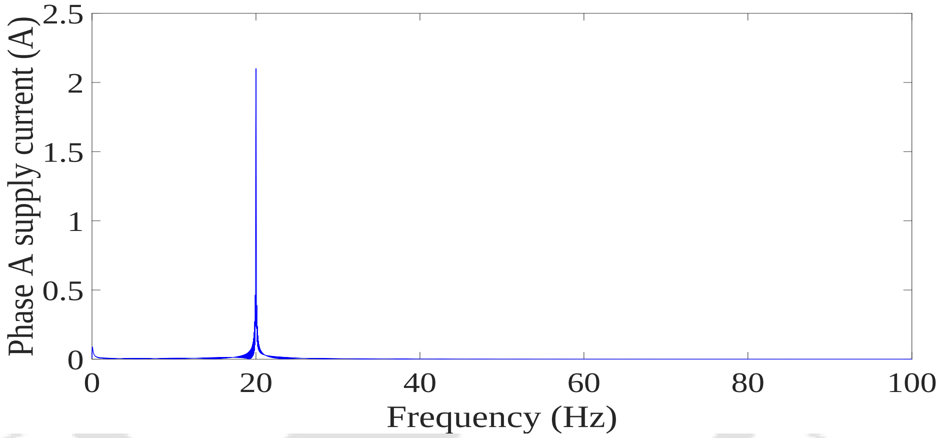

Figure 3.14: FFT of Phase A of the main current for a supply voltage of 20 V with frequency 20 Hz when the rotor is in dynamic eccentricity condition

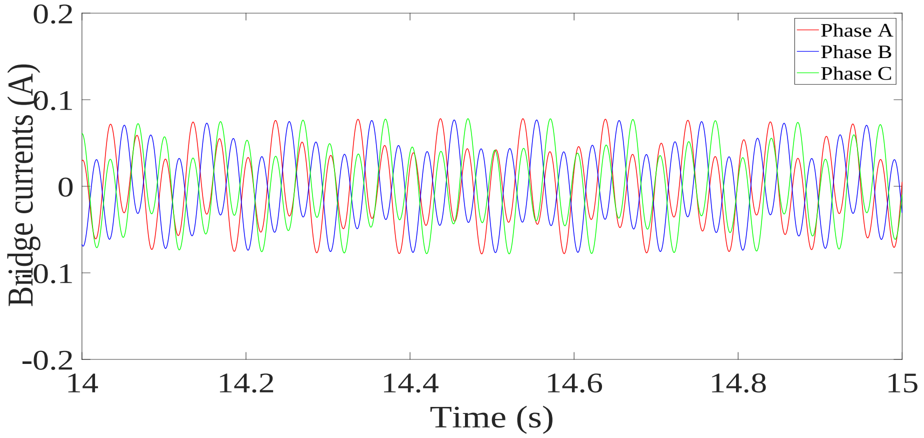

Figure 3.15: Three bridge currents for a supply voltage of 20 V with frequency 20 Hz in time domain when the rotor is in dynamic eccentricity condition

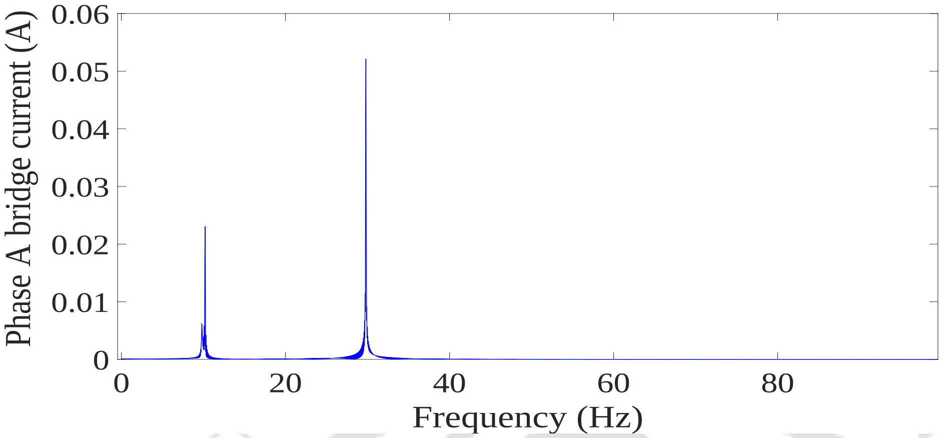

Figure 3.16: FFT of Phase A of the bridge current for a supply voltage of 20 V with frequency 20 Hz when the rotor is in dynamic eccentricity condition

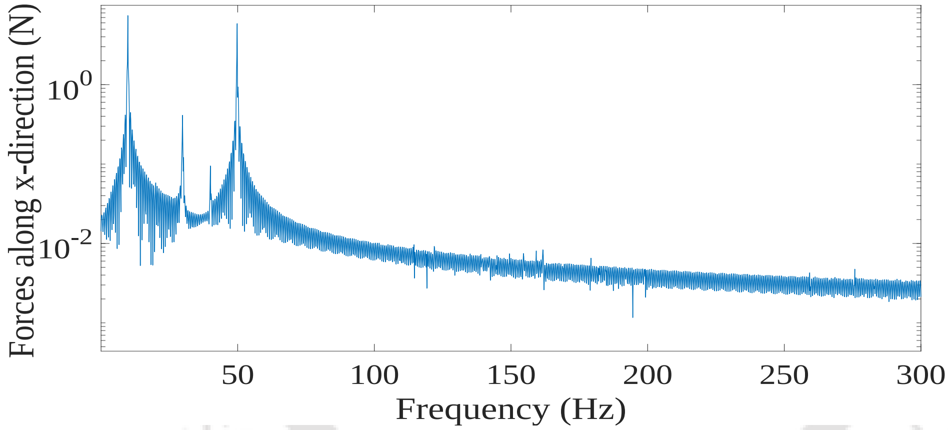

Figure 3.17: FFT of the force component along x-axis when the rotor is in dynamic eccentricity condition

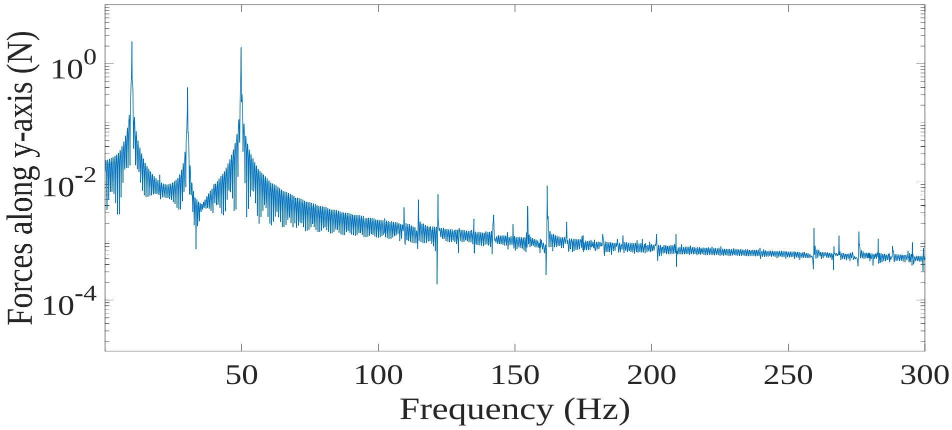

Figure 3.18: FFT of the force component along y-axis when the rotor is in dynamic eccentricity condition

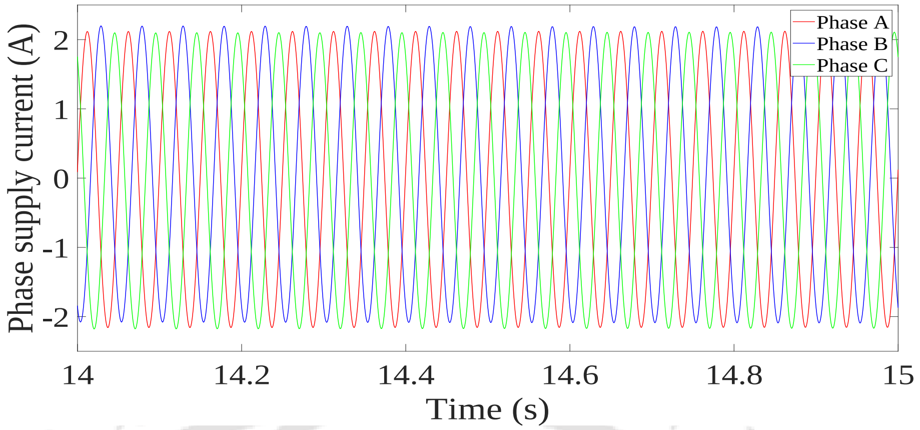

Figure 3.19: Three main currents at 20 V and 20 Hz in time domain for mixed eccentricity condition

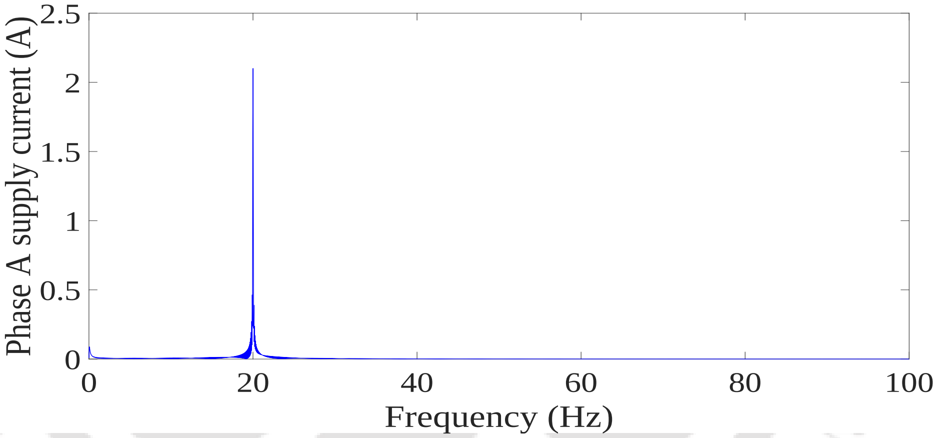

Figure 3.20: FFT of Phase A of the main current for a supply voltage of 20 V with frequency 20 Hz when the rotor is in mixed eccentricity condition

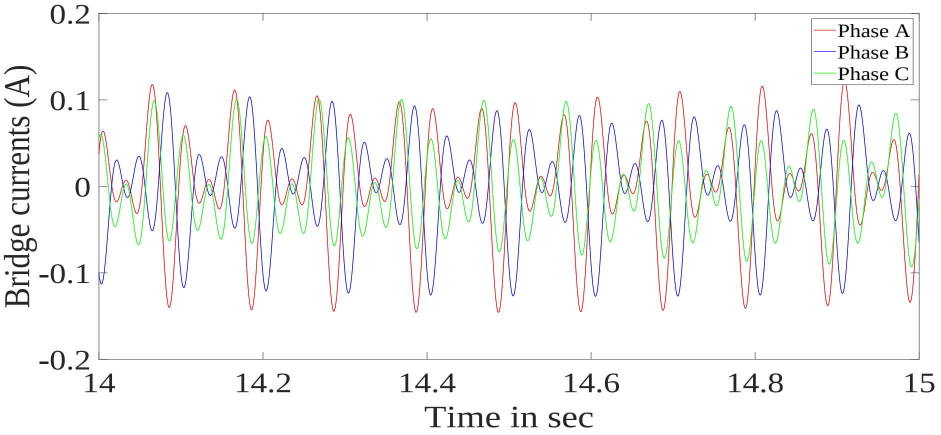

Figure 3.21: Three bridge currents for a supply voltage of 20 V with frequency 20 Hz in time domain when the rotor is in mixed eccentricity condition

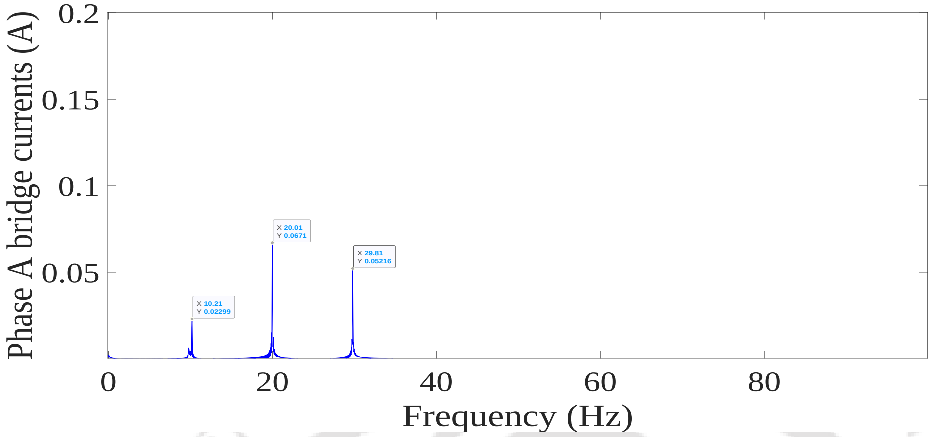

Figure 3.22: FFT of Phase A of the bridge current for a supply voltage of 20 V with frequency 20 Hz when the rotor is in mixed eccentricity condition

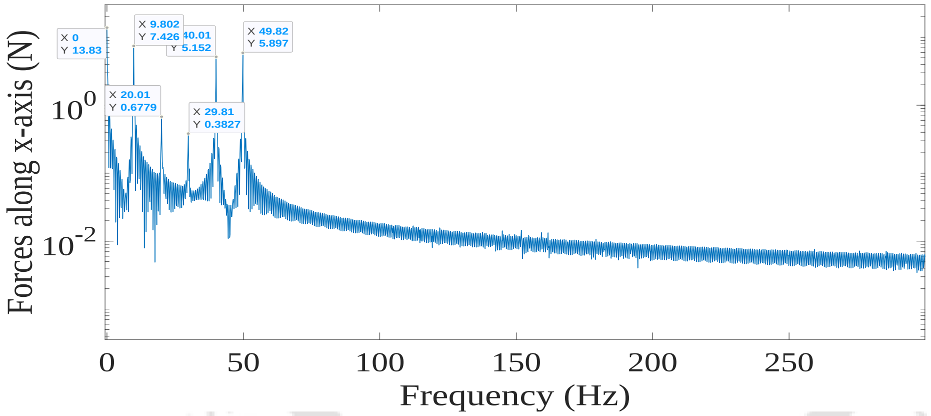

Figure 3.23: FFT of the force component along x-axis when the rotor is in mixed eccentricity condition

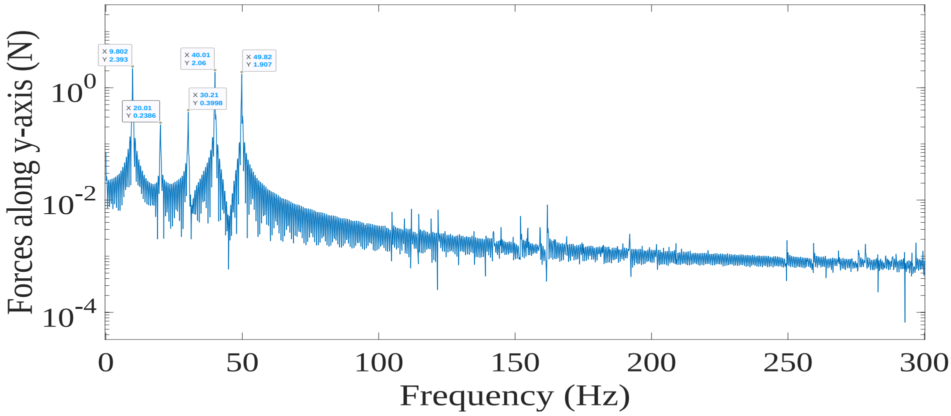

Figure 3.24: FFT of the force component along y-axis when the rotor is in mixed eccentricity condition

4

Numerical Simulation of Bridge Configured Winding Induction Machine using Commercial 2D FE Solver

Contents

4.1 Introduction

During recent decades, the use of FEM tool for the numerical simulation has become more popular because of its wide range of applications. The utilization of commercial software is now available for the implementation of finite element techniques. Opera FEM software is one of the finest tools for the 2D and 3D electromagnetic analyses. Most of the finite element problems have been solved by 2D solver in order to avoid the complexity in nature as well as the time and cost.

The present chapter discusses the modeling of the Bridge Configured Winding (BCW) induction machine by using OPERA 2-dimensional finite element solver. This chapter consists of two major parts: (i) steady state analysis of BCW Induction machine, (ii) transient (or) rotary motion analysis of BCW Induction machine. The steady state analysis (AC Solver) has been used to find the machine parameters such as torque and winding currents. In this steady state analysis, the torque and winding currents are measured for each step of the speeds of the machine. The Rotating Machine solver (Opera-2d/RM) is a transient eddy current solver which is extended to include the effects of rigid body (rotating) motion. In this Rotating Machine solver, the torque and winding currents are measured in transient condition.

The characterization of an Induction machine and the machine's performance has been analyzed by using different conductor material, different rotor core lamination material, different cross section of rotor bars and multi-slice method in Opera FE software are considered in the existing work in the literature. However, the bridge configured winding scheme which is also a double layered stator winding has not been implemented. The bridge currents are measured and the nature of the bridge currents have been analysed. The working principle of the Bridge Configured Winding has been presented in Section 4.2.

4.2 Bridge configured winding

The bridge configured winding (BCW) can produce both torque as well as a controllable transverse force. Figure 4.1 shows the double layered distributed three phase, four pole winding. The stator winding connection has been done according to the circuit connection as shown in Figure 4.2. An additional 2-pole magnetic field has been introduced purposefully with the 4-pole fundamental magnetic field by short circuiting the bridges. By the superimposition of this 2-pole magnetic field and 4-pole magnetic field can produce a force called levitation force or transverse force which can be used to counteract the UMP which may be present in the system due to the eccentric position of the rotor. Three isolated levitation power supply (i_{Alev}, i_{Blev}, and i_{Clev}) BCW can be applied along with the three phase main supply (i_{Aph}, i_{Bph}, and i_{Cph}). It is also possible to generate the radial forces in a passive manner simply by shot-circuiting the bridges S1, S2 and S3.

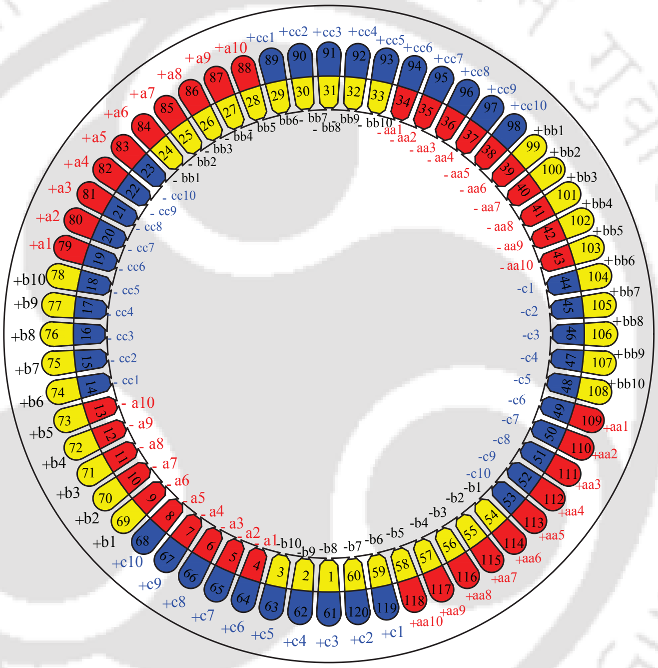

Figure 4.1: A winding scheme of a distributed double layered winding.

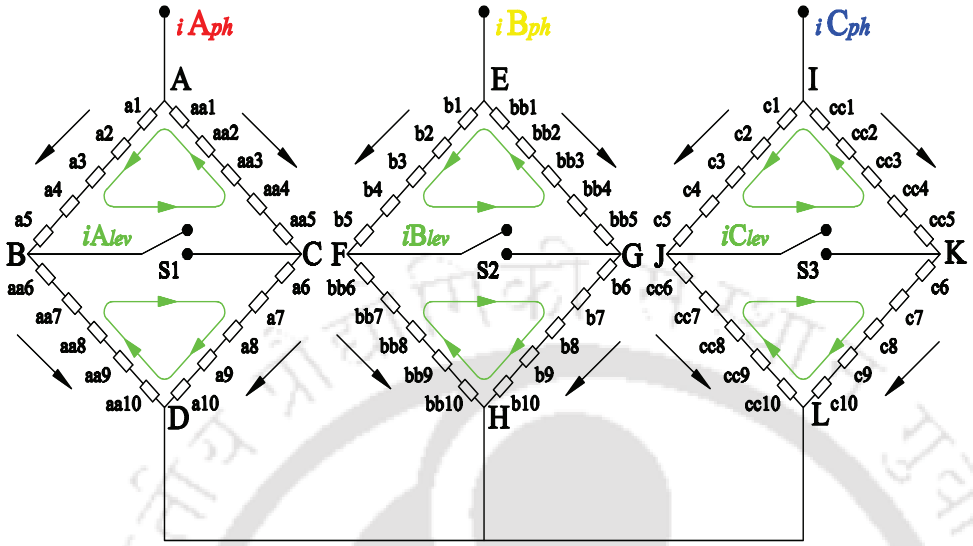

Figure 4.2: A bridge configured winding circuit.

The current responsible for the torque production are divided into two parallel paths in each phase. Consider Phase-A winding connection of the induction motor, with two parallel branches comprising ten series-connected coils each as shown in Figure 4.2. The currents flowing in arms AB and CD are same in direction and magnitude but both the arms were connected in diametrically opposite to each other at a span of 180^0. Similarly, AC and BD arms were connected in the same fashion. The branches AB and CD have the same polarity while both branches AC and BD have the opposite polarity with respect to AB and CD. The branches AB and CD have similar feature and they can be grouped together. Likewise, branches AC and BD are set to be an another group. These two coil groups are placed diametrically opposite to each other in the stator slots. The current flowing across BC is called levitation current or bridge current and it is very small when compared to the main supply current flowing across AD.

4.2.1 Working principle of bridge configured winding

An uneven flux density distribution due to rotor eccentricity or unbalance present in the system can produce an additional flux of pole pair ($p\pm1$), (where, p is the number of fundamental pole pairs). Any one of this additional flux pole pair can interact with the fundamental pole pair flux, a significant net transverse force (UMP) can be produced. BCW scheme works on this principle. An additional 2-pole field has been introduced purposefully with the 4-pole fundamental field by short circuiting the bridges. By superimposing this 2-pole field and 4-pole field, a levitation force can be produced to counteract the UMP which is already present in the system. The induced bridge currents has the capability of producing an additional 2-pole and 6-pole magnetic flux density components. These 2-pole and 6-pole fields can interact with the 4-pole main field and thus a radial magnetic flux density can be produced in the air gap. The radial magnetic flux density by the 2-pole, 4-pole and 6-pole fields has been given by Equation 4.1,

$$B\left(t,\varphi\right) = \mathrm{Re}\left\{\underline{\hat{B}}_1\left(t\right)e^{-j\varphi} + \underline{\hat{B}}_2\left(t\right)e^{-j2\varphi} + \underline{\hat{B}}_3\left(t\right)e^{-j3\varphi}\right\} \tag{4.1}$$

where t is the time, φ denotes the angular co-ordinate along the rotor periphery, $\underline{\hat{B}}_1$, $\underline{\hat{B}}_2$ and $\underline{\hat{B}}_3$ are the space vectors of the 2-pole, 4-pole and 6-pole magnetic flux density distribution in the airgap respectively.

Consider the Phase A winding connection of the Induction machine shown in Figure 4.2. When the induction machine is supplied with the main supply, the current will flow through the arm AB and BD in one path as well as AC and CD in an another path. A four pole magnetic field has been formed according to the winding pattern as shown in Figure 4.3. It has been realized that the presence of unbalance in the system, the current will flow through the arm BC, as soon as it is being short circuited and it is called as levitation current i_{Alev}. The levitation current i_{Alev} will flow in the arm AB through the arm CA in order to make a closed loop path. Similarly, the levitation current i_{Alev} will flow in the arm DB through CD. It has been observed in the arms AC and BD that the levitation current i_{Alev} flows in the opposite direction to the direction of main supply current i_{Aph} shown in Figure4.2. The polarity of the current flowing in the arms AC and BD have been reversed due the opposite direction of flow of levitation current which is shown in Figure 4.4 and thus the 2-pole field has been formed. The super imposed levitation field is a pole pair different with the main pole pair field. As a result, a net transverse force called levitation force is exerted on the rotor as shown in Figure 4.5. Therefore, a levitation force can be produced in any arbitrary direction with the combination of the bridge connections. The levitation force production by the interaction of a difference of one pole pair between the fields has been proved mathematically in [1].

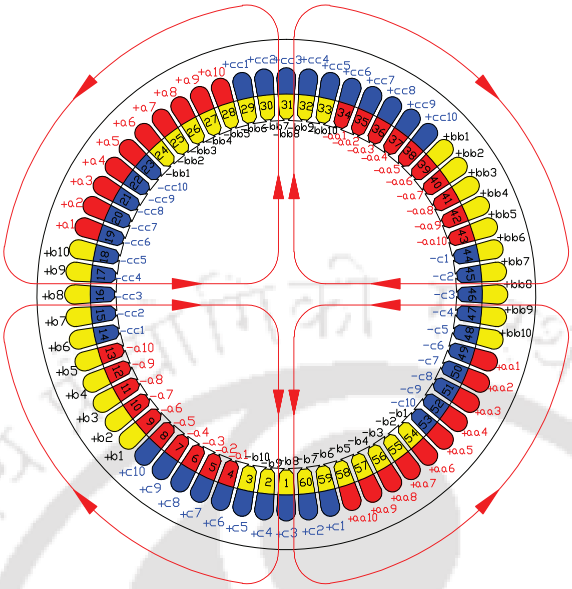

Figure 4.3: Main 4-Pole field formation.

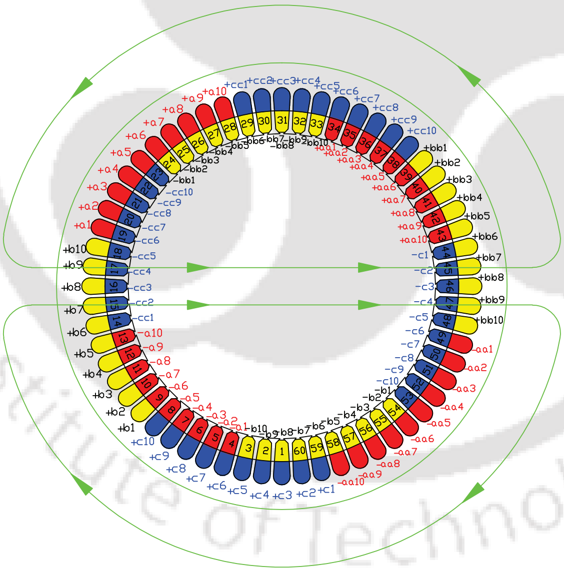

Figure 4.4: 2-Pole field formation.

4.3 Analysis of bridge configured based induction machine in Opera 2D FE solver

This section discusses the steady state analysis as well as transient analysis of the bridge configured induction machine. AC and RM solvers have been successfully used for the modeling of induction Machine.

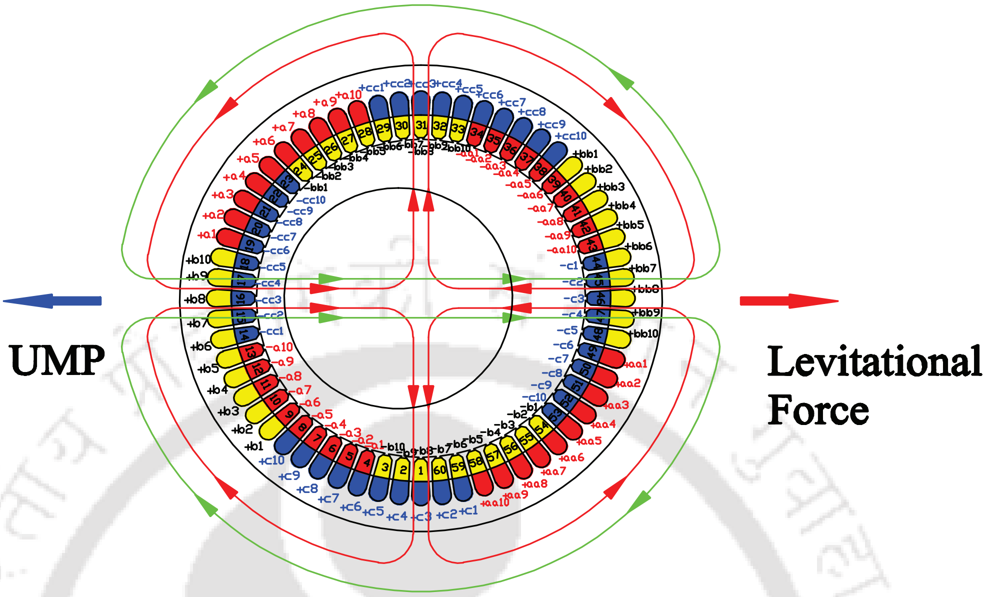

Figure 4.5: Superimposition of 4-Pole and 2-Pole fields.

4.3.1 Modeling of BCW induction machine

The induction machine model has 60 stator slots and 48 rotor slots. Machine parameters are given in Table 4.1. Initially, the stator and rotor constructions are drawn in AutoCAD dxf format according to the dimensions given in Figures 4.6 and 4.7. The AutoCAD dxf format has been imported in Opera 2D FE solver for modeling the induction machine. Figure 4.8 shows the dxf model imported from AutoCAD. Figure 4.9 shows the complete induction machine model. Nonlinear material properties have been considered for the stator and rotor laminations.

Table 4.1: Machine Parameters.

Sl No	Parameter	Value
1	Stator outer diameter	350.0 mm
2	Stator inner diameter	221.0 mm
3	Stator core length	212.0 mm
4	Rotor outer diameter	218.5 mm
5	Rotor inner diameter	75.0 mm
6	Rotor skew	5^o
7	Airgap	1.25 mm

4.3.2 Modeling of external circuits

Steady state and transient solutions can be obtained by exiting the model either by current sources or by external circuits connected to the Opera FE model. The latter option is employed in the induction

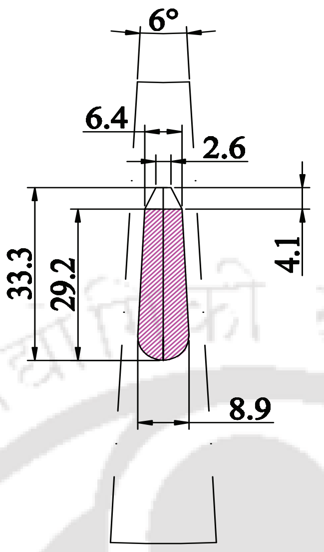

All Dimensions are in mm

Figure 4.6: A stator slot dimension.

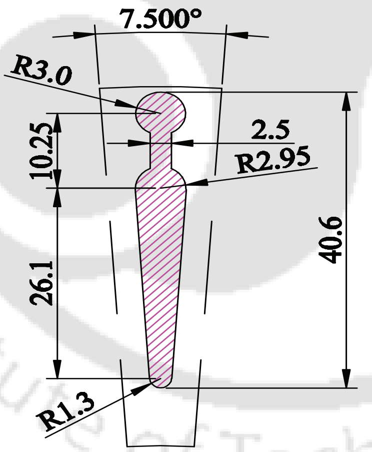

All dimensions are in mm

Figure 4.7: A rotor bar dimension.

machine modeling. Basically, the external circuit design allows a set of coils in the finite element model to be define within a circuit. The external circuit may contains passive and active components such as coil, resistor and inductor. A coil is the set regions that have the same conductor number N. Figure 4.10 shows the circuit model for the Bridge configured Winding connection. The external circuit model has been made based on the winding connection which has shown in Figures 3.2 and 3.3. In this model, there are external functional sources, specified by their phase voltage, amplitude,

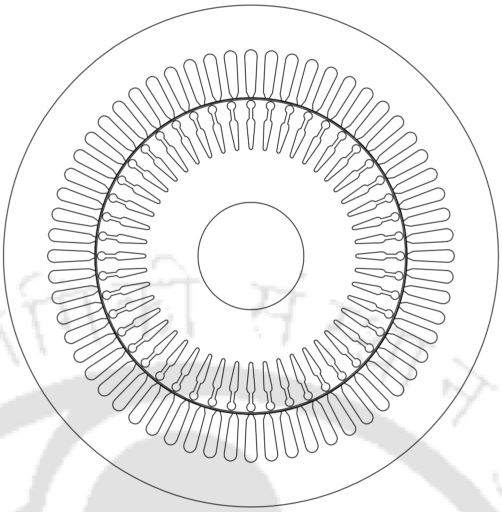

Figure 4.8: An AutoCAD DXF model.

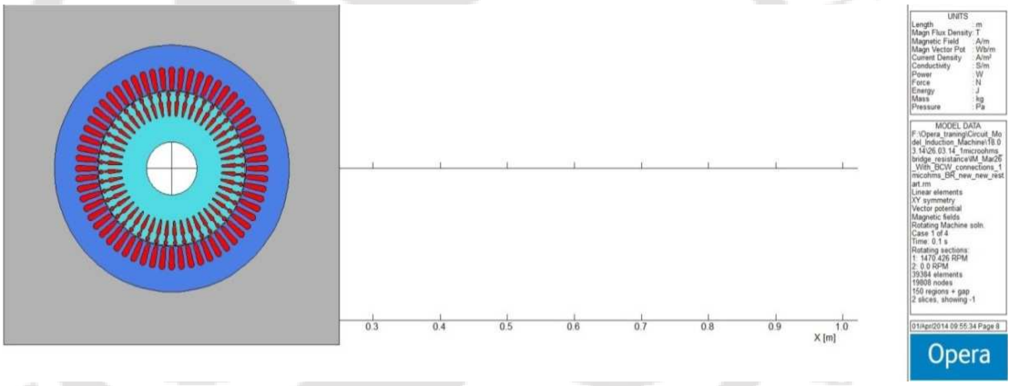

UNITS

Length	m
Magn Flux Density	T
Magnetic Field	A/m
Magn Vector Pot	Wb/m
Current Density	A/m²
Conductivity	S/m
Power	W
Force	N
Energy	J
Mass	kg
Pressure	Pa

MODEL DATA
F:\Opera_traning\Circuit_Model_Induction_Machine\18.03.14\26.03.14_1microohms_bridge_resistance\IM_Mar26_With_BCW_connections_1micohms_BR_new_new_restart.rm
Linear elements
XY symmetry
Vector potential
Magnetic fields
Rotating Machine soln.
Case 1 of 4
Time: 0.1 s
Rotating sections:
1: 1470.426 RPM
2: 0.0 RPM
39384 elements
19808 nodes
150 regions + gap
2 slices, showing -1

01/Apr/2014 09:55:34 Page 8

Figure 4.9: Opera 2D induction machine model with BCW.

phase and frequency. A *comi* file is a set of functions which has been used to drive the functional voltage sources with the phase difference instead of giving constant amplitude voltage at 50Hz. Each phase have four set of winding coils. Each winding coil assigned with 10 conductors (5 GO and 5 $RETURN$ conductors). Table 4.2 shows GO and $RETURN$ coil conductors of slot of stator winding according to the winding scheme model given in Figure 3.2.

4.4 Steady state analysis of BCW induction machine by using AC solver

The AC solver is capable of accurately modeling the currents induced in the cage rotor which result from the rotating 3-phase magnetic field generated in the stator. The induction motor performance can be characterized at a range of rotor speeds level. Typical motor performance parameters such as the variation of the torque with slip frequency, induced rotor currents and associated with power losses are readily computed in Opera-2d AC solver. In induction machine, the difference be-

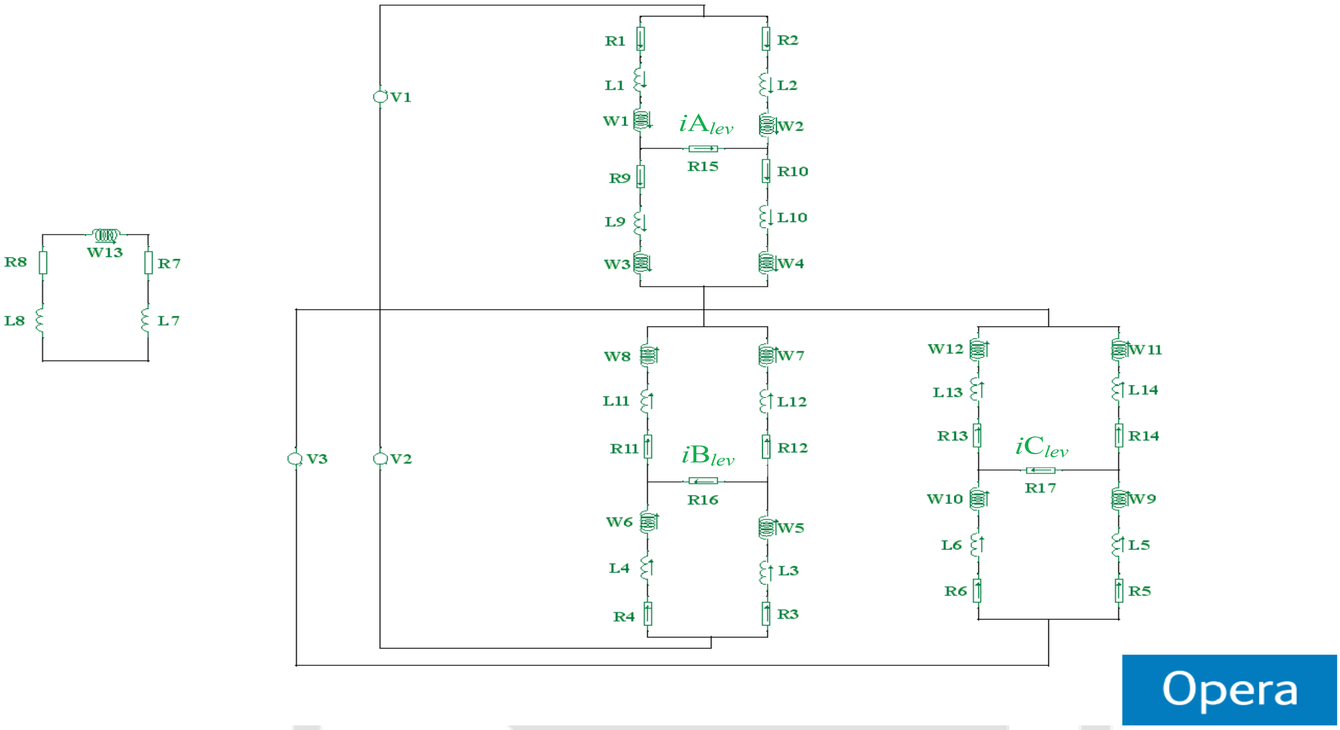

Figure 4.10: BCW connection in External circuit editor.

Table 4.2: Assignment of the conductor numbers in the external circuit editor.

Phase Winding	Winding	GO' Conductors	Return' Conductor
	W1	4, 5, 6, 7, 8	79, 80, 81, 82, 83
Phase A	W2	34, 34, 36, 37, 38	109, 110, 111, 112, 113
	W3	39, 40, 41, 42, 43	114, 115, 116, 117, 118
	W4	9, 10, 11, 12, 13	84, 85, 86, 87, 88
	W5	54, 55, 56, 57, 58	69, 70, 71, 72, 73
Phase B	W6	24, 25, 26, 27, 28	99, 100, 101, 102, 103
	W7	29, 30, 31, 32, 33	104, 105, 106, 107, 108
	W8	59, 60, 1, 2, 3	74, 75, 76, 77, 78
	W9	44, 45, 46, 47, 48	119, 120, 61, 62, 63
Phase C	W10	14, 15, 16, 17, 18	89, 90, 91, 92, 93
	W11	19, 20, 21, 22, 23	94, 95, 96, 97, 98
	W12	49, 50, 51, 52, 53	64, 65, 66, 67, 68

tween the rotation of the produced magnetic field and the rotor is called the slip speed. Effectively, this can be thought as the rotational frequency at which the stator-produced rotating field cuts the rotor bar. This phenomenon can be successfully modeled in Opera-2D, by setting the exciting stator field to rotate at the slip frequency, rather than the true AC frequency.

In Opera-2d/AC, the use of the slip frequency requires further adjustments to be made to any circuits which may be attached to the motor. The use of the slip frequency to drive the model results in values for variables such as the back-emf which are reduced by the ratio of slip frequency (f_{slip}) to synchronous frequency (f_{sync}). This can be remedied by scaling the length of the circuit. However, the resistance per unit length of the wire must then also be adjusted such that the true circuit resistance value is maintained. Equation 4.2 to Equation 4.6 have been used to get the scaled values of slip speed, slip frequency, machine length and for inductance. Table 4.3 shows the adjusted values of slip speed, slip frequency, machine length and inductance. The simulation has been done for each values of the slip. It has been noted that the bridge connection has not been considered in the static analysis.

$$N_{slip} = f_{sync} - f_{motor} \tag{4.2}$$

$$slip = \left\{ \frac{f_{sync} - f_{motor}}{f_{sync}} \right\} \tag{4.3}$$

$$f_{slip} = \left\{ \frac{N_{slip} * P}{120} \right\} \tag{4.4}$$

$$\text{Adjusted machine length} = \left\{ \text{Actual machine length} * \frac{f_{sync}}{f_{slip}} \right\} \tag{4.5}$$

$$\text{Adjusted Inductance} = \left\{ \text{Actual Inductance} * \frac{f_{sync}}{f_{slip}} \right\} \tag{4.6}$$

4.5 Transient analysis of BCW induction machine by using Rotation Motion (RM) solver

The Rotating Machine solver (Opera-2D/RM) is a transient eddy current solver extended to include the effects of rigid body (rotating) motion. The solver also provides the use of circuits similar to AC solver. Opera-2d/RM can model conventional motors and generators with a central rotating part inside an outer stationary part. The innermost part of the machine (the rotor of a conventional machine) is referred as section 1 and the outer parts as section 2. Thus the stator of a conventional machine is section 2.

The rotating parts are rotating relatively with the stationary parts. The important feature of this FEM tool is that it can rearrange the mesh in the airgap region in order to rejoin the rotating elements with the stationary elements after every rotation with an adjoining mesh. The FEM model has one airgap region to separate the stator and rotor parts in order to form the stator air gap region and rotor

Table 4.3: Scaled values for steady state analysis.

Sl. No.	Slip Speed	Slip	Slip Frequency (Hz)	Adjusted machine length (m)	Adjusted Inductance (H)
1	10	0.006666667	0.333333333	31.8	0.15
2	20	0.013333333	0.666666667	15.9	0.075
3	30	0.02	1	10.6	0.05
4	40	0.026666667	1.333333333	7.95	0.0375
5	60	0.04	2	5.3	0.025
6	100	0.066666667	3.333333333	3.18	0.015
7	110	0.073333333	3.666666667	2.890909091	0.013636364
8	150	0.1	5	2.12	0.01
9	200	0.133333333	6.666666667	1.59	0.0075
10	250	0.166666667	8.333333333	1.272	0.006
11	300	0.2	10	1.06	0.005
12	350	0.233333333	11.66666667	0.908571429	0.004285714
13	400	0.266666667	13.33333333	0.795	0.00375
14	450	0.3	15	0.706666667	0.003333333
15	500	0.333333333	16.66666667	0.636	0.003
16	550	0.366666667	18.33333333	0.578181818	0.002727273
17	600	0.4	20	0.53	0.0025
18	700	0.466666667	23.33333333	0.454285714	0.002142857
19	800	0.533333333	26.66666667	0.3975	0.001875
20	900	0.6	30	0.353333333	0.001666667
21	1000	0.666666667	33.33333333	0.318	0.0015
22	1100	0.733333333	36.66666667	0.289090909	0.001363636
23	1200	0.8	40	0.265	0.00125
24	1300	0.866666667	43.33333333	0.244615385	0.001153846
25	1400	0.933333333	46.66666667	0.227142857	0.001071429
26	1500	1	50	0.212	0.001

air gap region as shown in Figure 4.11. The airgap of the induction machine is 1.25 mm. The airgap is divided into three equal regions in order to create the annular airgap region of 0.426667 mm for stator airgap and rotor airgap region. It is important to give midairgap radius so that Opera 2D/RM can create the air polygon in between stator airgap region and rotor airgap region. The midairgap radius of the model is 109.875 mm. Triangular element has been chosen for the mesh. The complete model comprises of 19808 nodes and 39384 elements. Figure 4.12 shows the close view of the mesh in the airgap region. The effect of rotor skewness has been included in the simulation. The rotor bar connections are also considered in the external winding circuit.

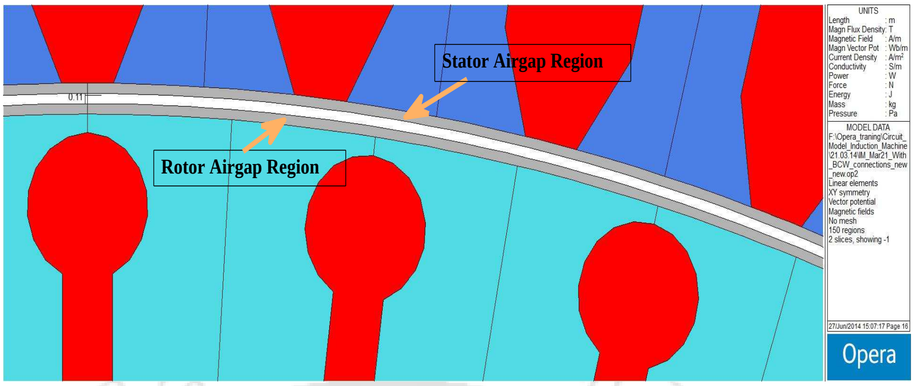

Figure 4.11: A close view of stator and rotor air gap region.

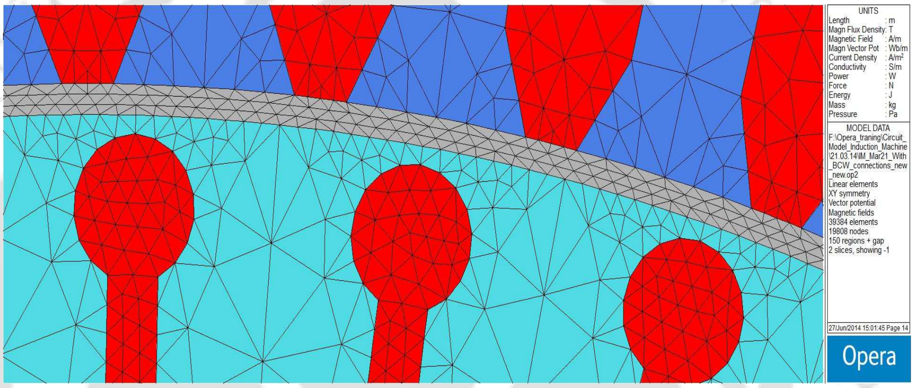

Figure 4.12: A close mesh view of the stator and rotor air gap region.

An external circuit has been coupled with the induction machine model for the transient analysis which has been already discussed in Section 4.3.2. The external circuit consists of winding coils, resistor, inductor and a functional voltage sources. A *comi* file is a set of functions which has been used to drive the functional voltage sources with the phase difference instead of giving constant amplitude voltage at 50Hz. The rotor bars are short circuited and the effect of rotor skewness is also included in the RM Analysis. The FFT of the bridge currents and main supply currents have been plotted in MATLAB$^{\text{TM}}$ by using Opera 2D *log* results file for the BCW Induction based Opera/RM model.

4.6 Results and discussions

4.6.1 Results of steady state analysis

Table 4.4 shows the obtained values of torque and main supply current by Opera AC solver. Figure 4.13 shows the vector potential plot of the double layered winding induction machine. Figure 4.14 shows the magnetic flux density distribution of the double layered winding induction machine. Torque

Table 4.4: Parameters obtained by Opera 2D AC Solver.

Sl. No.	SLIP	TORQUE OBTAINED (N-m)	Phase A Current(Amp)	Phase B Current(Amp)	Phase C Current(Amp)
1	0.006666667	8.682438444	5.0367	5.0637	5.0637
2	0.013333333	15.87352732	8.85	8.85	8.85
3	0.02	21.43977548	12.3198	12.3197	12.3197
4	0.026666667	25.57487393	15.405	15.4049	15.4049
5	0.04	30.50811506	20.4338	20.4337	20.4337
6	0.066666667	33.0906881	27.0194	27.0192	27.0192
7	0.073333333	33.08081682	28.1538	28.1537	28.1537
8	0.1	31.75352519	31.4758	31.476	31.4757
9	0.133333333	29.79765735	33.9974	33.9973	33.9777
10	0.166666667	28.27143134	35.5931	35.593	35.5938
11	0.2	27.27082454	36.7742	36.7741	36.7741
12	0.233333333	26.6885687	37.7347	37.7346	37.7366
13	0.266666667	26.40582729	38.5787	38.5786	38.5786
14	0.3	26.33940722	39.3576	39.3576	39.3575
15	0.333333333	26.42568675	40.102	40.1018	40.1018
16	0.366666667	26.6148125	40.8249	40.8249	40.8249
17	0.4	26.86591844	41.5329	41.5329	41.5329
18	0.466666667	27.4489219	42.9157	42.9209	42.9157
19	0.533333333	28.0433632	44.2555	44.2556	44.2556
20	0.6	28.57742362	45.5446	45.5444	45.5444
21	0.666666667	29.04258127	46.7749	46.7806	46.7749
22	0.733333333	29.40622964	47.949	47.9492	47.949
23	0.8	29.67872781	49.0569	49.0572	49.0567
24	0.866666667	29.85949775	50.091	50.0912	50.091
25	0.933333333	29.9606531	51.0617	51.0619	51.0619
26	1	29.9944108	51.969	51.9693	51.9693

and winding currents have been plotted against slip and shown in Figures 4.15 and 4.16. Figure 4.15 shows the torque vs slip curve. It has been observed that the break-down torque is 33.09 N-m at the speed of 1400rpm. At no-load condition, the torque Vs slip curve is almost linear. When the load increases in the motor (as slip increases), the torque which is also increases to pull down or break down torque. As the slip further increases, the torque decreases and reaches the steady state value. Figure 4.16 shows the phase currents vs slip. At very low values of slip, current induced in the coil is very small. It can be clearly noticed that the currents are increased with the increase of slip along with the load and reaches up to 51 Amps. It has been noticed that at any particular instance of slip,

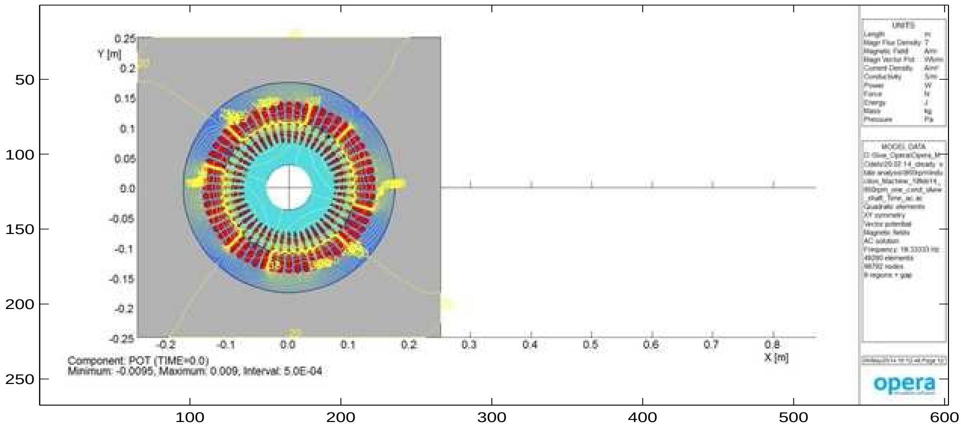

Figure 4.13: Vector potential plot of a BCW Induction machine.

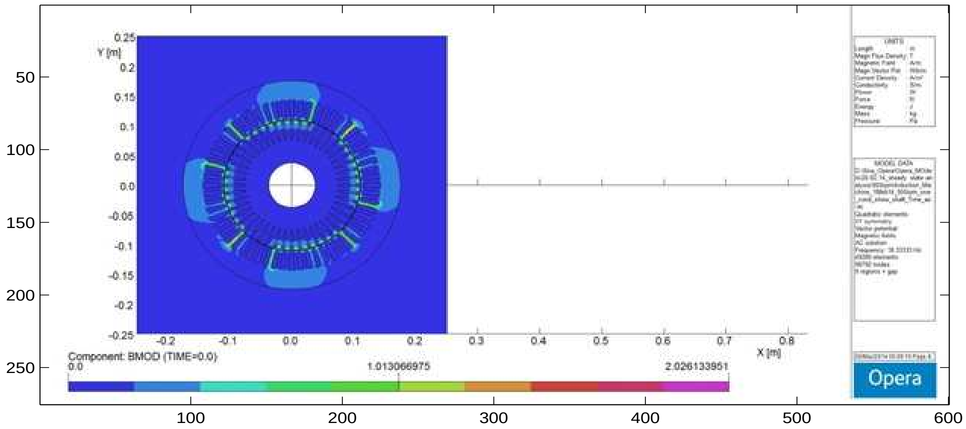

Figure 4.14: Magnetic flux density distribution plot of a BCW Induction machine.

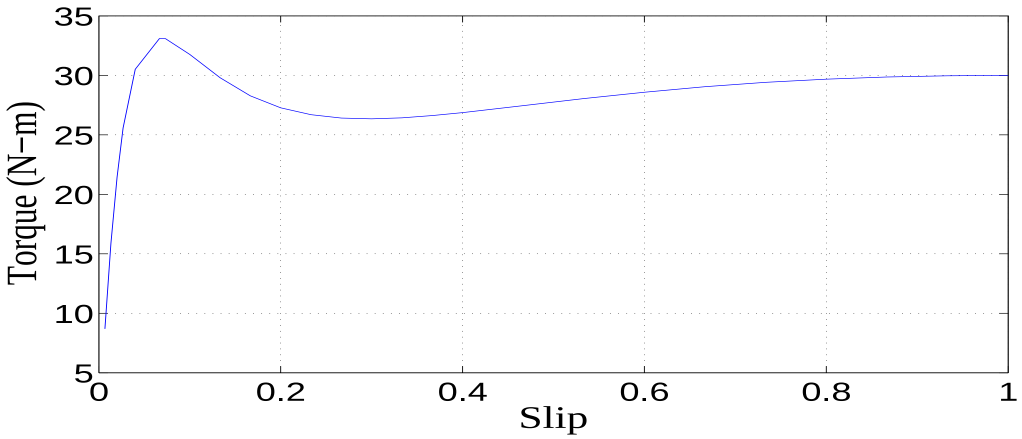

Figure 4.15: Torque vs Slip curve.

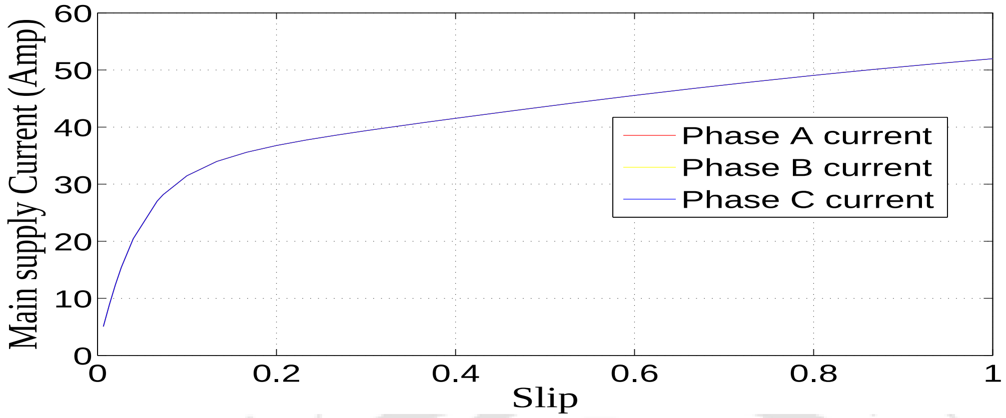

Figure 4.16: Main supply currents vs Slip curve.

the three phase winding currents are all same.

4.6.2 Results of transient analysis

The important parameters such as torque, main supply currents and bridge currents have been plotted using MATLAB with the use of Opera 2D/RM *log* file. Dynamic eccentricity has been incorporated in the machine. The main supply currents and bridge currents have been plotted in the time domain as well as frequency domain. The frequency component of the main supply current is 50 Hz and the frequency components of the bridge currents are approximately 25 Hz and 75 Hz. As discussed in the previous chapter the frequency components for dynamic analysis is $fs \pm f_r$, where f_s is the supply frequency of the main supply and f_r is the rotor frequency.

Figure 4.17 shows the torque curve in time domain. Figures 4.18 and 4.19 show the three phase main supply currents and the three phase bridge currents respectively. Figures 4.20 to 4.22 show the FFT plots of the three phase bridge currents along with main supply currents.

4.7 Conclusions

Finite element simulation of bridge configured based induction machine has been presented in this chapter. The FE simulation of BCW based Induction machine had been done for two cases, (i) steady state analysis, and (ii) transient analysis (or) Rotating Machine analysis. Results of steady state and transient analysis have been presented. Initially, the simulation has been done for steady state condition to get the machine parameters such as winding currents and torque of the induction

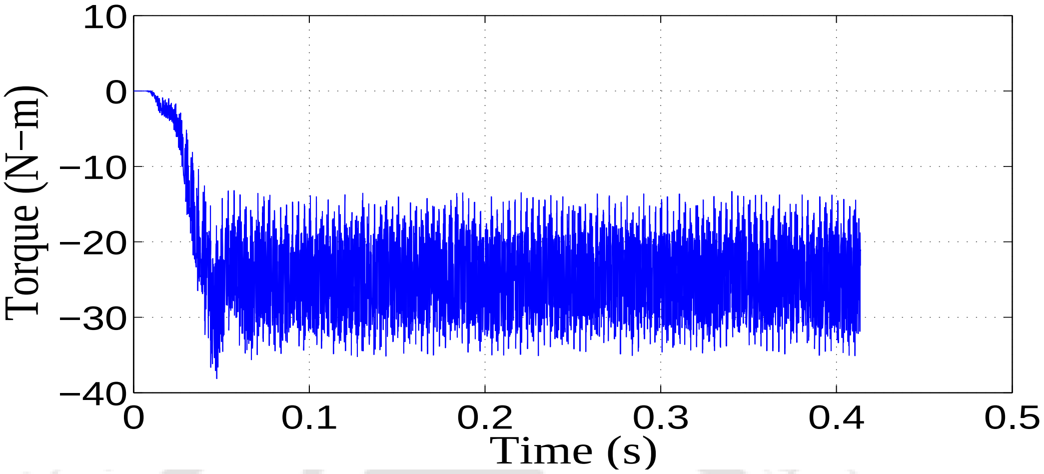

Figure 4.17: Main supply currents vs Slip curve.

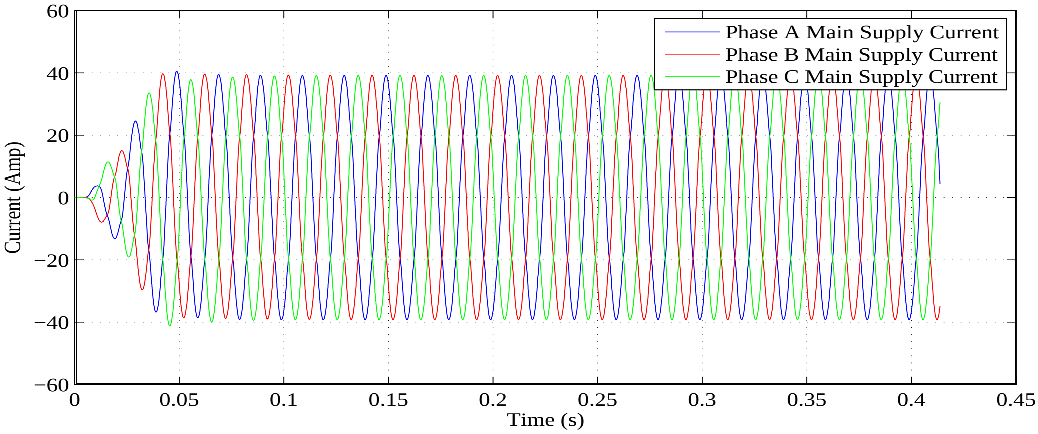

Figure 4.18: A three phase main supply currents for zero eccentricity model.

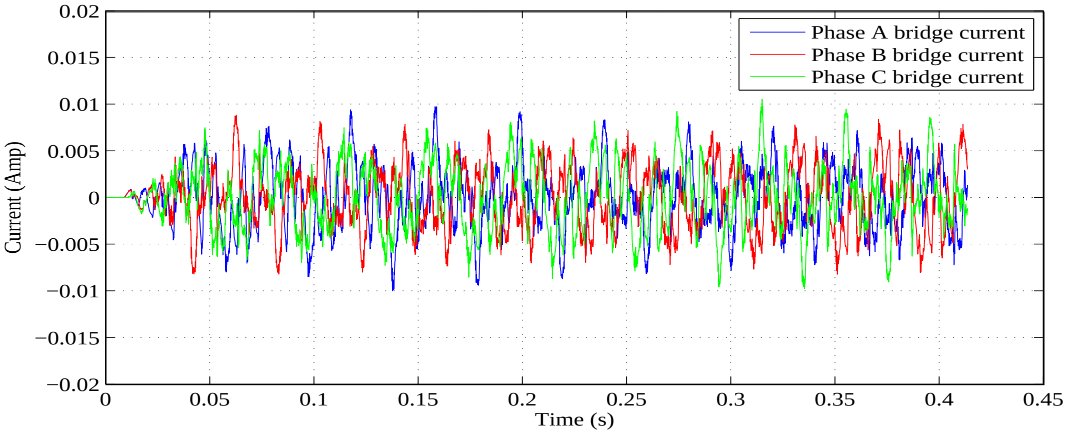

Figure 4.19: A three phase bridge currents for zero eccentricity model.

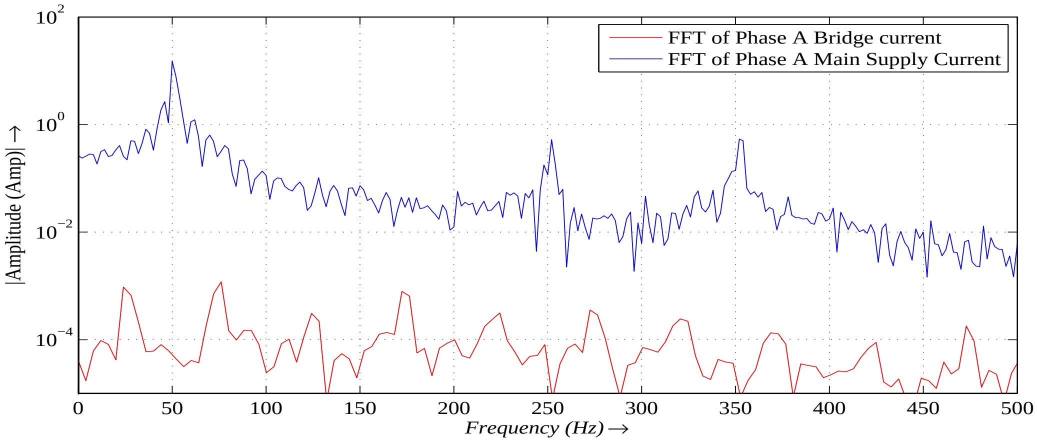

Figure 4.20: A FFT plot of Phase A bridge current with main supply current at 50Hz of BCW Induction machine.

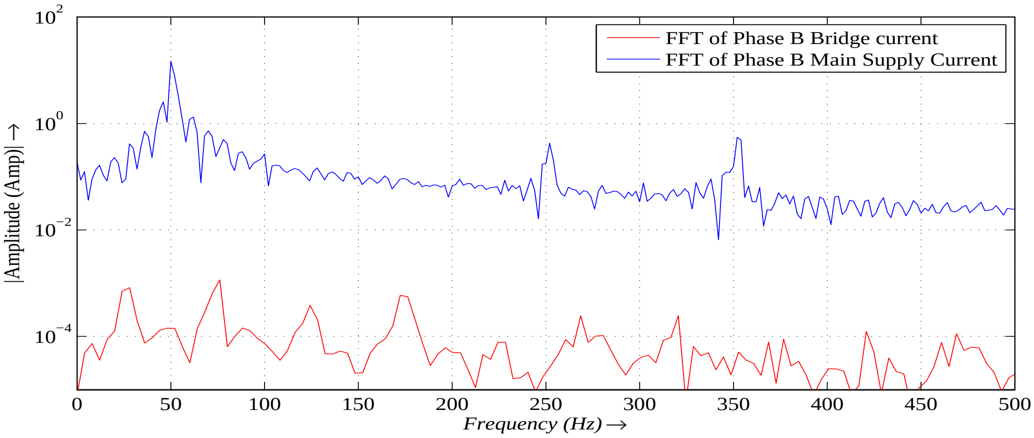

Figure 4.21: A FFT plot of Phase B bridge current with main supply current at 50Hz of BCW Induction machine.

machine. It has been observed that the maximum amplitude of winding current generated in the steady state solution is 51 A whereas in the transient solution it is 40 Amps. Similarly the torque generated in the induction machine by static analysis is 30 Nm and the torque generated by transient analysis is 26 Nm. The reason for the difference in the amplitude of the winding current as well as the torque is that the effect of rotor skewness and the rotor bar connection were not considered in the steady state analysis.

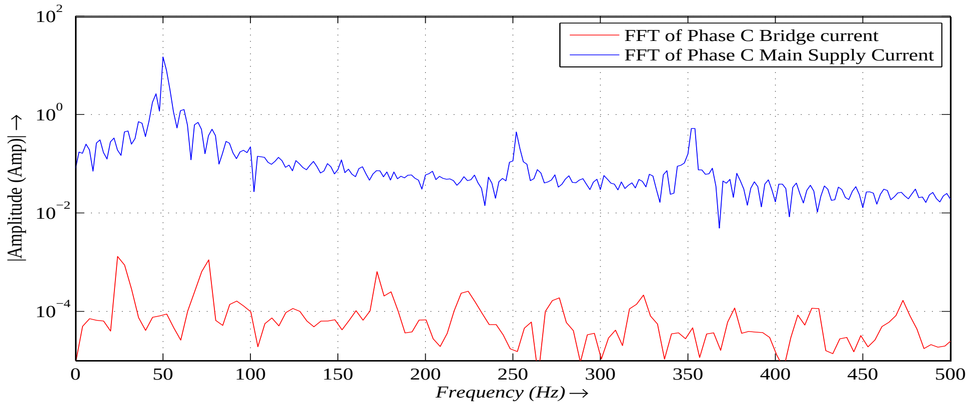

Figure 4.22: A FFT plot of Phase C bridge current with main supply current at 50Hz of BCW Induction machine.

5

Development of Experimental Rig Setup for Bridge Configured Winding Induction Machine

Contents

5.1 Introduction

Chapter 1 gives the introduction to the induction machine and Chapter 2 explains about the literature survey. Chapter 3 explain about the finite element modeling of the bridge configured based induction machine. Chapter 4 illustrates the working principle of the bridge configured winding. It also explains the finite element (FE) modeling of an induction machine with bridge configured winding which is developed using a commercial electromagnetic FE software called OPERA. The present chapter illustrates the development of an experimental rig for the passive and active vibration control in induction machine. The detail explanation about the development of the experimental setup has been presented in this Chapter. Several experiments have been carried out. The main supply voltages, main supply currents, bridge voltages and bridge currents are measured in Bridge ON and Bridge OFF conditions in order to study the characteristics of the bridge configured based induction machine. The rotor responses and also the rotor orbits in Bridge ON and Bridge OFF conditions are also calculated. The results obtained in Chapter 3 have been compared with the experimental results.

5.2 Description of the experimental rig

A 37 kW, three phase and four pole induction machine with squirrel cage rotor is used for the experimental rig. The original machine parameters have been given in Table 5.1. The existing rotor had a 0.8 m long shaft. The length of the shaft has been modified to 1.8 m to make the rotor flexible. Figure 5.1 shows the original rotor shaft. Figure 5.2 shows the dimensions of the modified shaft. The existing coil diameter is 1.22 mm (18 gauge number). The original stator winding is a three phase, double layer, 4-pole with concentrated winding. It consists of four strands and eleven turns. The original stator winding has been removed and replaced by a three phase, double layer and 4-pole distributed bridge configured winding. Table 5.2 shows the modified parameters of the original machine. The working principle of the bridge configured winding has been explained in Section 1.4 of Chapter 1. The modified winding has three strands and eleven turns and has the same coil diameter as the original winding. This will create some space in the stator slots and helps in accommodating the search coils. Search coils have been used to calculate the 2-pole. 4-pole and 6-pole magnetic field positions. Figures 5.4 and 5.5 show the pictures were taken during the incorporation of BCW. Figure

5.7 shows the modified machine for the active vibration control by using bridge configured winding. The winding has been made according to the winding scheme given in Figure 5.6.

Table 5.1: Original machine parameters.

Sl No	Parameter	Value
1	Stator outer diameter	350.0 mm
2	Stator inner diameter	221.0 mm
3	Stator core length	212.0 mm
4	Rotor outer diameter	218.5 mm
5	Rotor inner diameter	75.0 mm
6	Rotor skew	5^o
7	Airgap	1.25 mm
8	Number of stator slots	60
9	Number of rotor slots	48
10	Number of poles	4
11	Number of winding layers	2
12	winding Type	Concentrated
13	Diameter of Coil Wire	1.22 mm
14	Number of turns	11
15	Number of strands	4
16	weight of the rotor core	46.56 kg
17	Length of rotor shaft	0.8 m

Table 5.2: Modified parameters of machine.

Sl No	Parameter	Value
1	winding Type	Distributed
2	Number of strands	3
3	Length of rotor shaft	1.8 m

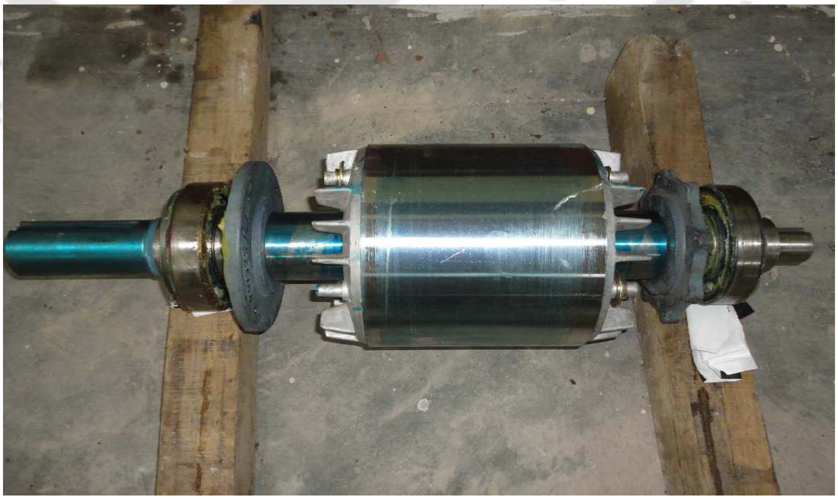

Figure 5.1: Original rotor shaft.

There are three rotors have been used in the experimental rig. The main reason for using three different rotors has been explained in Section 6.3 of Chapter 6. However, the same rotor core has been used for all the three rotors. These three rotors are referred as **Rotor I**, **Rotor II** and **Rotor III**.

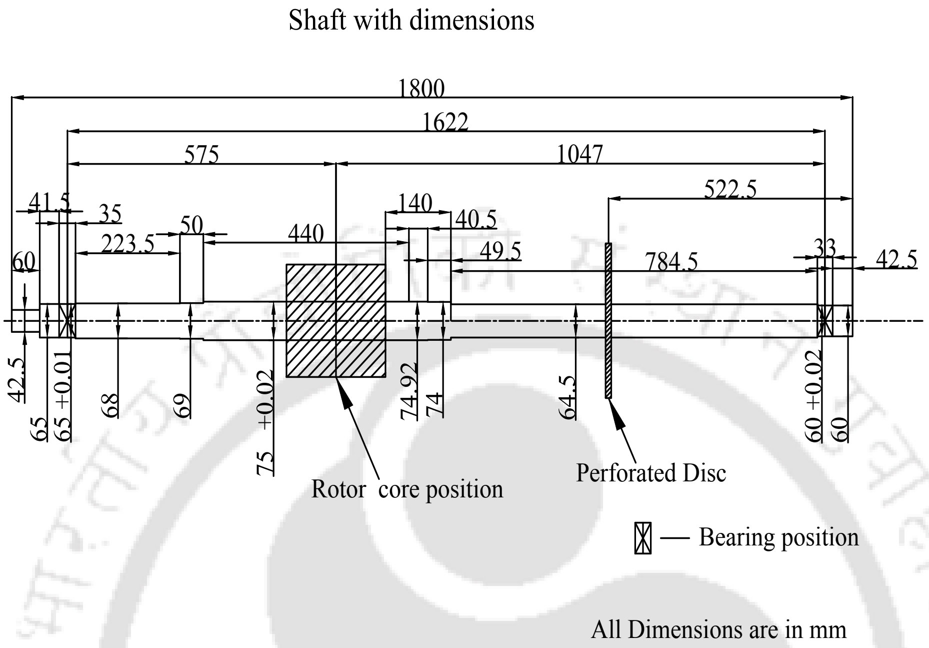

Figure 5.2: 1.8 m rotor shaft (or **Rotor I**) with dimensions.

Figure 5.3: 1.8 m long shaft.

Figure 5.2 shows the dimensions of **Rotor I**. Figure 5.8 shows the dimensions of **Rotor II**. Figure 5.9 shows the dimensions of **Rotor III**. However, the results obtained by using **Rotor I** are presented in Section 5.7.

A perforated disc has been inserted in the shaft so that a known unbalance can be created in the rotor system by inserting known mass in the perforated disc. The perforated disc has sixteen holes

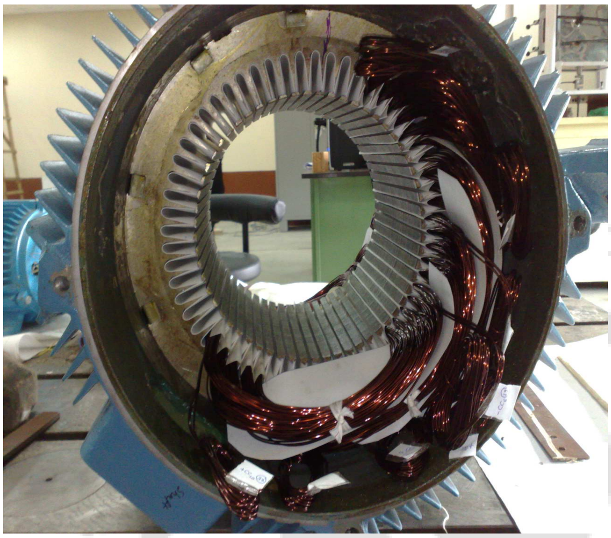

Figure 5.4: A picture during the incorporation of the bridge configured winding

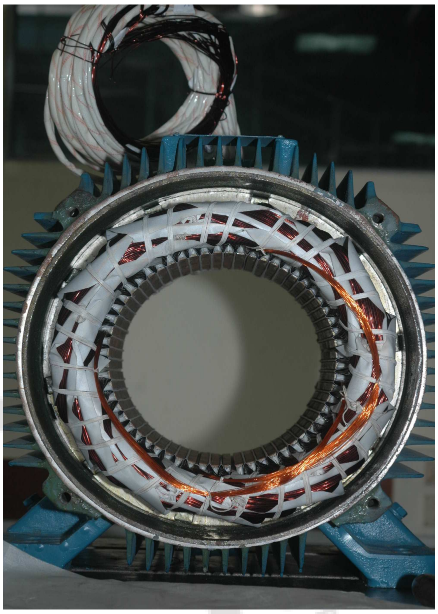

Figure 5.5: After completion of the incorporation of bridge configured winding.

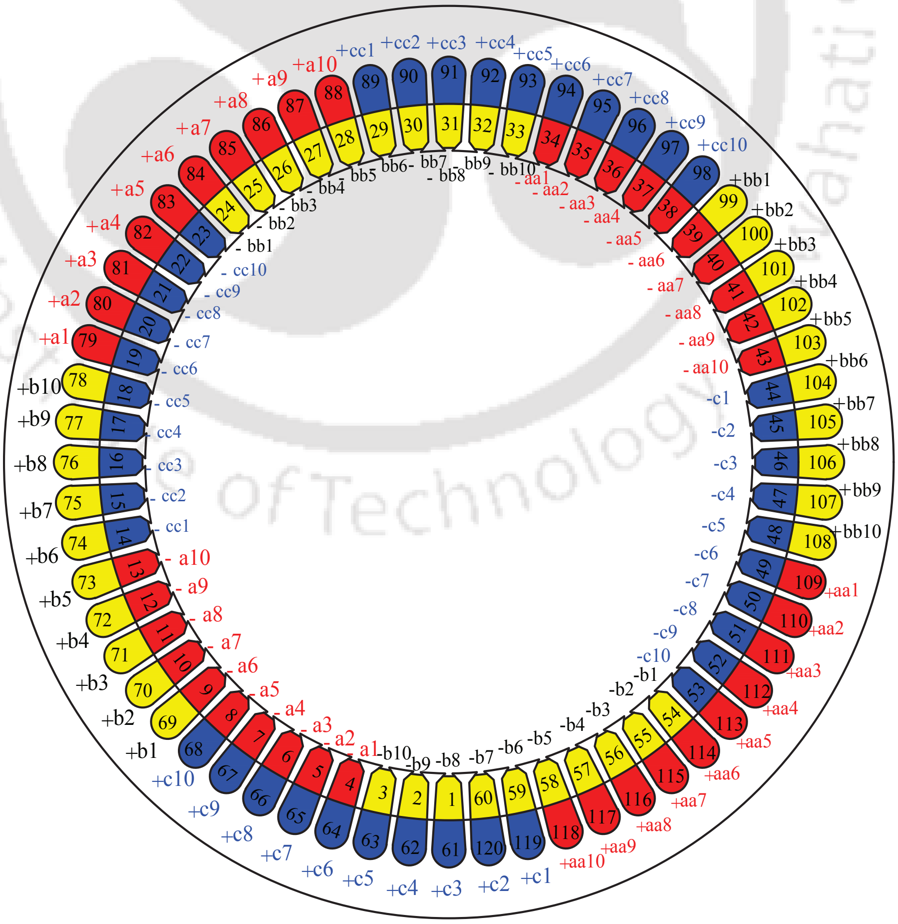

Figure 5.6: Bridge configured winding of an induction machine with 60 slots.

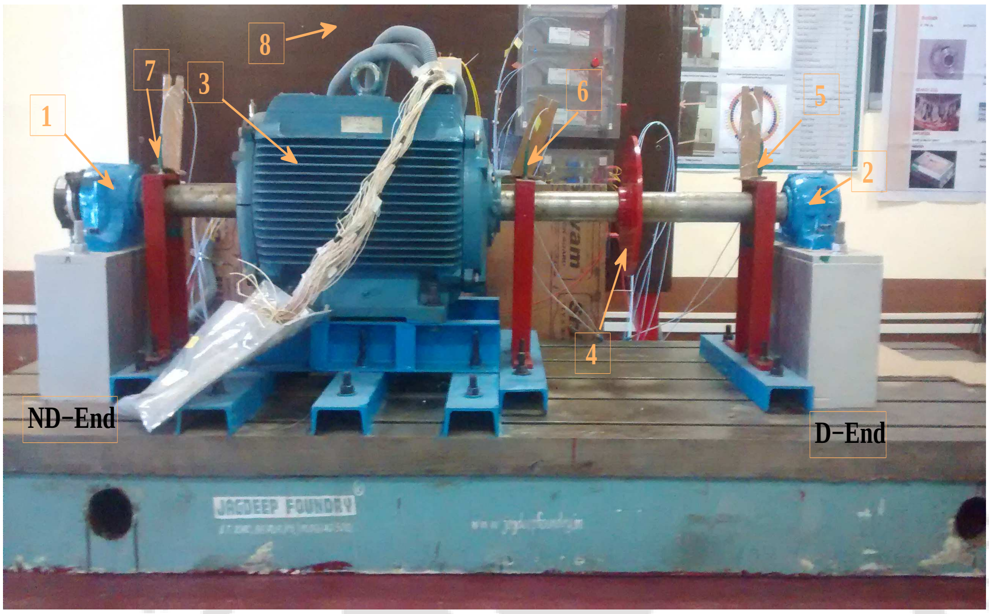

Figure 5.7: A modified 37kW induction machine.

In Figure 5.7. 1 - Bearing Housing at ND end, 2 - Bearing Housing at D end, 3 - Test Machine, 4 - Perforated Disc, 5, 6 and 7 - Locations for the rotor responses, 8- Panel board.

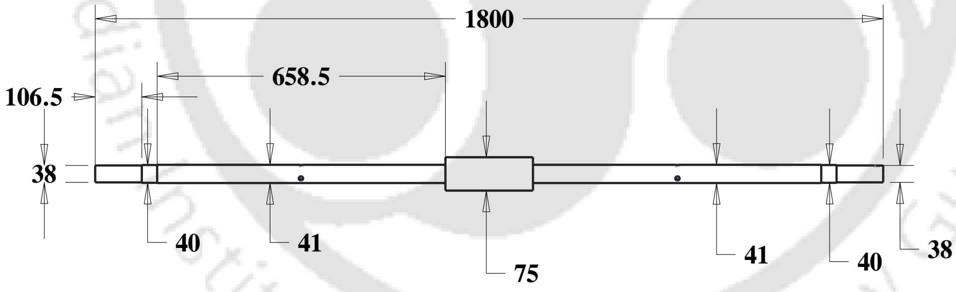

All dimensions are in mm

Figure 5.8: Dimensions of a flexible rotor shaft type **II** or **Rotor II**.

in which smaller masses can be added with the known unbalance masses. Figure 5.10 shows the perforated disc of the experimental rig. Figures 5.11 and 5.12 show the dimensions of the perforated disc. In the present analysis, the measured bridge currents have been discussed in order to identify the unbalance present in the system.

5.3 Search coil winding

The main purpose of using search coil winding is that to measure the 2-pole, 4-pole and 6-pole magnetic fields. The modified main coil winding and search coil winding are placed on the same

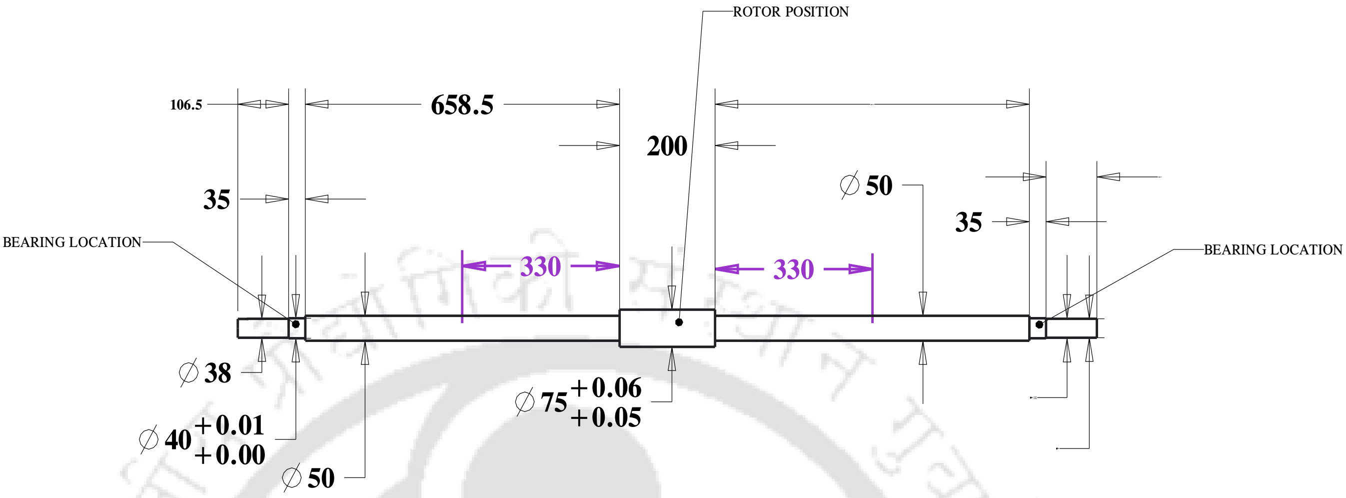

Figure 5.9: Dimensions of a flexible rotor shaft type **III** or **Rotor III**.

Figure 5.10: A perforated disc with known mass unbalance.

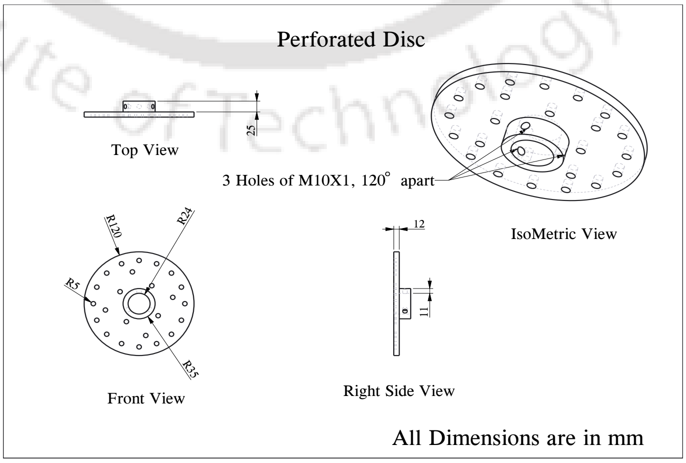

Figure 5.11: A Perforated disc with the dimensions.

slots of the stator with four pole main winding filling 75% of the slot leaving the other 25% for the Search coil winding with two-pole, four-pole and six-pole winding. The leads of the search coils

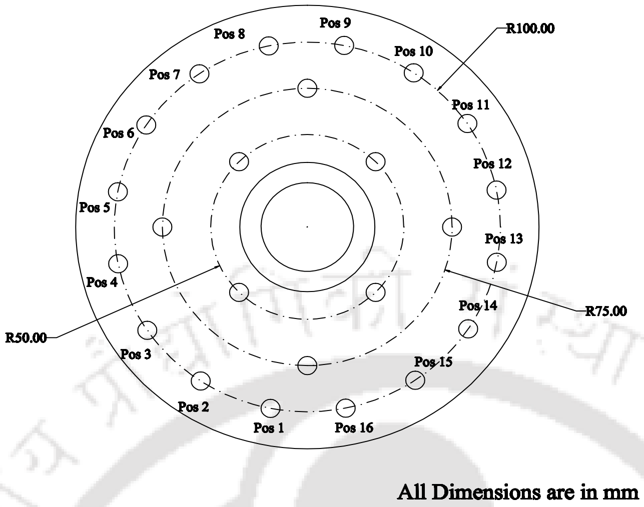

Figure 5.12: Two dimensional view of the perforated disc.

are connected to the NI Data Acquisition system to get the pole positions by means of a tiny voltage induced in the search coils. There are two set of search coil windings have been wounded and the second set of search coil has been made for redundant. A copper wire of 0.3 mm diameter has been used for 2-pole, 4-pole and 6-pole search coil winding. The numbers of turn and strand have been given in Table 5.3. The number of turns used for for 4-pole is 10 because the main pole field of the machine is 4-pole field. So, 10 turns can be high enough for the 4-pole field. However the measurement and the analysis of the search coil voltages have not done and it is not presented in this report.

Table 5.3: Numbers of turn and strand for search coil winding

Sl No	Type of field	Numbers of turn	Numbers of strand
1	2-pole	40	2
2	4-pole	10	2
3	6-pole	40	2

5.3.1 2-Pole search coil winding connection

The 2-pole winding connection has been made for two angular positions in the stator slot. These positions in the stator slot are placed perpendicularly in the stator geometry. So that, it can sense the optimum amount of 2-pole magnetic fields dynamically. These angular positions are named as **Position A** and **Position B**. The winding has been made for the coil pitch of 30 in the 60 slot induction machine. The stator slot number for the *GO* and *RETURN* conductor is given below in Table 5.4.

The output lead of the GO and $RETURN$ conductors have been connected to the NI DAQ system.

Table 5.4: Slot number for 2-pole search coil winding

Sl No	Set Number	GO conductor slot number	Label Name	RETURN conductor slot number	Label Name
1	Set I-Position A	5	$(a1_{2+})_1$	35	$(a1_{2-})_1$
2	Set I-Position B	20	$(b1_{2+})_1$	50	$(b1_{2-})_1$
3	Set II-Position A	6	$(a2_{2+})_2$	36	$(a2_{2-})_2$
4	Set II-Position B	21	$(b2_{2+})_2$	51	$(b2_{2-})_2$

5.3.2 4-Pole search coil winding connection

The 4-pole winding connection has been made for three angular positions. These positions are labeled as **Position A**, **Position B** and **Position B'**. The coil pitch of the four pole stator winding is 15. The winding has been made in such a way that it has to be perpendicular with each other. So that, the position B winding is exactly coming over the stator tooth. In order to avoid that the tooth sharing the slots have been chosen and one more winding has been made. This additional winding is named as **Position B'**. The average fields of **Position B** winding and **Position B'** winding have been taken for the exact field which is perpendicular to **Position A** winding. The number of turns and strands have been given in Table 5.3. Table 5.5 shows the GO and $RETURN$ conductor numbers of 4-pole search coil winding.

Table 5.5: Slot number for 4-pole search coil winding

Sl No	Type	GO conductor	Label Name	RETURN conductor	Label Name
1	Set I-Pos A	8	$(a1_{4+})_1$	23	$(a1_{4-})_1$
		38	$(a2_{4+})_1$	53	$(a2_{4-})_1$
2	Set I-Pos B	15	$(b1_{4+})_1$	30	$(b1_{4-})_1$
		45	$(b2_{4+})_1$	60	$(b2_{4-})_1$
3	Set I-Pos B'	16	$(b'1_{4+})_1$	31	$(b'1_{4-})_1$
		46	$(b'2_{4+})_1$	1	$(b'2_{4-})_1$
4	Set II-Pos A	3	$(a1_{4+})_2$	18	$(a1_{4-})_2$
		33	$(a2_{4+})_2$	48	$(a2_{4-})_2$
5	Set II-Pos B	10	$(b1_{4+})_2$	25	$(b1_{4-})_2$
		30	$(b2_{4+})_2$	55	$(b2_{4-})_2$
6	Set II-Pos B'	11	$(b'1_{4+})_2$	26	$(b'1_{4-})_2$
		31	$(b'2_{4+})_2$	56	$(b'2_{4-})_2$

5.3.3 6-pole search coil winding connection

The 6-pole winding connection has been made for two positions. The coil pitch of 6-pole winding is 10. The GO and $RETURN$ conductor slot numbers have been given below in Table 5.6. Figure 5.13 shows the winding slot representation of search coil winding for **Set I** and **Set II**. Figure 5.14 shows the search coil winding along with main stator winding.

Table 5.6: Slot number for 6-pole search coil winding

Sl No	Type	GO conductor	Label Name	RETURN conductor	Label Name
1	Set I-Pos A	2	$(a1_{6+})_1$	12	$(a1_{6-})_1$
		22	$(a2_{6+})_1$	32	$(a2_{6-})_1$
		42	$(a3_{6+})_1$	52	$(a3_{6-})_1$
2	Set I-Pos B	7	$(b1_{6+})_1$	17	$(b1_{6-})_1$
		27	$(b2_{6+})_1$	37	$(b2_{6-})_1$
		47	$(b3_{6+})_1$	57	$(b3_{6-})_1$
3	Set II-Pos A	4	$(a1_{6+})_1$	14	$(a1_{6-})_1$
		24	$(a2_{6+})_1$	34	$(a2_{6-})_1$
		44	$(a3_{6+})_1$	54	$(a3_{6-})_1$
4	Set II-Pos B	9	$(b1_{6+})_1$	19	$(b1_{6-})_1$
		29	$(b2_{6+})_1$	39	$(b2_{6-})_1$
		49	$(b3_{6+})_1$	59	$(b3_{6-})_1$

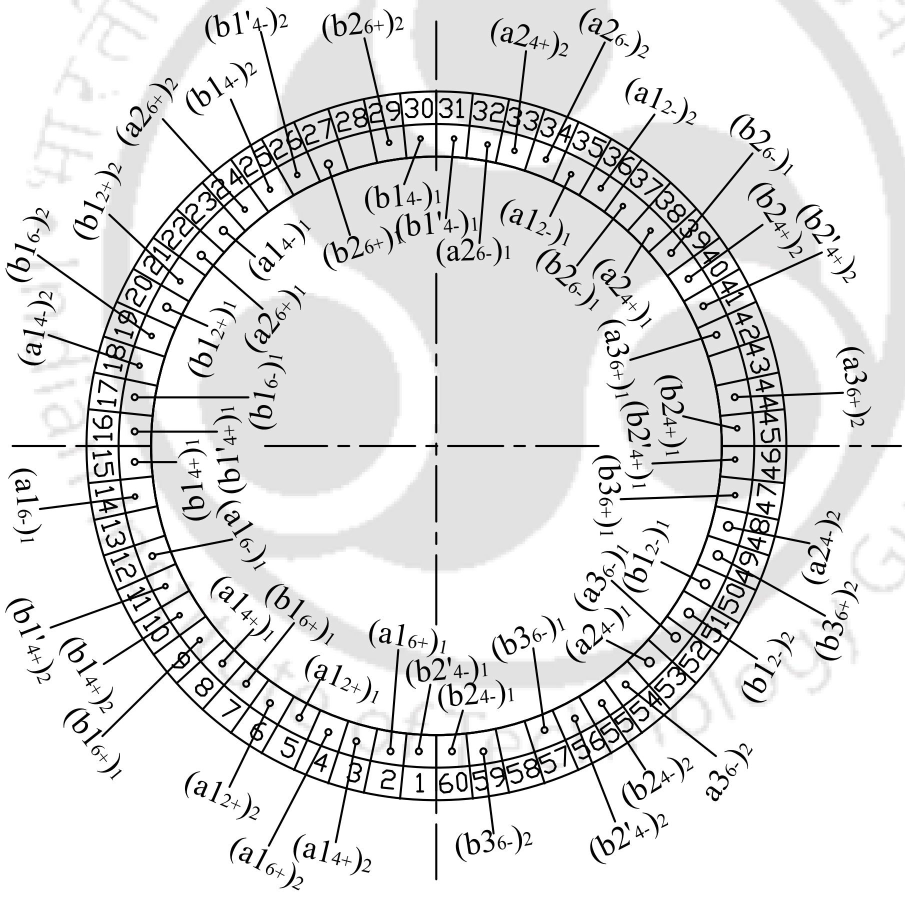

Figure 5.13: 2-pole, 4-pole and 6-pole winding position of Search coil winding for Set I and Set II.

5.4 Development of the panel

A panel has been fabricated in order to connect the windings for the power supply. It consists of the three main phase stator winding connection, bridge configured winding connection and search coil

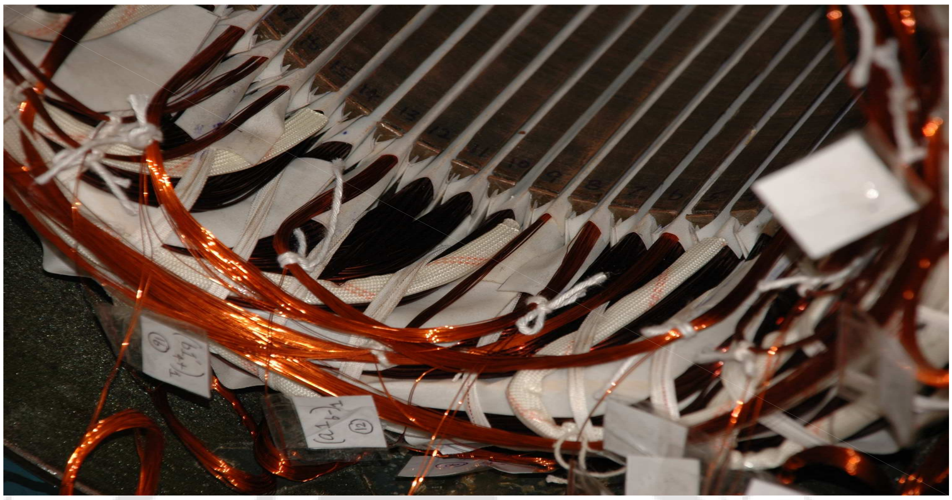

Figure 5.14: Search Coil winding with Stator Winding.

winding connection. The main stator winding connections have been done as the connections given in Figure 5.15. Figure. 5.16 shows the connections for bridge configured winding. Figures 5.17 and 5.18 show the connections for the search coil winding **Set 1** and **Set 2** respectively. The main power supply is fed by the variable frequency drive to the main winding connection. These three panels have been fixed on the panel board.

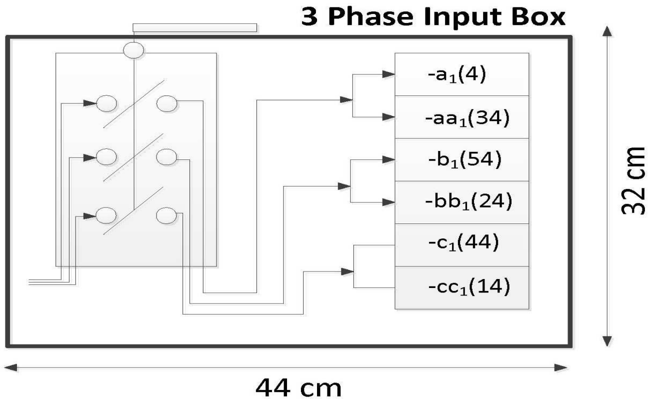

Figure 5.15: Connections for Main Stator Winding.

5.5 Development of sensor fixture

Six displacement transducers have been used to measure the rotor displacements in three locations are shown in Figure 5.7. In each locations, two proximity transducers have been used to measure the rotor displacements in X and Y-directions. A sensor fixture has been fabricated for each three locations in order to fix the proximity transducers for the measurement of rotor displacements. A

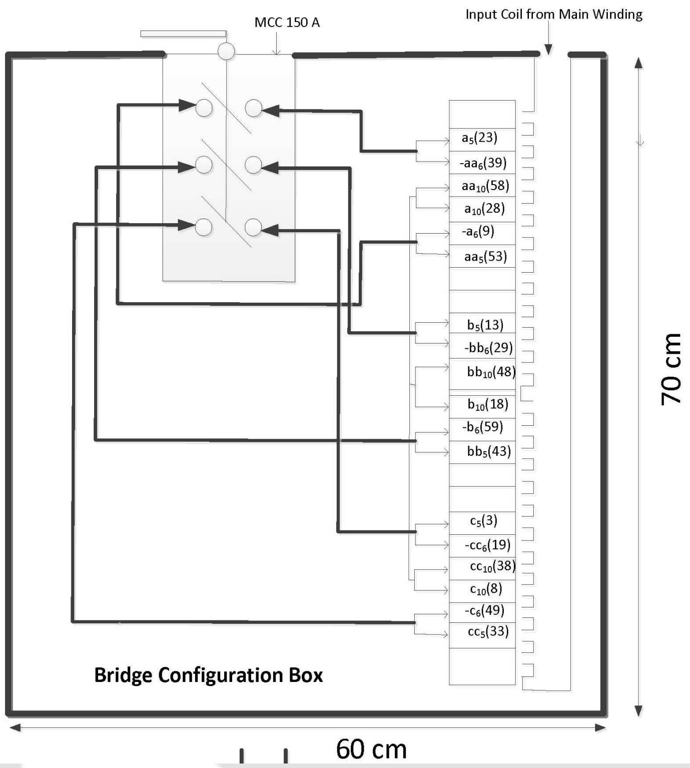

Figure 5.16: Connections for Bridge Configured Winding.

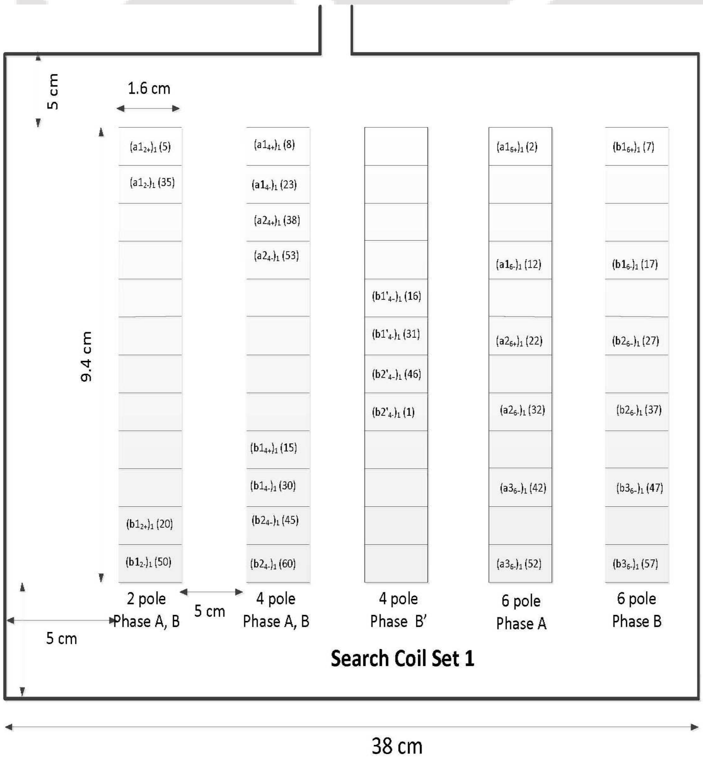

Figure 5.17: Connections for Search Coil Winding Set 1.

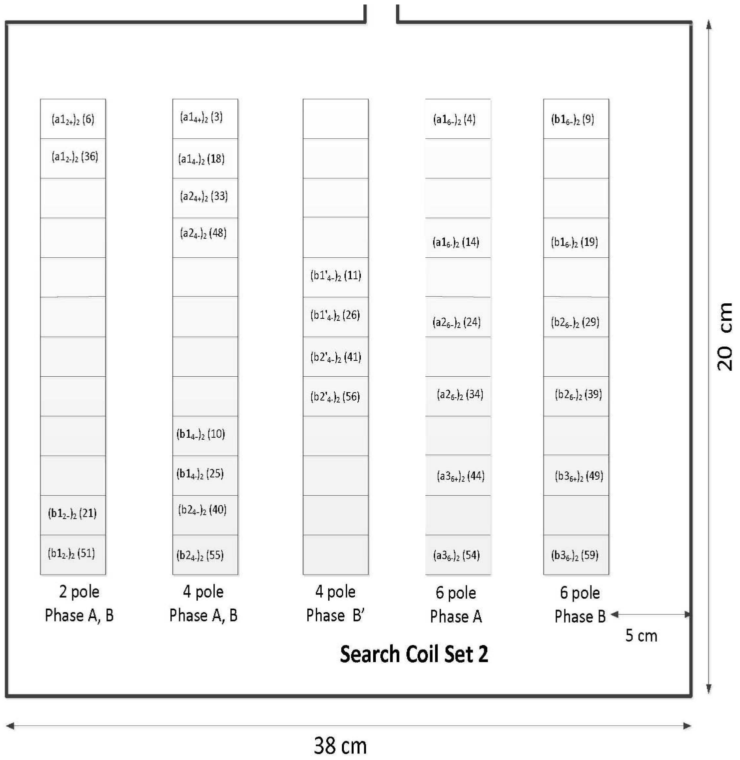

Figure 5.18: Connections for Search Coil Winding Set 2.

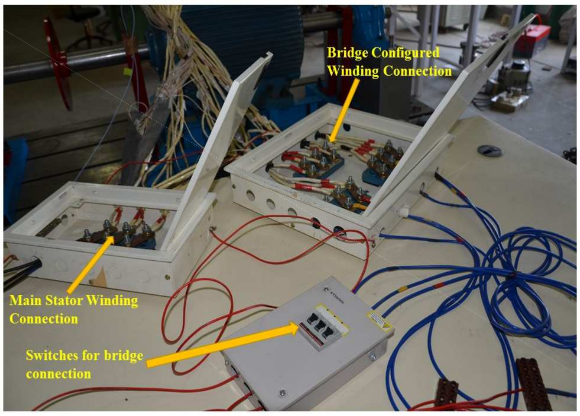

Figure 5.19: A panel for winding connections.

50X12 mm size of steel plate has been used for the fabrication of sensor fixture. Figure 5.20 shows the dimensions of sensor fixture for the location 5 and 7. Figure 5.21 shows the dimensions of sensor fixture for the location 6. Figure 5.22 shows the sensor fixture which is placed at location 6. This sensor fixture has been put over the double angle channel of size 100 ± 50 mm.

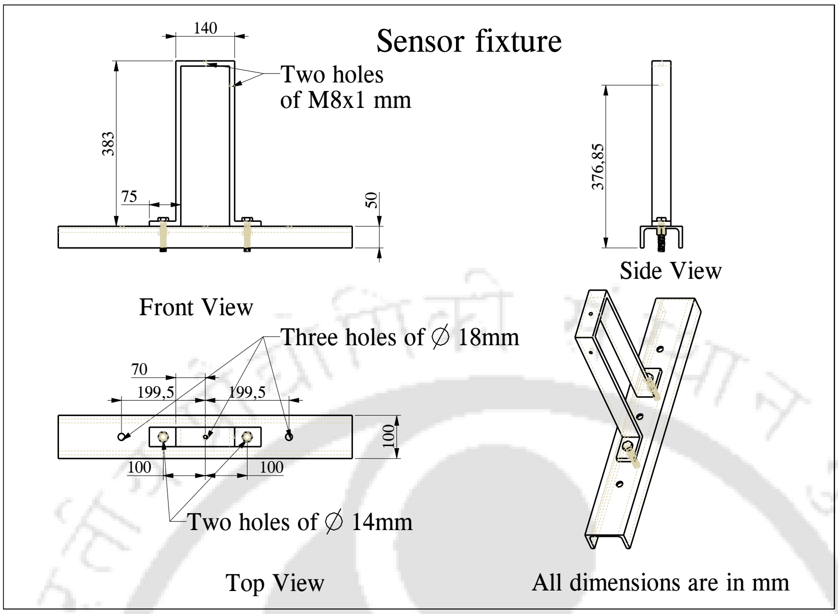

Figure 5.20: Dimensions of sensor fixture for the Location 5 and 7.

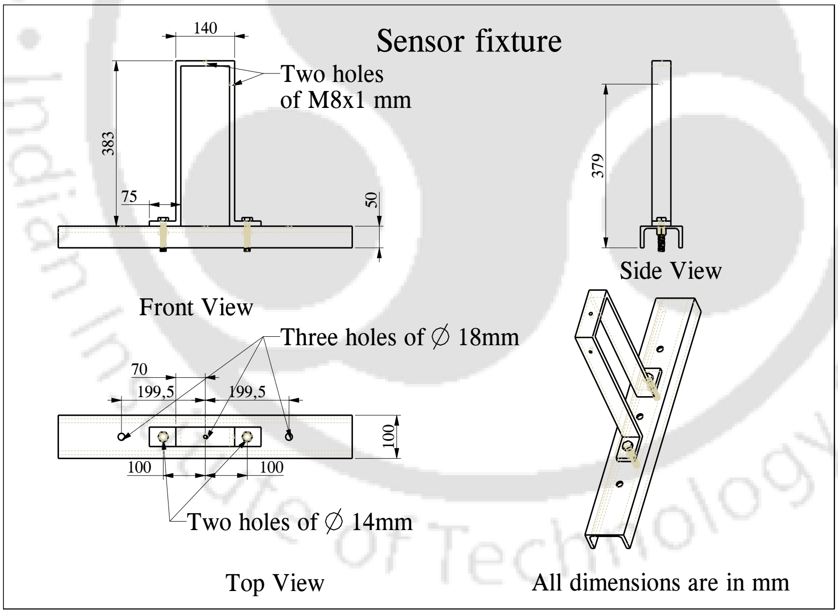

Figure 5.21: Dimensions of sensor fixture for the Location 6.

5.6 Measuring devices used in the experimental rig

Measuring devices have been used to measure the main supply voltages, main supply currents, bridge voltages, bridge currents, rotor displacements and search coil voltages. Six voltage transducers have been used to measure the three phase supply voltages as well as three phase bridge voltages. Three current transducers have been used to measure the three phase bridge currents. Six displacement transducers have been used to measure the rotor displacements in three locations are shown in Figure

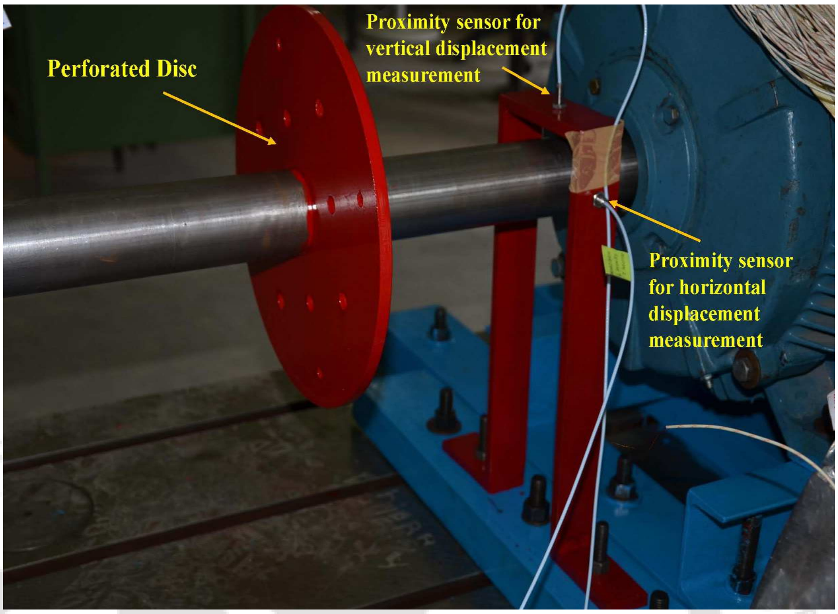

Figure 5.22: A sensor fixture very close to the induction machine.

5.7. In each locations, two proximity transducers have been used to measure the rotor displacements in X and Y-directions. The amplifiers for proximity transducers, voltage transducers and current transducers have been fixed in a panel board and shown in Figure 5.23. The model and make of the measuring devices have been shown in Table 5.7

Table 5.7: Measuring devices used in experimental rig

Sl No	Parameter	Make of the device	Model
1	Rotor displacement	Bently Nevada	3300 XL Proximity transducer system
2	Bridge Current	LEM Transducer	Current Transducer LTS 15-NP
3	Main supply voltage	LEM Transducer	Voltage Transducer LTS 15-NP
4	Bridge voltage	LEM Transducer	Voltage Transducer LTS 15-NP

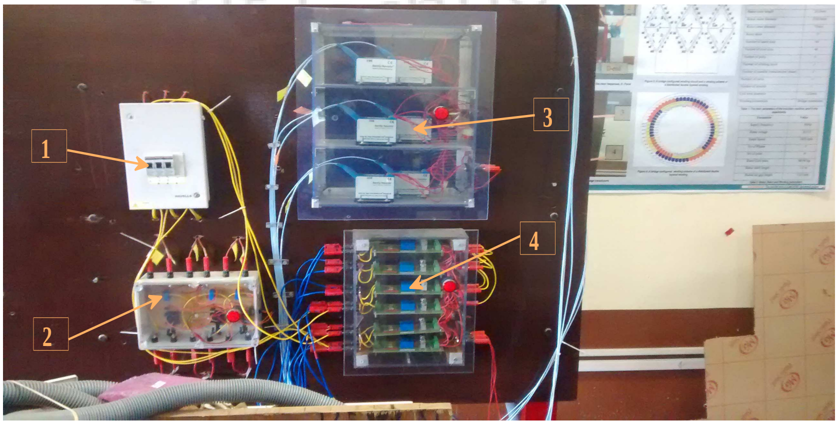

Figure 5.23: A panel board.

In Figure 5.7. 1 - Switches for bridges, 2 - Current transducers, 3 - Amplifiers for displacement sensors, 4 - Voltage transducers

A NI data acquisition system (DAQ) system has been used to acquire the physical signals from proximity transducers, voltage transducers and current transducers. The output lead of the sensors have been connected with the NI module through a coaxial cable. The coaxial cable is used to reduce the noises from the surroundings. The output signal from the current transducers, voltage transducers and displacement sensors have been connected to the NI DAQ system through shielded cover input and output box (SCB connector) shown in Figure 5.24. PXI-6221 module, PXI-6283 module and TB-2708 module have been used in the DAQ system for acquiring the signals. The sampling frequency of the system is 10 kHz; however, only 1 kHz sample data has been taken for the analysis. The data has been calibrated for each displacement sensors, current transducers and voltage transducers.

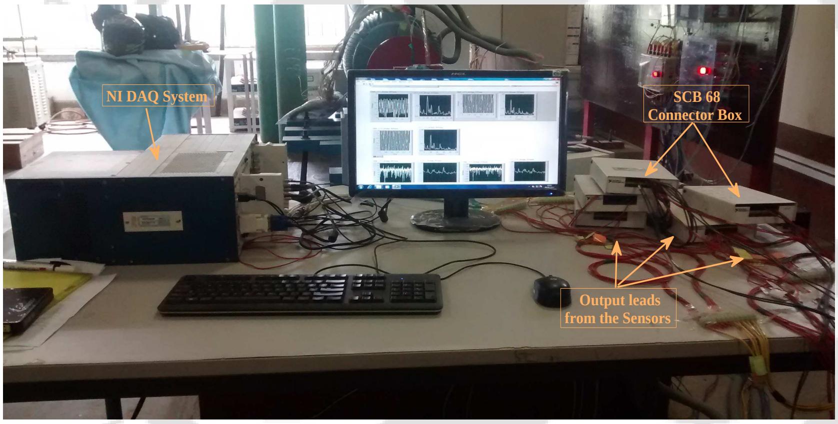

Figure 5.24: A NI DAQ system.

5.7 Experimental results and discussion

The three phase bridge currents and rotor displacements along X and Y directions have been measured for the main supply frequencies of 20Hz, 25Hz, 30Hz, 40Hz, 50Hz, and 60Hz respectively. The three phase bridge currents, bridge voltages and rotor orbits have been measured for two cases, (i) Bridge OFF, (ii) Bridge ON (Passive Control). The switches for bridge connections are shown in Figure 5.23. With reference to Figure 3.2, the switches S1, S2 and S3 are in open condition in Bridge OFF and the switches $S1$, $S2$ and $S3$ are in closed condition in Bridge ON condition. The bridge currents were measured at bridge points S1, S2 and S3 as soon as the bridge points are short circuited. The comparison of three bridge currents and rotor displacements have been presented in the following sections for the main supply frequencies of 20Hz, 25Hz and 30Hz. The three bridge currents and rotor displacements have been measured only when the bridge is in ON condition at higher frequencies such 40Hz, 50Hz and 60Hz. The reason is that to avoid the contact of rotor with the stator at higher supply frequencies when the bridge is in ON condition. The results shown in the subsequent sections are obtained by using **Rotor I** with the machine. There is no load applied in the machine and hence the slip will be zero.

5.7.1 Bridge currents for Bridge OFF and Bridge ON conditions

The comparison of measured three phase bridge currents in Bridge OFF and Bridge ON conditions in time and frequency domains are presented in this subsection. Figure 5.25 to 5.27 show the comparison of measured three phase bridge currents at 20 Hz in Bridge OFF and Bridge ON conditions in time domain. Figures 5.28 to 5.30 show the comparison of measured three Phase bridge currents at 20 Hz in Bridge OFF and Bridge ON conditions in frequency domain.

The frequency component of the bridge currents are 10 Hz ($f_s - f_r$), 20 Hz (f_s) and 30 Hz ($f_s + f_r$), where f_s is the frequency of the main supply and f_r is the rotor frequency. Since the machine has been run at no-load condition, then $f_r = \frac{1}{2} f_s$. The frequency components of the bridge currents obtained from the numerical analysis is presented in Table 3.3. The frequency component obtained from the experiments matches with the frequency components obtained for the case of mixed eccentricity. This has suggested that the machine has mixed eccentricity condition.

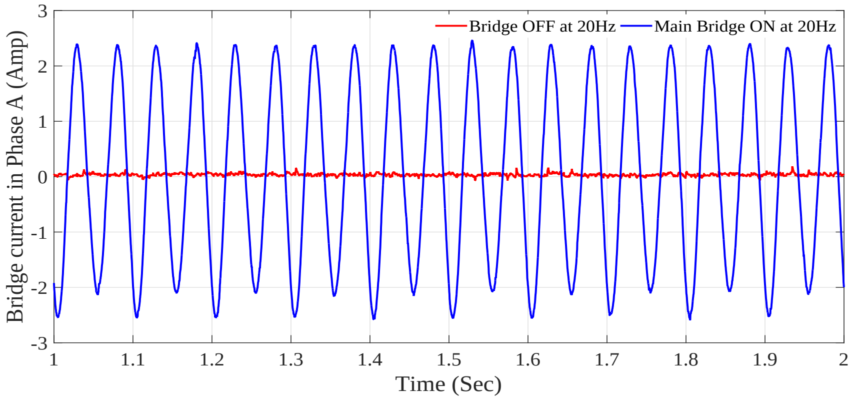

Figure 5.25: Time domain plot of Phase A bridge currents in Bridge OFF and Bridge ON conditions at 20 Hz.

Figure 5.31 shows the comparison of measured Phase A bridge currents at 25 Hz in Bridge OFF and Bridge ON conditions in frequency domain.

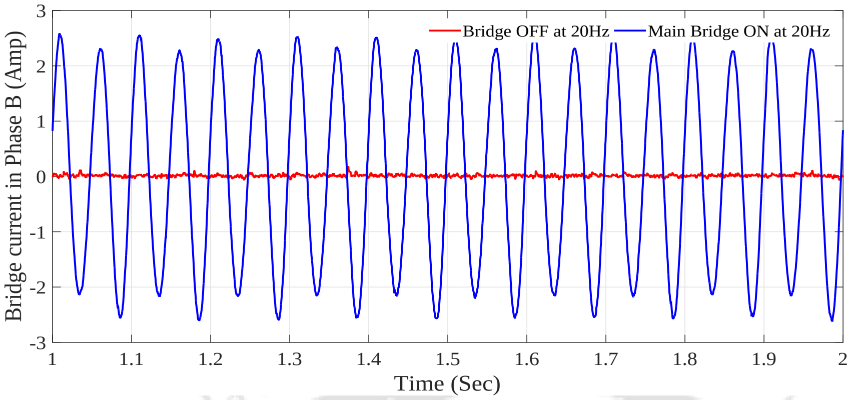

Figure 5.26: Time domain plot of Phase B bridge currents in Bridge OFF and Bridge ON conditions at 20 Hz.

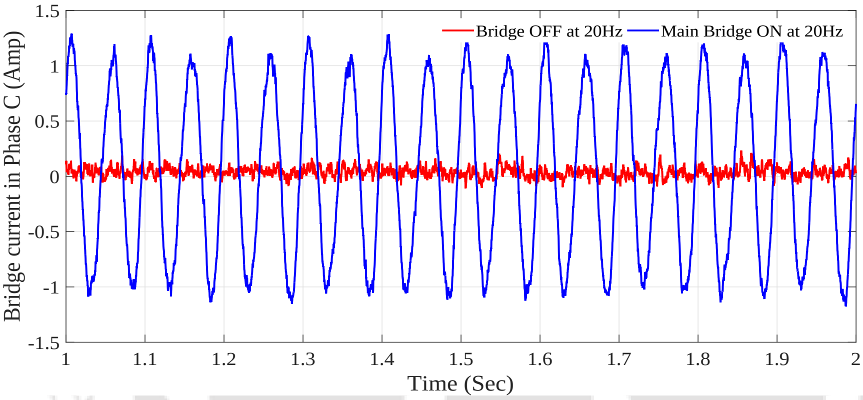

Figure 5.27: Time domain plot of Phase C bridge currents in Bridge OFF and Bridge ON conditions at 20 Hz.

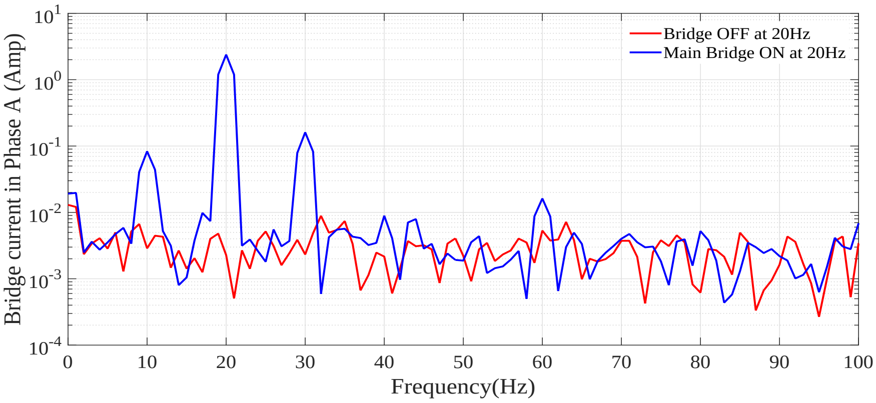

Figure 5.28: FFT of phase A bridge currents in Bridge OFF and Bridge ON conditions at 20 Hz.

Figure 5.32 shows the comparison of measured Phase A bridge currents at 30 Hz in Bridge OFF and Bridge ON conditions in frequency domain.

Figure 5.33 shows the comparison of measured Phase A bridge currents at 40 Hz in Bridge ON condition in frequency domain.

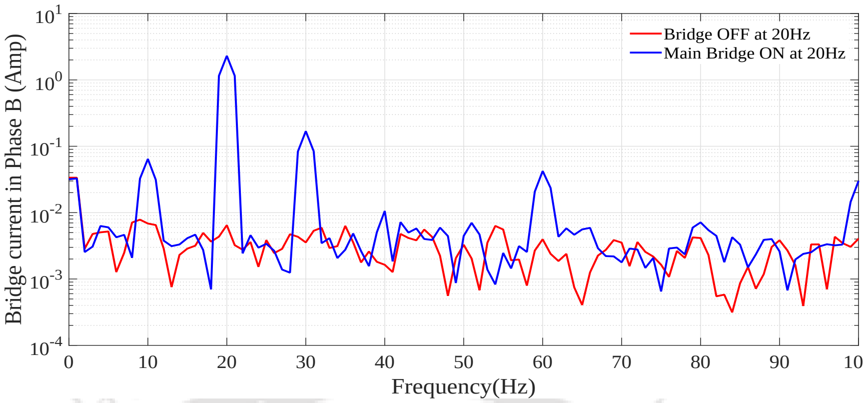

Figure 5.29: FFT of phase B bridge currents in Bridge OFF and Bridge ON conditions at 20 Hz.

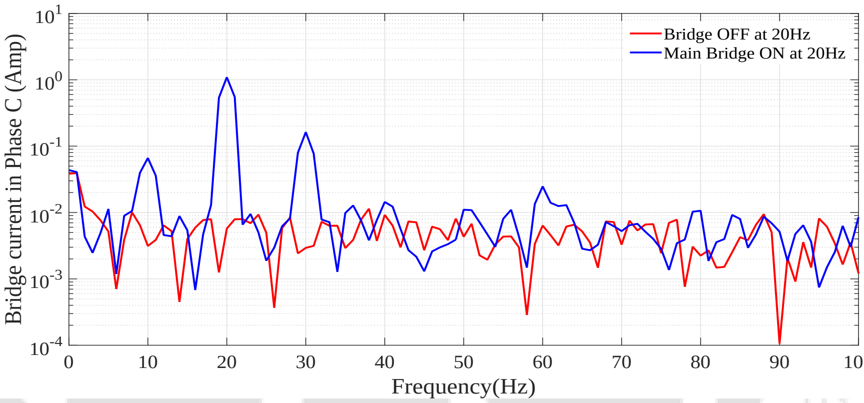

Figure 5.30: FFT of phase C bridge currents in Bridge OFF and Bridge ON conditions at 20 Hz.

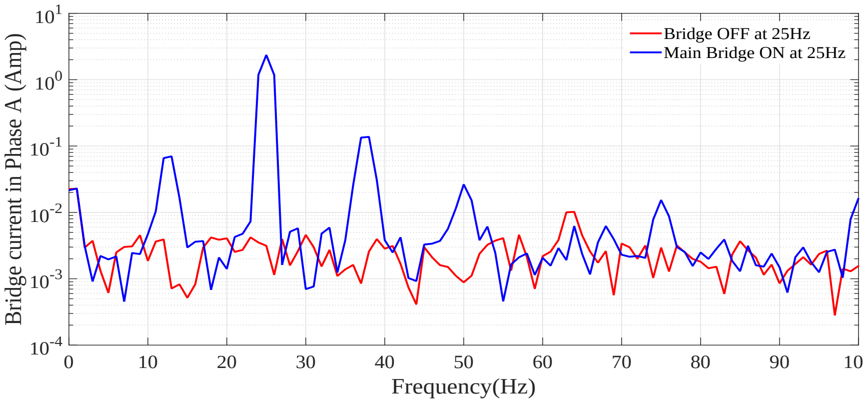

Figure 5.31: FFT of phase A bridge currents in Bridge OFF and Bridge ON conditions at 25 Hz.

Figure 5.34 shows the comparison of measured Phase A bridge currents at 50 Hz in Bridge ON condition in frequency domain. Figure 5.35 shows the comparison of measured Phase A bridge currents at 60 Hz in Bridge ON condition in frequency domain.

Table 5.8 shows the summary of the induced bridge currents for different frequency of the main

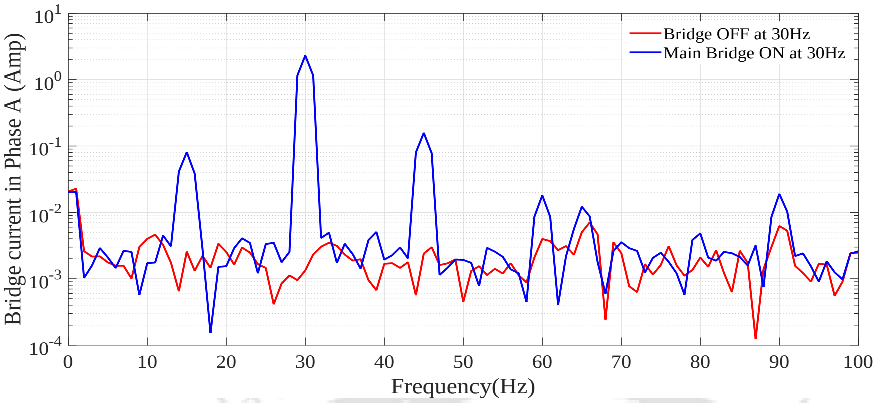

Figure 5.32: FFT of phase A bridge currents in Bridge OFF and Bridge ON conditions at 30 Hz.

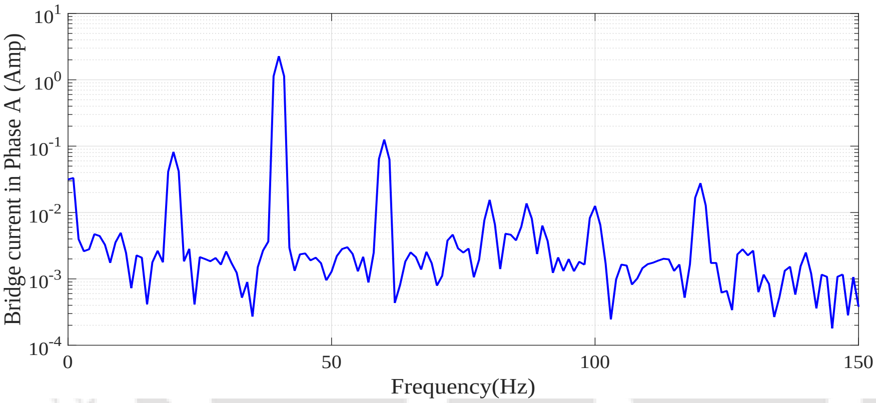

Figure 5.33: FFT of phase A bridge currents in Bridge ON condition at 40 Hz.

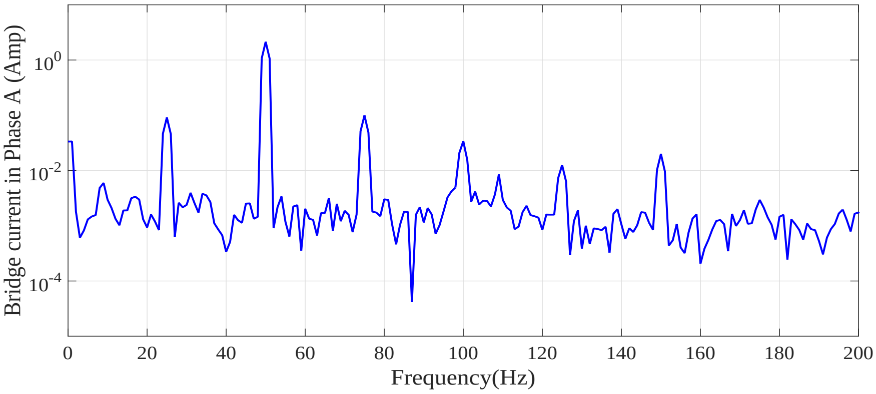

Figure 5.34: FFT of phase A bridge currents in Bridge ON condition at 50 Hz.

supply. It is to be noted here that the frequency components of the bridge currents for mixed eccentricity in no-load condition are $\frac{1}{2}f_s$, f_s and $\frac{3}{2}f_s$, where f_s is the frequency of the main supply. The magnitudes of the bridge current of the frequency component of $\frac{1}{2}f_s$ and $\frac{3}{2}f_s$ is the measure of the dynamic eccentricity present in the system and the magnitude of the bridge current of the frequency

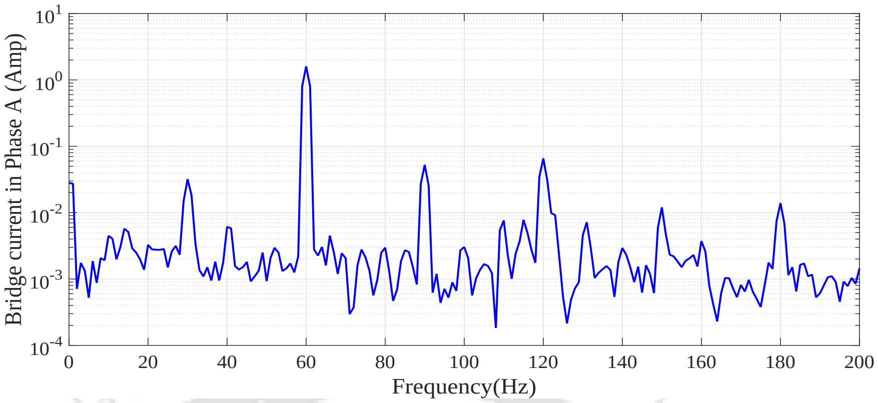

Figure 5.35: FFT of phase A bridge currents in Bridge ON condition at 60 Hz.

Table 5.8: Summary of the bridge currents for different frequency of the main supply

Frequency of the main supply	Bridge currents (Hz)
20 Hz	10, 20, 30
25 Hz	12.5, 25, 37.5
30 Hz	15, 30, 45
40 Hz	20, 40, 60
50 Hz	25, 50, 75
60 Hz	30, 60, 90

component of f_s is the measure of the static eccentricity present in the system.

5.7.2 Displacements of the rotor in Bridge OFF and Bridge ON conditions

Figures 5.36 and 5.37 show the comparison of the measured rotor response in X and Y- directions at 20 Hz in Bridge OFF and Bridge ON conditions in frequency domain. Figures 5.38 and 5.39 show the comparison of the measured rotor response in X and Y- directions at 25 Hz in Bridge OFF and Bridge ON conditions in frequency domain. Figures 5.40 and 5.41 show the comparison of the measured rotor response in X and Y- directions at 30 Hz in Bridge OFF and Bridge ON conditions in frequency domain. Figures 5.42 and 5.43 show the comparison of the measured rotor response in X and Y- directions at 40 Hz in Bridge ON condition in frequency domain. Figures 5.44 and 5.45 show the comparison of the measured rotor response in X and Y- directions at 50 Hz in Bridge ON condition in frequency domain. Figures 5.46 and 5.47 show the comparison of the measured rotor response in X and Y- directions at 60 Hz in Bridge ON condition in frequency domain.

The frequency component of the rotor responses along X- and Y- directions for a main supply

Table 5.9: Summary of the rotor responses for different frequency of the main supply

Frequency of the main supply	Rotor responses (Hz)
20 Hz	0, 10, 20, 30, 40, 50
25 Hz	0, 12.5, 25, 37.5, 50, 62.5
30 Hz	0, 15, 30, 45, 60, 75
40 Hz	0, 20, 40, 60, 80, 100
50 Hz	0, 25, 50, 75, 100, 125
60 Hz	0, 30, 60, 90, 120, 150

frequency of 20 Hz are 0 Hz ($f_s - f_s$), 10 Hz ($f_s - \frac{1}{2}f_s$), 20 Hz (f_s), 30Hz ($f_s + \frac{1}{2}f_s$), 40 Hz ($2f_s$) an 50 Hz ($f_s + \frac{3}{2}f_s$) where f_s is the frequency of the main supply. The frequency components can be obtained from the relationship $\pm f_s \pm f_{bridge}$, where f_{bridge} is the frequency of the bridge currents. The frequency component of the transverse forces acting on the rotor or UMP obtained from the numerical analysis is presented in Table 3.3.The frequency component obtained from the experiments matches with the frequency components obtained for the case of mixed eccentricity from the numerical analysis. This has suggested that the machine has mixed eccentricity condition. It has been observed in Figures 5.36 and 5.37 that 40 Hz ($2f_s$) components almost vanishes in Bridge ON condition. This frequency component occurs due to the static eccentricity of the machine. It can be concluded that in Bridge ON condition the induced EMF can reduce the static eccentricity of the rotor and tries to bring the rotor towards the centre of the stator. To investigate this further the rotor orbits are plotted for main supply frequencies of 20 Hz, 25 Hz, 30 Hz, 40 Hz, 50 Hz and 60 Hz.

Table 5.9 shows the summary of the induced bridge currents for different frequency of the main supply.

5.7.3 Rotor orbits in Bridge OFF and Bridge ON conditions

Figures 5.48, 5.49 and 5.50 show the rotor orbits in Bridge OFF and Bridge ON conditions for main supply frequencies of 20 Hz, 25 Hz and 30 Hz respectively. it has been very clear from Figures 5.48, 5.49 and 5.50 that Bridge ON condition tries to bring the rotor to the centre of the stator thus reducing the static eccentricity. This has been confirmed by the reduction of $2f_s$ component of the rotor response in Bridge ON condition. Figures 5.51, 5.52 and 5.53 show the rotor orbits in Bridge ON conditions only for main supply frequencies of 40 Hz, 50 Hz and 60 Hz respectively.

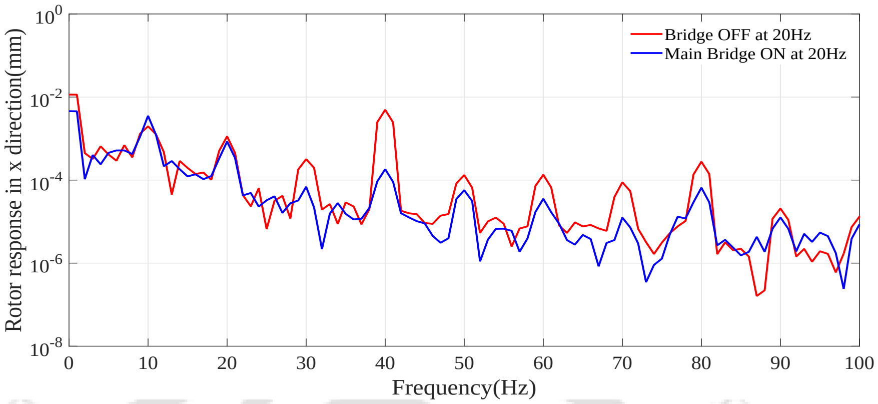

Figure 5.36: FFT of the rotor responses in X-direction in Bridge OFF and Bridge ON conditions for a main supply frequency of 20 Hz.

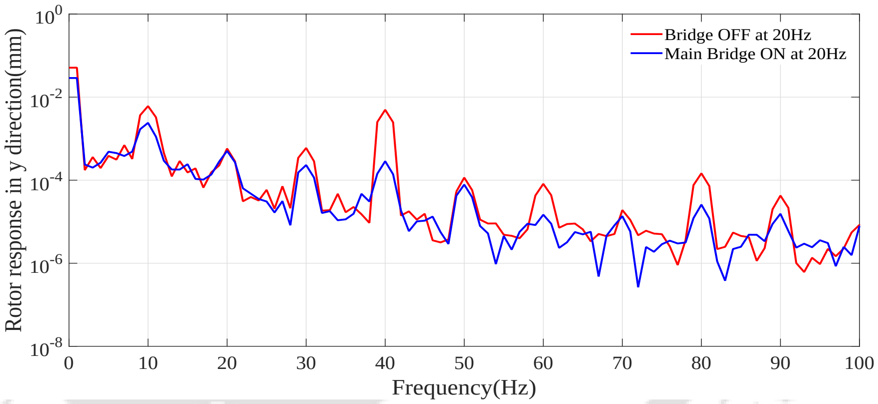

Figure 5.37: FFT of the rotor responses in Y-direction in Bridge OFF and Bridge ON conditions for a main supply frequency of 20 Hz.

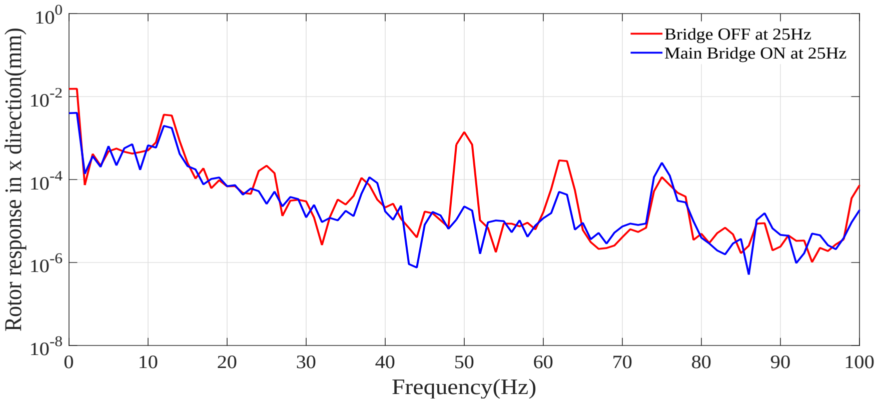

Figure 5.38: FFT of the rotor responses in X-direction in Bridge OFF and Bridge ON conditions for a main supply frequency of 25 Hz.

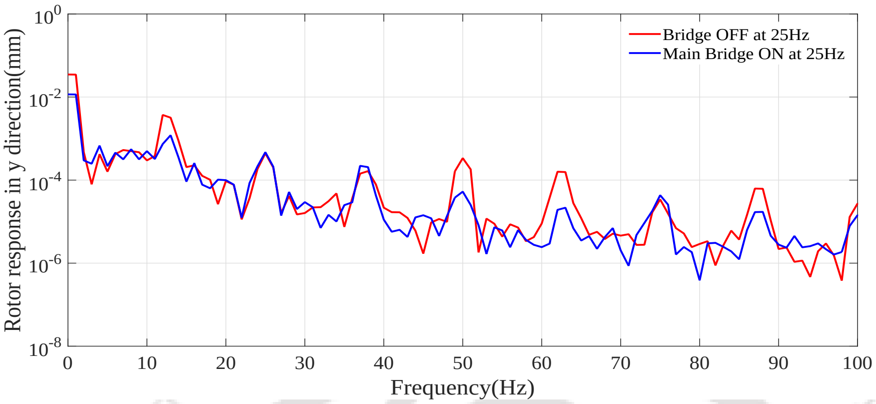

Figure 5.39: FFT of the rotor responses in Y-direction in Bridge OFF and Bridge ON conditions for a main supply frequency of 25 Hz.

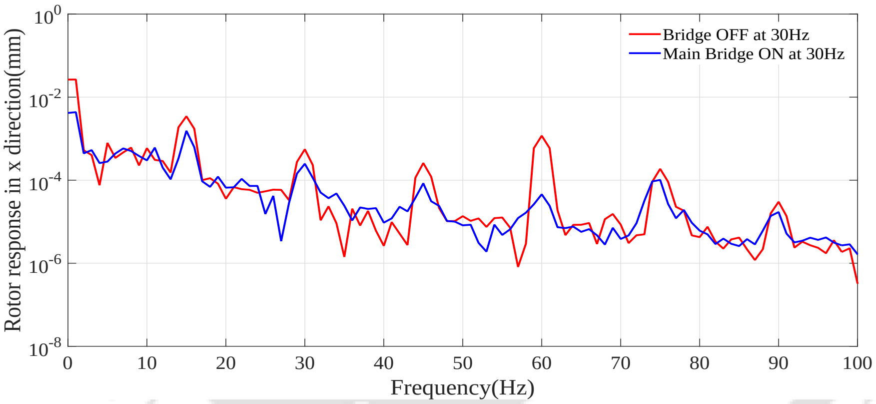

Figure 5.40: FFT of the rotor responses in X-direction in Bridge OFF and Bridge ON conditions for a main supply frequency of 30 Hz.

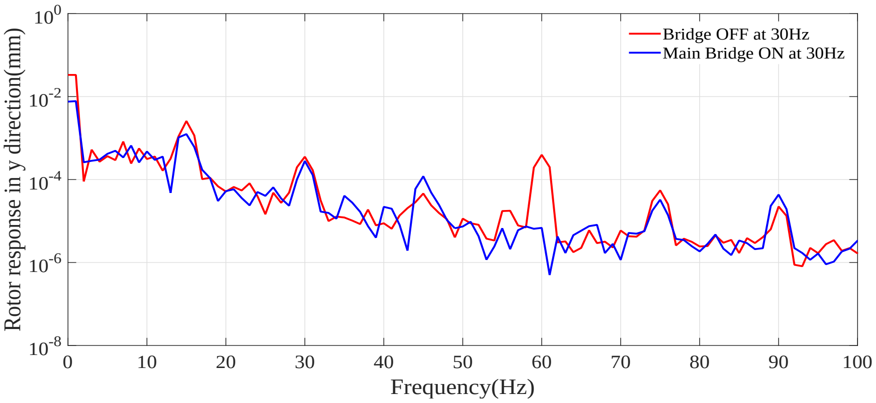

Figure 5.41: FFT of the rotor responses in Y-direction in Bridge OFF and Bridge ON conditions for a main supply frequency of 30 Hz.

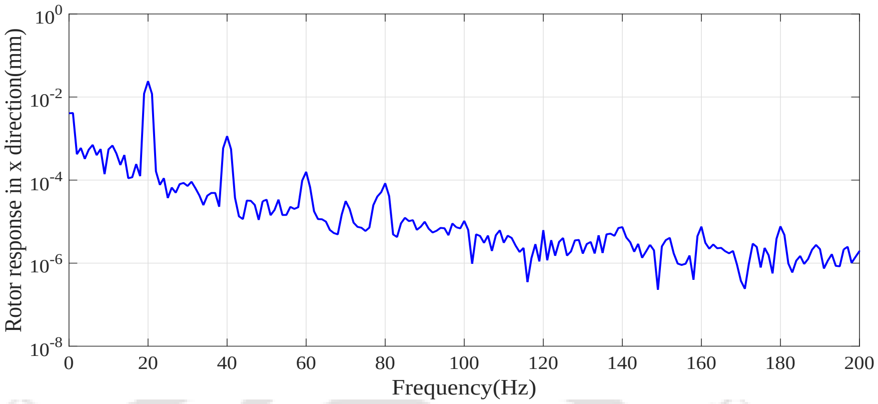

Figure 5.42: FFT of the rotor response in X-direction in Bridge ON condition for a main supply frequency of 40 Hz.

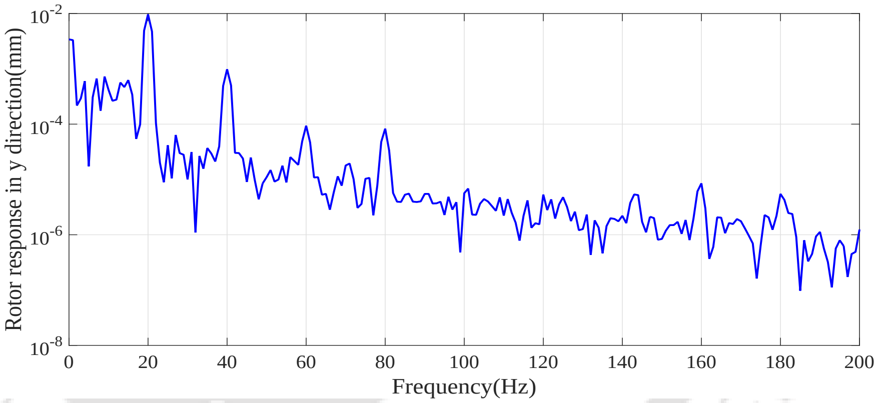

Figure 5.43: FFT of the rotor response in Y-direction in Bridge ON condition for a main supply frequency of 40 Hz.

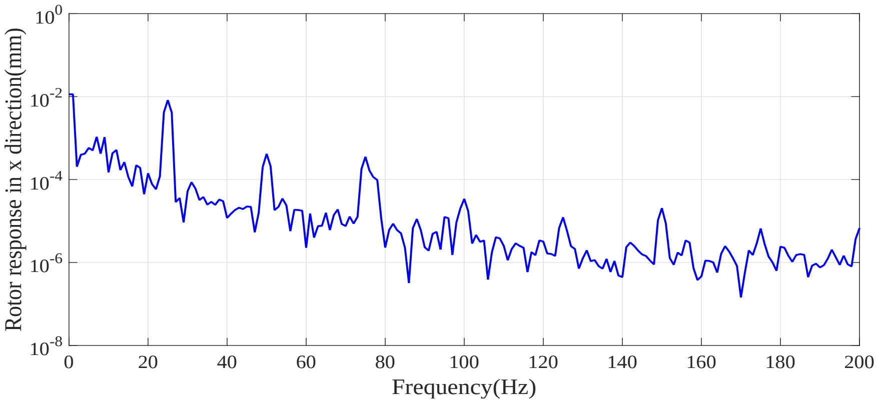

Figure 5.44: FFT of the rotor responses in X-direction in Bridge ON condition for a main supply frequency of 50 Hz.

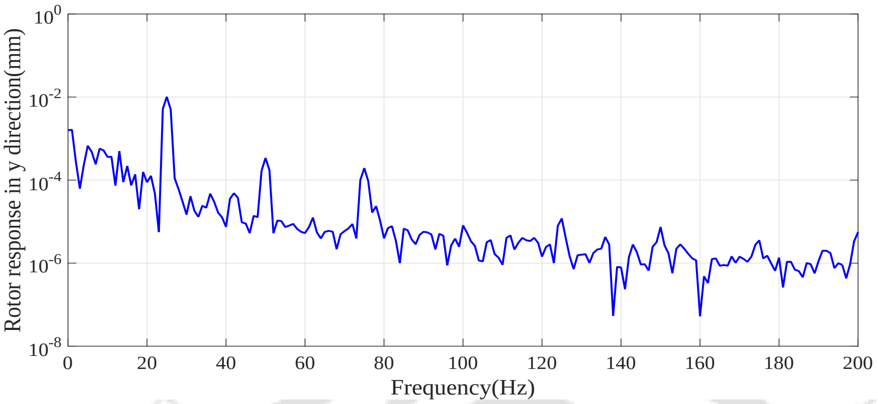

Figure 5.45: FFT of the rotor responses in Y-direction in Bridge ON condition for a main supply frequency of 50 Hz.

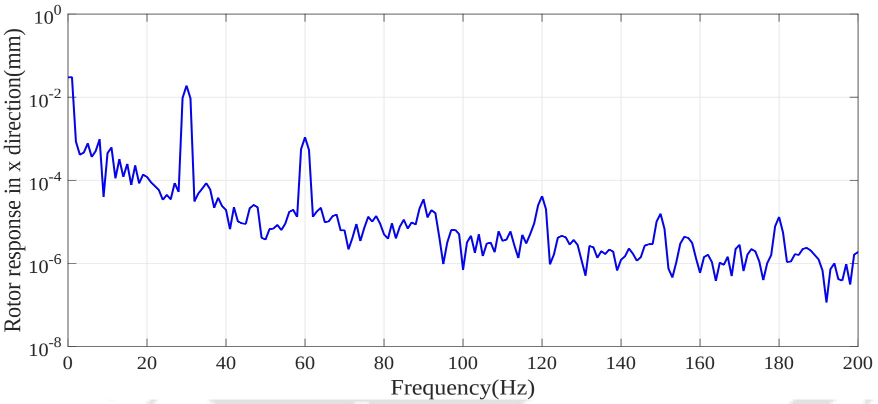

Figure 5.46: FFT of the rotor responses in X-direction in Bridge ON condition for a main supply frequency of 60 Hz.

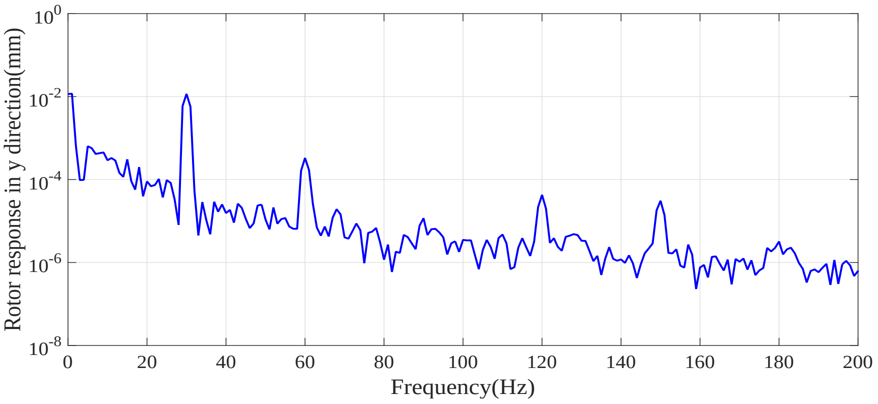

Figure 5.47: FFT of the rotor responses in Y-direction in Bridge ON condition for a main supply frequency of 60 Hz.

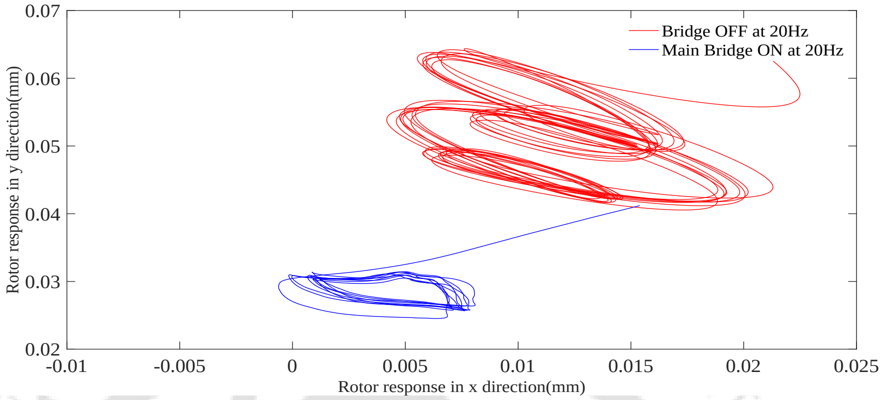

Figure 5.48: Rotor orbits in Bridge OFF and Bridge ON conditions at 20 Hz main supply frequency.

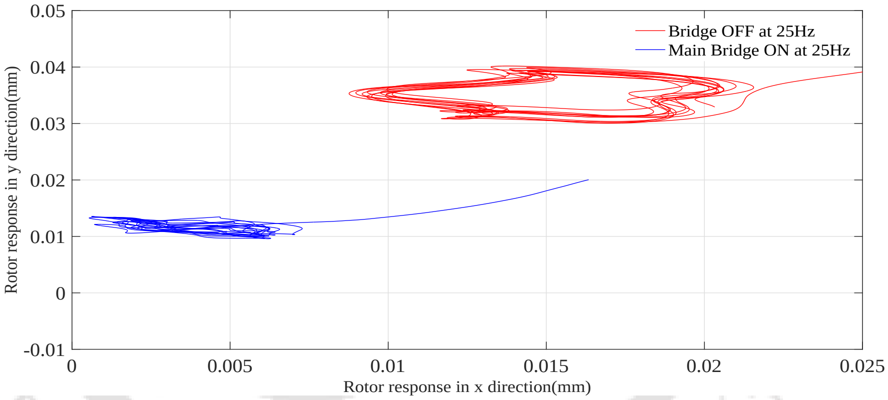

Figure 5.49: Rotor orbits in Bridge OFF and Bridge ON conditions at 25 Hz main supply frequency.

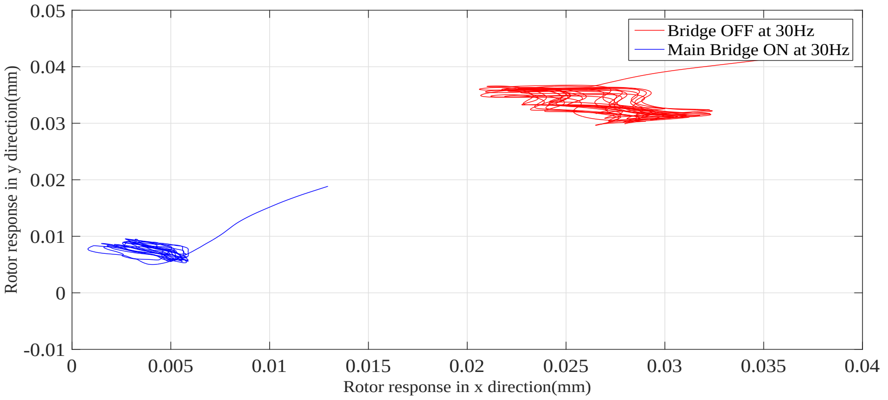

Figure 5.50: Rotor orbits in Bridge OFF and Bridge ON conditions at 30 Hz main supply frequency.

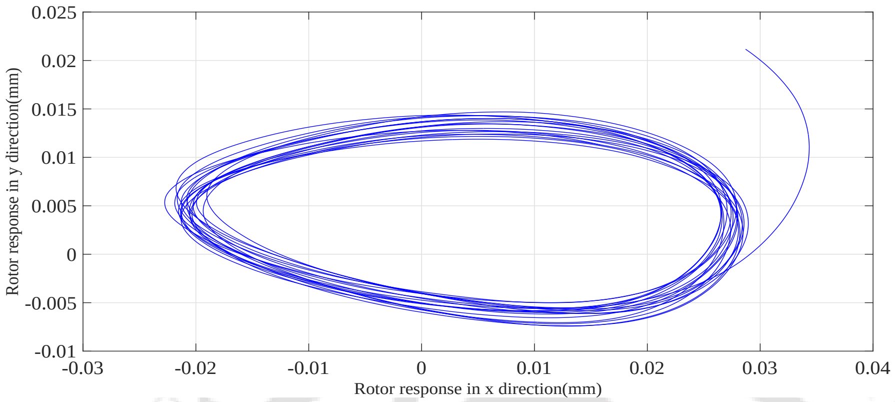

Figure 5.51: Rotor orbits in Bridge ON condition at 40 Hz main supply frequency.

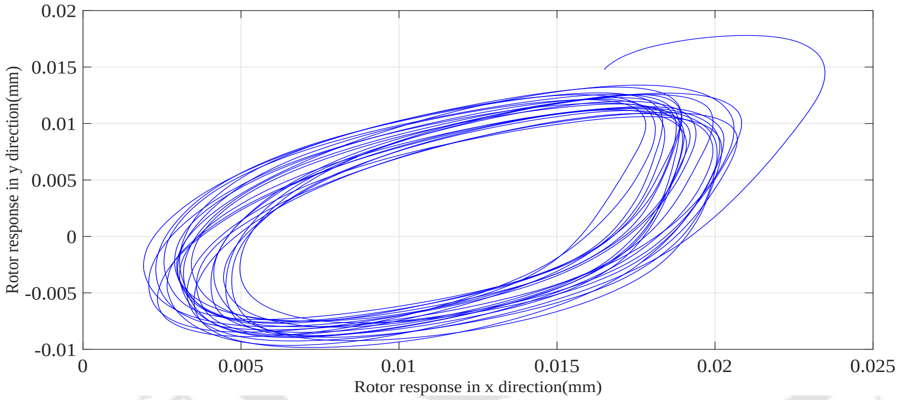

Figure 5.52: Rotor orbits in Bridge ON condition at 50 Hz main supply frequency.

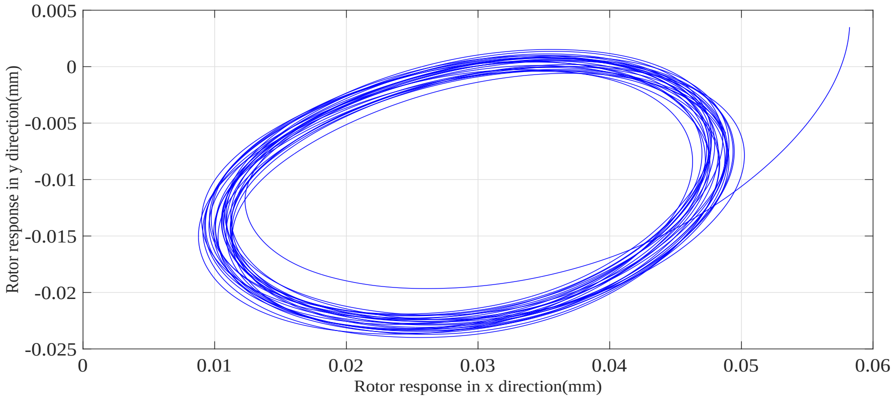

Figure 5.53: Rotor orbits in Bridge ON condition at 60 Hz main supply frequency.

5.8 Conclusions

The development of experimental rig to incorporate the bridge configured winding in an induction machine has been presented. The parameters of the original machine have been presented. A 37 kW, three phase and four pole induction machine with squirrel cage rotor is used for the development of experimental rig. The original stator winding is a three phase, double layer, 4-pole with concentrated winding. The original stator winding has been removed and replaced by a three phase, double layer and 4-pole distributed bridge configured winding. The devices used for the measurement of bridge currents, bridge voltages, main supply currents and main supply voltages have been explained. The measurements of main currents, main voltages, bridge currents, bridge voltages, rotor responses are obtained for up to a supply frequency of 60 Hz. The bridge currents, rotor responses along X- and Y- directions, rotor orbits for main supply frequencies of 20 Hz, 25 Hz, 30Hz, 40 Hz, 50 Hz and 60 Hz are presented in this Chapter. There is no-load applied on this machine. The results obtained from the experiments confirmed that the machine has mixed eccentricity. The frequency components of the bridge currents are $f_s - \frac{1}{2}f_s$, f_s and $f_s + \frac{1}{2}f_s$, where f_s is the supply frequency. The frequency components of the rotor responses are $(f_s - f_s)$, $(f_s - \frac{1}{2}f_s)$, (f_s), $(f_s + \frac{1}{2}f_s)$, $(2f_s)$ and $(f_s + \frac{3}{2}f_s)$, where f_s is the frequency of the main supply. The rotor responses confirmed that Bridge ON condition suppresses the $2f_s$ component of the UMP. The Bridge ON condition reduces the static eccentricity by shifting the rotor towards the stator centre. The numerical results obtained in Chapter 3 have been verified by the experimental results obtained in this Chapter. The frequency of the bridge currents are the measure of eccentricities present in the machine. The f_s component of the bridge current is a measure of static eccentricity in the machine and $\frac{1}{2}f_s$ and $\frac{3}{2}f_s$ components of the bridge currents are measure of dynamic eccentricity present in the machine. An attempt has been made to develop a relationship between the eccentricity present in the machine with the bridge currents. Relationship between the dynamic eccentricity and bridge currents has been developed using experimental results. Known values of unbalance masses have been introduced in the rotor system to incorporate dynamic eccentricity in the system and the corresponding bridge currents are calculated. The analysis is presented in the next chapter. Relationship between the static eccentricity and bridge currents has been developed by carrying out numerical experiments. The analysis is also presented in the next chapter.

6

Experimental Analysis of Bridge Currents with respect to Known Unbalance Masses

Contents

6.1 Introduction

The working principle of bridge configured winding has been explained in Section 1.4 of Chapter 1. The development of the experimental rig has been explained in Chapter 5. The 37 kW, 4-pole induction machine with the bridge configured winding stator winding is the critical component of the rig. The bridge currents and rotor responses are measured for different main supply frequencies. The bridge currents, rotor responses and rotor orbits are presented in Chapter 5. The bridge currents and rotor responses obtained from the numerical model are verified by experimental results. It has been confirmed that the static eccentricity in the rotor induces bridge currents with one dominant frequency, i.e. f_s, where f_s is the main supply frequency. It has also been confirmed that the dynamic eccentricity in the rotor in no-load condition induces bridge currents with two dominant frequencies, i.e. $\frac{1}{2}f_s$ and $\frac{3}{2}f_s$. In this chapter an attempt has been made to develop a relationship between the level of eccentricity and the magnitude of the concerned components of the bridge currents by conducting series of experiments. The experiments are conducted by incorporating known mass unbalances in the perforated disc attached with the shaft. There are sixteen holes (positions) in the disc in which smaller masses can be added in order to incorporate known mass unbalances. The known masses were added in the holes of the perforated disc as shown in Figure 5.10 of Chapter 5. Three types of rotor shafts have been used in the experimental rig. In this chapter, the experimental results are presented which have been obtained by using the **Rotor I** and **Rotor III**. The dimensions of the **Rotor I** have been given in Figure 5.2. The experimental rig is tested up to 70Hz. However, the results have been presented here for 10Hz, 15Hz, 20Hz, 25Hz, 30Hz and 50Hz for **Rotor I**. The known masses were in the range of 0 gm to 1000 gm with an increment of 50 gm for flexible **Rotor I**. The masses were added in the holes of the perforated disc at Position 1 and the bridge currents were measured. The known masses were chosen only up to 450 gm for the speeds 50Hz in order to avoid the damage of the stator with respect to the rotor.

Figure 5.8 shows the dimensions of **Rotor III**. The **Rotor III** is flexible in nature, so that the experiments were conducted at lower speeds in order to prevent the rotor and stator contact. The experiments were carried out at 8Hz, 9Hz, 10Hz,11Hz, 12Hz, 13Hz and 14Hz. The known masses were in the range of 0 gm to 700 gm with an increment of 50 gm. Initially, the bridge currents were measured without any mass added in the holes of the perforated disc and this has been taken as reference. The measured three phase currents were plotted against the known mass balances. The known masses were added in all of holes of the perforated disc individually and the bridge currents were measured. This chapter illustrates the relationship between the known mass unbalances and the measured three phase bridge currents.

In addition to the above, a series of numerical experiments has been conducted to develop a relationship between the level of static eccentricity and the magnitude of the f_s components of the induced bridge currents.

6.2 Experimental results and discussion for Rotor I

The experiments were conducted to develop a relationship between the known mass unbalances and the three phase bridge currents. The experiments were carried at 10Hz, 15Hz, 20Hz, 25Hz, 30Hz and 50Hz. Figure 3.2 shows the bridge point connections for bridge configured based induction machine. However, the results have been presented here for 30Hz and 50Hz. The bridge currents were measured at bridge points S1, S2 and S3 once the bridge switches were short circuited. The amplitude of $0.5f_s$ and $1.5f_s$ frequency components of bridge currents were plotted against the weights for Position 1. f_s is the main supply frequency.

6.2.1 Results of $0.5f_s$ and $1.5f_s$ frequency components of bridge currents for Position 1

Figures 6.1 to 6.5 show the peak amplitudes of $0.5f_s$ frequency components for the three phase bridge currents with respect to the known mass unbalances. Figures 6.6 to 6.10 show the peak amplitudes of $1.5f_s$ frequency components for the three phase bridge currents with respect to the known mass unbalances. The main supply frequencies of the induction machine are 10Hz, 15Hz, 20Hz, 25Hz and 30Hz.

6.2.2 Results of $0.5f_s$ and $1.5f_s$ frequency components of bridge currents for Position 1 at 50Hz

Figures 6.11 and 6.12 show the $0.5f_s$ and $1.5f_s$ frequency components of bridge currents for Position 1 for supply frequency of 50Hz.

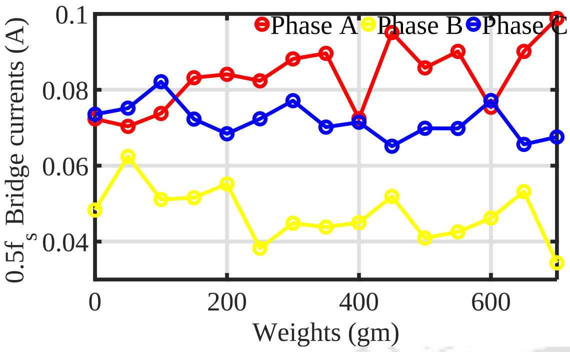

Figure 6.1: Amplitude of three phase Bridge current (A) at $0.5f_s$ vs unbalance mass (gm) at main supply frequency 10 Hz at Pos 1.

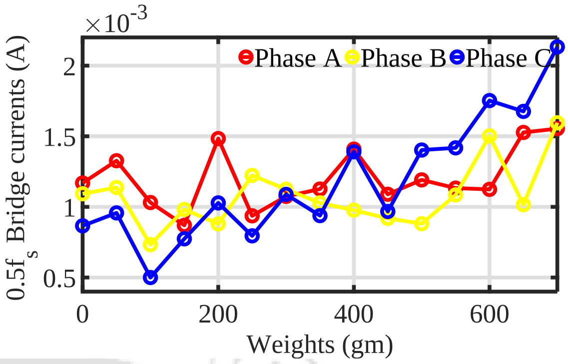

Figure 6.2: Amplitude of three phase Bridge current (A) at $0.5f_s$ vs unbalance mass (gm) at main supply frequency 15 Hz at Pos 1.

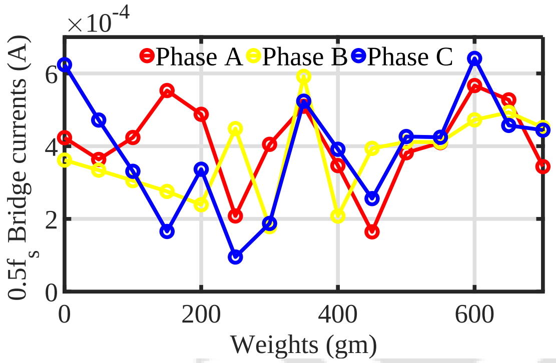

Figure 6.3: Amplitude of three phase Bridge current (A) at $0.5f_s$ vs unbalance mass (gm) at main supply frequency 20 Hz at Pos 1.

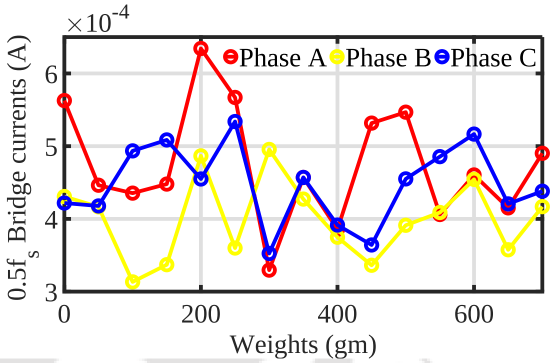

Figure 6.4: Amplitude of three phase Bridge current (A) at $0.5f_s$ vs unbalance mass (gm) at main supply frequency 25 Hz at Pos 1.

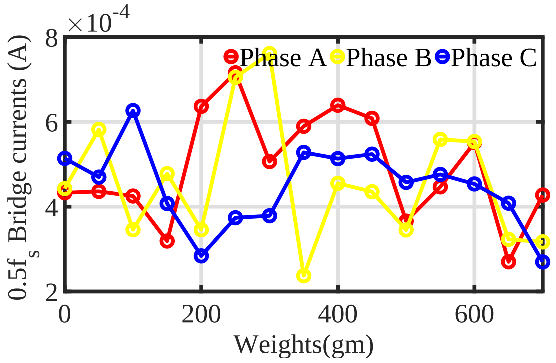

Figure 6.5: Amplitude of three phase Bridge current (A) at $0.5f_s$ vs unbalance mass (gm) at main supply frequency 30 Hz at Pos 1.

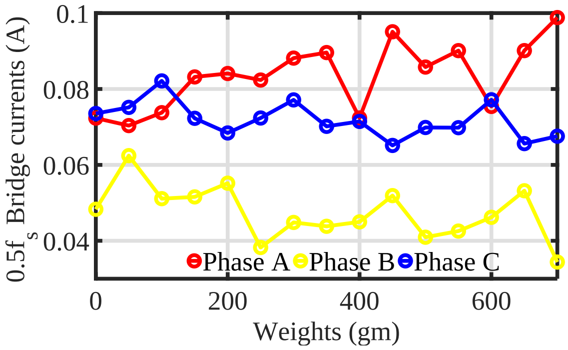

Figure 6.6: Amplitude of three phase Bridge current (A) at $1.5f_s$ vs unbalance mass (gm) at main supply frequency 10 Hz at Pos 1.

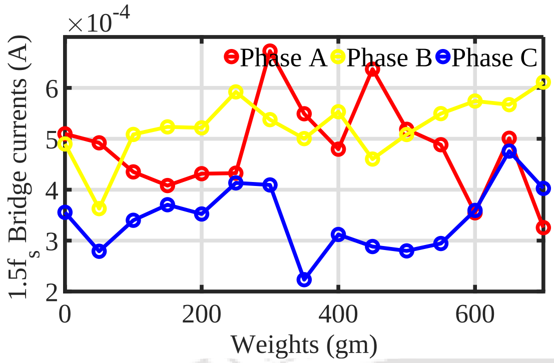

Figure 6.7: Amplitude of three phase Bridge current (A) at $1.5f_s$ vs unbalance mass (gm) at main supply frequency 15 Hz at Pos 1.

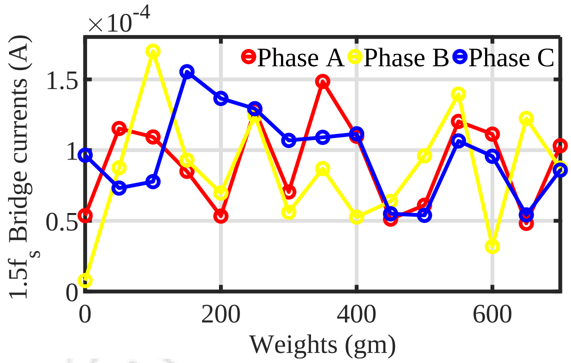

Figure 6.8: Amplitude of three phase Bridge current (A) at $1.5f_s$ vs unbalance mass (gm) at main supply frequency 20 Hz at Po s1.

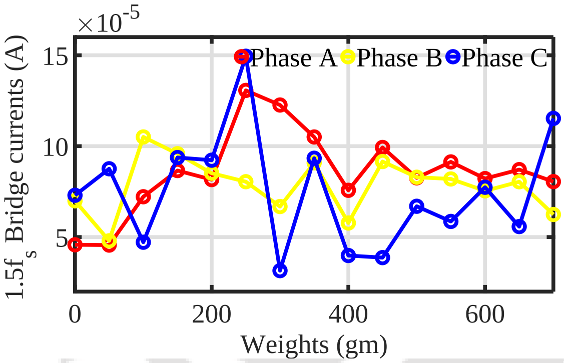

Figure 6.9: Amplitude of three phase Bridge current (A) at $1.5f_s$ vs unbalance mass (gm) at main supply frequency 25 Hz at Pos 1.

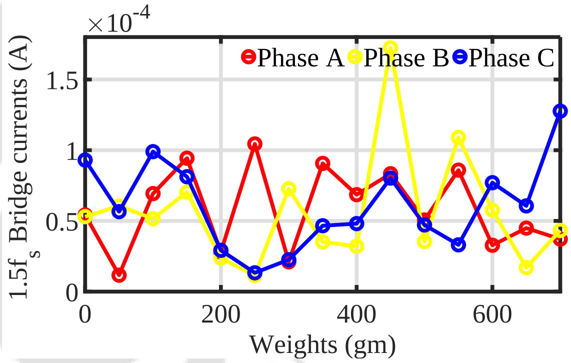

Figure 6.10: Amplitude of three phase Bridge current (A) at $1.5f_s$ vs unbalance mass (gm) at main supply frequency 30 Hz at Pos 1.

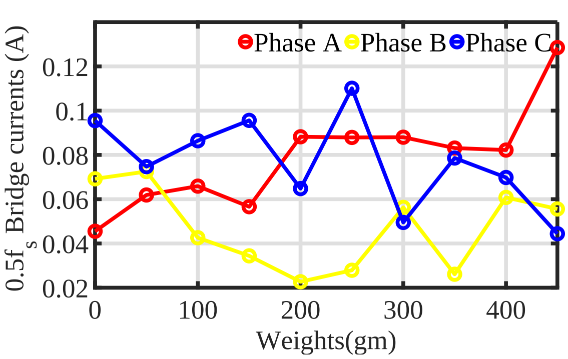

Figure 6.11: Amplitude of three phase Bridge current (A) at $0.5f_s$ vs unbalance mass (gm) at main supply frequency 50 Hz at Pos 1.

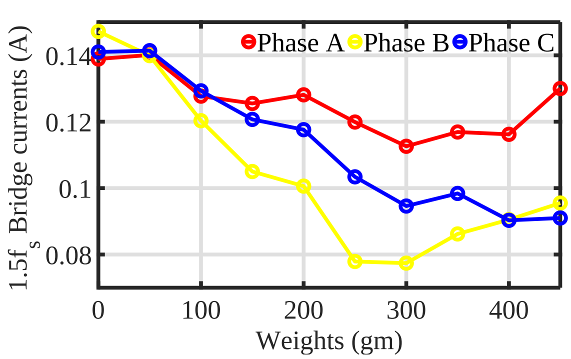

Figure 6.12: Amplitude of three phase Bridge current (A) at $1.5f_s$ vs unbalance mass (gm) at main supply frequency 50 Hz at Pos 1.

6.3 Replacement of shafts

Figures 6.1 to 6.10 show the $0.5f_s$ and $1.5f_s$ frequency components of the amplitudes of three phase bridge currents at 10Hz, 15Hz, 20Hz, 25Hz and 30Hz supply frequency. It has been observed that there were no changes of the amplitudes in the three phase bridge currents with an increase in unbalance masses. Obviously, for all supply frequencies there were no noticeable changes in the amplitudes of the three phase bridge currents for $0.5f_s$ and $1.5f_s$. The experiments were carried out at 50Hz. Figure 6.11 and Figure 6.12 show the amplitudes of the three phase bridge currents for $0.5f_s$ and $1.5f_s$ frequency components when the supply frequency is 50 Hz. It has been realized that there were no changes of the amplitudes of the three phase bridge currents for $0.5f_s$ and $1.5f_s$ frequency component even at very high speed.

This may happen due to the high stiffness of the **Rotor I**. So, it has been decided to replace the **Rotor I** with a flexible rotor. The **Rotor I** has been replaced by the **Rotor II**. Figure 5.5 shows that dimensions of **Rotor II**. It has been noticed that the **Rotor II** is too flexible and the rotor touched the stator of the machine even in static condition. So, it was difficult to rotate the **Rotor II** even at free run. In that case, there were no possibility of conducting the experiments. It has been decided to replace the **Rotor II**. Figure 5.5 shows the dimensions of **Rotor III**. The **Rotor II** has been replaced by the **Rotor III**.

6.4 Experimental Results and Discussion for Rotor III

The experimental results of amplitude of three phase bridge currents have been presented for **Rotor III**. Due to the nature of flexibility of the shaft **III**, the main supply frequency were chosen as 10 Hz, 11 Hz, 12 Hz, 13 Hz and 14 Hz in order to prevent the stator and rotor contact. The bridge current were measured when the weights are added in the holes of perforated disc. The weights were added in the holes for each sixteen positions and the bridge currents were measured. The peak amplitude value of three phase bridge currents have been measured at $0.5f_s$ and $1.5f_s$ for 10 Hz, 11 Hz, 12 Hz, 13 Hz and 14 Hz respectively and plotted against the known mass unbalances. However, the results have been presented for Pos 6, Pos 7, Pos 8, Pos 14, Pos 15 and Pos 16.

6.4.1 Results of 0.5f_s and 1.5f_s frequency components of three phase bridge currents for Position 6

The known mass unbalances are added to Pos 6 in the perforated disc and then the three phase bridge currents were measured. Figures 6.13 to 6.17 show the peak amplitudes of 0.5f_s frequency components for of three phase bridge currents with respect to the known mass unbalances for main supply frequencies of 10 Hz, 11 Hz, 12 Hz, 13 Hz and 14 Hz respectively. Figures 6.18 to 6.22 show the peak amplitudes of 1.5f_s frequency components for the three phase bridge currents with respect to the known mass unbalances for main supply frequencies of 10 Hz, 11 Hz, 12 Hz, 13 Hz and 14 Hz respectively. It has been observed that the peak amplitudes of 0.5f_s and 1.5f_s components of the bridge currents decrease with the increase in mass unbalances for all the supply frequencies for Pos 6.

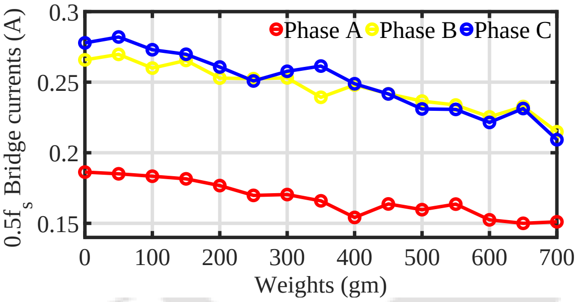

Figure 6.13: Amplitude of three phase Bridge current (A) at 0.5f_s vs unbalance mass (gm) at main supply frequency 10 Hz at Pos 6.

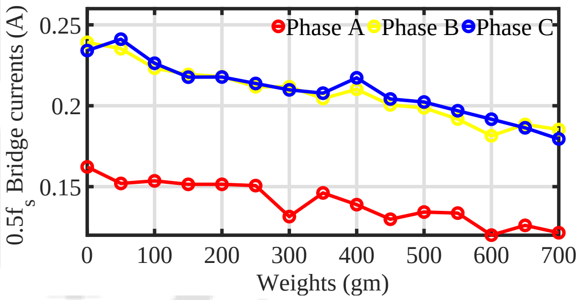

Figure 6.14: Amplitude of three phase Bridge current (A) at 0.5f_s vs unbalance mass (gm) at main supply frequency 11 Hz at Pos 6.

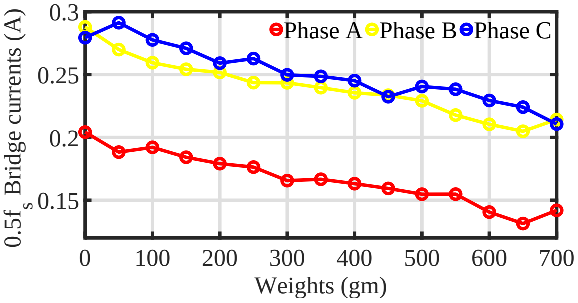

Figure 6.15: Amplitude of three phase Bridge current (A) at 0.5f_s vs unbalance mass (gm) at main supply frequency 12 Hz at Pos 6.

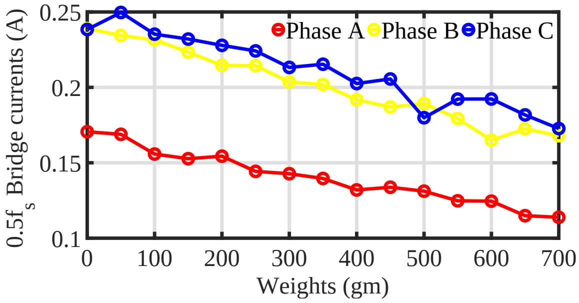

Figure 6.16: Amplitude of three phase Bridge current (A) at 0.5f_s vs unbalance mass (gm) at main supply frequency 13 Hz at Pos 6.

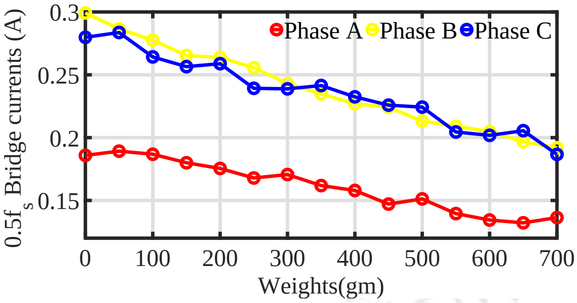

Figure 6.17: Amplitude of three phase Bridge current (A) at $0.5f_s$ vs unbalance mass (gm) at main supply frequency 14 Hz at Pos 6.

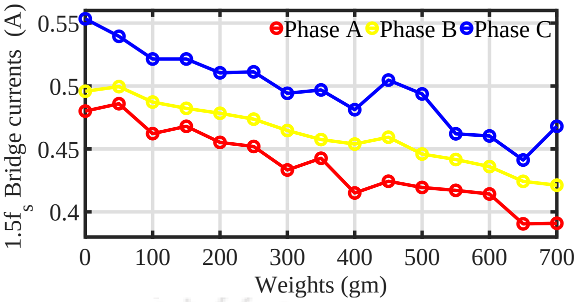

Figure 6.18: Amplitude of three phase Bridge current (A) at $1.5f_s$ vs unbalance mass (gm) at main supply frequency 10 Hz at Pos 6.

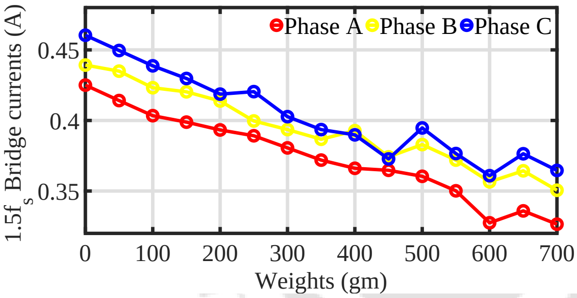

Figure 6.19: Amplitude of three phase Bridge current (A) at $1.5f_s$ vs unbalance mass (gm) at main supply frequency 11 Hz at Pos 6.

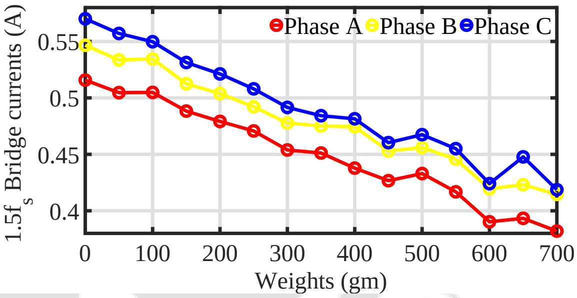

Figure 6.20: Amplitude of three phase Bridge current (A) at $1.5f_s$ vs unbalance mass (gm) at main supply frequency 12 Hz at Pos 6.

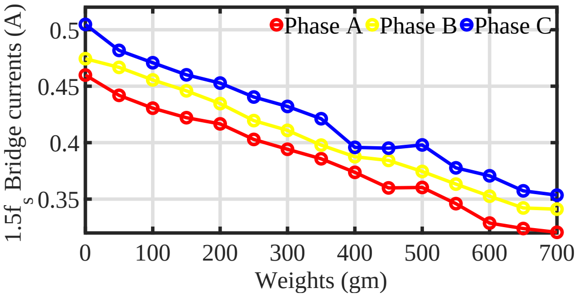

Figure 6.21: Amplitude of three phase Bridge current (A) at $1.5f_s$ vs unbalance mass (gm) at main supply frequency 13 Hz at Pos 6.

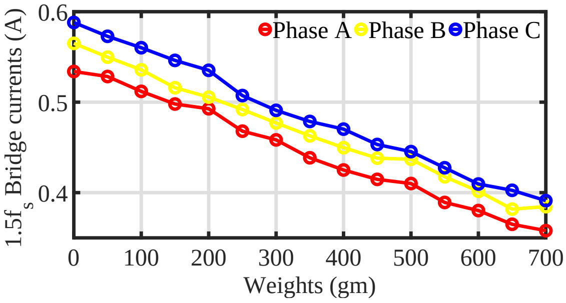

Figure 6.22: Amplitude of three phase Bridge current (A) at $1.5f_s$ vs unbalance mass (gm) at main supply frequency 14 Hz at Pos 6.

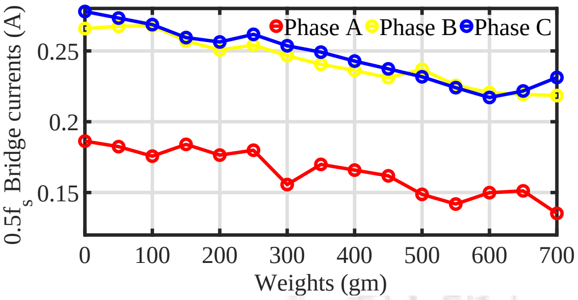

Figure 6.23: Amplitude of three phase Bridge current (A) at $0.5f_s$ vs unbalance mass (gm) at main supply frequency 10 Hz at Pos 7.

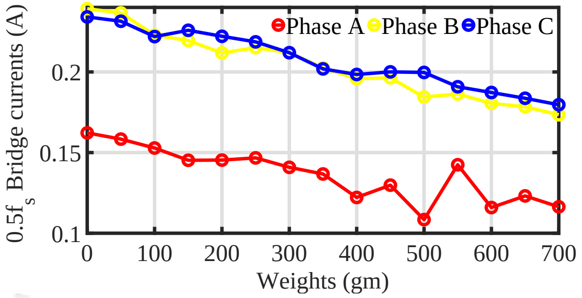

Figure 6.24: Amplitude of three phase Bridge current (A) at $0.5f_s$ vs unbalance mass (gm) at main supply frequency 11 Hz at Pos 7.

6.4.2 Results of $0.5f_s$ and $1.5f_s$ frequency components of three phase bridge currents for Position 7

The known mass unbalances are added to Pos 7 in the perforated disc and then the three phase bridge currents were measured. Figure 6.23 to Figure 6.27 show the peak amplitudes of $0.5f_s$ frequency components of the three phase bridge currents with respect to the known mass unbalances for main supply frequencies of 10 Hz, 11 Hz, 12 Hz, 13 Hz and 14 Hz respectively. Figure 6.28 to Figure 6.32 show the peak amplitudes of $1.5f_s$ frequency components for the three phase bridge currents with respect to the known mass unbalances for main supply frequencies of 10 Hz, 11 Hz, 12 Hz, 13 Hz and 14 Hz respectively. It has been observed that the peak amplitudes of $0.5f_s$ and $1.5f_s$ components of the bridge currents decrease with the increase in mass unbalances for all the supply frequencies for Pos 7.

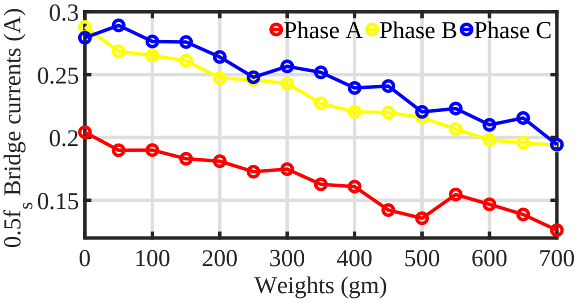

Figure 6.25: Amplitude of three phase Bridge current (A) at $0.5f_s$ vs unbalance mass (gm) at main supply frequency 12 Hz at Pos 7.

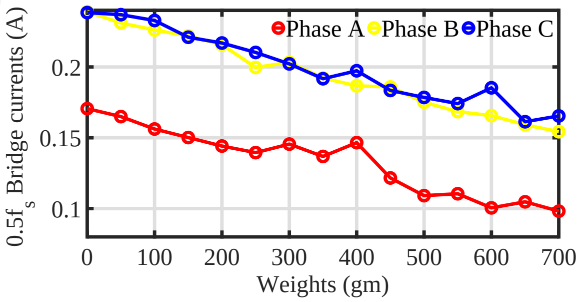

Figure 6.26: Amplitude of three phase Bridge current (A) at $0.5f_s$ vs unbalance mass (gm) at main supply frequency 13 Hz at Pos 7.

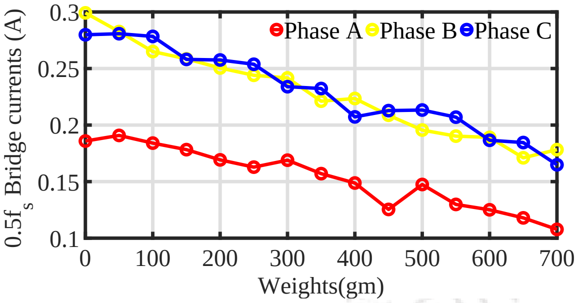

Figure 6.27: Amplitude of three phase Bridge current (A) at $0.5f_s$ vs unbalance mass (gm) at main supply frequency 14 Hz at Pos 7.

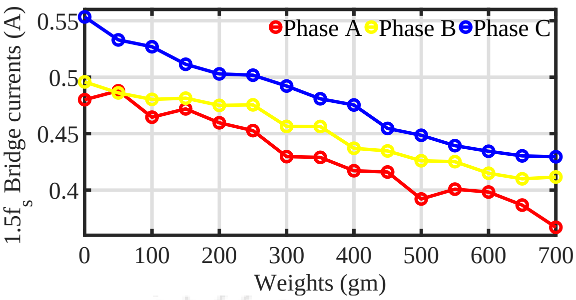

Figure 6.28: Amplitude of three phase Bridge current (A) at $1.5f_s$ vs unbalance mass (gm) at main supply frequency 10 Hz at Pos 7.

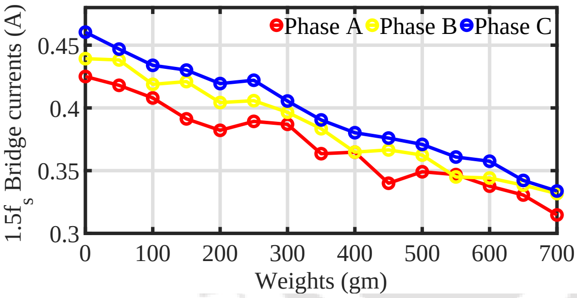

Figure 6.29: Amplitude of three phase Bridge current (A) at $1.5f_s$ vs unbalance mass (gm) at main supply frequency 11 Hz at Pos 7.

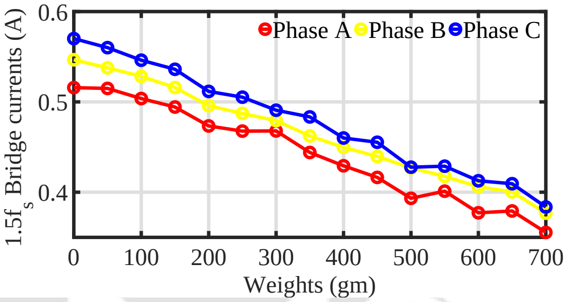

Figure 6.30: Amplitude of three phase Bridge current (A) at $1.5f_s$ vs unbalance mass (gm) at main supply frequency 12 Hz at Pos 7.

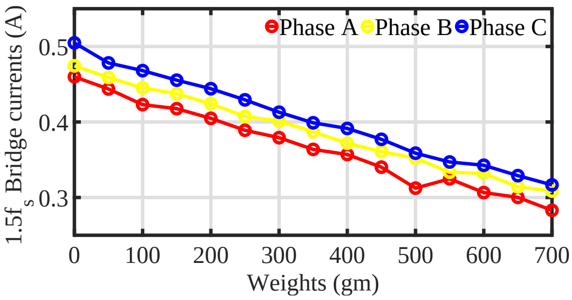

Figure 6.31: Amplitude of three phase Bridge current (A) at $1.5f_s$ vs unbalance mass (gm) at main supply frequency 13 Hz at Pos 7.

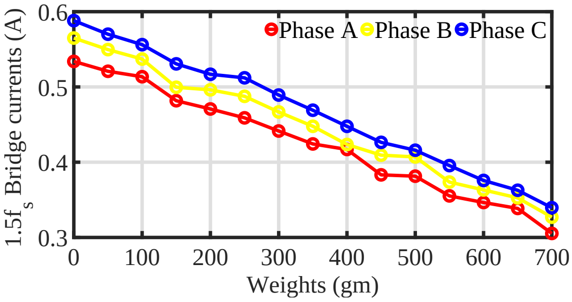

Figure 6.32: Amplitude of three phase Bridge current (A) at $1.5f_s$ vs unbalance mass (gm) at main supply frequency 14 Hz at Pos 7.

6.4.3 Results of 0.5f_s and 1.5f_s frequency components of three phase bridge currents for Position 8

The known mass unbalances are added to Pos 8 in the perforated disc and then the three phase bridge currents were measured. Figure 6.33 to Figure 6.37 show the peak amplitudes of 0.5f_s frequency components of the three phase bridge currents with respect to the known mass unbalances for main supply frequencies of 10 Hz, 11 Hz, 12 Hz, 13 Hz and 14 Hz respectively. Figure 6.38 to Figure 6.42 show the peak amplitudes of 1.5f_s frequency components for the three phase bridge currents with respect to the known mass unbalances for main supply frequencies of 10 Hz, 11 Hz, 12 Hz, 13 Hz and 14 Hz respectively. It has been observed that the peak amplitudes of 0.5f_s and 1.5f_s components of the bridge currents decrease with the increase in mass unbalances for all the supply frequencies for Pos 8.

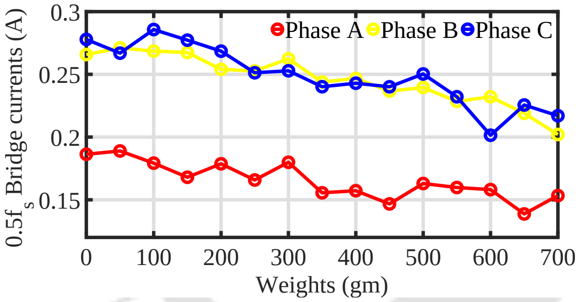

Figure 6.33: Amplitude of three phase Bridge current (A) at 0.5f_s vs unbalance mass (gm) at main supply frequency 10 Hz at Pos 8.

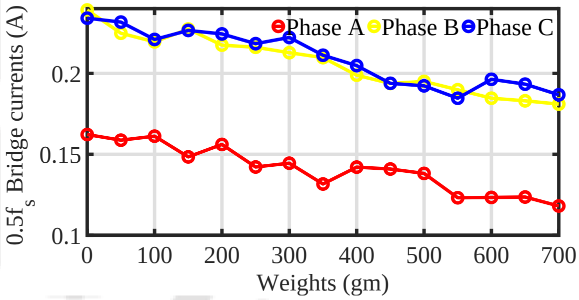

Figure 6.34: Amplitude of three phase Bridge current (A) at 0.5f_s vs unbalance mass (gm) at main supply frequency 11 Hz at Pos 8.

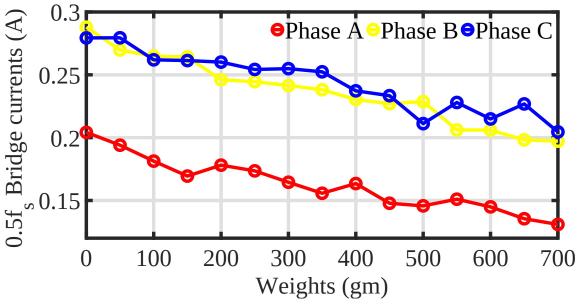

Figure 6.35: Amplitude of three phase Bridge current (A) at 0.5f_s vs unbalance mass (gm) at main supply frequency 12 Hz at Pos 8.

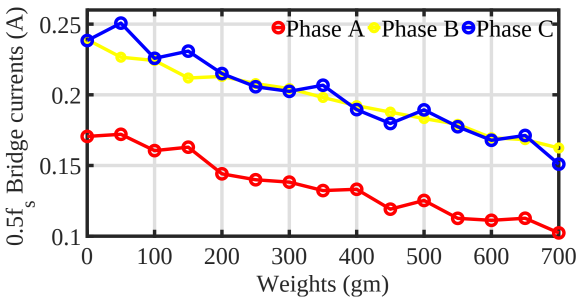

Figure 6.36: Amplitude of three phase Bridge current (A) at 0.5f_s vs unbalance mass (gm) at main supply frequency 13 Hz at Pos 8.

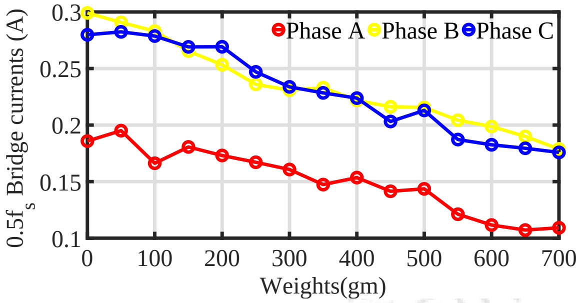

Figure 6.37: Amplitude of three phase Bridge current (A) at $0.5f_s$ vs unbalance mass (gm) at main supply frequency 14 Hz at Pos 8.

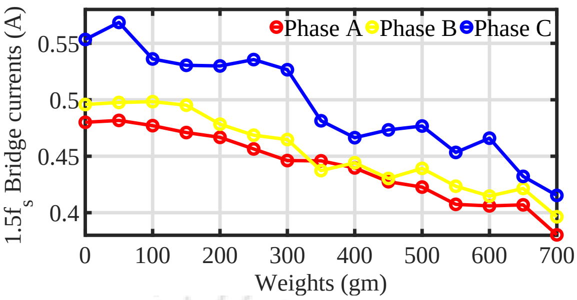

Figure 6.38: Amplitude of three phase Bridge current (A) at $1.5f_s$ vs unbalance mass (gm) at main supply frequency 10 Hz at Pos 8.

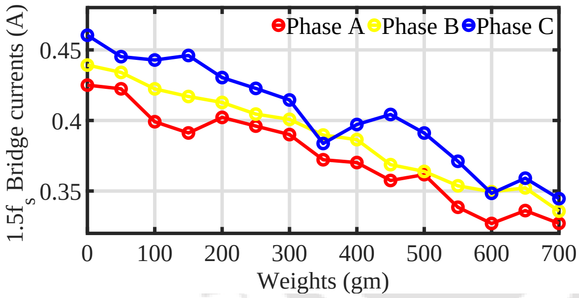

Figure 6.39: Amplitude of three phase Bridge current (A) at $1.5f_s$ vs unbalance mass (gm) at main supply frequency 11 Hz at Pos 8.

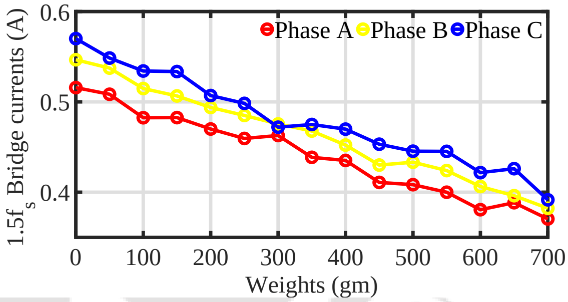

Figure 6.40: Amplitude of three phase Bridge current (A) at $1.5f_s$ vs unbalance mass (gm) at main supply frequency 12 Hz at Pos 8.

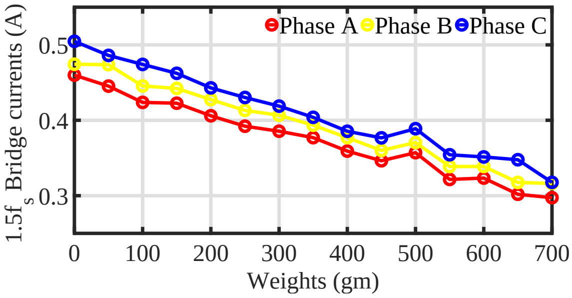

Figure 6.41: Amplitude of three phase Bridge current (A) at $1.5f_s$ vs unbalance mass (gm) at main supply frequency 13 Hz at Pos 8.

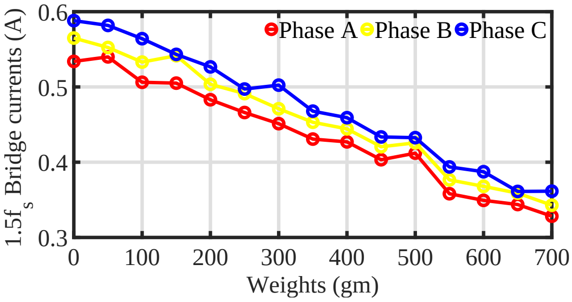

Figure 6.42: Amplitude of three phase Bridge current (A) at $1.5f_s$ vs unbalance mass (gm) at main supply frequency 14 Hz at Pos 8.

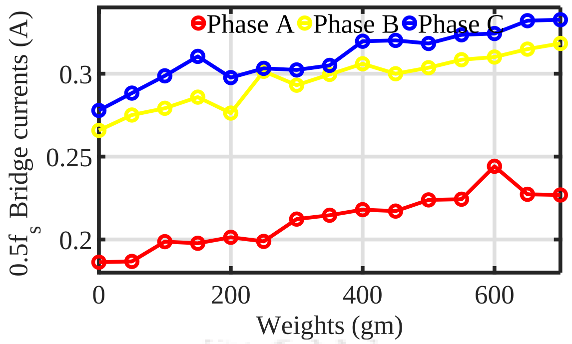

Figure 6.43: Amplitude of three phase Bridge current (A) at $0.5f_s$ vs unbalance mass (gm) at main supply frequency 10 Hz at Pos 14.

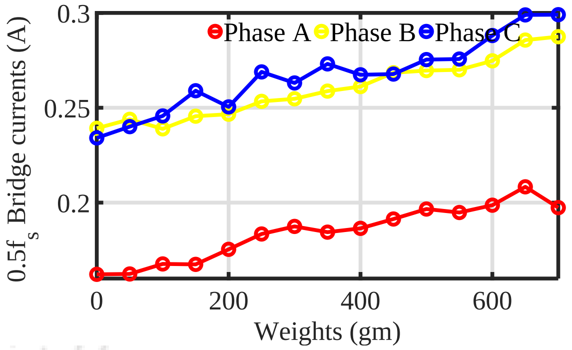

Figure 6.44: Amplitude of three phase Bridge current (A) at $0.5f_s$ vs unbalance mass (gm) at main supply frequency 11 Hz at Pos 14.

6.4.4 Results of $0.5f_s$ and $1.5f_s$ frequency components of three phase bridge currents for Position 14

The known mass unbalances are added to Pos 14 in the perforated disc and then the three phase bridge currents were measured. Figure 6.43 to Figure 6.47 show the peak amplitudes of $0.5f_s$ frequency components of the three phase bridge currents with respect to the known mass unbalances for main supply frequencies of 10 Hz, 11 Hz, 12 Hz, 13 Hz and 14 Hz respectively. Figure 6.48 to Figure 6.52 show the peak amplitudes of $1.5f_s$ frequency components for the three phase bridge currents with respect to the known mass unbalances for main supply frequencies of 10 Hz, 11 Hz, 12 Hz, 13 Hz and 14 Hz respectively. It has been observed that the peak amplitudes of $0.5f_s$ and $1.5f_s$ components of the bridge currents increase with the increase in mass unbalances for all the supply frequencies for Pos 14.

6.4.5 Results of $0.5f_s$ and $1.5f_s$ frequency components of three phase bridge currents for Position 15

The known mass unbalances are added to Pos 14 in the perforated disc and then the three phase bridge currents were measured. Figure 6.53 to Figure 6.57 show the peak amplitudes of $0.5f_s$ frequency components of the three phase bridge currents with respect to the known mass unbalances for main supply frequencies of 10 Hz, 11 Hz, 12 Hz, 13 Hz and 14 Hz respectively. Figure 6.58 to Figure 6.62 show the peak amplitudes of $1.5f_s$ frequency components for the three phase bridge currents with respect to the known mass unbalances for main supply frequencies of 10 Hz, 11 Hz, 12 Hz, 13 Hz and 14 Hz respectively. It has been observed that the peak amplitudes of $0.5f_s$ and $1.5f_s$ components

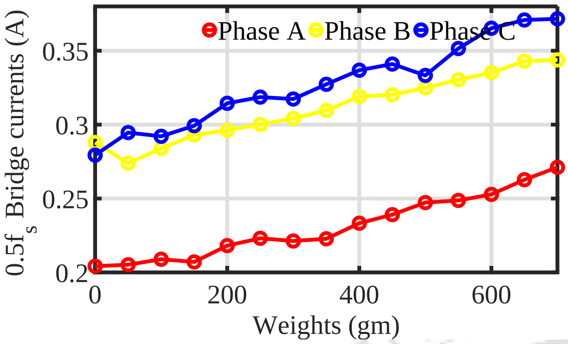

Figure 6.45: Amplitude of three phase Bridge current (A) at $0.5f_s$ vs unbalance mass (gm) at main supply frequency 12 Hz at Pos 14.

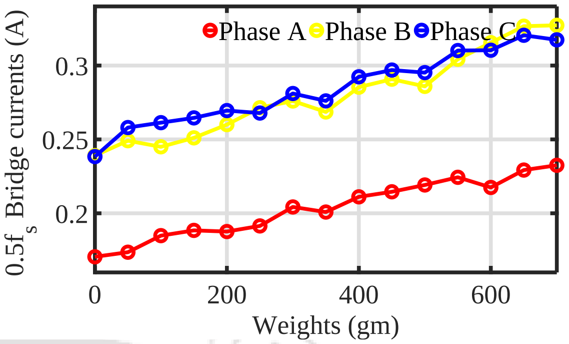

Figure 6.46: Amplitude of three phase Bridge current (A) at $0.5f_s$ vs unbalance mass (gm) at main supply frequency 13 Hz at Pos 14.

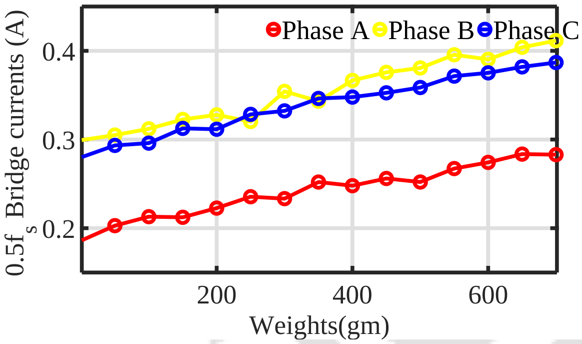

Figure 6.47: Amplitude of three phase Bridge current (A) at $0.5f_s$ vs unbalance mass (gm) at main supply frequency 14 Hz at Pos 14.

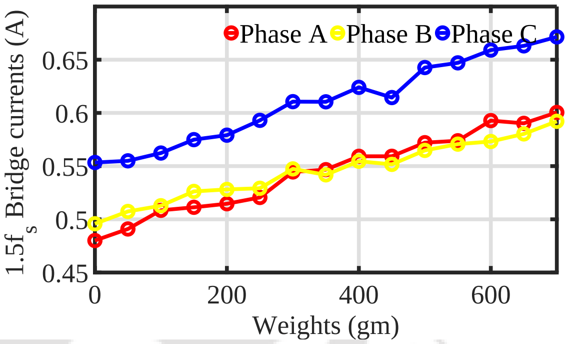

Figure 6.48: Amplitude of three phase Bridge current (A) at $1.5f_s$ vs unbalance mass (gm) at main supply frequency 10 Hz at Pos 14.

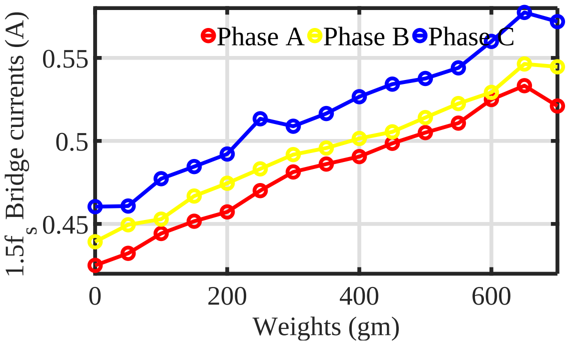

Figure 6.49: Amplitude of three phase Bridge current (A) at $1.5f_s$ vs unbalance mass (gm) at main supply frequency 11 Hz at Pos 14.

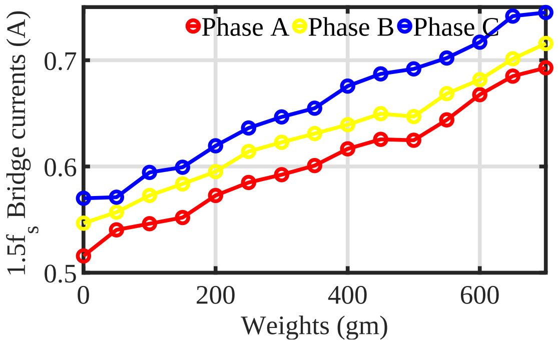

Figure 6.50: Amplitude of three phase Bridge current (A) at $1.5f_s$ vs unbalance mass (gm) at main supply frequency 12 Hz at Pos 14.

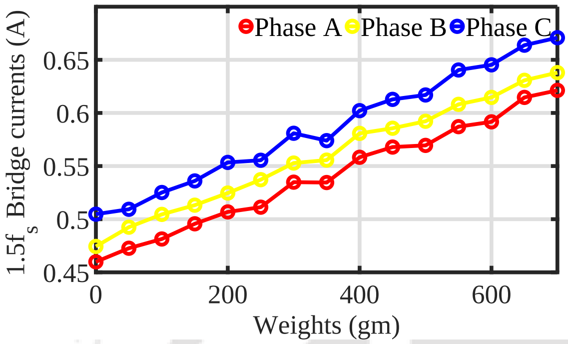

Figure 6.51: Amplitude of three phase Bridge current (A) at $1.5f_s$ vs unbalance mass (gm) at main supply frequency 13 Hz at Pos 14.

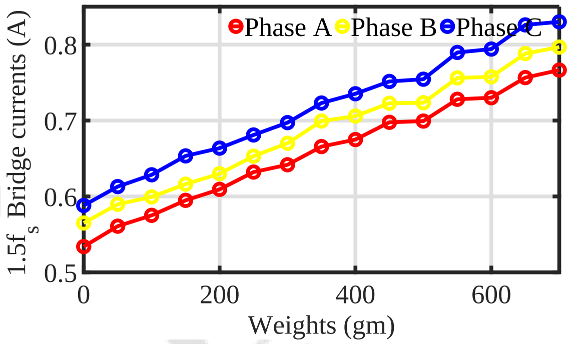

Figure 6.52: Amplitude of three phase Bridge current (A) at $1.5f_s$ vs unbalance mass (gm) at main supply frequency 14 Hz at Pos 14.

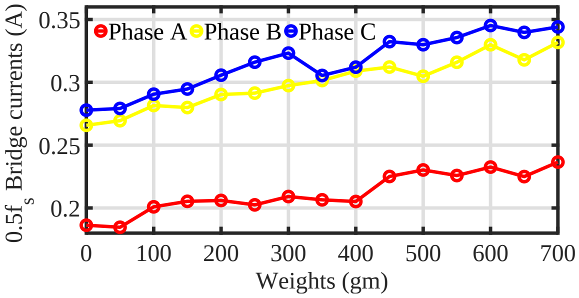

Figure 6.53: Amplitude of three phase Bridge current (A) at $0.5f_s$ vs unbalance mass (gm) at main supply frequency 10 Hz at Pos 15.

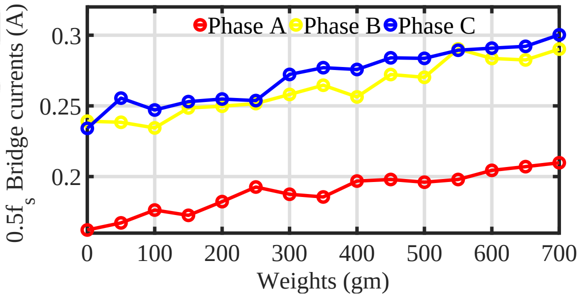

Figure 6.54: Amplitude of three phase Bridge current (A) at $0.5f_s$ vs unbalance mass (gm) at main supply frequency 11 Hz at Pos 15.

of the bridge currents increase with the increase in mass unbalances for all the supply frequencies for Pos 15.

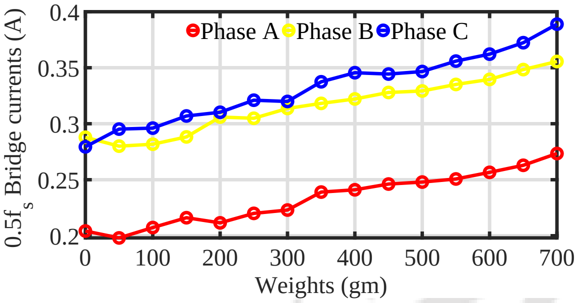

Figure 6.55: Amplitude of three phase Bridge current (A) at $0.5f_s$ vs unbalance mass (gm) at main supply frequency 12 Hz at Pos 15.

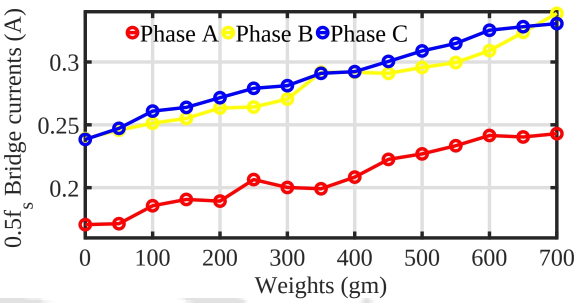

Figure 6.56: Amplitude of three phase Bridge current (A) at $0.5f_s$ vs unbalance mass (gm) at main supply frequency 13 Hz at Pos 15.

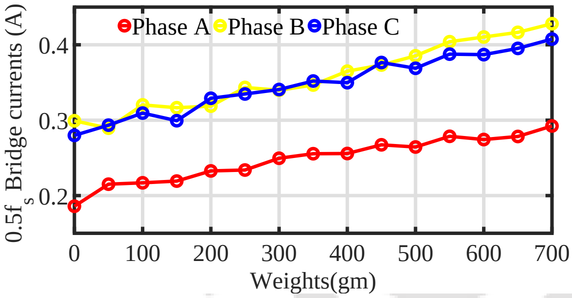

Figure 6.57: Amplitude of three phase Bridge current (A) at $0.5f_s$ vs unbalance mass (gm) at main supply frequency 14 Hz at Pos 15.

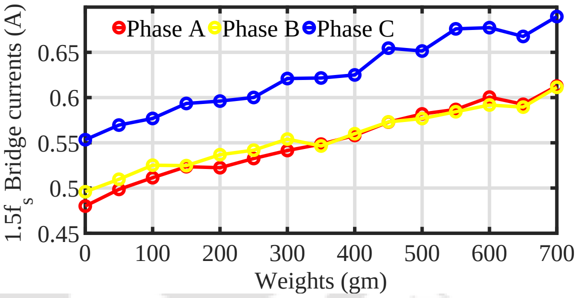

Figure 6.58: Amplitude of three phase Bridge current (A) at $1.5f_s$ vs unbalance mass (gm) at main supply frequency 10 Hz at Pos 15.

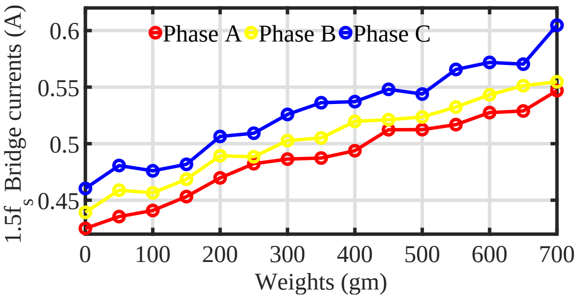

Figure 6.59: Amplitude of three phase Bridge current (A) at $1.5f_s$ vs unbalance mass (gm) at main supply frequency 11 Hz at Pos 15.

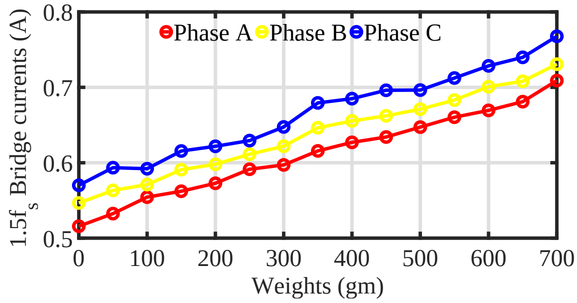

Figure 6.60: Amplitude of three phase Bridge current (A) at $1.5f_s$ vs unbalance mass (gm) at main supply frequency 12 Hz at Pos 15.

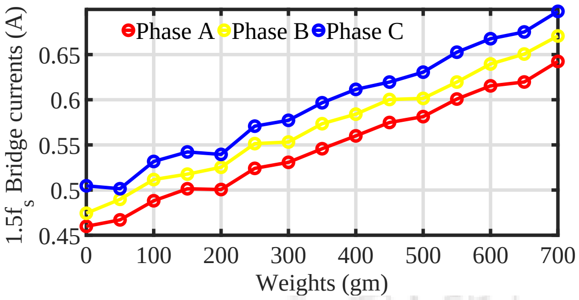

Figure 6.61: Amplitude of three phase Bridge current (A) at $1.5f_s$ vs unbalance mass (gm) at main supply frequency 13 Hz at Pos 15.

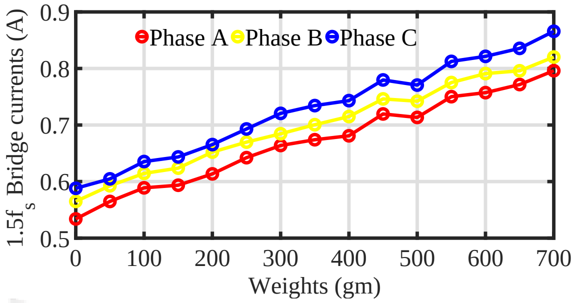

Figure 6.62: Amplitude of three phase Bridge current (A) at $1.5f_s$ vs unbalance mass (gm) at main supply frequency 14 Hz at Pos 15.

6.4.6 Results of $0.5f_s$ and $1.5f_s$ frequency components of three phase bridge currents for Position 16

The known mass unbalances are added to Pos 14 in the perforated disc and then the three phase bridge currents were measured. Figure 6.63 to figure 6.67 show the peak amplitudes of $0.5f_s$ frequency components of the three phase bridge currents with respect to the known mass unbalances for main supply frequencies of 10 Hz, 11 Hz, 12 Hz, 13 Hz and 14 Hz respectively. Figure 6.68 to Figure 6.72 show the peak amplitudes of $1.5f_s$ frequency components for the three phase bridge currents with respect to the known mass unbalances for main supply frequencies of 10 Hz, 11 Hz, 12 Hz, 13 Hz and 14 Hz respectively. It has been observed that the peak amplitudes of $0.5f_s$ and $1.5f_s$ components of the bridge currents increase with the increase in mass unbalances for all the supply frequencies for Pos 16.

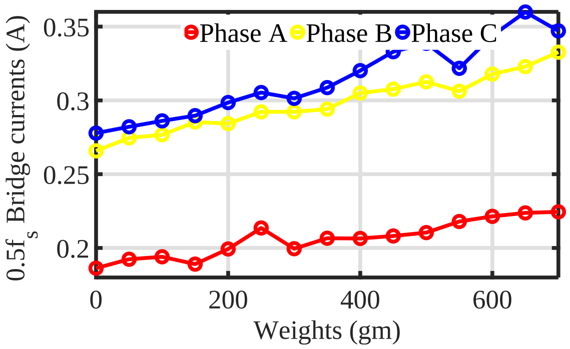

Figure 6.63: Amplitude of three phase Bridge current (A) at $0.5f_s$ vs unbalance mass (gm) at main supply frequency 10 Hz at Pos 16.

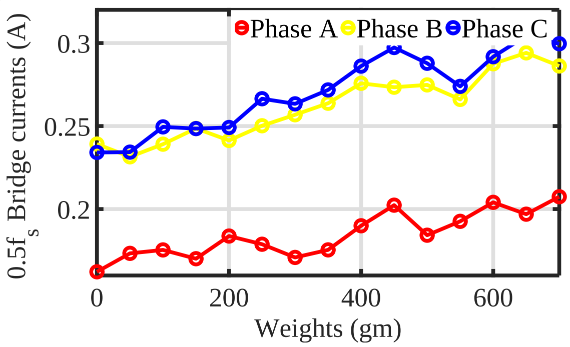

Figure 6.64: Amplitude of three phase Bridge current (A) at $0.5f_s$ vs unbalance mass (gm) at main supply frequency 11 Hz at Pos 16.

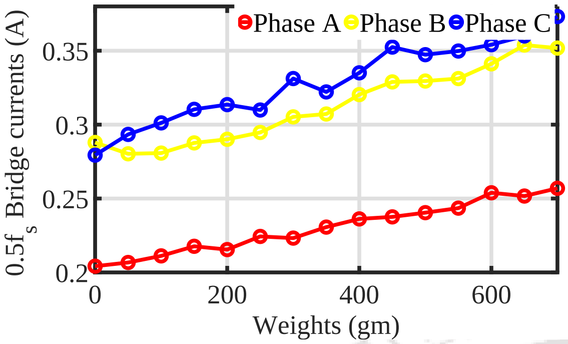

Figure 6.65: Amplitude of three phase Bridge current (A) at $0.5f_s$ vs unbalance mass (gm) at main supply frequency 12 Hz at Pos 16.

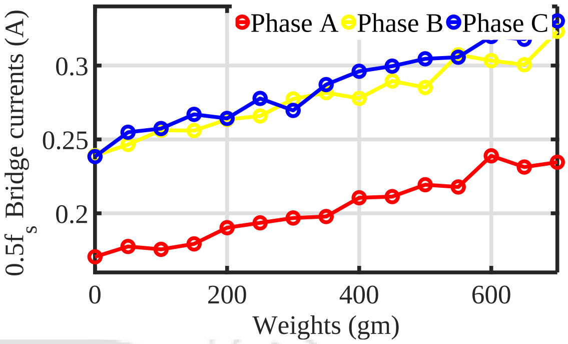

Figure 6.66: Amplitude of three phase Bridge current (A) at $0.5f_s$ vs unbalance mass (gm) at main supply frequency 13 Hz at Pos 16.

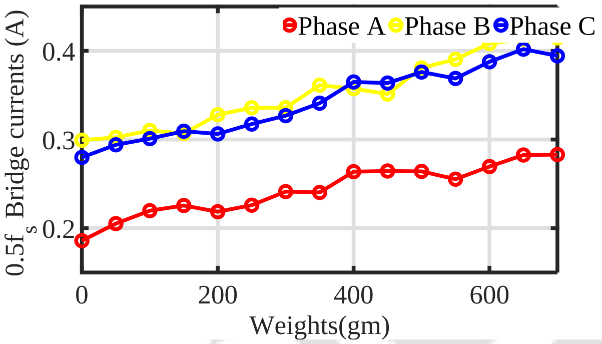

Figure 6.67: Amplitude of three phase Bridge current (A) at $0.5f_s$ vs unbalance mass (gm) at main supply frequency 14 Hz at Pos 16.

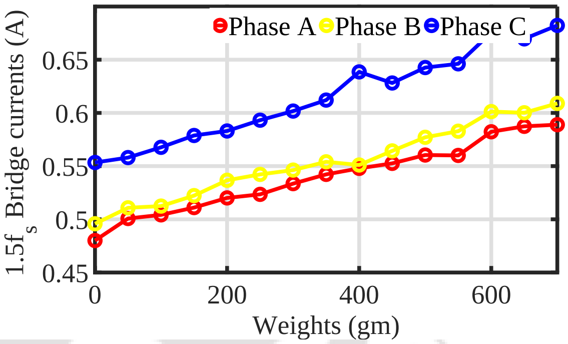

Figure 6.68: Amplitude of three phase Bridge current (A) at $1.5f_s$ vs unbalance mass (gm) at main supply frequency 10 Hz at Pos 16.

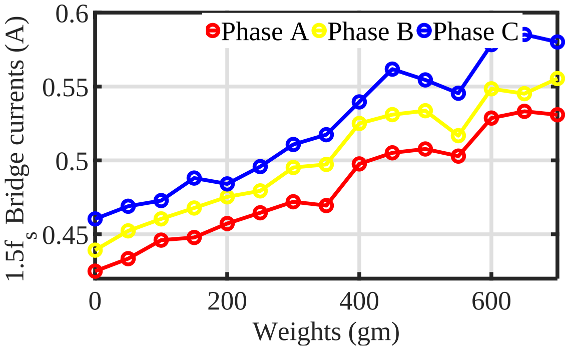

Figure 6.69: Amplitude of three phase Bridge current (A) at $1.5f_s$ vs unbalance mass (gm) at main supply frequency 11 Hz at Pos 16.

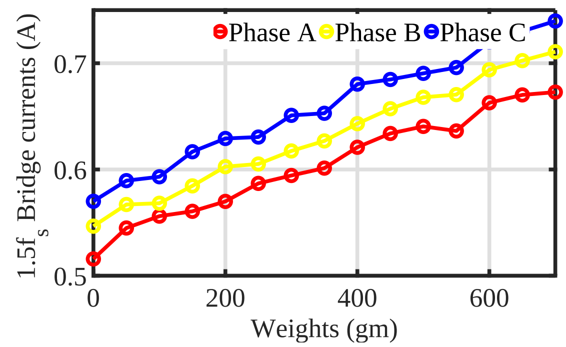

Figure 6.70: Amplitude of three phase Bridge current (A) at $1.5f_s$ vs unbalance mass (gm) at main supply frequency 12 Hz at Pos 16.

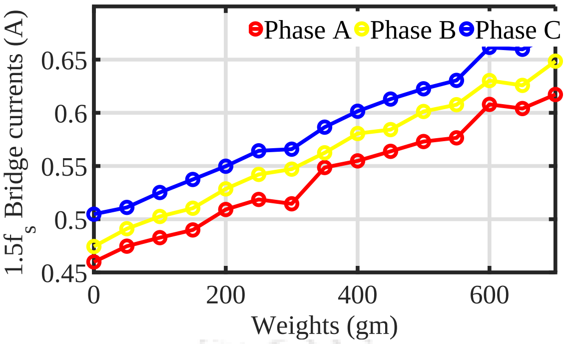

Figure 6.71: Amplitude of three phase Bridge current (A) at $1.5f_s$ vs unbalance mass (gm) at main supply frequency 13 Hz at Pos 16.

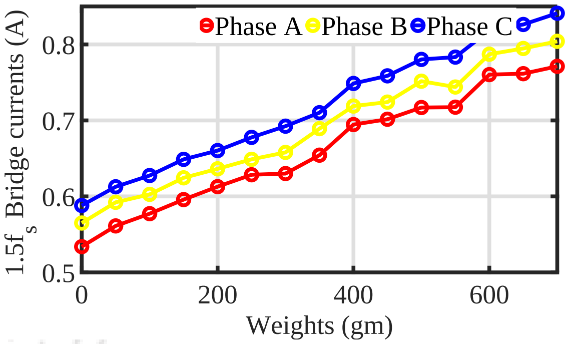

Figure 6.72: Amplitude of three phase Bridge current (A) at $1.5f_s$ vs unbalance mass (gm) at main supply frequency 14 Hz at Pos 16.

6.5 Results and discussions of experimental analysis

Figure 6.73 shows the representation of the variation in the amplitude of the $0.5f_s$ of frequency component of three phase bridge currents respect to the known masses. It has been seen that the amplitude of three phase bridge currents at $0.5f_s$ were decreasing with the increasing of known masses in the system at Position 6, 7 and 8 respectively. It has also been noticed that the amplitude of three phase bridge currents at $0.5f_s$ were increasing with the increasing of known masses in the system at which Position 1, 2, 13, 14, 15 and 16 respectively. Red colour indicates that the amplitudes of the frequency components of the bridge currents are increasing and the green colour indicates that the the amplitudes of the frequency components of the bridge currents are decreasing.

Figure 6.74 shows the representation of variation in the the amplitudes of the frequency components of the bridge currents at $1.5f_s$ of the supply frequency when the weights are added too the disc. It has been seen that for the amplitudes of the $1.5f_s$ frequency components of the bridge currents are decreasing with the increasing of known unbalance masses in the system at Position 6, 7, 8 and 9 respectively. It has also noticed that the the amplitudes of the frequency components of the bridge currents at $1.5f_s$ are increasing with the increasing of known unbalance masses in the system at Position 1, 2, 13, 14, 15 and 16 respectively. It has been concluded that the position at which the peak amplitudes of the frequency components of the bridge currents are decreasing which means the unbalance pull by the known mass is acting against the actual unbalance pull present in the system. It has also been concluded that the position at which the peak amplitudes of the frequency components

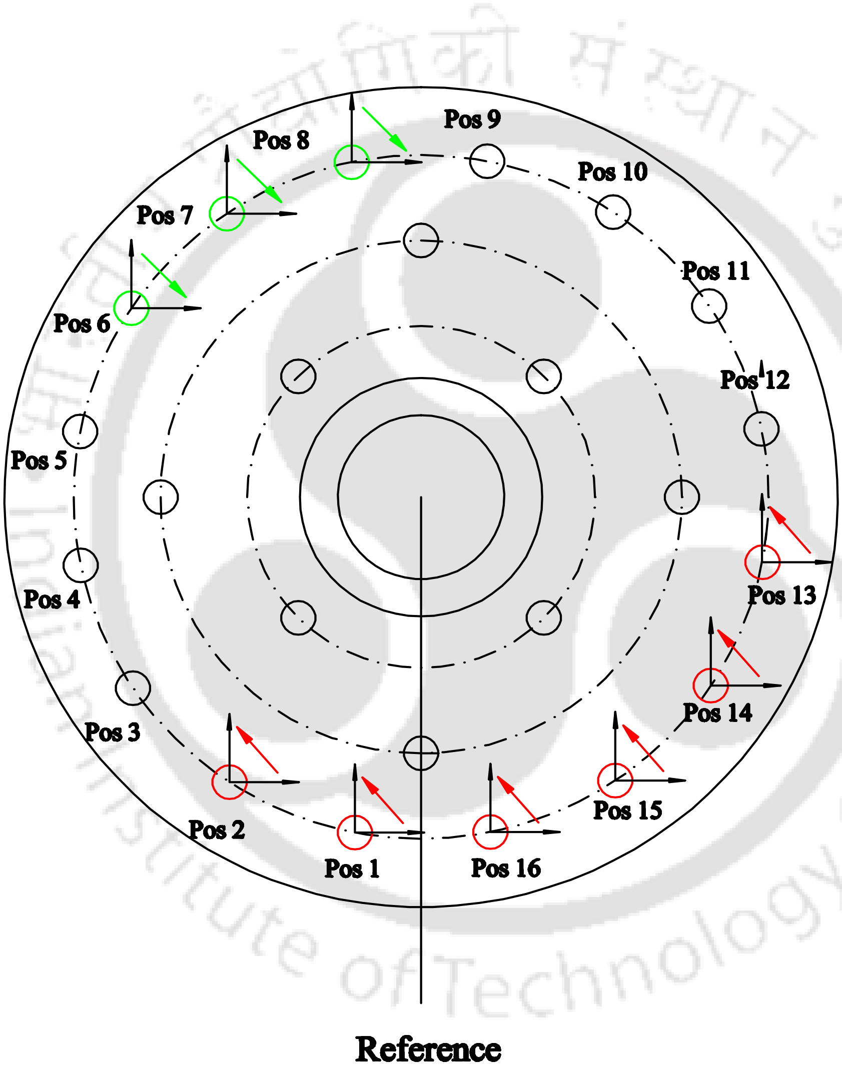

Figure 6.73: A representation of variation in the the amplitudes of the frequency components of the bridge currents at $0.5f_s$ of the supply frequency.

of the bridge currents are increasing which means the unbalance pull by the known mass is acting along the actual unbalance pull present in the system.

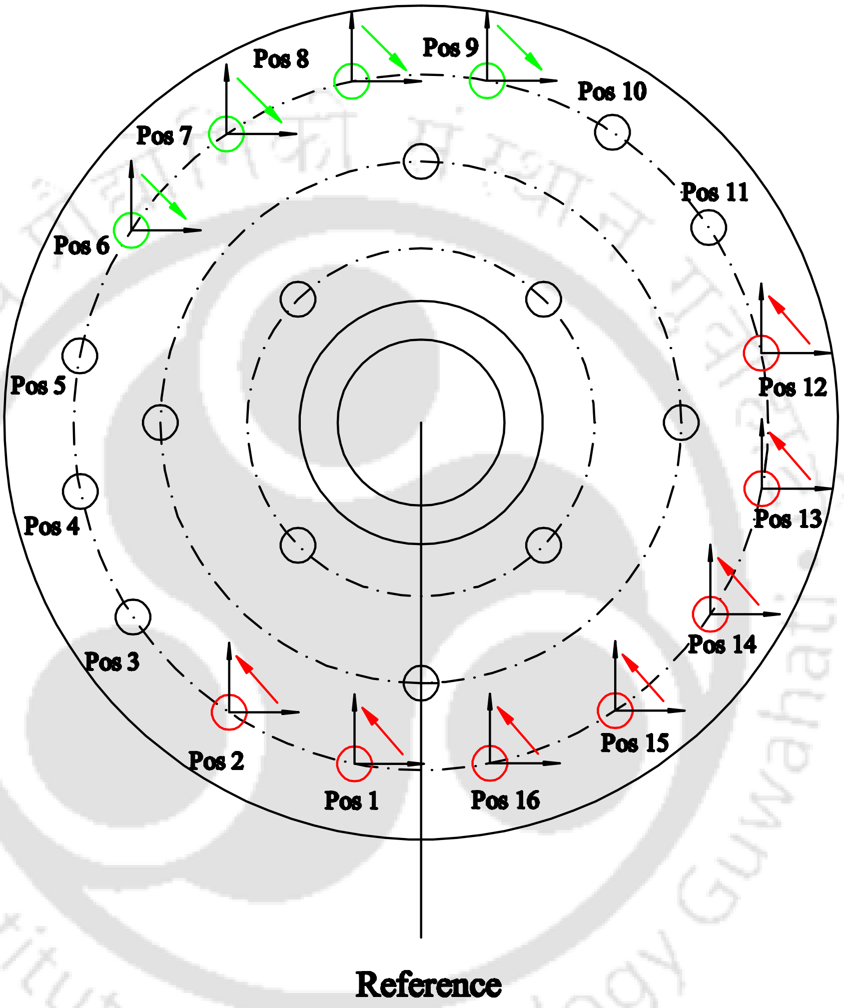

Figure 6.74: A representation of variation in the the amplitudes of the frequency components of the bridge currents at $1.5f_s$ of the supply frequency.

6.6 Numerical simulation of a BCW induction machine with varied static eccentricity

It has been established in Chapter 3 that the eccentricity of the rotor has profound impact in the bridge currents of a BCW induction machine. Chapter 5 presents the bridge currents and the corresponding transverse forces on the rotor obtained from experiments. It has been verified that the eccentricity of the rotor has effect on the bridge currents. It has also been verified that dynamic eccentricity of a rotor produces $f_s \pm f_r$ frequency components of the bridge currents in a BCW induction machine. Here, f_s is the frequency of the main supply voltage and f_r is the rotor frequency and it's a function of slip. For a no-load or or for a very very small load (very small slip value) these two frequency components will be simply $\frac{1}{2}f_s$ and $\frac{3}{2}f_s$. The previous sections discuss the effect dynamic eccentricity on $\frac{1}{2}f_s$ and $\frac{3}{2}f_s$ frequency components of the bridge currents. Some conclusions have been drawn.

In this section a numerical analysis have been carried out to develop a relationship between the static eccentricity and bridge currents. For this purpose a 2D finite element model of a 3.7 kW four pole induction motor with cage rotor has been developed in COMSOL MULTIPHYSICS®. The stator has 36 slots and 26 rotor bars. Triangular elements have been used for the discretization of the geometry of the machine. 65136 triangular elements, 10422 edge elements and 586 vertex elements are used in the finite element mesh. Figure 6.75 shows a part of the finite element mesh of the model. Table 6.1 presents the parameters of the machine.

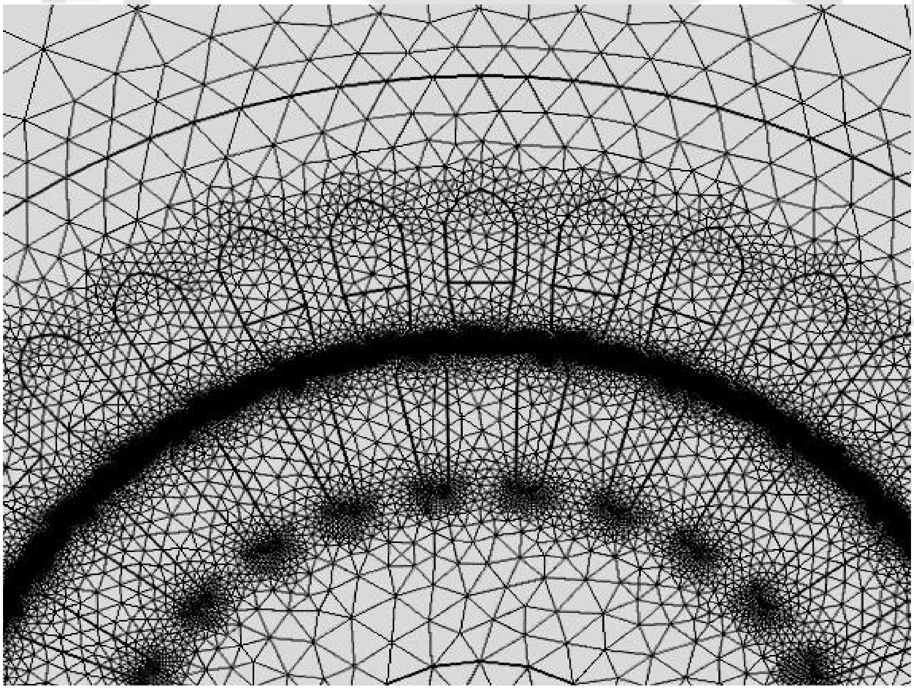

Figure 6.75: A part of the finite element mesh of the model

6.6.1 Incorporation of known static eccentricity

Known static eccentricities of the rotor are incorporated in the machine by shifting the rotor center. The rotor centre is shifted as the following to incorporate a known eccentricity in the machine and the

Table 6.1: Parameters of the induction machine

Parameters	Value
No. of poles	4
No. of stator slots	36
No. of rotor bars	26
Outer dia. of stator	160 mm
Outer dia. of rotor	103 mm
Air gap length	1 mm
Axial length of the motor	135 mm
Resistance per phase	6.8 Ω
End winding inductance	3.94 e-4 A/m
Resistance of each rotor bar	1e-05 Ω
Rotor end ring resistance	2.49e-06 Ω
Rotor end ring inductance	1.54e-08 A/m
Supply voltage	270V, 50 Hz
Slip	0.05

rotor is rotated about this point.

$$\left.\begin{aligned} \epsilon_x &= \epsilon_0 \cos\left(\theta_\epsilon\right) \\ \epsilon_y &= \epsilon_0 \sin\left(\theta_\epsilon\right) \end{aligned}\right\} \tag{6.1}$$

where ϵ_x and ϵ_y are the $x-$ and $y-$ coordinates of the centre of the displaced rotor, ϵ_0 is the eccentricity of the rotor along radial direction, $\epsilon_0 = \sqrt{(\epsilon_x^2 + \epsilon_y^2)}$, θ_ϵ is the angle subtended by the line joining the centre of the displaced centre and the centre of the stator with the $x-$ axis. The angle θ_ϵ is varied from 0^0 to 180^0 in steps of 5^0. Figure 6.76 shows such locations i, j, and k where the angles are θ_{ϵ_i}, θ_{ϵ_j}, and θ_{ϵ_k} respectively. Three level of eccentricities i.e. $\epsilon_1 = \frac{1}{16}\delta_a$, $\epsilon_2 = \frac{1}{8}\delta_a$ and $\epsilon_3 = \frac{1}{4}\delta_a$. Here δ_a is the thickness of the airgap.

6.6.2 Bridge currents for known static eccentricity

In Chapter 3 it has been established that the frequency component of the bridge currents induced due to the static eccentricity is f_s, where f_s is the frequency of the supply voltage. The machine with the BCW having the parameter presented in Table 6.1 is solved for the three level of known static eccentricities ($\epsilon_1, \epsilon_2, \epsilon_3$) for the main currents and bridge currents. These static eccentricities are applied from 0^0 to 180^0 in steps of 5^0 in clockwise direction. The 50 Hz frequency components of the bridge currents are extracted. Figure 6.77 and 6.78 and 6.79 show the 50 Hz component of the

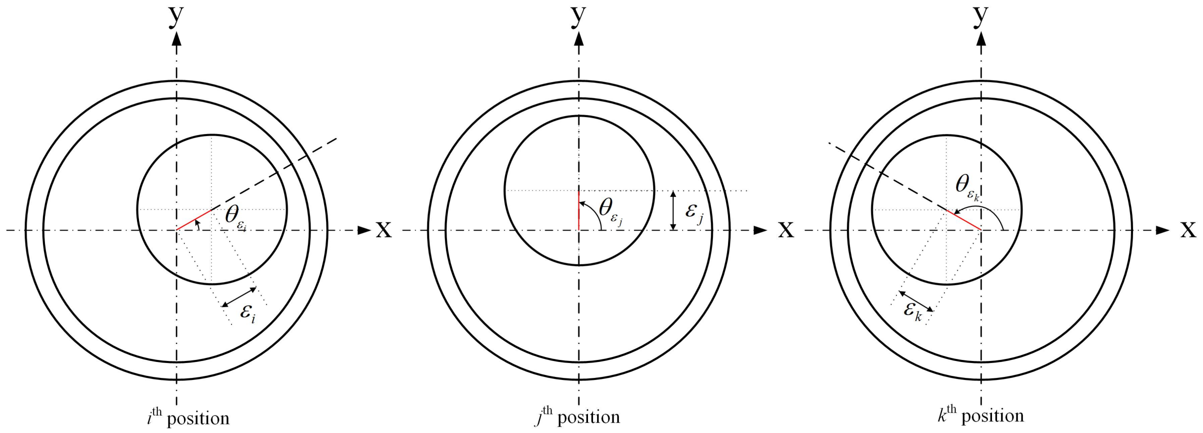

Figure 6.76: Rotor locations to show the static eccentricity at *i*, *j* and *k* positions

bridge currents for ϵ_1, ϵ_2 and ϵ_3 respectively. The angle θ_ϵ is considered from 0^0 to 180^0 in steps of 5^0 and these static static eccentricity is considered. It has been clear that a relationship exist between the static eccentricity of the rotor and the 50 Hz component of the bridge currents of a BCW induction motor. This has also been established already in Chapter 3 and Chapter 5. The bridge currents in Figure 6.80 are fitted with sinusoidal functions and they are

$$\left.\begin{aligned} &\text{For} \quad \text{Phase A,} \quad I_{bA} = I_{b0A} + I_{b1A}\sin\left(2\theta_\epsilon + \phi_\epsilon\right) \\ &\text{For} \quad \text{Phase B,} \quad I_{bB} = I_{b0B} + I_{b1B}\sin\left(2\theta_\epsilon - 2\frac{\pi}{3} + \phi_\epsilon\right) \\ &\text{For} \quad \text{Phase C,} \quad I_{bC} = I_{b0C} + I_{b1C}\sin\left(2\theta_\epsilon - 4\frac{\pi}{3} + \phi_\epsilon\right) \end{aligned}\right\} \tag{6.2}$$

where I_{bA}, I_{bB} and I_{bC} are bridge currents for Phase A, Phase B and Phase C respectively. I_{b0A}, I_{b0B}, I_{b0C}, I_{b1A}, I_{b1B}, I_{b1C} and ϕ_ϵ are constants. These constants can be found from the bridge currents obtained from numerical analysis as shown in Figure 6.78. For a static eccentricity value of ϵ_1, once these constants are obtained then I_{bA}, I_{bB} and I_{bC} are function of θ_ϵ only. The value of these constants obtained from Figure 6.78 for a static eccentricity value of $\epsilon_1 = \frac{1}{8}\delta_a$, where δ_a is the thickness of the airgap are

$$\left.\begin{aligned} I_{b0A} &= 0.27282046500 \\ I_{b0B} &= 0.27248794050 \\ I_{b0C} &= 0.27294685499 \\ I_{b1A} &= 0.01319373600 \\ I_{b1B} &= 0.01425781050 \\ I_{b1C} &= 0.01318896400 \\ \phi_{\epsilon} &= \frac{\pi}{10} \end{aligned}\right\}$$

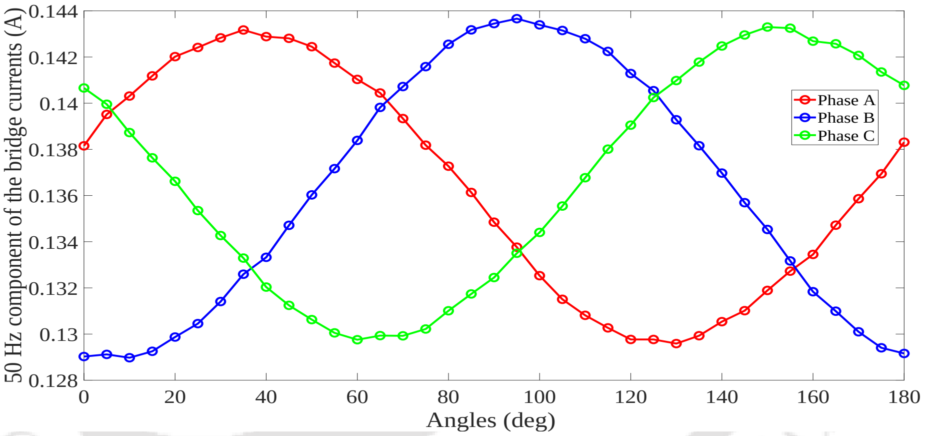

Figure 6.77: Bridge currents for static eccentricity of $\epsilon_1 = \frac{1}{16}\delta_a$ at different angles

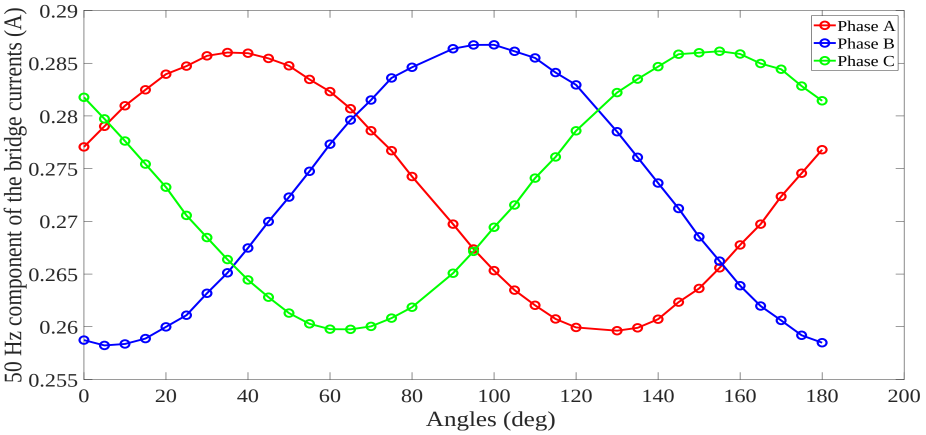

Figure 6.78: Bridge currents for static eccentricity of $\epsilon_2 = \frac{1}{8}\delta_a$ at different angles

Another numerical experiment have been carried out to know the effect of material non-linearity on the f_s component of the bridge current in a BCW induction induced due to the static eccentricity.

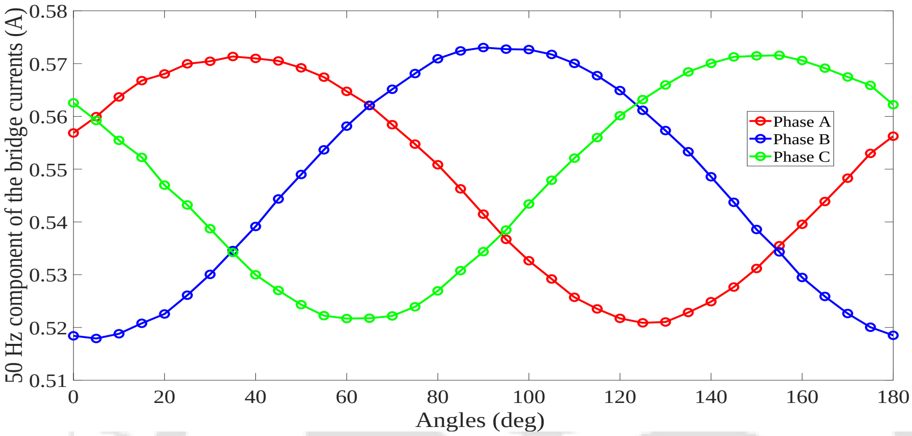

Figure 6.79: Bridge currents for static eccentricity of $\epsilon_3 = \frac{1}{4}\delta_a$ at different angles

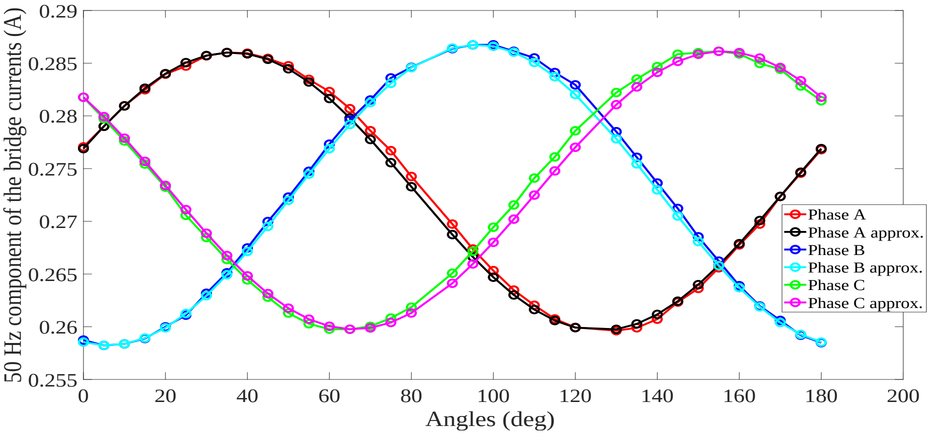

Figure 6.80: Bridge currents with fitted functions for static eccentricity $\epsilon_2 = \frac{1}{8}\delta_a$ at different angles

The rotor is shifted by known amount of static eccentricity along $x-$axis keeping the rotor in position $\theta_\epsilon = 0^0$. The machine with the BCW having the parameter presented in Table 6.1 is solved for different level of known static eccentricities. Figure 6.81 shows the f_s component of the bridge current induced due to these static eccentricities. It has been observed that the material non-linearity has no effect on the bridge currents.

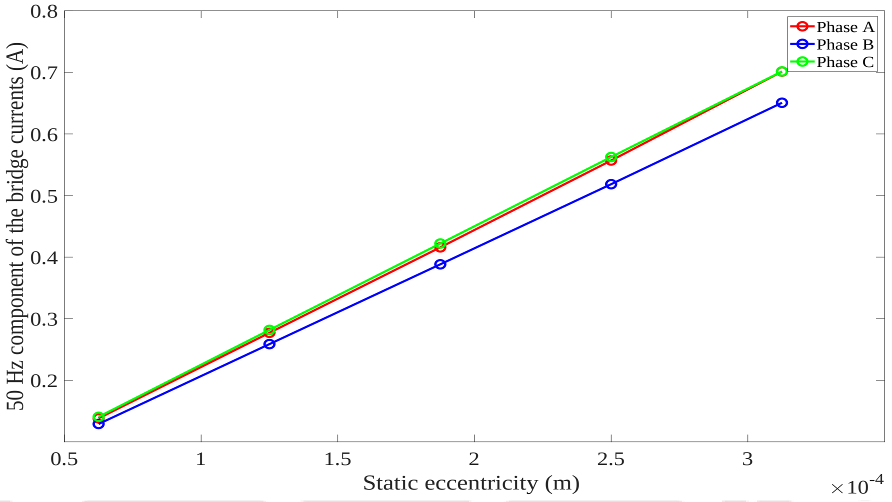

Figure 6.81: Bridge currents for different static eccentricity at a particular angles

6.7 Conclusions

The following conclusions have been drawn from the present chapter:

- A set of experiments have been conducted to develop a relationship between known unbalance mass and the measured bridge currents. The peak amplitudes of the frequency components of three phase bridge currents for $0.5f_s$ and $1.5f_s$ were measured and plotted against the known unbalance masses.
- The known masses were added in the holes (Positions) of the perforated disc to develop the relationship between bridge currents and the known masses.
- Initially, the bridge currents were measured for **Rotor I**. The experiments were carried out at 10Hz, 15Hz, 20Hz, 25Hz, 30Hz and 50Hz for **Rotor I**. However, the results have been presented only for 30hz and 50Hz of main supply frequencies in this chapter.The known masses were in the range of 0 gm to 1000 gm with an increment of 50 gm for **Rotor I**.

- It has been observed that there were no changes of the amplitudes in the three phase bridge currents with an increase in unbalance masses. Obviously, for all supply frequencies there were no noticeable changes in the amplitudes of the three phase bridge currents for $0.5f_s$ and $1.5f_s$.

- This may happen due to the high stiffness of the **Rotor I**. So, it has been decided to replace **Rotor I** with a flexible shaft. The **Rotor I** has been replaced by **Rotor II**.

- It has been noticed that **Rotor II** is too flexible and the rotor touched the stator of the machine. It was difficult to rotate **Rotor II** even at free run. In that case, there were no possibility of conducting the experiments. It has been decided to replace **Rotor II**. The **Rotor II** has been replaced by **Rotor III**.

- The **Rotor III** is flexible in nature, so that the experiments were conducted at lower speeds in order to prevent the rotor and stator contact. The experiments were carried out at 8Hz, 9Hz, 10Hz,11Hz, 12Hz, 13Hz and 14Hz. The known masses were in range of 0 gm to 700 gm with an increment of 50 gm.

- It has been observed that there were changes of the amplitudes of the three phase bridge currents bridge currents for $0.5f_s$. The bridge currents were decreasing with an increase in known unbalance masses in the system for the Position 6, 7 and 8.

- It has been noticed that there were changes of the amplitudes of the three phase bridge currents bridge currents for $0.5f_s$. The bridge currents were increasing with an increase in known unbalance masses in the system for the Position 1, 2, 13, 14, 15 and 16.

- It has also been noticed that there were no significant changes of the amplitudes of the three phase bridge currents bridge currents for $0.5f_s$ for Positions 3, 4, 5, 9, 10, 11 and 12.

- It has been observed that there were changes of the amplitudes of the three phase bridge currents bridge currents for $1.5f_s$. The bridge currents were decreasing with an increase in known unbalance masses in the system for Positions 6, 7, 8 and 9.

- It has been noticed that there were changes of the amplitudes of the three phase bridge currents bridge currents for $1.5f_s$. The bridge currents were increasing with an increase in known unbalance masses in the system for Positions 1, 2, 13, 14, 15 and 16.

- It has also been noticed that there were no significant changes of the amplitudes of the three phase bridge currents bridge currents for $1.5f_s$ for Positions 3, 4, 5, 9, 10, 11 and 12.

- It has been concluded that the position at which the peak amplitudes of the frequency components of the bridge currents are decreasing which means the unbalance pull by the known mass is acting against the actual unbalance pull present in the system. It has also been concluded that the position at which the peak amplitudes of the frequency components of the bridge currents are increasing which means the unbalance pull by the known mass is acting along the actual unbalance pull present in the system.

- A relationship between the static eccentricity and bridge currents is developed by conducting a series of numerical simulations.

- Three bridge currents are calculated for static eccentricity levels from 6.25% to 31.25% of the airgap length at a particular location of the rotor. Bridge currents vary linearly with the static eccentricity at least up to 31.25% of the airgap length.

7

Development of Controller for Active Vibration Control

Contents

7.1 Introduction

The development of the experimental setup has been illustrated in Chapter 5. Chapter 5 explains about the incorporation of the bridge configured winding in a 4-pole, three phase, 37 kW induction machine. The three phase bridge currents and rotor displacements have been measured for the main bridge connection. The analysis of bridge currents and rotor displacements have been presented in Section 5.7 of Chapter 5. The important feature of BCW is that it requires a relatively low current and low voltage supply for the lateral force production. BCW provides three phase levitation supply which have been isolated from the three main power supplies. A controller has been developed to incorporate the three phase external voltage supply at the bridge points. The present chapter illustrates the development of the controller which have been utilized for the active vibration control in a bridge configured based induction machine. The development of the experimental setup has been explained in Chapter 5. This controller system has three bridge points which have maintained at different ground level from each other. Experiments have been carried out at 20Hz, 25Hz and 30Hz of main supply frequencies. Bridge currents and rotor displacements have been measured when the controller bridges are being short circuited. The rotor displacements have been measured with the various combinations such as Phase A alone, Phase B alone, Phase C alone, Phase A and Phase B together, Phase B and Phase C together and Phase A and Phase C together. The rotor responses are measured at location near the drive which is marked as 6 in Figure 5.7. This location is referred here as Location 2.

7.2 Description of the controller

The controller has different components mainly isolation amplifier, Copley controller, isolation transformer and a rectifier with filter. Table 7.1 show the name of the devices used in the development of controller. The make and model of the devices are also included in the table. Figure 7.1 shows the isolation amplifier along with servo amplifier. Figure 7.2 and Figure 7.3 show the isolation transformer, rectifier with filter respectively. Figure 7.4 and Figure 7.5 show the voltage transducer and current transducer respectively. Figure 7.6 shows the flow diagram of the assembly of devices for the controller. Figure 7.7 shows the controller set up.

Three isolation amplifiers have been used to break the loops between common ground level of

Table 7.1: Devices used in controller.

Sl No	Name of the device	Make of the device	Model
1	Isolation Amplifier	Analog Devices	AD202JN
2	Servo Amplifier	Copley Controller	5221 CE
3	Isolation Transformer	RKD	RKD 100/2x24
4	Current Transducer	LEM Transducer	LTS 15-NP
5	Voltage Transducer	LEM Transducer	LV 25-P

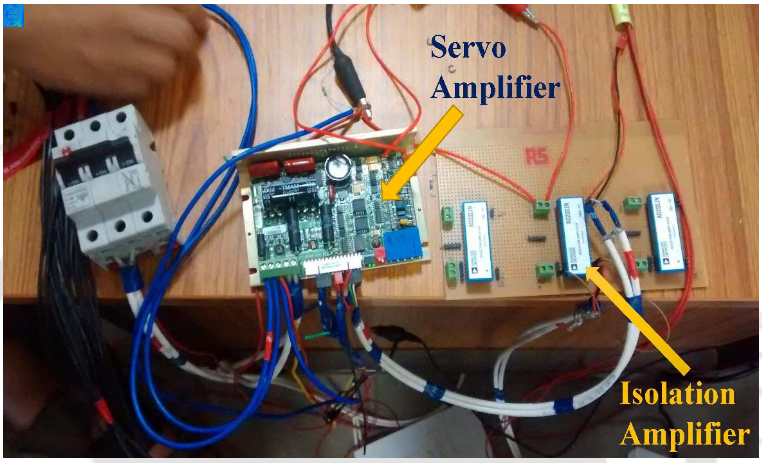

Figure 7.1: A isolation amplifier with servo amplifier.

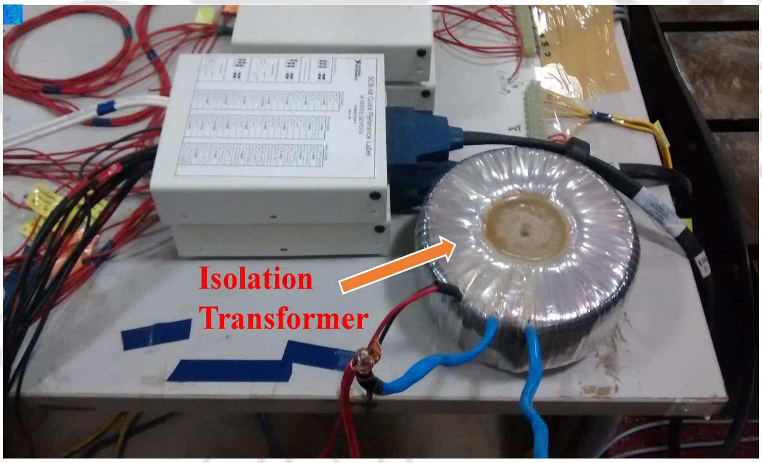

Figure 7.2: A toroidal isolation transformer.

reference signal and the controller for safety purpose. A 15 V_{dc} battery power source has been used as a power supply for the isolation amplifier. Three DC servo amplifiers have been used to supply the required controlled voltage in three bridges as per the reference signal provided by the DAQ system. The controller bridge switches have been shown in Figure 7.6. Three isolation transformers have been used to step down the 220 V_{ac} to 24 V_{ac} supply. A rectifier filter circuit has been used to convert 24 V_{ac} signal to a 24 V_{dc} signal and this 24 V_{dc} supply has been used as a power source for the servo amplifiers.

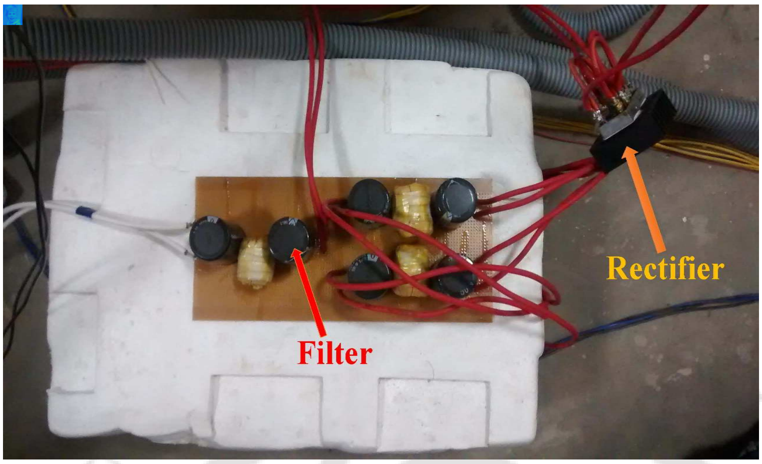

Figure 7.3: A rectifier with filter.

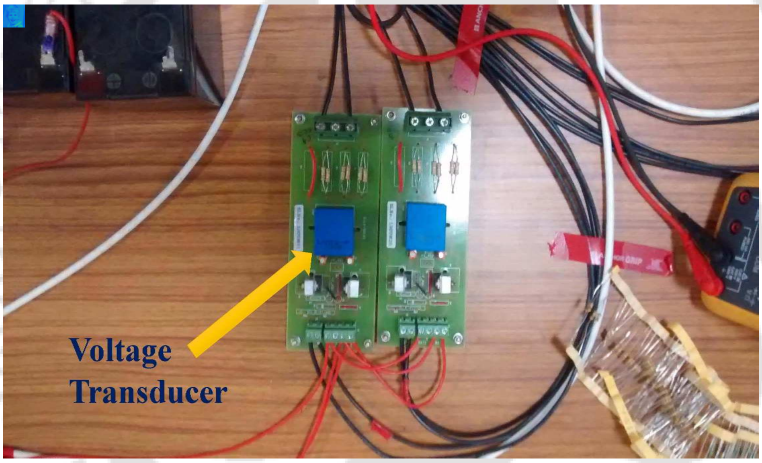

Figure 7.4: A voltage trasnducer.

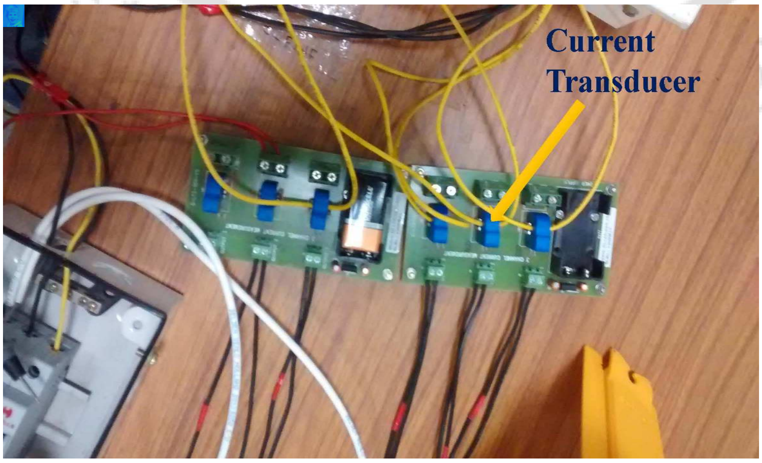

Figure 7.5: A current transducer.

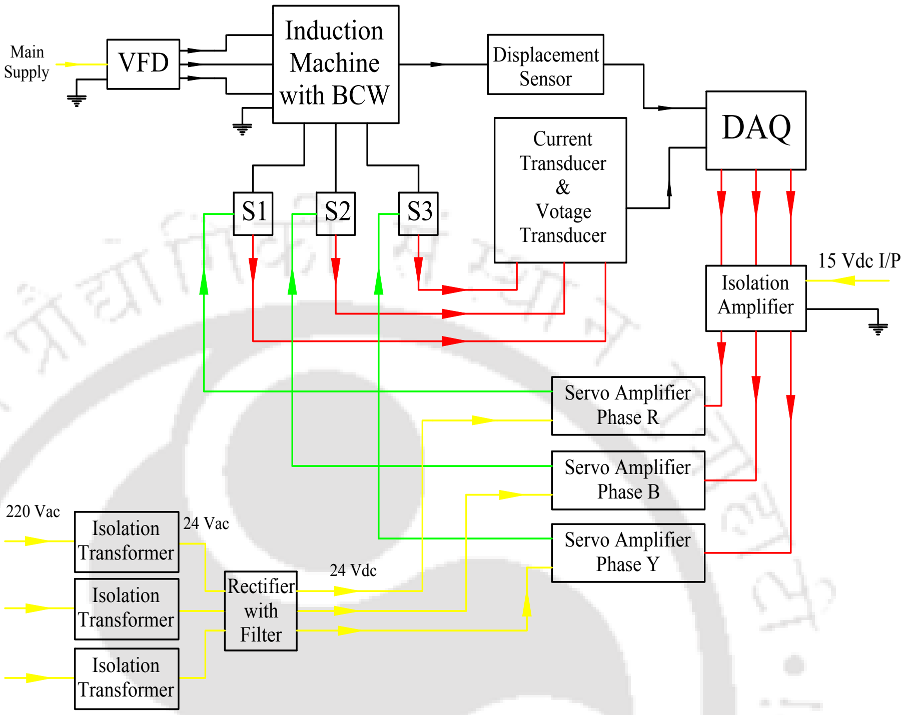

Figure 7.6: A flow diagram of connection of devices.

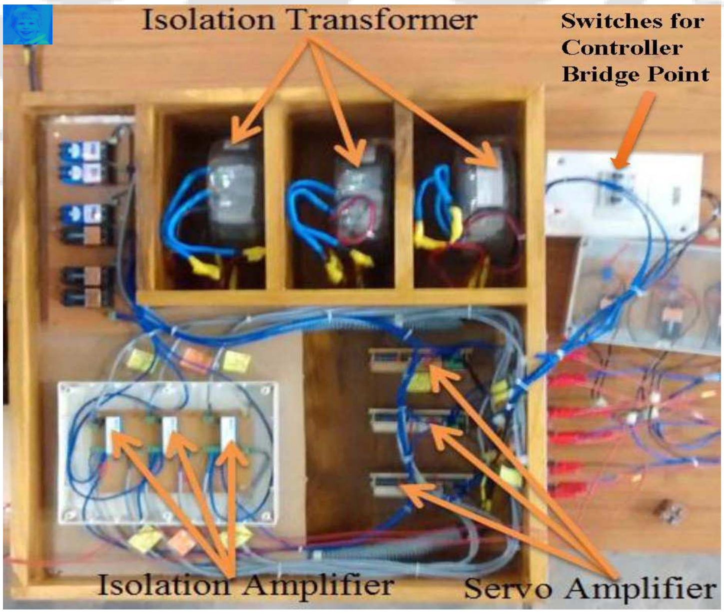

Figure 7.7: A controller set up for active vibration control.

7.3 Experimental analysis for the controller

The three phase controller bridge currents and corresponding rotor displacements (in X and Y-directions) have been measured for the main supply frequencies of 20Hz, 25Hz and 30Hz respectively. The three phase bridge currents and rotor orbits have been obtained for two cases, (i) Bridge OFF and (ii) Bridge ON (Controller). The switches for the controller bridge connections are shown in Figure 7.7. With reference to Figure 7.7, controller Bridge OFF condition means, the switches S1, S2 and S3 are in open condition. Controller Bridge ON condition means, the switches S1, S2 and S3 are in closed condition. The bridge currents were measured at bridge points S1, S2 and S3 as soon as the controller bridge points are short circuited. The comparison of three bridge currents and rotor displacements have been presented in the following section for only 20Hz, 25Hz and 30Hz. The results shown in the subsequent sections are obtained by using **Rotor I** which is supported by two mechanical bearings at its both ends.

7.3.1 Investigation without using external supply

Experiments have been carried out at different supply frequency such as 20Hz, 25Hz and 30Hz. Initially three phase bridge currents, bridge voltages and rotor orbits have been measured for three cases, (i) Bridge OFF, (ii) Bridge ON (Passive Control) and (iii) Controller Bridge ON without an external voltage source supply. The bridge currents and rotor responses in Bridge OFF and Bridge ON (passive control) have been presented in Chapter 5. The bridge currents and rotor orbits in Bridge OFF and controller Bridge ON are presented in this section.

7.3.1.1 Bridge currents in Bridge OFF and controller Bridge ON conditions

Figure 7.8 to Figure 7.10 show the Bridge currents in time domain at 20 Hz supply frequency in Bridge OFF and controller Bridge ON conditions. The corresponding FFT plots are presented in Figure 7.11 to 7.13. The frequency component of the bridge currents are 10 Hz ($f_s - f_r$), 20 Hz (f_s) and 30 Hz ($f_s + f_r$), where f_s is the frequency of the main supply and f_r is the rotor frequency. Since the machine has been run at no-load condition, then $f_r = \frac{1}{2} f_s$. Similar frequency components are obtained from Bridge ON condition as shown in Figures 5.25, 5.26 and 5.25. However, 60 Hz component of the bridge current is much higher in controller Bridge ON condition compared to Bridge ON condition.

Figures 7.14 and 5.23 shows the FFT of the bridge currents for main supply frequencies of 25

Hz and 30 Hz respectively in Bridge OFF and controller Bridge ON condition. The frequency components are similar to the frequency components obtained from Bridge ON condition as shown in Figures 5.31 and 5.32. It confirms that the controller can also be used for passive vibration control. However, $2f_s$ component is much higher in controller Bridge ON condition as compared to simple Bridge ON condition. The controller perhaps incorporates additional dynamics in the system. Further analysis are not carried out to identify the reason.

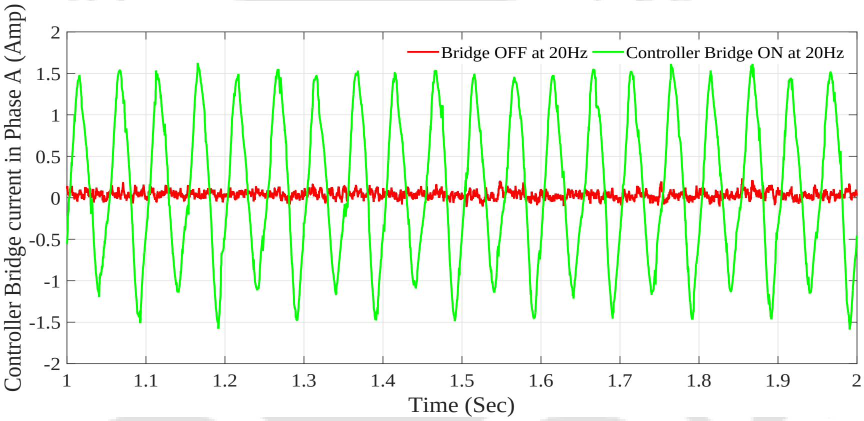

Figure 7.8: Phase A Bridge currents in time domain at 20 Hz supply frequency in Bridge OFF and controller Bridge ON conditions.

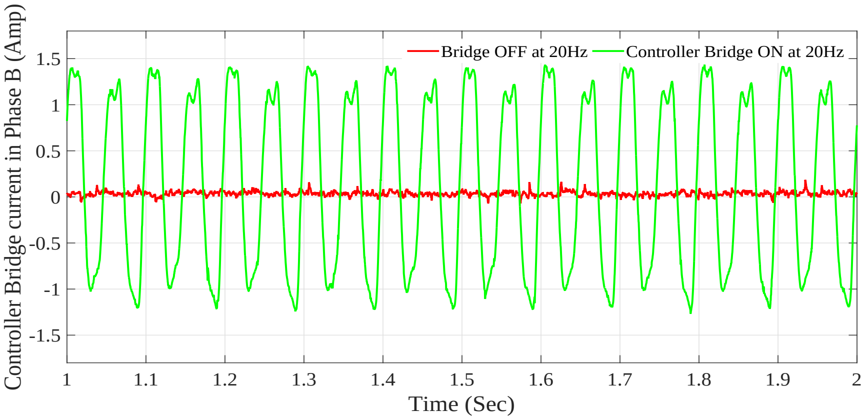

Figure 7.9: Phase B Bridge currents in time domain at 20 Hz supply frequency in Bridge OFF and controller Bridge ON conditions.

7.3.1.2 Rotor responses and rotor orbits in Bridge OFF and controller Bridge ON conditions

Figure 7.16 to Figure 7.17 show the FFT of the rotor responses in X and Y-directions respectively at 20 Hz supply frequency in Bridge OFF and controller Bridge ON conditions. The frequency component of the rotor responses along X- and Y- directions for a main supply frequency of 20 Hz are 0

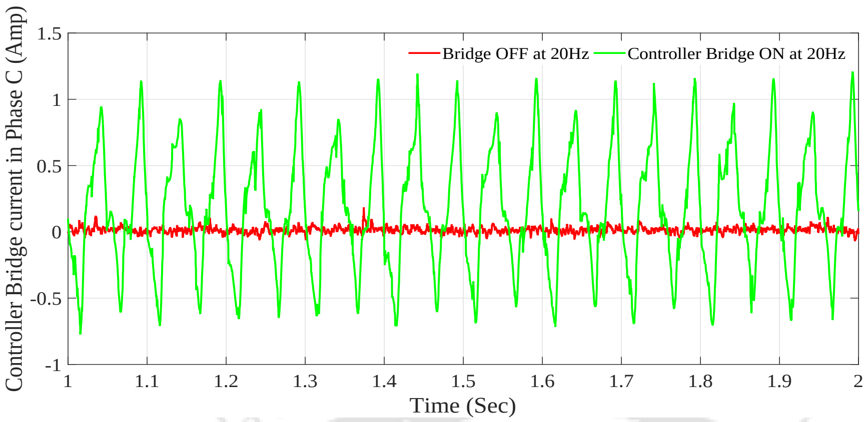

Figure 7.10: Phase C Bridge currents in time domain at 20 Hz supply frequency in Bridge OFF and controller Bridge ON conditions.

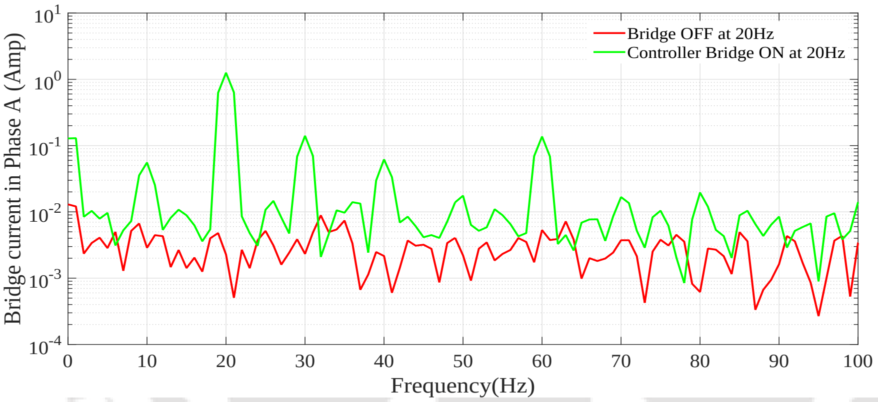

Figure 7.11: FFT of the Phase A Bridge currents at 20 Hz supply frequency in Bridge OFF and controller Bridge ON conditions.

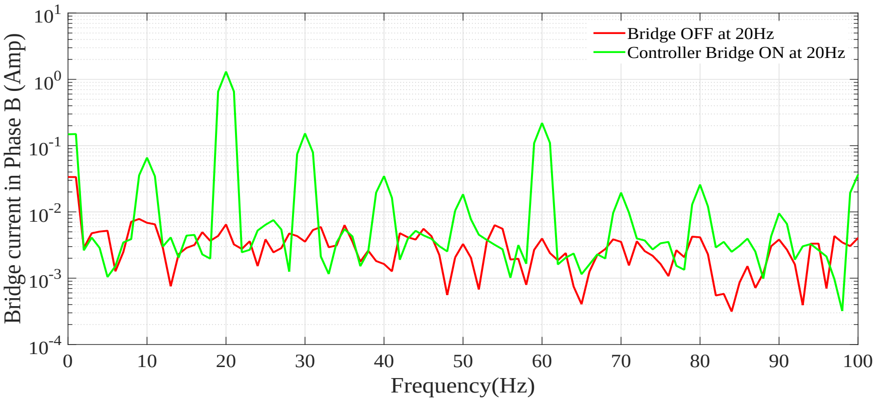

Figure 7.12: FFT of the Phase B Bridge currents at 20 Hz supply frequency in Bridge OFF and controller Bridge ON conditions.

Hz ($f_s - f_s$), 10 Hz ($f_s - \frac{1}{2}f_s$), 20 Hz (f_s), 30Hz ($f_s + \frac{1}{2}f_s$), 40 Hz ($2f_s$) and 50 Hz ($f_s + \frac{3}{2}f_s$) where f_s is the frequency of the main supply. The bridge currents also induced in the same frequencies for

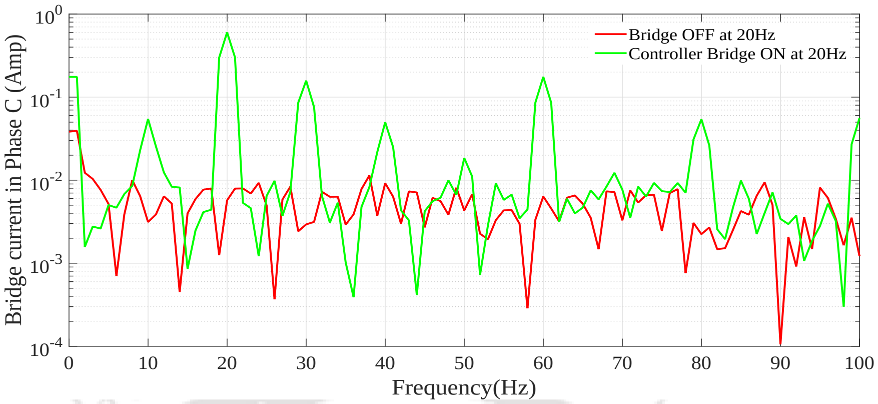

Figure 7.13: FFT of the Phase A Bridge currents at 20 Hz supply frequency in Bridge OFF and controller Bridge ON conditions.

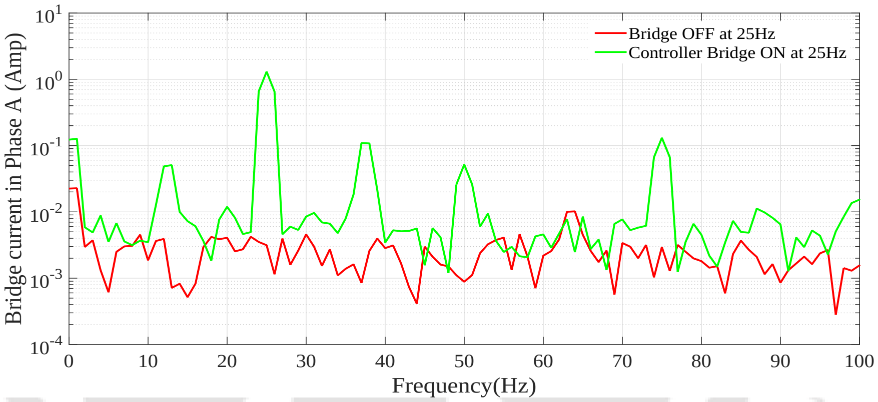

Figure 7.14: FFT of the Phase A Bridge currents at 25 Hz supply frequency in Bridge OFF and controller Bridge ON conditions.

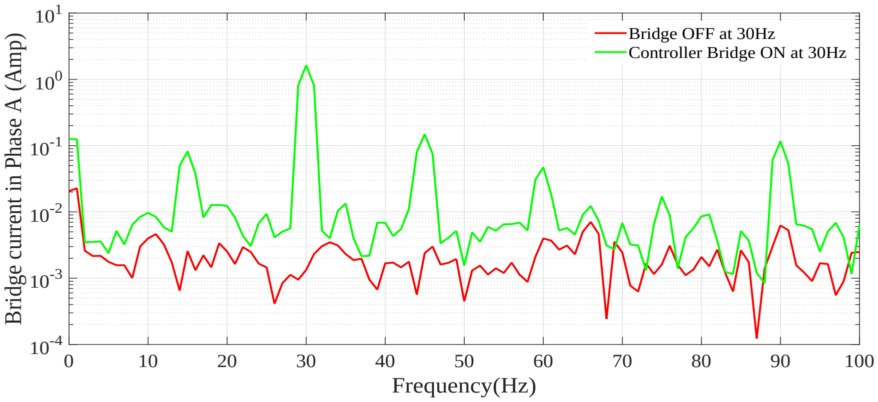

Figure 7.15: FFT of the Phase A Bridge currents at 30 Hz supply frequency in Bridge OFF and controller Bridge ON conditions.

simple Bridge ON condition and these figures are shown in Figures 5.36 and 5.37. However, simple Bridge ON condition reduces the $2f_s$ components of the rotor response but controller Bridge ON condition is unable to reduce the $2f_s$. Figure 7.18 to Figure 7.19 show the FFT of the rotor responses in X and Y-directions respectively at 25 Hz supply frequency in Bridge OFF and controller Bridge ON conditions. Figure 7.20 to Figure 7.21 show the FFT of the rotor responses in X and Y-directions respectively at 30 Hz supply frequency in Bridge OFF and controller Bridge ON conditions. Figures 7.22, 7.23 and 7.24 show the rotor orbits at 20 Hz, 25 Hz and 30 Hz supply frequency respectively in Bridge OFF and controller Bridge ON conditions. It has been observed that controller Bridge ON condition also reduce the static eccentricity by shifting the rotor towards the stator centre.

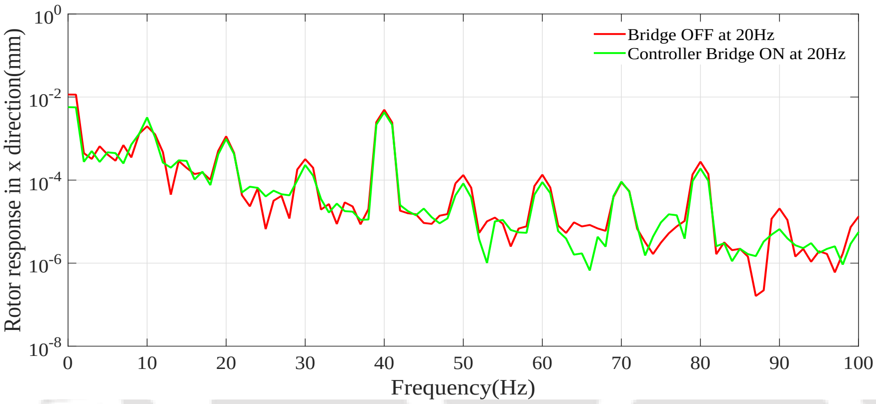

Figure 7.16: FFT of the rotor displacements in X-direction at Location 2 when the main supply frequency is 20Hz.

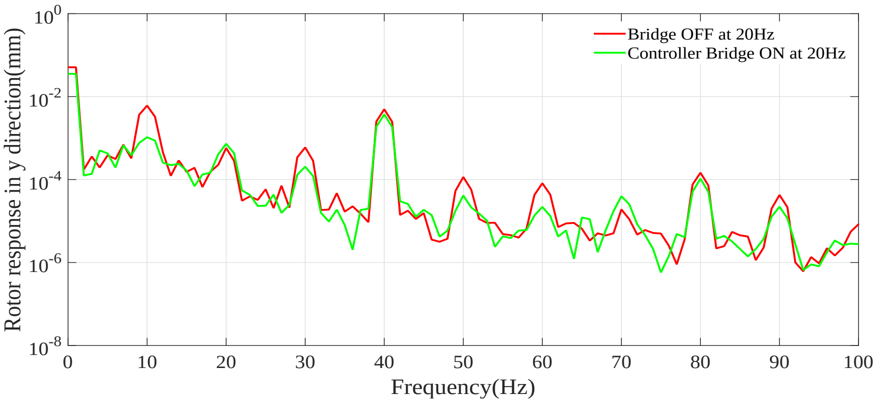

Figure 7.17: FFT of the rotor displacements in Y-direction at Location 2 when the main supply frequency is 20Hz.

7.4 Conclusions

The development of the controller for active vibration control has been presented. The bridge currents and rotor responses are obtained for main supply frequencies of 20 Hz, 25 Hz and 30 Hz for

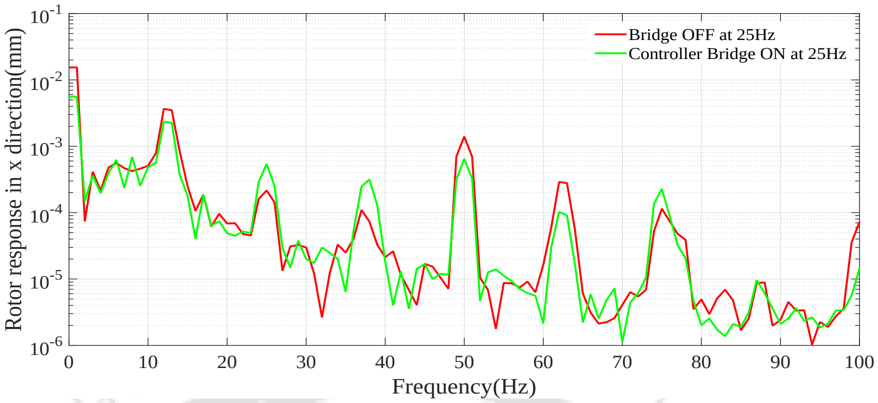

Figure 7.18: FFT of the rotor displacements in X-direction at Location 2 when the main supply frequency is 25Hz.

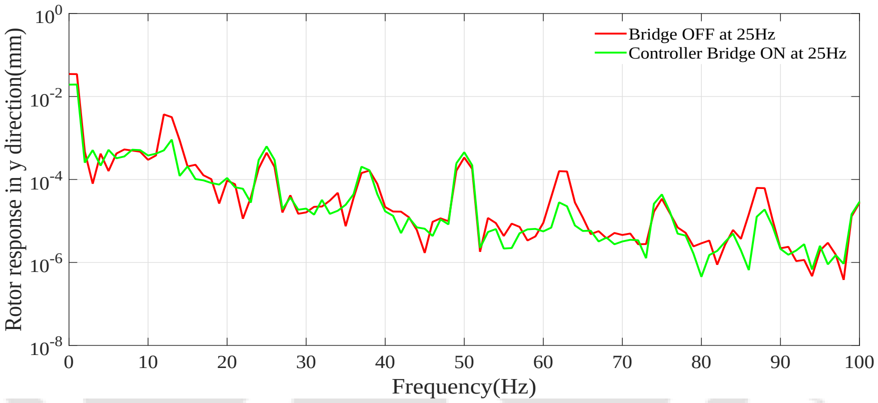

Figure 7.19: FFT of the rotor displacements in Y-direction at Location 2 when the main supply frequency is 25Hz.

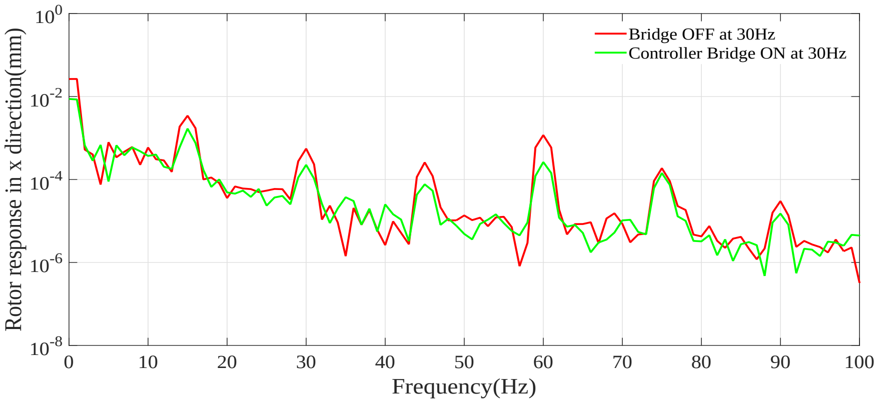

Figure 7.20: FFT of the rotor displacements in X-direction at Location 2 when the main supply frequency is 30Hz.

Bridge OFF and controller Bridge ON conditions. The frequency components of the bridge currents in controller Bridge ON condition are $(f_s - f_r)$, (f_s) and $(f_s + f_r)$, where f_s is the frequency of the

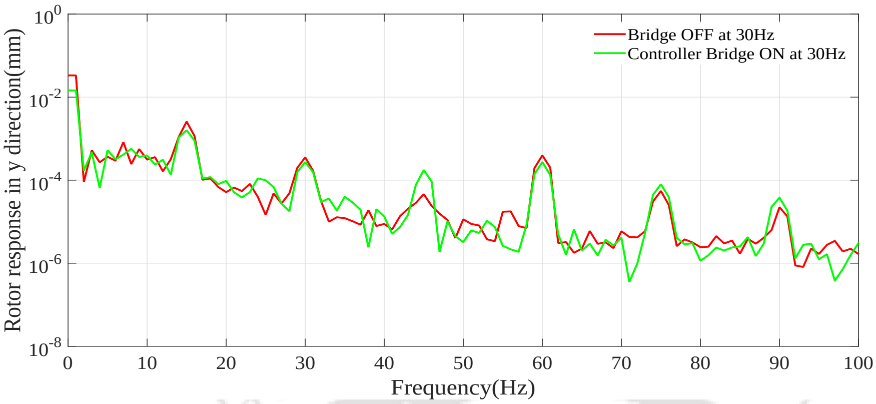

Figure 7.21: FFT of the rotor displacements in Y-direction at Location 2 when the main supply frequency is 30Hz.

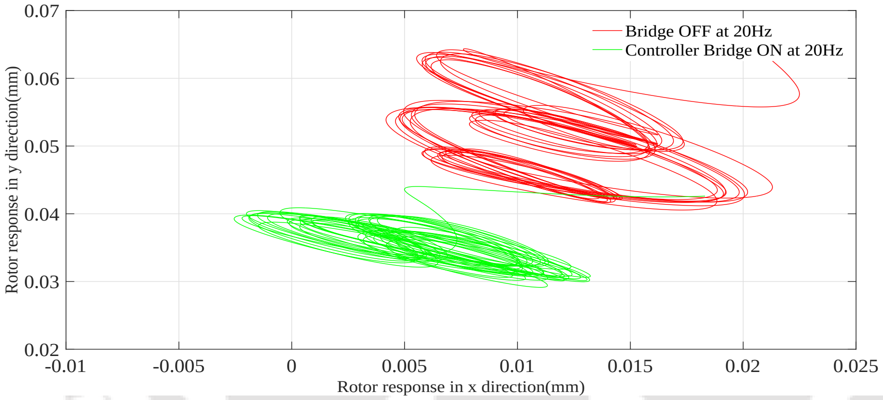

Figure 7.22: Rotor orbit at 20 Hz main supply frequency

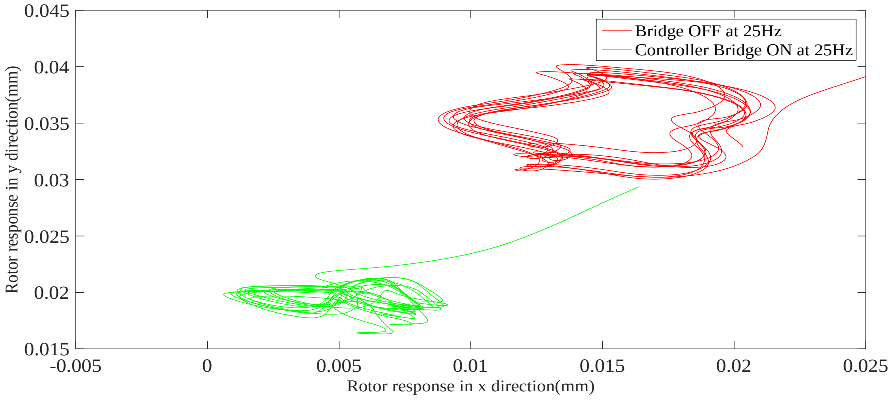

Figure 7.23: Rotor orbit at 25 Hz main supply frequency

main supply and f_r is the rotor frequency. Since the machine has been run at no-load condition, then $f_r = \frac{1}{2} f_s$. The frequency components are same as the simple Bridge ON condition. However, there is an additional frequency component of the bridge currents in controller Bridge ON condition and that

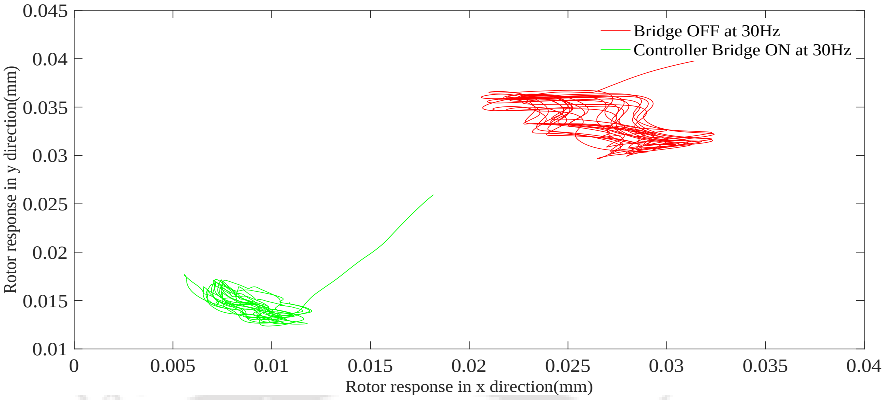

Figure 7.24: Rotor orbit at 30 Hz main supply frequency

component is $3f_s$. This perhaps introduce by the controller dynamics and needs further investigation. The frequency components of the rotor response are $(f_s - f_s)$, $(f_s - \frac{1}{2}f_s)$, (f_s), $(f_s + \frac{1}{2}f_s)$, $(2f_s)$ and $(f_s + \frac{3}{2}f_s)$ where f_s is the frequency of the main supply. Controller Bridge ON is unable to suppress the $2f_s$ component of the rotor response. There are challenges for active vibration control. If the switches of the bridge controller are short circuited, it changes the nature and magnitude of the current flowing across the bridges compared to the current flowing across the bridges when we directly short circuit the bridge using a wire as in case of passive control.

8

Conclusions and Future Work

8.1 Conclusions

The active vibration control of rotating machine is very important for the safe operation of any rotating machine. This thesis laid the foundation for active vibration control in an electrical machine using bridge configured winding in the stator. The relationship between the dynamic eccentricity and the bridge currents has been established. Similarly, the relationship between the static eccentricity and the bridge currents has also been established. It will help in the development of the controller using bridge configured winding.

8.2 Summary of contribution

The contribution of this thesis are enumerated below:

(i) A coupled magnetic field and electric circuit model of a 4-pole induction having bridge configured winding (BCW) in the stator has been developed. A finite element code has been developed in MATLAB to solve this coupled magnetic field and electric circuit equation. The airgap is divided into three radial bands and the outer two bands which are nearer to the stator are combined with stator. The machine is divided into there regions, i.e. stator which also includes the two radial bands of the airgap, rotor and the airgap. The finite element mesh for rotor and the stator are generated completely independently using 8-noded quadrilateral elements and are coupled using 6-noded triangular elements. Appropriate transformation matrices are proposed for transforming phase currents to the nodal currents. Unlike conventional stator winding scheme, BCW has six input voltages, i.e. three main voltages and three bridge voltages. Proper transformation matrix has been developed to accommodate six input voltages in the electric circuit equation. Bridge configured winding is a special stator winding scheme where the coils are connected in Wheatstone bridge format having two parallel branches. In the thesis when the mid-points of the bridge are not connected it is referred are Bridge OFF condition and when the mid-points of the bridge are short-circuited it is referred as Bridge ON condition. For an eccentric rotor in Bridge ON condition an EMF will induce to drive currents in the links connecting the mid-points of the bridge. These currents are called levitation currents or bridge currents. The transformation matrix is developed with an assumption that equal bridge currents will flow in the two parallel branches of the bridge configured winding. Crank-Nicolson method has been used to solve the coupled magnetic field and electric circuit equation. The magnetic vector potentials at each node, the main currents and the bridge currents are calculated from the analysis. For a concentric rotor the transverse forces acting on the rotor along $x-$ and $y-$ axes are zero. The magnetic vector potentials at each node, the main and bridge currents are calculated for three eccentricity conditions, i.e. static, dynamic and mixed of the rotor in Bridge ON condition. The corresponding transverse forces acting on the rotor are calculated. The frequency of the bridge currents (f_{bridge}) for static eccentricity is $f_{bridge} = f_s$, where f_s is the frequency of the main supply voltage. The frequency of the bridge currents (f_{bridge}) for dynamic eccentricity are $f_{bridge} = f_s \pm f_r$, where f_s is the frequency of the main supply voltage and f_r is the rotor frequency. $f_r = \frac{(1-s)f_s}{p}$, where s is the slip, f_s is the frequency of the main supply voltage and p is the pole pair of the machine. The frequency of the bridge currents f_{bridge} for mixed eccentricity are $f_{bridge} = f_s$ and $f_s \pm f_r$. The frequency components of the corresponding transverse forces acting on the rotor for static eccentricity are $0, 2f_s$. The frequency components of the corresponding transverse forces acting on the rotor for dynamic eccentricity are $f_s \pm f_{bridge}$ where $f_{bridge} = f_s \pm f_r$ and The frequency components of the corresponding transverse forces acting on the rotor for mixed eccentricity are $f_s \pm f_{bridge}$ where $f_{bridge} = f_s$ and $f_s \pm f_r$. The eccentricities i.e. static, dynamic and mixed have profound impact on the bridge currents. For static eccentricity f_s component of three bridge currents is a measure of the eccentricity present in the machine. For dynamic eccentricity $f_s \pm f_r$ components of the three bridge currents are measures of the eccentricity present in the machine. Similarly, for mixed eccentricity f_s and $f_s \pm f_r$ components of the three bridge currents are measures of the eccentricity present in the machine. When there is no load in the machine f_r will simply be $\frac{1}{2}f_s$. The results are shown in tabulated form in Chapter 3. The results are shown in tabulated form in Chapter 3.

(ii) The bridge configured winding can produce controllable transverse force without affecting the torque of the machine. The steady state analysis of an induction machine with BCW stator winding and the transient (or) rotary motion analysis of induction machine with BCW stator winding have been carried out using a commercial FE package called OPERA®. The Steady state analysis (AC Solver) has been used to find the machine parameters such as torque and winding currents. In this steady state analysis, the torque and winding currents are measured for each step of the speeds of the machine. The Rotating Machine solver (Opera-2d/RM) is a transient eddy current solver which is extended to include the effects of rigid body (rotating) motion. In this Rotating Machine solver, the torque and winding currents are measured in transient condition. A detail description about the working principle of bridge configured winding has been presented. The main currents and bridge currents have been calculated using the transient analysis when a dynamic eccentricity of 10% of the airgap length has been introduced.

(iii) An experimental setup has been developed. The setup has a 4-pole, three phase, 37 kW induction machine having squirrel cage rotor with bridge configured winding in the stator. The parameters of the original machine have been presented. The original stator winding is a three phase, double layer, 4-pole with concentrated winding. The original stator winding has been removed and replaced by a three phase, double layer and 4-pole distributed bridge configured winding. The devices used for the measurement of bridge currents, bridge voltages, main supply currents and main supply voltages have been explained. The measurements of main currents, main voltages, bridge currents, bridge voltages, rotor responses are obtained for up to a supply frequency of 60 Hz. The bridge currents, rotor responses along X- and Y- directions, rotor orbits for main supply frequencies of 20 Hz, 25 Hz, 30Hz, 40 Hz, 50 Hz and 60 Hz are presented in this Chapter. There is no load applied on this machine. The following are the key findings from the experimental results.

   (a) The results obtained from the experiments confirmed that the machine has mixed eccentricity.

   (b) The frequency components of the bridge currents are $f_s - \frac{1}{2}f_s$, f_s and $f_s + \frac{1}{2}f_s$, where f_s is the supply frequency.

   (c) The frequency components of the rotor responses are $(f_s - f_s)$, $(f_s - \frac{1}{2}f_s)$, (f_s), $(f_s + \frac{1}{2}f_s)$, $(2f_s)$ and $(f_s + \frac{3}{2}f_s)$, where f_s is the frequency of the main supply. The rotor responses confirmed that Bridge ON condition suppresses the $2f_s$ component of the UMP.

(d) The Bridge ON condition reduces the static eccentricity by shifting the rotor towards the stator centre.

(e) The numerical results obtained in Chapter 3 have been verified by the experimental results obtained in this Chapter. The frequency of the bridge currents are the measure of eccentricities present in the machine.

(f) The f_s component of the bridge current is a measure of static eccentricity in the machine and $\frac{1}{2}f_s$ and $\frac{3}{2}f_s$ components of the bridge currents are measure of dynamic eccentricity present in the machine.

(g) A relationship between the eccentricity present in the machine with the bridge currents can be developed.

(iv) An attempt has been made to develop a relationship between the eccentricity present in the machine with the bridge currents. Relationship between the dynamic eccentricity and bridge currents has been developed using experimental results. Known values of unbalance masses have been introduced in the rotor system to incorporate dynamic eccentricity in the system and the corresponding bridge currents are calculated. Relationship between the static eccentricity and bridge currents has been developed by carrying out numerical experiments.

- A set of experiments have been conducted to develop a relationship between known unbalance mass and the measured bridge currents. The peak amplitudes of the frequency components of three phase bridge currents for $0.5f_s$ and $1.5f_s$ were measured and plotted against the known unbalance masses.
- The known masses were added in the holes (Positions) of the perforated disc to develop the relationship between bridge currents and the known masses.
- Initially, the bridge currents were measured for **Rotor I**. The experiments were carried out at 10Hz, 15Hz, 20Hz, 25Hz, 30Hz and 50Hz for **Rotor I**. The known masses were in the range of 0 gm to 1000 gm with an increment of 50 gm for flexible **Rotor I**.

- It has been observed that there were no changes of the amplitudes in the three phase bridge currents with an increase in unbalance masses. Obviously, for all supply frequencies there were no noticeable changes in the amplitudes of the three phase bridge currents for $0.5f_s$ and $1.5f_s$.
- This may happen due to the high stiffness of **Rotor I**. So, it has been decided to replace rotor shaft **I** with a flexible shaft. The **Rotor I** has been replaced by **Rotor II**.
- The **Rotor III** is flexible in nature, so that the experiments were conducted at lower speeds in order to prevent the rotor and stator contact. The experiments were carried out at 8Hz, 9Hz, 10Hz,11Hz, 12Hz, 13Hz and 14Hz. The known masses were in range of 0 gm to 700 gm with an increment of 50 gm.
- It has been observed that there were changes of the amplitudes of the three phase bridge currents bridge currents for $0.5f_s$. The bridge currents were decreasing with an increase in known unbalance masses in the system for the Position 6, 7 and 8.
- It has been noticed that there were changes of the amplitudes of the three phase bridge currents bridge currents for $0.5f_s$. The bridge currents were increasing with an increase in known unbalance masses in the system for the Position 1, 2, 13, 14, 15 and 16.
- It has also been noticed that there were no significant changes of the amplitudes of the three phase bridge currents bridge currents for $0.5f_s$ for Positions 3,4,5,9,10,11 and 12.
- It has been observed that there were changes of the amplitudes of the three phase bridge currents bridge currents for $1.5f_s$. The bridge currents were decreasing with an increase in known unbalance masses in the system for Positions 6, 7, 8 and 9.
- It has been noticed that there were changes of the amplitudes of the three phase bridge currents bridge currents for $1.5f_s$. The bridge currents were increasing with an increase in known unbalance masses in the system for Position 1, 2, 13, 14, 15 and 16.
- It has also been noticed that there were no significant changes of the amplitudes of the three phase bridge currents bridge currents for $1.5f_s$ for Position 3, 4, 5, 9, 10, 11 and 12.

- It has been concluded that the position at which the peak amplitudes of the frequency components of the bridge currents are decreasing which means the unbalance pull by the known mass is acting against the actual unbalance pull present in the system. It has also been concluded that the position at which the peak amplitudes of the frequency components of the bridge currents are increasing which means the unbalance pull by the known mass is acting along the actual unbalance pull present in the system.
- As the eccentricity of the rotor increases, the unbalanced magnetic pull which acts along the smallest air gap also increases. This is due to the increase of the voltage difference between the bridge points. The 0.5 f_s and 1.5 f_s components of the generated bridge currents due to the difference of the voltages also increases. Similarly, the 0.5 f_s and 1.5 f_s components of the generated bridge currents due to the difference of the voltages decreases when the eccentricity decreases. When the known unbalance masses act opposite to the residual unbalance the eccentricity of the rotor decreases and the net result is the reduction of the 0.5 f_s and 1.5 f_s components of the generated bridge currents. Similarly, when the known unbalance masses act along the residual unbalance the eccentricity of the rotor increases and the net result is the increase of the 0.5 f_s and 1.5 f_s components of the generated bridge currents.
- A relationship between the static eccentricity and bridge currents is developed by conducting a series of numerical simulations.
- Three bridge currents are calculated for static eccentricity levels from 6.25% to 31.25% of the airgap length at a particular location of the rotor. Bridge currents vary linearly with the static eccentricity at least up to 31.25% of the airgap length.

A controller has been developed for the application of active vibration control. The bridge currents and rotor responses are obtained for main supply frequencies of 20 Hz, 25 Hz and 30 Hz for Bridge OFF and controller Bridge ON conditions.

- The frequency components of the bridge currents in controller Bridge ON condition are $(f_s - f_r)$, (f_s) and $(f_s + f_r)$, where f_s is the frequency of the main supply and f_r is the rotor frequency. Since the machine has been run at no-load condition, then $f_r = \frac{1}{2} f_s$. The frequency components are same as the simple Bridge ON condition. However, there is an additional frequency component of the bridge currents in controller Bridge ON condition and that component is $3 f_s$. This perhaps introduce by the controller dynamics and needs further investigation.

- The frequency components of the rotor response are $(f_s - f_s)$, $(f_s - \frac{1}{2} f_s)$, (f_s), $(f_s + \frac{1}{2} f_s)$, $(2 f_s)$ and $(f_s + \frac{3}{2} f_s)$ where f_s is the frequency of the main supply. Controller Bridge ON is unable to suppress the $2 f_s$ component of the rotor response. There are challenges for active vibration control.
- If the switches of the bridge controller are short circuited, it changes the nature and magnitude of the current flowing across the bridges compared to the current flowing across the bridges when we directly short circuit the bridge using a wire as in case of passive control.

8.3 Future work

Based on the work presented in the thesis the following direction is suggested as possible future work,

- A coupled electromagnetic field equation and electric circuit equation has been developed. However, it is important to couple the motion equation to fully understand the electromechanical interactions in an electrical machine. The rotor model can be incorporated in future study of electromechanical interactions of electrical machines.

- Passive vibration control capability of the bridge configured winding has been demonstrated. It is required to develop the close loop active control of vibration.

- There will be losses when an additional magnetic field is incorporated in an electrical machine. The calculation of loss can be taken in future.

- Thermal calculation of an electrical machine with bridge configured winding will be an important study in future.

Bibliography

[1] W. K. S. Khoo, "Bridge configured winding for polyphase self-bearing machines," *IEEE Transactions on Magnetics*, vol. 41, no. 4, pp. 1289–1295, 2005.

[2] H. Frohne, "The practical importance of unbalanced magnetic pull, possiblities of calculating and damping it," *CONTI ELEKTRO BERICHTE*, vol. 13, pp. 81–92, December 1967.

[3] K. J. Binns and M. Dye, "Identification of principal factors causing unbalanced magnetic pull in cage induction motors," *IEE Proceedings*, vol. 120, no. 3, pp. 349–354, March 1973.

[4] D. G. Dorrell and A. C. Smith, "Calculation of ump in induction motors with series or parallel winding connections," *IEEE Transaction on Energy Conversion*, vol. 9, no. 2, pp. 304–310, June 1994.

[5] R. Belmans, A. Vandenput, and W. Geysen, "Calculation of the flux density and the unbalanced magnetic pull in two pole induction machines," *Archives of Elektrotechnik*, vol. 70, pp. 151–161, 1987.

[6] R. Belmans, W. G. H. Jordan, and A. Vandenput, "Unbalanced magnetic pull in three phase two pole induction motors with eccentric rotor," *IEEE Conference Publication*, pp. 65–69, 1982.

[7] A. C. Smith and D. G. Dorrell, "Calculation and measurement of unbalanced magnetic pull in cage induction motors with eccentric rotors. part 1: Analytical model," *IEE Proceedings of Electrical Power Applications*, vol. 143, no. 3, pp. 193–201, May 1996.

[8] ——, "Calculation and measurement of unbalanced magnetic pull in cage induction motors with eccentric rotors. part 2: Experimental investigation," *IEE Proceedings of Electrical Power Applications*, vol. 143, no. 3, pp. 202 – 210, May 1996.

[9] A. Arkkio, M. Antila, K. Pokki, A. Simon, and E. Lantto, "Electromagnetic force on a whirling cage rotor," *IEE Proceedings of Electrical Power Applications*, vol. 147, no. 5, pp. 353–360, September 2000.

[10] A. Tenhunen, "Finite element calculation of ump and circulating current between parallel windings in induction with non-uniform eccentric motor," *Proceedings of Electromotion'01*, pp. 19–24, June 2001.

[11] A. D. Gerlando, G. M. Fogila, and R. Perini, "Analytical modelling of ump in isotropic electrical machines," in *2008 18th International Conference on Electrical Machines*, September 2008.

[12] M. Bradford, "Unbalanced magnetic pull in a 6-pole induction motor," *Proceedings of the Institution of Electrical Engineers*, vol. 115, no. 11, pp. 1619–1627, November 1968.

[13] R. Belmans, A. Vandenput, and W. Geysen, "Influence of unbalanced magnetic pull on the radial stability of flexible-shaft induction machines," *IEE Proceedings B - Electric Power Applications*, vol. 134, no. 2, pp. 101–109, March 1987.

[14] D. G. Dorrell and M.-F. Hsieh, "Calculation of radial forces in cage induction motors at start- the effect of rotor differential," *IEEE Transaction on Magnetics*, vol. 46, no. 8, pp. 3029–3032, August 2010.

[15] A. Arkkio, “Unbalanced magnetic pull in cage induction motors with asymmetry in rotor structures,” in *1997 Eighth International Conference on Electrical Machines and Drives (Conf. Publ. No. 444)*, September 1997.

[16] D. G. Dorrell, “Experimental behaviour of unbalanced magnetic pull in 3-phase induction motors with eccentric rotors and the relationship with tooth saturation,” *IEEE Transactions on Energy Conversion*, vol. 14, no. 3, pp. 304–309, September 1999.

[17] M. Berman, “On the reduction of magnetic pull in induction motors with off-centre rotor,” in *Industry Applications Society Annual Meeting1993, Conference Record of the 1993 IEEE 1993*, 1993.

[18] D. Guo, F. Chu, and D. Chen, “The unbalanced magnetic pull and its effects on vibration in a three-phase generator with eccentric rotor,” *Journal of Sound and Vibration*, vol. 254, no. 2, pp. 297–312, 2002.

[19] B. Yang, Y. Kim, and B. Son, “Instability and imbalance response of large induction motor rotor by unbalanced magnetic pull,” *Journals of Vibration and Control*, vol. 10, pp. 447–460, 2004.

[20] A. Tenhunen, T. P. Holopainen, and A. Arkkio, “Effect of saturation on the forces in induction motors with whirling cage rotor,” *IEEE Transactions on Magnetics*, vol. 40, no. 2, pp. 766–769, March 2004.

[21] P. Pennacchi and L. Frosini, “Dynamical behaviour of a three-phase generator due to unbalanced magnetic pull,” *IEE Proceedings in Electrical Power Applications*, vol. 152, no. 6, pp. 1389–1400, November 2005.

[22] P. Pennacchi, “Computational model for calculating the dynamical behaviourof generators caused by unbalanced magnetic pulland experimental validation,” *Journal of Sound and Vibrations*, vol. 12, pp. 332–353, 2008.

[23] Y. Calleecharan and J. O. Aidanpaa, “Stability analysis of an hydropower generator subjected to unbalanced magnetic pull,” *IET science and Mesurement and Technology*, vol. 5, no. 6, pp. 231–243, 2011.

[24] S. A. Swann, “Effect of rotor eccentricity on the magnetic field in the air-gap of a non-salient-pole machine,” *Proceedings of the Institution of Electrical Engineers*, vol. 110, no. 5, pp. 903–915, 1963.

[25] A. J. Ellison and S. J. Yang, “Effects of rotor eccentricity on acoustic noise from induction machines,” *Proceedings of the Institution of Electrical Engineers*, vol. 118, no. 1, pp. 174–184, 1971.

[26] R. L. Stoll, “Simple computational model for calculating the unbalanced magnetic pull on a two-pole turbogenerator rotor due to eccentricity,” *IEE Proceedings of Electrical Power Application*, vol. 144, no. 4, pp. 263–270, July 1997.

[27] D. G. Dorrell, W. T. Thomson, and Roach, “Analysis of airgap flux, current, and vibration signals as a function of the combination of static and dynamic airgap eccentricity in 3-phase induction motors,” *IEEE Transaction on Industry Applications*, vol. 33, no. 1, pp. 24–34, 1997.

[28] G. M. Joksimovic, “Dynamic simulation of cage induction machine with air-gap eccentricity,” *IEE Proceedings of Electrical ower Applications*, vol. 152, no. 4, pp. 803–811, July 2005.

[29] D. Hyun, S. Lee, V. Hong, S. B. Lee, and S. Nandi, “Detection of air-gap eccentricity for induction motors using the single-phase rotation test,” *IEEE Transactions on Energy Conversion*, vol. 27, no. 3, pp. 689–696, September 2012.

[30] M. J. Debortoli, Salon, D. Burow, and C. Slavik, “Effects of rotor eccentricity and parallel windings on induction machine behavior: A study using finite element analysis,” *IEEE Transactions on Magnetics*, vol. 29, no. 2, pp. 1676–1682, March 1993.

[31] A. Arkkio and A. Burakov, “Comparision of the ump mitigation by the parallel paths in the stator and rotor windings,” *IEEE Transaction on Magnetics*, vol. 43, no. 12, pp. 4083–4088, January 2008.

[32] W. Oliveira, M. Uemori, J. Rocha, and R. Carlson, “Reduction of unbalanced magnetic pull (ump) due to equipotential connections among parallel circuits of the stator winding,” in *IEEE International Electric Machines and Drives Conference*, May 2009.

[33] D. G. Dorrell, J. K. Shek, M. A. Mueller, and M. Hsieh, “Damper windings in induction machines for reduction of unbalanced pull and bearing wear,” *IEEE Transactions on*, vol. 49, no. 5, pp. 2206–2216, 2013.

[34] I. P. Brown, D. M. Ionel, and D. G. Dorrell, “Influence of parallel paths on current-regulated sine-wave interior-permanent-magnet machines with rotor eccentricity,” *IEEE Transaction on Industry Applications*, vol. 48, no. 2, pp. 642–652, April 2012.

[35] T. P. Holopainen, “Electromechanical interaction in rotordynamics of cage induction motors,” *Doctoral Dissertation, Helsinki University*, pp. 1–86, 2004.

[36] A. Laiho, T. P. Holopainen, P. Klinge, and A. Arkkio, “Distributed model for electromechanical interaction in rotordynamics of cage rotor electrical machines,” *Journal of Sound and Vibrations*, vol. 302, pp. 683–698, 2007.

[37] A. Laiho, K. Tammi, K. Zenger, and A. Arkkio, “A model-based flexural rotor vibration control in cage induction electrical machines by a built-in force actuator,” *Electrical Engineering*, vol. 90, no. 6, pp. 407–421, 2008.

[38] P. Pennacchi, “Nonlinear effects due to electromechanical interaction in generators with smooth poles,” *Nonlinear Dynamics*, vol. 57, no. 4, pp. 607–622, 2009.

[39] A. Arkkio, B. R. Nepal, and A. Sinervo, “Electromechanical interaction in a synchronous reluctance machine,” *SPEEDAM 2010, International Symposium on Power Electronics, Electrical Drives, Automation and Motion*, pp. 501–506, 2010.

[40] H. Haase, H. Jordan, and K. P. Kovacs, “Vibratory forces as a result of shaft fluxes with two-pole induction machines,” *Electrotech (ETZ)*, vol. 93, pp. 485–486, 1972.

[41] K. P. Kovacs, “Two-pole induction motor vibrations caused by homopolar alternating fluxes,” *IEEE Transaction on Power Appratus and Systems*, vol. 96, no. 4, pp. 1105–1108, July 1977.

[42] A. Laiho, A. Sinervo, J. Orivuori, K. Tammi, A. Arkkio., and K. Zenger, “Attenuation of harmonic rotor vibration in a cage rotor induction machine by a self-bearing force actuator,” *IEEE Transactions on Magnetics*, vol. 45, no. 12, pp. 5388–5398, December 2009.

[43] A. Sinervo, A. Laiho, and A. Arkkio, “Low-frequency oscillation in rotor vibration of a two-pole induction machine with extra four-pole stator winding,” *IEEE Transactions on Magnetics*, vol. 47, no. 9, pp. 2292–2302, September 2011.

[44] A. Sinervo, T. Jokela, and A. Arkkio, “Controlling rotor vibrations of a two-pole induction machine with unipolar actuator,” *IEEE Transactions on Magnetics*, vol. 48, no. 7, pp. 2205–2210, July 2012.

[45] J. R. Cameron, W. T. Thomson, and A. B. Dow, “Vibration and current monitoring for detecting airgap eccentricity in large induction motors,” *IEE Proceedings*, vol. 133, no. 3, pp. 155–163, May 1986.

[46] S. Williams, R. C. Healey, J. D. Lloyd, and J. L. Tevaawerk, “Rotor cage anomalies and ump pull in single-phase induction motors.” *IEEE TRANSACTIONS ON INDUSTRY APPLICATIONS*, vol. 33, no. 6, pp. 1553–1562, November 1997.

[47] M. E. H. Benbouzid, “A review of induction motors signature analysis as a medium for faults detection,” *IEEE Transactions on Industrial Electronics*, vol. 47, no. 5, pp. 984–993, October 2000.

[48] P. V. J. Rodriguez, A. Belahcen, A. Arkkio, A. Lahio, and J. A. A. Daviu, “Airgap force distribution and vibration pattern of induction motors under dynamic eccentricity,” *Electrical Engineering*, vol. 90, no. 3, pp. 209–218, February 2008.

[49] V. Fireteanu and P. Taras, “Diagnosis of induction motor rotor faults based on finiite element evaluation of voltage harmonics of coil sensors,” *IEEE Sensor Application Symposium.*, pp. 1–5, March 2012.

[50] J. F. Gieras and J. Saari, “Performance calculation for a high-speed solid-rotor induction motor,” *IEEE Transaction on Industrial Electronics.*, vol. 59, no. 6, pp. 2689–2700, 2012.

[51] S. P. Loiu and W. Wang, “Indirect rotor position sensing for switched reluctance motor using search coil,” *IEEE Conference-CCECE’96.*, pp. 939–942, 1996.

[52] H. B. Ertan and O. Keysan, “External search coil as a means of measuring rotor speed of an induction motor,” *IEEE-ELECTROMOTION,2009- ‘Electric Drives’ Joint Symposium.*, pp. 1–6, 2009.

[53] J. P. A. Bastos and N. Sadowski, *Electromagnetic Modeling by Finite Element Methods.* CRC Press, 2003.

[54] S. Salon, M. DeBortoli, and R. Palma, “Coupling of transient fields, circuits, and motion using finite element analysis,” *Journal of Electromagnetic Waves and Applications*, vol. 4, no. 11, pp. 1077–1106, 1990.

[55] V. N. Savov, Z. D. Georgiev, and E. S. Bohdanov, “Analysis of cage induction motor by means of the finite element method and coupled system of field, circuit and motion equations,” *Journal of Electrical Engineering*, vol. 80, no. 1, pp. 21–28, 1997.

[56] A. Laiho, K. Kalita, K. Tammi, and S. Garvey, “Dynamics of bridge configured built-in force actuator for vibration control in four-pole cage induction machine,” in *18th International congress on sound and vibration*, July 2011.

List of Publications

Journal Publications

1 **Natesan S**, Kalita K, Venkatesu S, ”**Numerical and Experimental Investigation of Bridge Currents of an Induction Machine Equipped with Bridge Configured Winding**,” *International Journal of Electrical and Computer Engineering,IJECE*, Vol. 5, No. 6, December 2015, 1262-1274, ISSN: 2088-8708.

Conferences

1 **Natesan Sivaramakrishnan**, Kumar Gaurav, Kalita Karuna, Rahman Mafidur, ”**Unbalance Detection in Flexible Rotor Using Bridge Configured Winding Based Induction Motor**,” *Proceedings of the 1st International and 16th National Conference on Machines and Mechanisms (iNaCoMM2013)*, IIT Roorkee, India, Dec 2013, pp 312-317.

2 **Sivaramakrishnan Natesan**, Kumar G., Saikia, D, Kalita K., Tammi, K, ”**Experimental investigation of equalizing voltages in induction machine equipped with bridge configured winding**,” *Proceedings of the National Symposium on Rotor Dynamics (NSRD-2014)*, Feb 2014.

3 Karuna kalita, **Sivaramakrishnan Natesan**, Gaurav Kumar, and kari Tammi, ”**Vibration Control in Electrical Machines using Built-in Force Actuator**,” *Proceedings of the 9th IFToMM International Conference of Rotor Dynamics, Mechanisms and Machine Science*, DOI10.1007/978-3-319-06590-8.

4 Kumar G, Choudhury M.D, **Natesan S**, Kalita K, ”**Design and Analysis of a Radial Active Magnetic Bearing for Vibration Control**,” *Proceedings of the 12th International Conference on Vibration Problems (ICOVP)*, IIT Guwahati, (14-17th December, 2015).